N° d'ordre: 2011-ISAL-0026
Année 2011

Thèse

DEVELOPMENT OF NUMERICAL MODELS OF VERTICAL GROUND HEAT EXCHANGERS AND EXPERIMENTAL VERIFICATION:
Domain Decomposition and State Model Reduction Approach

Présentée devant
L'institut national des sciences appliquées de Lyon (INSA de Lyon)

Pour obtenir
Le grade de docteur

Formation doctorale: Génie Civil
École doctorale: Mécanique, Énergétique, Génie Civil, Acoustique (MEGA)
Laboratoire d'accueil: Centre de Thermique de Lyon (CETHIL)

Par
Eui-Jong KIM

Directeur de thèse:
Prof. Jean-Jacques ROUX

Soutenue le 21 mars 2011 devant la Commission d'examen

Jury:

BERNIER	Michel	Professeur (Ecole Polytechnique de Montréal)	Examinateur
CAURET	Odile	Docteur (EDF R&D)	Examinateur
LEFEBVRE	Gilles	Professeur (CERTES, Université Paris-Est)	Rapporteur
MARCHIO	Dominique	Professeur (CEP, MINES Paris Tech)	Examinateur
ROUX	Jean-Jacques	Professeur (CETHIL, INSA de Lyon)	Examinateur
SPITLER	Jeffrey	Professeur (Oklahoma State University)	Rapporteur

« Celui qui trouve sans chercher est celui
qui a longtemps cherché sans trouver. »

Gaston Bachelard (1884-1962)
Philosophe épistémologue et essayiste français

그 사랑으로 말미암아...

List of (Écoles Doctorales)

SIGLE	ECOLE DOCTORALE	NOM ET COORDONNEES DU RESPONSABLE
CHIMIE	**CHIMIE DE LYON**	M. Jean Marc LANCELIN Université Claude Bernard Lyon 1 Bâtiment CPE 43 bd du 11 novembre 1918 69622 VILLEURBANNE Cedex Tél : 04.72.43 13 95 lancelin@hikari.cpe.fr
E.E.A.	**ELECTRONIQUE, ELECTROTECHNIQUE, AUTOMATIQUE**	M. Alain NICOLAS Ecole Centrale de Lyon Bâtiment H9 36 avenue Guy de Collongue 69134 ECULLY Tél : 04.72.18 60 97 eea@ec-lyon.fr
E2M2	**EVOLUTION, ECOSYSTEME, MICROBIOLOGIE, MODELISATION**	M. Jean-Pierre FLANDROIS UMR 5558 Université Claude Bernard Lyon 1 Bât G. Mendel 69622 VILLEURBANNE Cédex Tél : 04.26.23.59.50 Fax 04.26.23.59.49 e2m2@biomserv.univ-lyon1.fr
INFOMATHS	**INFORMATIQUE ET MATHEMATIQUE POUR LA SOCIETE**	M. Alain MILLE Université Claude Bernard Lyon 1 LIRIS - INFOMATHS Bâtiment Nautibus 43 bd du 11 novembre 1918 69621 VILLEURBANNE Cedex Tél : 04.72. 44 82 94 Fax 04 72 43 13 10 infomaths@bat710.univ-lyon1.fr
EDISS	**INTERDISCIPLINAIRE SCIENCES-SANTE**	M. Didier REVEL Hôpital Cardiologique de Lyon Bâtiment Central 28 Avenue Doyen Lépine 69500 BRON Tél : 04.72.68 49 09 Fax :04 72 35 49 16 Didier.revel@creatis.uni-lyon1.fr
Matériaux	**MATERIAUX DE LYON**	M. Jean Marc PELLETIER INSA de Lyon MATEIS Bâtiment Blaise Pascal 7 avenue Jean Capelle 69621 VILLEURBANNE Cédex Tél : 04.72.43 83 18 Fax 04 72 43 85 28 Jean-marc.Pelletier@insa-lyon.fr
MEGA	**MECANIQUE, ENERGETIQUE, GÉNIE CIVIL, ACOUSTIQUE**	M. Hamda BENHADID Université Claude Bernard Lyon 1 UFR de Mécanique Bâtiment OMEGA 2ème étage 43 Boulevard du 11 novembre 1918 69622 VILLEURBANNE Tél :04.72.43.10.04 Fax : 04 72 44 80 54 benhadid@mecalpha.univ-lyon1.fr
ScSo	**ScSo**	M. OBADIA Lionel Université Lyon 2 86 rue Pasteur 69365 LYON Cedex 07 Tél : 04.78.77.23.88 Fax : 04.37.28.04.48 Lionel.Obadia@univ-lyon2.fr

Acknowledgments

During the course of my PhD, I've realized that all the successful research work can be achieved by discussions, collaborations, and support as we are not alone in life. It is a pleasure to thank those who have been so helpful to me. The following lines are dedicated to all of them.

First of all, I wish to express my gratitude to Professor Jean-Jacques Roux, the thesis supervisor and mentor, who was abundantly helpful and offered invaluable assistance, support and guidance. His experience on the subject of reduced models has always given me plenty of inspiration. His support was not limited to the research work, but his kindness since my master course and his offer to pursue a PhD have eventually made me a better individual. To me, it was also very fortunate to have another supervisor, Professor Michel Bernier. His abundant knowledge in the geothermal domain has guided me from the inception of this work up to the final stage, enabling me to develop an understanding of the subject. The precious discussions we had during my stay in Montréal will not be forgotten. I would also like to deeply thank Doctor Odile Cauret, the thesis promoter, who always gives her confidence to me. Her industrial and technical point of view helped me keep a balance between academic research and the real world. Furthermore, her contribution to the experimental set-up and results analysis were so valuable to this work. Without all of them, this thesis would not have been possible.

I wish to thank Professors Jeffrey Spitler and Gilles Lefebvre for their interest in my research work and for their willingness to be reviewers of this thesis. I also want to thank Professor Dominique Marchio who has agreed to participate in the jury board. Personally, it is a great honor to have such prominent jury members. I look forward to hearing valuable remarks.

The EDF (Électricité de France) research center has supported me throughout this work. Special thanks go to research directors Doctors Pascal Dalicieux and Jean-Luc Hubert. Whenever I met them, they were very supportive.

The discussions and cooperation with all of my colleagues at CETHIL (Centre de Thermique de Lyon) have contributed substantially to this work as well. I would like to mention here Ion, Damien, Tiberiu, Pascal, Valentin, Brigitte, Noël, Nathanaël, Johann, Kontantinos. I am also indebted to Associate Professors Gilles Rusaouen and Frédéric Kuznik for their precious comments and solutions. Thanks also go to Christine for her continued support. Together with them, my friends met here in Lyon have also encouraged and inspired me through daily discussions and jokes on various subjects.

I owe my deepest gratitude to my parents and my family for their endless love, support, and presence. In fact, their instructions and priorities in life have shaped me. Last but not least, I want to express my appreciation to my fiancé Yéram for her patience, encouragement, and love especially in these moments.

I would like to thank everybody as well as express my apology that I could not mention everyone.

Eui-Jong KIM

Abstract

Ground-source heat pump systems with vertical ground heat exchangers (GHE) are gaining popularity worldwide for their higher coefficients of performance and lower CO_2 emissions. However, the higher initial cost of installing the borehole GHEs is a main obstacle to spread the systems. To reduce the required total GHE length and efficiently operate the systems, various systems such as hybrid ones (e.g. solar heat injection) have recently been introduced.

Accurate prediction of heat transfer in and around boreholes of such systems is crucial to avoid costly overdesigns or catastrophic failures of undersized systems as it is for typical GCHP systems. However, unlike the traditional sizing methods, it is increasingly required to take into account detailed borehole configuration and transient effects (e.g. short circuit effects between U-tubes). Many of the existing GHE models have been reviewed. Some of these models have serious limitations when it comes to transient heat transfer, particularly in the borehole itself.

Accordingly, the objective of this thesis is to develop a model that is capable to accurately predict thermal behaviors of the GHEs. A precise response to input variations even in a short time-step is also expected in the model. The model also has to account for a correct temperature and flux distribution between the U-tubes and inside the borehole that seems to be important in the solar heat injection case.

Considering these effects in 3D with a detailed mesh used for describing the borehole configurations is normally time-consuming. This thesis attempts to alleviate the calculation time using state model reduction techniques that use fewer modes for a fast calculation but predict similar results. Domain decomposition is also envisaged to sub-structure the domain and vary the time-step sizes. Since the decomposed domains should be coupled one another spatially as well as temporally, new coupling methods are proposed and validated particularly in the FEM.

For the simulation purpose, a hybrid model (HM) is developed that combines a numerical solution, the same one as the 3D-RM but only for the borehole, and well-known analytical ones for a fast calculation.

An experimental facility used for validation of the model has been built and is described. A comparison with the experimental results shows that the relatively fast transients occurring in the borehole are well predicted not only for the outlet fluid temperature but also for the grout temperatures at different depths even in very short time-steps.

Even though the current version of 3D-RM is experimentally validated, it is still worth optimizing the model in terms of the computational time. Further simulations with the 3D-RM are expected to be carried out to estimate the performance of new hybrid systems and propose its appropriate sizing with correspondent thermal impacts on the ground. Finally, the development of the model 3D-RM can be an initiation to accurately model various types of GHE within an acceptable calculation time.

Keywords: ground heat exchanger, GCHP, state model reduction technique, domain decomposition, experimentation, hybrid model, TRNSYS

Résumé

Dans le contexte énergétique actuel, les pompes à chaleur (PAC) géothermiques sont parmi les technologies les plus performantes pour augmenter l'efficacité énergétique des bâtiments. Par contre le coût initial et l'encombrement des capteurs enterrés traditionnels peuvent être un obstacle à sa diffusion sur le marché des énergies renouvelables. Pour réduire ces coût et encombrement, une réflexion sur l'adjonction d'un système d'appoint et/ou de recharge thermique du sol aux capteurs enterrés est actuellement en cours de tests.

Les outils actuels de modélisation des capteurs enterrés obtiennent en effet de bons résultats mais seulement pour un dimensionnement classique en régime permanent. Les modèles existants ne permettent donc pas de représenter correctement les dynamiques rapides des échanges entre le sol et les tubes et cela est d'autant plus vrai si l'on adjoint le système de recharge solaire.

Par conséquence, cette thèse a pour objectif de développer les modèles fins et dynamiques nécessaires à l'analyse des phénomènes transitoires dans les capteurs enterrés eux-mêmes. Un maillage fin, sur les bases de la triangulation de *Delaunay*, est choisi pour le forage ainsi que pour le sol avoisinant. Une approche numérique en 3D (FVM + FEM) peut être obtenue sur les bases de la discrétisation spatiale du domaine. Cette approche appliquée brutalement induirait des temps de calcul très élevés et de toute façon incompatible avec les moyens informatiques ordinaires. Afin de répondre à l'ensemble de ces problèmes, différentes techniques ont été utilisées afin d'accélérer le temps de calcul: décomposition de domaine, emboîtement des pas de temps de calcul pour chaque sous-domaine, réduction des modèles d'états de chaque sous-domaine et finalement couplages temporels et spatiaux des équations de transferts de l'ensemble du problème. Ce dernier est développé particulièrement sur les bases de la méthode des éléments finis.

Par ailleurs, un modèle hybride est développé en combinaison de différentes approches. Une approche numérique est adoptée pour la modélisation du puits et la modélisation des transferts de chaleur dans le sol environnant est faite par l'utilisation de solutions analytiques. Ainsi, ce modèle est implanté dans TRNSYS.

Une plate-forme expérimentale comprenant trois puits verticaux couplés à une pompe à chaleur géothermique est également présentée. Les résultats expérimentaux sont comparés avec les résultats de la simulation aussi bien au niveau de la température du fluide qu'à la température à différentes profondeurs dans les puits. Le modèle développé donne des résultats très similaires avec ceux qui sont obtenus grâce à l'expérimentation même lors que les pas de temps sont très petits.

Il y a des choses à améliorer dans ce modèle développé, mais cela concerne essentiellement l'accélération du temps de calcul. Nous avons constaté que les modèles que nous avons dévéloppés donnent des résultats meilleurs à pas de temps courts que les modèles classiques. Il faut donc bien préciser le domaine d'utilisation de chacun des modèles: consommation sur le long terme, stratégie de contrôle de la PAC, les transferts de chaleur à l'intérieur du puits et etc. De plus, une application du modèle dans le dimensionnement d'échangeurs ainsi que l'investigation de son impact sur le sol avoisinant est également envisagée. Finalement, la méthodologie de modélisation présentée dans ce travail pourrait être aussi utilisé pour différents types d'échangeurs, ouvrant aussi la porte à une analyse fine dans le domaine géothermique.

Mots-clefs: PAC géothermique, exchangeurs géothermique verticaux, réduction des modèles d'état, décomposition de domaine, modèle hybride

Nomenclature

Symbols

H	Characteristic distance between boreholes	m
C	Heat capacity	$J/^{\circ}C$
c	Specific heat	$J/kg^{\circ}C$
D	Top depth of borehole	m
d	Diameter	m
d_i	Center to center distance between tube and borehole	m
H	Borehole depth	m
h_f	Convective heat transfer coefficient inside tubes	$W/m^{\circ}C$
k	Conductivity	$W/m^{\circ}C$
L	Borehole design length	m
L_s	Shank-spacing defined as center-to-center one (Eq. 1.3)	m
$\dot{m}$	Mass flow rate	kg/s
nb	Number of boreholes	
R	Resistance	$m^{\circ}C/W$
q	Heat flux	W/m
r	Radius	m
T_p	Penalty temperature (Eq. 1.54)	$^{\circ}C$
T_m	Average fluid temperature $(\mathrm{EFT} + \mathrm{ExFT})/2$ (Eq. 1.54)	$^{\circ}C$
t_s	Steady-state time-scale	s
x	Shank-spacing, the shortest one between pipe (Eq. 1.4)	$W/m^{\circ}C$

Greek letters

α	Thermal diffusivity	m^2/s
α	Absorption coefficient (Section 2.3.2)	
ρ	Density	kg/m^3
λ	Conductivity (Eq. 1.56,1.57,1.60 and Section 2)	$W/m^{\circ}C$
μ	Dynamic viscosity	kg/ms
λ	Eigenvalue (Section 1.2)	
τ	Time constant (Section 1.2)	
ψ	Eigenvector (Section 1.2)	
φ	Heat flux	$W/m^{2\circ}C$
ω	Hankel singular value (Section 1.2)	

Subscripts

b	Borehole
bot	Lower sub-zone
dw	Downward flow
e	Equivalent model
eff	Effective
ext	External or ambient
f	Fluid
h	Hour
m	Month
p	Pipe or tube
pi	Pipe inner radius/ diameter
po	Pipe outer radius/ diameter
s	Soil
top	Upper sub-zone
uw	Upward flow
y	Year
0	Zero, initial condition

Superscripts

e	Element in FEM
Si	ith sub-zone in the 2D case
$\mathbf{S}i$	ith slice sub-zone in the 3D case

Dimensionless numbers

Re	Reynolds number
Pr	Prandtl number
F_O	Fourier number

Etc.

$\overline{()}$	Average value
$\perp$	Vertical direction
$\vdash$	Horizontal direction

Acronyms

BEC	Buried Electrical Cable
BHE	Borehole Heat Exchanger1
BFTM	Borehole Fluid Thermal Mass
CHS	Cylindrical Heat Source
CM	Complete Model
COP	Coefficient of Performance
DST	Duct Storage Model
EFTbore	Entering Fluid Temperature to boreholes at the borehole head
EFTcol	Entering Fluid Temperature to boreholes at the collectors
ExFTbore	Exiting Fluid Temperature from boreholes at the borehole head
ExFTcol	Exiting Fluid Temperature from boreholes at the collectors
FLS	Finite Line Source
FDM	Finite Difference Method
FVM	Finite Volume Method
FEM	Finite Element Method
GCHP	Ground Coupled Heat Pump
GHE	Ground Heat Exchanger
ILS	Infinite Line Source
MLAA	Multiple Load Aggregation Algorithm
RM	Reduced Model
1D	One-Dimensional
2D	Two-Dimensional
3D	Three-Dimensional

Contents

List of Figures

List of Tables

Synthèse

Introduction

En France, dans le contexte énergétique et environnemental actuel, l'amélioration de l'efficacité énergétique des bâtiments est devenu un enjeu majeur. Le développement et la promotion de technologies de chauffage, climatisation et production d'eau chaude sanitaire très performantes constituent, avec l'amélioration de la qualité du bâti, un levier important pour parvenir à la conception ou la rénovation de bâtiments à faible consommation énergétique.

Dans ce contexte français favorable aux énergies renouvelables, les pompes à chaleur (PAC) géothermiques, systèmes de production de chaleur des plus performants, doivent jouer un rôle important. Cependant, en raison du coût et de l'encombrement des capteurs enterrés, ces systèmes voient aujourd'hui leur développement marquer le pas, après quelques années de forte croissance sur le marché de la maison individuelle neuve. Les PAC géothermiques sont notamment quasi-absentes des marchés de la rénovation individuelle et du tertiaire. Pour parvenir un développement pérenne de la PAC géothermique, l'enjeu est de faire évoluer les offres concernant les capteurs enterrés, en particulier les capteurs enterrés verticaux (sondes géothermiques), afin de les rendre acceptables pour les deux marchés précédemment cités.

Ainsi, cette thèse s'inscrit dans le cadre d'une réflexion sur le couplage d'un système d'appoint et/ou de recharge thermique du sol avec des capteurs enterrés verticaux, afin d'en réduire le coût et l'encombrement. Elle a pour objectif de développer les modèles fins et dynamiques nécessaires à l'analyse des phénomènes transitoires dans les capteurs enterrés eux-mêmes, liés au couplage au système d'appoint (recharge solaire) et à un éventuel sous-dimensionnement des capteurs enterrés. Il s'agit plus précisément de reproduire très finement et avec un pas de temps de l'ordre de quelques minutes les variations de température et les différentes interférences thermiques au sein même du puits géothermique et dans son proche environnement; ceci sur un temps de simulation long (plusieurs mois a minima).

Ce travail part du constat que les outils de modélisation des puits géothermiques et du sol environnant actuellement disponibles, qu'ils soient analytiques ou numériques, ne peuvent répondre à l'ensemble des prescriptions liées à une analyse précise de phénomènes transitoires rapides sur un temps de simulation long. Les outils analytiques sont basés sur des hypothèses simplificatrices qui réduisent leur précision et autorisent un pas de temps de simulation minimum de l'ordre de l'heure. Les outils numériques sont quant à eux précis mais un pas de temps court et un maillage fin du système induisent des temps de calcul extrêmement longs, incompatibles avec l'objectif de simulation du fonctionnement du système sur plusieurs mois.

Pour y parvenir, un modèle dynamique, numérique 3D a été développé et a été as-

socié à deux méthodes de calcul permettant de réduire le temps de calcul sans affecter la précision. La première est une méthode de structuration du système décrit en sous-domaines afin de décomposer le système en plusieurs parties ayant chacune un pas de temps de simulation différent. La seconde est une technique de réduction de modèles d'état afin de réduire la taille des matrices traduisant l'évolution du système.

Chapitre 1 - Bibliographie

Ce chapitre présente un état de l'art des deux thèmes principaux que ce travail va aborder pour le développement du modèle décrit ci-dessus: la modélisation des échangeurs géothermiques et la réduction des modèles d'état.

Dans un premier temps, les méthodes de modélisation des échangeurs géothermiques verticaux sont présentées, en fonction du nombre de dimensions du modèle (1 à 3D) et du type de domaine traité (puits géothermique lui-même ou sol environnant). Les puits sont généralement traités en 1D, en supposant un régime permanent. Plusieurs modèles de résistance thermique ont été proposés. Des différences sont observées entre eux et le meilleur modèle dépend du cas. Par contre, l'approche numérique a été aussi adoptée dans ce domaine en repère cylindrique. Il a mis en évidence les erreurs induites et en particulier celles dues à l'approximation des formes circulaires représentant le forage et les tuyaux.

Pour le sol, les solutions analytiques sont largement utilisées. Parmi les plus utilisées, citons la «source linéique infinie» et la «source cylindrique infinie» qui supposent toutes deux que la diffusion de chaleur est uniquement dans la direction radiale (1D). Le modèle de la «source linéique finie», quant à lui, prend en compte l'échange thermique dans la direction axiale, ce qui mène à une modélisation 2D. Toutes ces solutions ont été développées dans le cas d'un seul puits. Pour plusieurs puits, il est nécessaire d'utiliser une méthode pour tenir compte de l'interférence thermique entre eux. Ceci est réalisé en utilisant la technique de la superposition «spatiale». Cette technique, de même que la superposition dite «temporelle», qui prend en compte les flux de chaleur variables, sont également présentées.

Dans la catégorie des modèles 3-D, les g-function d'Eskilson ainsi que le modèle DST sont présentés en expliquant leurs principes et leurs limites d'utilisation.

La technique de réduction des modèles d'état a été développée par la communauté des automaticiens afin de diminuer le nombre des modes dirigeant l'évolution des états du système lors de simulations transitoires. Parmi les méthodes existantes, les techniques de «troncature» ont des avantages au niveau de leur facilité de mise en œuvre. L'idée de départ commune aux méthodes dites de «troncature» est de changer la base initiale du système (Eq. 0.1-0.2) en base modale (Eq. 0.3) par la diagonalisation avec les relations (Eq. 0.4). Ensuite, l'idée est de n'utiliser que les modes considérés «dominants» dans la reconstitution des grandeurs observés Y (les flux entre les tranches et les températures sur les tuyaux, par exemple).

$$\dot{T}(t) = C^{-1}AT(t) + C^{-1}B'U(t) \tag{0.1}$$

$$Y(t) = JT(t) + DU(t) \tag{0.2}$$

$$\dot{X}(t) = WX(t) + BU(t) \tag{0.3a}$$

$$Y(t) = HX(t) + DU(t) \tag{0.3b}$$

où,

$$T(t) = PX(t) \qquad W = P^{-1}C^{-1}AP \qquad B = P^{-1}C^{-1}B' \qquad H = JP \tag{0.4}$$

Le système final avec lequel seront conduites les simulations est obtenu par la troncature des matrices d'origine et s'exprime sous la forme des équations Eq. 0.5a et Eq. 0.5b dans lesquelles la matrice d'état W_1 est de taille très inférieure à celle de la matrice d'état d'origine $C^{-1}A$.

Trois méthodes de choix des modes dominants peuvent être distinguées - Marshall, Litz et l'agrégation linéaire - hormis la méthode de Moore dont l'approche est quelque peu différente. La méthode proposée par Marshall base le choix des modes à conserver uniquement sur une dominance temporelle. La distinction est faite par Marshall entre modes lents et modes rapides, ces derniers étant considérés comme ayant des régimes transitoires plus rapides que le pas de temps d'observation et donc ne contribuant finalement que dans la reconstitution du régime statique. La méthode de Litz conduit à l'analyse des nombreux spectres «entrées-sorties» afin de déterminer les modes dominants dans la reconstitution des sorties observées Y sous les sollicitations U.

$$\dot{X}_1(t) = W_1X(t)_1 + B_1U(t) \tag{0.5a}$$

$$Y(t) = H_1X(t)_1 + GU(t) \tag{0.5b}$$

où,

$$X_2 = -W_2^{-1}B_2U, \qquad G = D - H_2W_2^{-1}B_2 \tag{0.6}$$

La méthode d'agrégation linéaire (AL) qui utilise la notion de contribution énergétique afin de choisir les modes dominants. Le terme général de la matrice des contributions énergétiques est définie par la relation (Eq. 0.7). Comme le montre cette équation, AL est en quelque sorte d'une version synthétique de la méthode Litz, basé sur tous les cas de couplages entrées-sorties, ce qui permet de choisir des modes dominants (les plus énergétiques) avec un critère simple et explicit (Eq. 0.8). Étant plus performant parmi les autres, AL est utilisé dans cette thèse.

$$E_{ij} = -\frac{\sum_{l=1}^{q} H_{li}H_{lj} \sum_{k=1}^{p} B_{ik}B_{jk}}{(\lambda_i\lambda_j)^r(\lambda_i + \lambda_j)} \tag{0.7}$$

$$\sum_{i=1}^{m} E_{ii} / \sum_{i=1}^{n} E_{ii} \times 100 \geq 99(\%) \tag{0.8}$$

Chapitre 2 - Développement d'un modèle 3D

En adoptant une modélisation purement numérique, les hypothèses de mises en œuvre sont moins nombreuses et le code de calcul obtenu permet la description de situations plus complexes. Par contre, la croissance des temps de calcul est très forte dès qu'il y a nécessité d'affiner le maillage. Dans cette étude, où par ailleurs il est impératif de prendre en compte les effets tri-dimensionnels de la conduction dans le sol, notre première préoccupation a été de réduire le nombre d'équations mises en jeux dans le calcul des échanges des tuyaux avec le sol par la technique de réduction montrée ci-dessus.

Par ailleurs, il est impératif de réécrire un nouveau code afin d'obtenir l'ensemble des matrices du système d'état, nécessaires pour cette phase de réduction. Le code développé utilise les informations concernant le maillage ayant été produit par *Gmsh* (Fig. 1 montre un exemple obtenu par *Gmsh*).

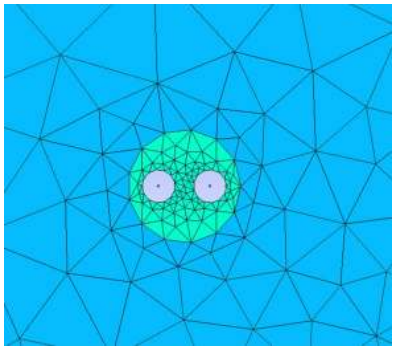

Figure 1: Exemple du maillage Delaunay triangulation obtenu par *Gmsh*

La méthode des éléments finis (EF) a l'avantage d'autoriser le traitement de configurations complexes tout en conservant des relations parfaitement réciproques, ce qui garantit la symétrie pour la matrice des conductances. Cette variante de la méthode des éléments finis est donc toute indiquée pour la modélisation que nous désirons mettre en place et qui fait appel aux techniques de réduction des modèles d'état.

Le volume de sol influencé par la présence du puits géothermique a été décomposé en tranches horizontales d'égale épaisseur. Nous avons choisi des éléments finis d'ordre 1 qui utilisent l'interpolation linéaire pour le calcul des températures intérieurs d'un élément. Le modèle est donc 2D pour chaque plan horizontal. Chaque élément est ensuite extrudé verticalement afin de construire un modèle 3D en connectant les plans horizontaux entre eux. La modélisation du transfert de la chaleur dans la direction verticale est, quant à elle, traitée par la méthode des volume finis. L'intérêt du traitement par tranches est que celles-ci sont toutes identiques (sol homogène) et que par conséquent les matrices d'état concernant chaque tranche seront identiques. Il ne sera donc nécessaire de diagonaliser, et donc de réduire, qu'un seul jeu de matrices pour représenter l'ensemble du pavé 3D.

Quand à la tranche qui est obtenu par cette décompostion verticale du volume de sol, il est encore suivi d'une autre décomposition en direction horizontale. Cette sous-structuration a l'avantage d'emboîter des pas de temps à chaque sous-domaine. Un pas de temps petit sera adopté dans le premier sous-domaine où le puits se trouvent donc où le gradient radial des températures est fort. Par hasard, cet emboîtement des pas de temps est obligé afin d'utiliser la méthode de réduction. Car la méthode est généralement sensible selon le pas de temps choisi. Par exemple, un modèle réduit décrivant le «grand» domaine éloigné du puits ne peut pas correctement donner des réponses si le pas de temps adopté est petit (une heure par example). Ce dernier peut aussi être vérifié par un test de fréquences entre le modèle initial (complet) et le modèle réduit comme le diagram de bode.

Le choix des modes considérés importants est basé sur la méthode «Aggrégation linéaire», en utilisant un critère «énergie». La constitution de ce critère est obtenue par l'évaluation de la contibution de chaque mode à la restitution des grandeurs d'observation sous couplage des entrée-sortie.

Concernant la méthode de couplage spatial et temporel, nous avons proposé de nouvelles conditions limites (Fig. 2) afin de bien coupler les sous-domaines sans perdre les informations matricielles de la méthode des EF avec une fonction d'interpolation et d'extrapolation permettant de temporellement coïncider le niveau des pas de temps qui sont différemment définis en chaque sous-domaine.

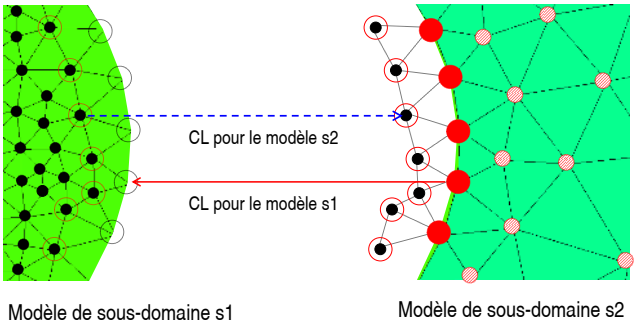

Figure 2: Proposition de nouvelles conditions aux limites dans EF

Pour le modèle complet, les sous-domaines décomposés sont assemblés et un modèle considérant le fluide est ajouté. Suite au calcul des flux entre le fluide et la paroi des tuyaux pour chaque pas de temps dans chaque tranche, ces flux sont repartis atour de la parois du tuyau. Comme montré dans la Fig. 3, les sous-domaines se couplent itérativement en communiquant avec les sous-domaines avoisinants dans les directions horizontale et verticale.

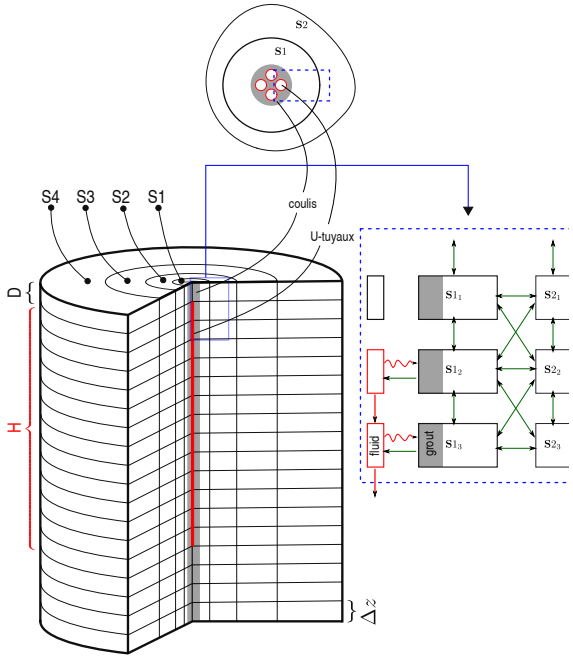

Figure 3: Assemblement des sous-domaines

En termes de temps de calcul, comme très peu de modes sont sélectionnés dans le modèle réduit, ce type de modèle est généralement rapide par rapport au modèle com-

plet. Le tableau 1 indique les temps de calcul (en CPU) pour différentes simulations. Ces résultats ont été obtenus en utilisant un flux constant pendant un mois avec un pas de temps d'une heure. Dans ce tableau, le modèle complet (MC) indique une version non réduite utilisant tous les modes initiaux alors que MR représente le modèle réduit. Trois MC ont été simulés, dont chacun est différemment défini avec ou sans les méthodologies décrites au-dessus: décomposition et emboîtement des pas de temps. Le cas 2D (une tranche) est utilisé pour cette comparaison. Car un modèle 3D pose le problème de mémoire pour une description du modèle entier (le premier cas (MC1) dans ce tableau).

Ces résultats montrent que les techniques utilisées dans ce travail sont pertinentes pour réduire le temps de calcul. On remarque que, par rapport au modèle de tranche initiale (entière), le modèle décomposé est plus rapide, mais pas tant ce qui était prévu; ceci serait due aux itérations dans les sous-domaines. Cependant, cette méthode de décomposition permet de mettre en œuvre les autres méthodes: emboîtement des pas de temps et la réduction pour chaque sous-domaine, qui sont suffisamment efficaces comme on le voit dans le tableau.

Table 1: «CPU time» de MR en comparaison de différentes versions de MC (2D)

Modèle	Déscription	CPU time
MC1	Modèle d'une tranche entière (pas de sous-domaines)	2454s
MC2	Un pas de temps pour les sous-domaines	1968s
MC3	Pas de temps diférents Δt_1, Δt_2, Δt_3, Δt_4	675s
MR	Δt_1, Δt_2, Δt_3,Δt_4 + réduction (AL)	91s

Chapitre 3 - Modèle hybride

Un modèle construit grâce aux approches analytiques et numériques est présenté dans ce chapitre. Ce modèle hybride (MH) a été conçu afin d'obtenir un temps de calcul très réduit par rapport à un modèle tout numérique tout en conservant une très bonne précision des résultats de paramètres globaux tels que la température du fluide caloporteur à la sortie du capteur enterré. Ce modèle est donc plus susceptible d'être utilisés pour l'optimisation des stratégies de régulation et la détermination des performances énergétiques de la pompe à chaleur.

Ce modèle est composé d'un modèle simplifié pour représenter le fluide, d'un modèle numérique du puits et de la réponse thermique du champ de capteurs. Cet assemblage implique l'utilisation de deux boucles itératives (Fig. 4).

Ce modèle hybride a été implanté dans TRNSYS. Deux «TYPE» ont été crées soit le TYPE «générateur de réponses thermiques» et le TYPE «modèle hybride». Le premier sera d'abord utilisé dans une pré-simulation afin d'obtenir les valeurs de réponses thermiques (i.e les g-fucntion) pour un champ de capteur donné (position x, y, hauteur H etc..). Ce type génère les valeurs de réponses qui sont stockées dans un fichier «.txt». Dans le deuxième TYPE, ces valeurs sont interpolées afin de donner la température moyenne sur la paroi des puits.

Finalement il est à noter que l'approche proposée permet d'étudier des géométries de champs irrégulières (en L ou en U etc.), ce que le modèle DST ne peut faire. De plus, le modèle MH se distingue du TYPE 451 qui ne peut étudier qu'un seul puits.

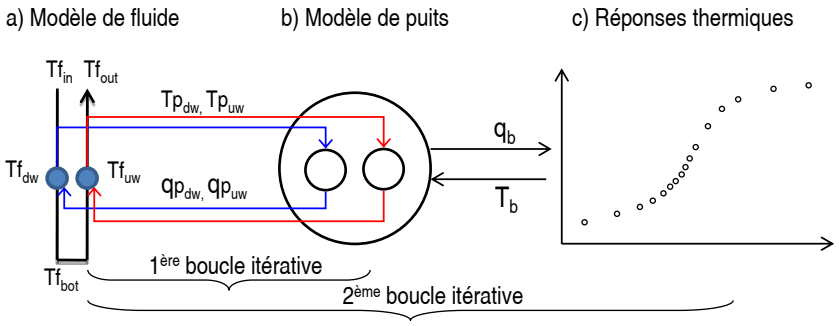

Figure 4: Structure du MH et boucles iteratives

Chapitre 4 - Vérification expérimentale

La validation du modèle numérique 3D réduit (3D-RM) est effectuée par comparaison avec des résultats expérimentaux obtenus sur une plate-forme d'essais d'EDF R&D. Cette plate-forme permet de tester des systèmes géothermiques (PAC + capteurs enterrés) en configuration et climat réels. Les besoins de chauffage et la réponse thermique d'un bâtiment sont simulés au moyens de deux boucles hydrauliques connectées à la pompe à chaleur. Une installation de trois sondes verticales de 40 mètres de profondeur a ainsi été réalisée et instrumentée selon la figure 5.

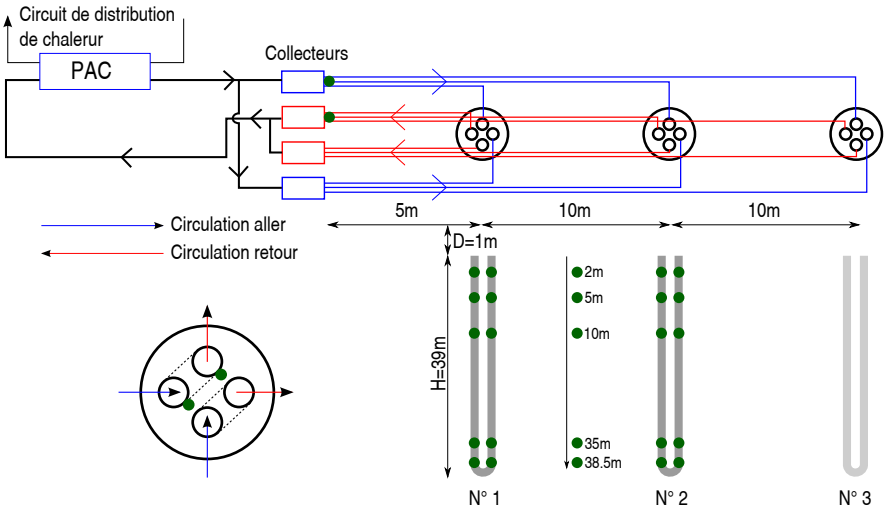

Figure 5: Configuration et instrumentation des trois puits géothermiques

L'ensemble des mesures est réalisé au moyen de sondes PT100. Les capteurs mesurant la température du fluide (eau glycolée) à l'entrée et la sortie des capteurs enterrés sont intrusifs et positionnés dans les collecteurs et non en tête des puits géothermiques[1]. Par ailleurs, des capteurs de température ont été collés sur les parois des deux tubes (ascendant et descendant) d'un U pour deux puits, numérotés N°1 et N°2, à différentes profondeurs. Dans un puits d'instrumentation équidistant, des sondes de température ont été introduites aux mêmes profondeurs (cf Fig. 5).

[1]Des capteurs intrusifs dans les tubes en polyéthylène des capteurs enterrés auraient provoqué des fuites.

L'expérimentation est en cours depuis décembre 2009. Les données expérimentales du premier mois ont été utilisées pour la validation du modèle. Par conséquent et compte tenu de l'écartement de 10 mètres des puits géothermiques, aucune interférence thermique n'est à craindre. Un seul puits géothermique (N°2) a été modélisé. Par son instrumentation, cette installation permet de valider le modèle en fonction de la température de fluide en sortie des capteurs mais également en fonction des températures au sein du puits géothermique lui-même. Les propriétés du sol, du coulis et du fluide utilisées sont basées sur des valeurs typiques ou fournies par le fabricant. En revanche, la conductivité thermique du sol, paramètre essentiel, a été déterminée par un test de réponse thermique.

Température du fluide

Du fait du positionnement des sondes de température du fluide dans les collecteurs, le transfert de chaleur dans les conduits de raccordement a dû être modélisé, au moyen d'un modèle 2D, afin de pouvoir effectuer la validation du modèle en fonction de la température du fluide.

La figure 6 reproduit ainsi la température du fluide au niveau du collecteur de sortie des capteurs enterrés, mesurée et calculée; ceci pendant 4500 pas de temps de 10 minutes, soit un mois. Pour cela, les données expérimentales mesurées chaque minute sont moyennées sur 10 minutes. Cette figure permet de constater que le modèle reproduit fidèlement la dynamique de la température du fluide. L'écart modèle/expérimentation est par ailleurs toujours inférieur à 1°C.

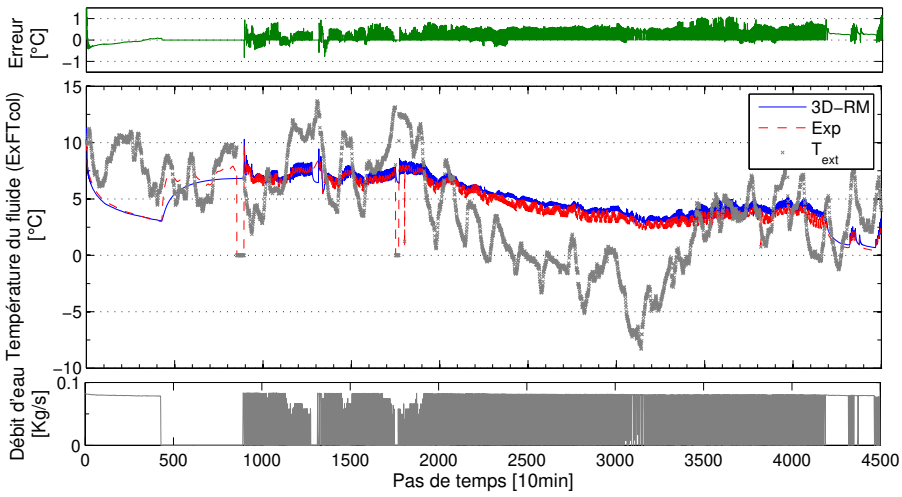

Figure 6: Comparaison modèle/exp. sur la température du fluide (pas de temps 10min)

Cet écart est principalement dû au pas de temps de 10 minutes : le fait de moyenner les valeurs expérimentales, notamment de débit du fluide, sur une telle durée induit des erreurs. Une simulation au pas de temps d'une minute a été réalisée sur une période où l'écart est important avec un pas de temps de 10 min. Cette simulation met en évidence qu'un pas de temps court permet d'obtenir un écart modèle/exp. inférieur à 0.5°C (figure 7).

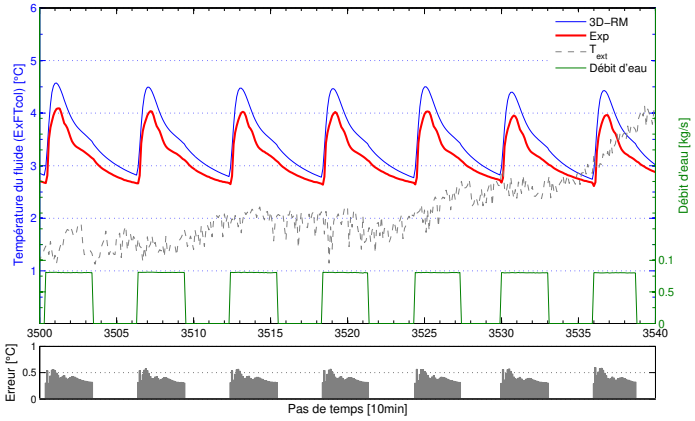

Figure 7: Comparaison modèle/exp. sur la température du fluide (pas de temps 1min)

Température des parois dans le puits

Le modèle permet de calculer 8 températures sur la circonférence du tube à une profondeur donnée, selon la figure 8.

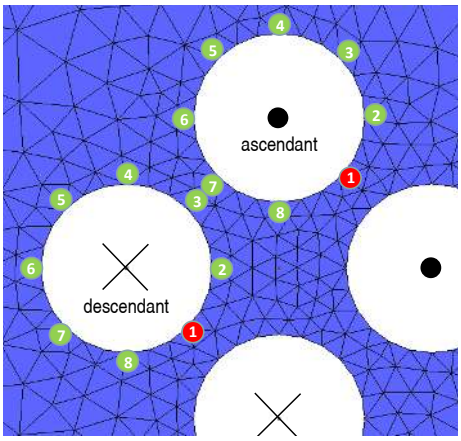

Figure 8: position des températures calculées par le modèle

Deux méthodes de calcul des flux sont comparées dans cette étude et illustrée par la figure 9: le cas 1 correspond à un flux également réparti sur la circonférence du tube, obtenu en moyennant les valeurs de température; le cas 2 le flux est séparément calculé dans chaque segment de la paroi. Le cas 1 est une approximation généralement utilisée dans ce type de modélisation.

Les capteurs de température sont théoriquement positionnés au niveau du point de calcul n°1 (figure 8). Cependant, la mise en place des tubes et le remplissage du puits avec du coulis ont pu modifier ce positionnement. Les capteurs de température peuvent donc se trouver entre les points 2 et 8. Le principe de validation consiste donc à comparer les résultats expérimentaux avec les valeurs de températures calculées aux points 1, 2 et 8 à différentes profondeurs et pour les deux cas de calcul de flux. La figure 10 montre un exemple, représentatif, à une profondeur de 35 m et pendant 700 min. L'évolution des températures est très similaire entre le modèle et l'expérimentation, pour les deux cas.

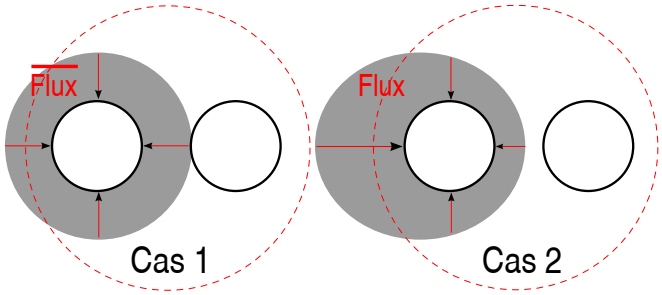

Figure 9: Schématisation des méthodes de calcul des flux à la paroi des tubes

Par ailleurs, la valeur expérimentale se trouve bien positionnée entre les points calculés 2 et 8. Ces résultats constituent une première validation intéressante du modèle.

Il est à noter que la dispersion des températures calculées sur la circonférence du tube dans le cas 1 de calcul de flux est plus importante que dans le cas 2. Ce résultat est logique dans la mesure où tous les effets d'interférence entre tubes ne peuvent se traduire qu'en température, le flux étant également réparti sur le pourtour du tube.

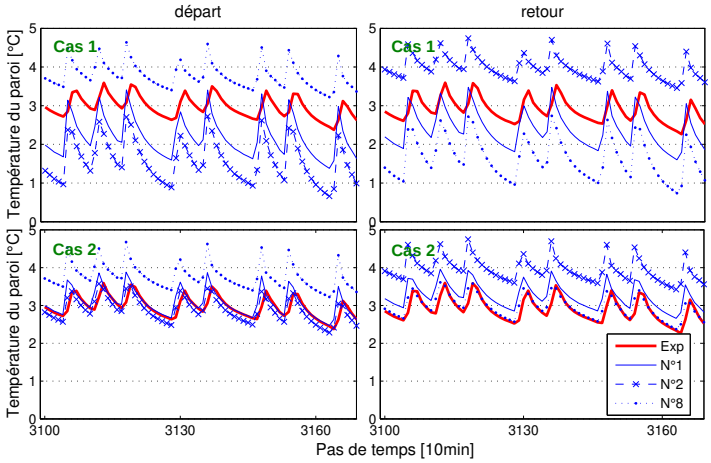

Figure 10: Températures de paroi à 35m de profondeur

Chapitre 5 - Comparaison intermodèles

Dans ce chapitre, des modèles existants sont comparés avec le modèle réduit (3D-RM) développé. Les modèles DST et Type 451 sont choisis dans cet exercice de comparaison. La figure 11 montre les réponses des modèles dans une scénario d'alimentation des températures du fluide. Ce test montre les différents comportements suivant qu'ils prennent en compte la capacité du coulis ou non. Le modèle DST (non capacitif) répond très rapidement aux sollicitations avec d'importantes amplitudes par rapport aux deux autres modèles[2].

[2]Par contre, Type 451 ne peut prendre en compte qu'un seul forage alors que le modèle 3D-RM est très flexible au niveau de la description d'une configuration quelconque souhaitée d'un champ de puits

Ensuite, les modèles sont utilisés pour simuler un cas typique de système de PAC géothermique. Cette simulation a été faite dans l'environnement TRNSYS. Même si les modèles sont basés sur différentes approches et en conséquence donne différentes réponses thermiques, des résultats très similaires sont obtenus de ces modèles pour une estimation de la consommation d'énergie (Tab. 2). Cependant, plus de simulations décrivant des configurations variées du système devront être réalisées avant de tirer des conclusions définitives.

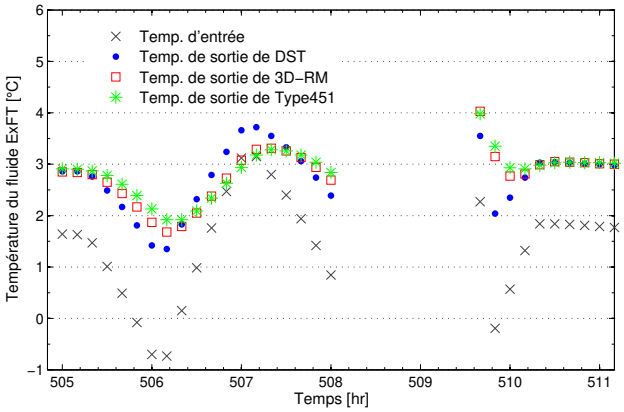

Figure 11: Réponse des modèles DST / RM / type 451

Table 2: Consommation d'énergie totale

Modèle	Energie transféré au bâtiment [kWh]	Consommation de la PAC [kWh]	Appoint [kWh]	COP
DST	12517	2777	60	4, 41
3D-RM	12528	2698	73	4, 52
Type 451	12524	2698	65	4, 53

Conclusion

L'enjeu de ce travail, inscrit dans le cadre d'une étude de réduction du coût des pompes à chaleur géothermiques, était de répondre à un besoin de simulation fine des phénomènes transitoires au sein de puits géothermiques et dans leur proche environnement. L'outil développé devait ainsi répondre à deux objectifs aux implications techniques contradictoires : reproduire des phénomènes transitoires rapides, sur une période de simulation longue (a minima plusieurs mois).

Un modèle numérique 3D, utilisant différentes méthodologies afin de réduire le temps de calcul et la mémoire requise, a ainsi été développé. Afin d'améliorer la précision de ce modèle, le domaine décrit (puits géothermique + sol environnant) a été détaillé par un maillage non structuré; ce qui a permis de s'affranchir des hypothèses habituellement posées dans ce type de modélisation.

La validation de ce modèle a été menée au moyen d'une étude expérimentale spécifiquement menée sur une plate-forme d'essais en climat réel. Cette étude a démontré

la pertinence de ce modèle détaillé et sa capacité à simuler finement l'évolution de la température du fluide caloporteur et des températures au sein du puits géothermique et dans le sol environnant. Cette étude a également mis en évidence une bien meilleure précision du modèle avec un pas de temps de simulation très court dans la simulation de la température du fluide caloporteur. Ce résultat implique la nécessité d'améliorer encore le modèle développé en terme de temps de calcul si l'on souhaite l'utiliser pour simuler avec une très grande précision ce paramètre sur le long terme.

Par ailleurs, un modèle construit grâce aux approches analytiques et numériques a été développé dans le cadre de ce travail. Ce modèle hybride est composé d'un modèle simplifié du fluide, d'un modèle numérique du puits et de la réponse thermique du champ de capteurs (sol + autres puits). Il a été conçu afin d'obtenir un temps de calcul très réduit par rapport au modèle numérique détaillé sans altérer la précision de la simulation de paramètres globaux tels que la température du fluide caloporteur.

Ces deux modèles développés, dont il a été constaté qu'ils donnent de meilleurs résultats à pas de temps courts que les modèles classiques, n'ont pas les mêmes qualités et fonctionnalités. Leur domaine d'utilisation respectif sera ainsi certainement différent. Si le modèle hybride est parfaitement adapté à des études de long terme: consommation énergétique de la pompe à chaleur, stratégie de régulation du système complet, etc., le modèle numérique détaillé est lui dédié à des études de précision sur des temps relativement limités concernant le transfert de chaleur dans le puits, l'impact du puits sur le sol environnant. L'utilisation de cet outil pour le dimensionnement des échangeurs, avec notamment la stratégie à adopter en cas de couplage avec un appoint, et la simulation fine d'échangeurs géothermiques innovants est également envisagée.

Introduction

General context

Nowadays, the greenhouse gas emissions is one of the main world-wide issues together with the progressive exhaustion of fossil fuels in terms of economical and environmental impacts. These two issues are very closely related as most efforts of diversifying energy resources to cope with depletion of fossil fuels can at the same time lead to less greenhouse gas emissions . Recent developments of various renewable energy sources can be linked to the need to address these issues.

In this context, the European Union (EU) has agreed to the so-called "three 20" objective: reducing greenhouse gas emissions by 20% and increasing the share of renewable energy sources in the energy consumption to 20% by 2020. This encourages the developments of renewable (low-carbon) and energy-efficient systems.

In France, the building sector contribution to the total greenhouse gas emissions is approximately 25% while its share of the total energy consumption is 43% (ADEME: www.ademe.fr). This sector is the biggest consumer of energy among all the economic sectors. More than 40% are due to space heating while specific uses of electricity, hot water production and air-conditioning share the rest of the pie.

The development of efficient space heating systems has become a great challenge, driven by more and more constraining regulations in France. Heat pumps, which produce 3 to 4 times more heat than electricity they consume in running, should have a major role in this development. Despite this favorable context, ground-coupled heat pumps (GCHP), the most efficient heat pumps and recognized as renewable systems, hardly develop their market share in France, in particular for existing buildings.

GCHP systems

The heat pump principle is to extract heat from a heat source (ground, water or air) and to transfer it to a sink (water of the heating radiators or air emitters in a house for example). Since temperatures of heat source is always lower than sink temperatures, this transfer is achieved by a refrigerant cycle. GCHP systems utilize the ground as the heat source by ground-embedded pipe loops connected to the evaporator of the heat pump. Various loop types can be used: closed or open, horizontal or vertical loops. In France, the most common type of the system is the horizontal loop consisting of a coil tube buried about 1 m deep, in the ground. However, the vertical loop type is more suitable for the purpose of developing the individual retrofit market, in terms of occupied area and performances.

A vertical ground heat exchanger (GHE) is typically composed of closed loops as shown schematically in Fig. 12.

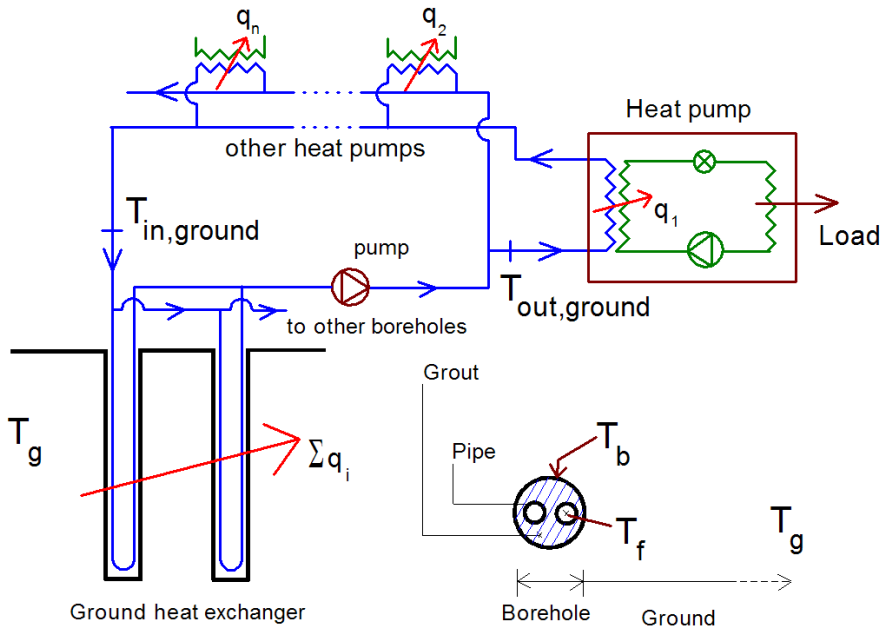

Figure 12: Schematic of a vertical closed-loop GCHP system [Bernier 2006]

For the operation of the system, a pump circulates a working fluid from the GHE to a HP. The GHE is typically 100 m deep. One or two U-tubes are generally inserted into the boreholes which are then filled with grout to enhance heat transfer between the fluid and the ground and to prevent ground water contamination. In heating mode, the GHE plays a role of heat source, transferring heat from the ground to the building by the HP via the fluid loop. In cooling mode, the HP operates inversely, so that the GHE acts as a sink.

Uprising issues

In France, the higher initial cost for the GHE installation is the main market barrier for sustainable development of GCHP. A GCHP can be 30-40% more expensive than an air-source heat pump. Consequently, several studies on the optimum sizing of GHE or coupling of boreholes with other sources have been carried out [Chiasson & Yavuzturk 2003] [Trillat-Berdal *et al.* 2006] [Yavuzturk & Spitler 2000] [Man *et al.* 2010] [Bernier & Shirazi 2007]. All these studies aim to reduce GHE sizing and consequently the total system cost.

Appropriate sizing of GHEs is critical for the long-term performance of the GCHP since undersizing of GHE unexpectedly decreases the ground temperature in the vicinity of the borehole. This reduces heat transfer between the ground and the borehole and leads to the system failure sometimes with irreversible damages in the ground.

Consequently, efforts to reduce the required GHE length must be evaluated with reliable tools which allow to accurately simulate the thermal behavior inside and around boreholes in order to avoid possible damages. These tools have to be able to observe with a short time-step (minute or few minutes) the borehole temperature in "critical" zones in order to predict the consequences of undersizing of the GHE. In particular, thermal inter-

ferences between each tube of borehole have to be precisely evaluated as well (e.g. short circuit effects).

However, such models are not currently found among existing models whatever it is analytical or numerical because of the following limits. Analytical models, commonly used for classic design of GHE, cannot accurately predict fluid temperatures even in hourly simulations since inappropriate assumptions for the current purpose are supposed: e.g. the steady-state assumption in the borehole. On the other hand, numerical models are time-consuming and require large computer memory[3] when a detailed modeling is necessary.

From all these uprising issues, some requirement on the GHE modeling arises. First, direct programming is preferred to use of commercial software packages since a GHE model has to be flexible to be implemented in a building simulation software to let the HP operation determine the input parameters of the model. Second, the mentioned problems in computing and memorizing have to be mitigated for a practical use.

Main objective of this thesis

The main objective of this thesis is to develop the required model as described above in order to simulate with a high accuracy and a short time-step the thermal behavior of the borhole and its vicinity along the GHE depth. In particular, the model has to correctly account for temperature and flux distribution between the U-tubes and inside the borehole. Therefore, it is desirable to develop a three-dimensional numerical model with a detailed mesh used for describing the borehole configuration. For this 3-D model, this thesis propose to use state model reduction techniques to reduce computational time and domain decomposition to reduce required computer memory.

This thesis consists of five main chapters in addition to an introduction and a conclusion.

In Chapter 1, existing GHE models are reviewed. These include classic analytical solutions as well as numerical models for heat transfer in the ground and inside boreholes.

Chapter 2 focuses on the development of the new proposed numerical model. A 2D case is first introduced followed by a complete 3D reduced model (3D-RM). Domain decomposition and state model reduction are presented. New methods are proposed to couple the decomposed sub-domains particularly in regards to the use of the Finite Element Method. The proposed methodology is validated with existing solutions or by self-tests.

In Chapter 3, a hybrid model (HM) is presented that combines analytical solutions and numerical ones for a fast calculation of borefields. This is particularly useful when used in conjunction with building simulation software.

Chapter 4 presents results of a comparison between experimental results and the 3D-RM model. The experimental apparatus is described. Inlet and outlet fluid temperatures and pipe wall temperatures at different depths are measured and compared with simulation results with an emphasis on short-time steps transient effects inside the borehole.

In Chapter 5, simulation results obtained by the proposed models are compared to other existing models for a typical GCHP configuration.

[3] Actually, in common computer resources, around 10,000 meshes cause already the memory problem and only a time-step calculation for such a mesh number is time-consuming unless special techniques will be used.

Finally, the work is reviewed in the conclusion and recommendations for future work are proposed.

Chapter 1

Literature Review

1.1 GHEs Modeling

Ground exchanger exchangers (GHE) can be divided into three parts: the fluid, the borehole and the ground. As Yang et al. [Yang *et al.* 2010], each part can be categorized as a calculation domain, each with its own modeling approach. Each model will be influenced by how fast a domain reacts to a change of inlet conditions. For example, the borehole domain model will require short-time steps to accurately model the rapid changes occurring in that region. On the other hand, the ground domain may not need short simulation time steps and calculations with a long time step may be sufficient.

1.1.1 Short-time scale region

Generally, the so-called short-time scale region is an area including the fluid, the U-tubes, the grout in the borehole and also a portion of the ground in the vicinity of the borehole. This short-time scale region can be defined differently depending on the simulation purpose, the thermal properties, and the modeling methods. For simplicity, this section considers the borehole and the fluid as the short-time scale region; keeping in mind that the ground region near the borehole could be important for accurate short-time results.

Generally, borehole have relatively complicated, in terms of modeling, geometries because of the position of U-tubes in the borehole. Therefore, many approximations have been proposed numerically or analytically for this region. The fluid part models, which are relatively well-known, are not reviewed in this section.

1.1.1.1 Steady-state borehole models

From an engineering point of view, transient effects in the borehole can be neglected. For instance, in borehole sizing programs a long heat pulse, generally of the order of 6 hours, is used. Considering that the time constant of a borehole is of the order of one hour, it is reasonable to neglect transient effects when sizing a borehole. Several steady state borehole models have been developed in last decades.

Firstly, an approximated model that regarded the U-pipes as a equivalent single pipe can be used:

$$R_b = \frac{1}{2\pi k_b} \ln \frac{d_b}{d_e} \tag{1.1}$$

For the equivalent pipe diameter d_{pe}, Bose [Bose 1984] was one of the first to suggest a simple formula (1.2) for a single U-pipe (2 pipes), and afterwards Shonder et al. [Shonder & Beck 1999] used this value in their work.

$$d_e = \sqrt{2} d_{po} \tag{1.2}$$

In this equation, the shank spacing, i.e. the center-to-center distance between the two legs of U-pipe, is not considered. To take into account this distance L_s, another equivalent diameter was suggested by Gu et al. [Gu & O'Neal 1998] as follows:

$$d_e = \sqrt{2 d_{po} L_s} \quad (d_{po} < L_s < d_b) \tag{1.3}$$

Additionally, Kavanaugh [Kavanaugh 1985] proposed another formula using a correction factor x (Eq. 1.4). Here, the factor x represents the shank spacing, but it is defined differently as the shortest distance between the outer pipe walls of each leg of the U-tube.

$$r_e = \sqrt{2} r_{po} + x \tag{1.4}$$

These equivalent diameter models neglect the two-dimensional temperature variations over the borehole cross-section by simplifying the problem to one-dimensional radial heat transfer problem. This approximation may lead to over-sizing of the GHEs [Sharqawy *et al.* 2009].

Paul [Paul 1996] proposed the effective pipe-to-borehole thermal resistance (Eq. 1.5) that was obtained using experimental data and a two dimensional finite element program (ANSYS) under the steady-state regime in different configurations of the U-pipes in the borehole: A, B, and C (see Fig. 1.1). By varying the thermal conductivities of the grout, a curve-fitted correlation on the resistance was obtained giving shape factor (S) for each case (see tab. 1.1). However, these values were partly obtained from an experimental set-up that could not exactly set the borehole configuration because of the uncertainty on the installation of GHEs such as bore washout. It might result in a borehole diameter larger than planned. In fact, in a similar work done by Remund [Remund 1999], it is shown that the scatter in the results between the correlation and the experimental values can be as high as 23%.

$$R_b = \frac{1}{k_b S}, S = \beta_0 \left(\frac{d_b}{d_{po}} \right)^{\beta_1} \tag{1.5}$$

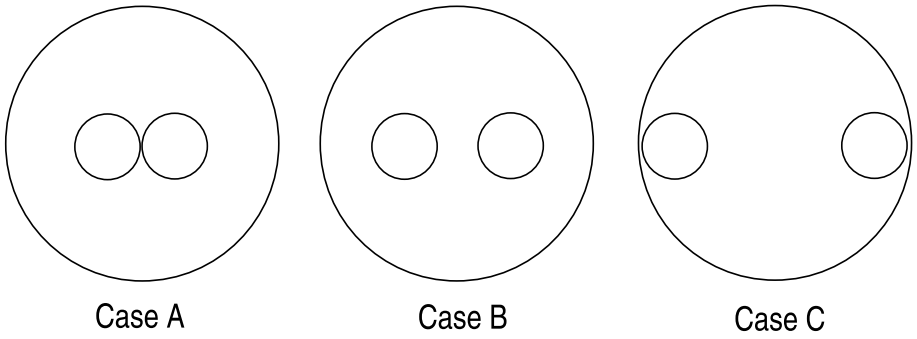

Figure 1.1: Paul's test cases

Table 1.1: Paul Curve Fit Parameters for Eq. 1.5

configuration	β_0	β_0
A	20.10038	-0.9447
B	17.44268	-0.6052
C	21.90587	-0.3796

Sharqawy et al. [Sharqawy *et al.* 2009] introduced a new effective pipe-to-borehole resistance with a numerical approach. They used a commercial computational fluid dynamics solver under steady-state and isotropic conditions of the T_b, T_{p1}, T_{p2}: 30, 50, and 40˚C, respectively. Each effective resistance of different cases was calculated from the FLUENT simulation results by Eq. 1.6. A best-fit estimate of the resulting resistance values is given in Eq. 1.7.

$$R_{b,eff} = \frac{\overline{T_p} - T_b}{q_b} \tag{1.6}$$

$$R_{b,eff} = \frac{1}{2\pi k_s}\left[-1.49\left(\frac{s}{d_b}\right) + 0.656\ln\left(\frac{d_b}{d_p}\right) + 0.436\right] \tag{1.7}$$

It is shown in the work that the equivalent models such as the ones described earlier tend to over-estimate the resistance values, which was concluded from different test cases by varying the value of s/d_b. In fact, an error of about 39% was found for the case of close-spacing between the U-tube legs.

Hellström [Hellström 1991] proposed a resistance model that is directly obtained from the physical correlation among the two legs of the tube and the borehole wall. First, a simple expression of R_b for the case of $2d_i = L_s$ was given in his work. The resistance was expressed by a fluid-to-borehole circuit (Eq. 1.8). Here, q_b indicates heat transfer rate per unit length (Wm^{-1}).

$$R_b = \frac{T_f - T_b}{q_b} \quad T_f = \frac{T_{f1} + T_{f2}}{2} \tag{1.8}$$

$$\begin{aligned} R_b &= \frac{1}{2\pi k_b}\left[\ln\left(\frac{r_b}{r_p}\right) + \ln\left(\frac{r_b}{2d_i}\right) + \sigma\ln\left(\frac{r_b^4}{r_b^4 - d_i^4}\right)\right] + R_p \\ &\text{where, } \sigma = \frac{k_b - k_s}{k_b + k_s}, \quad R_p = \frac{\ln\left(\frac{r_{po}}{r_{pi}}\right)}{2\pi k_p} + \frac{1}{2\pi h_f r_{pi}} \end{aligned} \tag{1.9}$$

These formulas can be expressed in 2-D form to explicitly take into account the interference between the two legs, using T_{f1}, T_{f2}, T_b that are considered constant:

$$\begin{aligned} T_{f1} - T_b &= R_{11}q_1 + R_{12}q_2 \\ T_{f2} - T_b &= R_{12}q_1 + R_{22}q_2 \end{aligned} \tag{1.10}$$

For the typical case of the symmetric configuration of the U-tube, R_{11}= R_{22}, which results in the following:

$$
\begin{aligned}
R_{11} &= \frac{1}{2\pi k_b}\left[\ln\left(\frac{r_b}{r_p}\right) + \sigma \ln\left(\frac{r_b^2}{r_b^2 - d_i^2}\right)\right] + R_p \\
R_{12} &= \frac{1}{2\pi k_b}\left[\ln\left(\frac{r_b}{2d_i}\right) + \sigma \ln\left(\frac{r_b^2}{r_b^2 + d_i^2}\right)\right]
\end{aligned}
\tag{1.11}
$$

For the general use of the resistance models presented above, an average heat transfer rate per unit length q $(\mathrm{W/m})$ over the depths H is used. In a real situation, q varies in the axial direction. This is due to variations of the borehole wall temperature along the borehole length as well as the fluid temperature.

In this context, Zeng et al. [Zeng *et al.* 2003] proposed a quasi-three-dimensional model where the fluid temperature variation along the borehole depth is taken into account, but the conductive heat flow in the fluid in the axial direction is neglected. New resistance expressions can be obtained by a linear transformation of Eq. 1.10.

$$
\begin{aligned}
q_1 &= \frac{T_{f1} - T_b}{R_1^\Delta} + \frac{T_{f1} - T_{f2}}{R_{12}^\Delta} \\
q_2 &= \frac{T_{f2} - T_b}{R_2^\Delta} + \frac{T_{f2} - T_{f1}}{R_{12}^\Delta}
\end{aligned}
\tag{1.12}
$$

Consequently, we get the new expressions:

$$
\begin{aligned}
R_1^\Delta &= \frac{R_{11}R_{22} - R_{12}^2}{R_{22} - R_{12}} \\
R_2^\Delta &= \frac{R_{11}R_{22} - R_{12}^2}{R_{11} - R_{12}} \\
R_{12}^\Delta &= \frac{R_{11}R_{22} - R_{12}^2}{R_{12}}
\end{aligned}
\tag{1.13}
$$

Here, in the symmetric case of the U-tube, these resistances reduce to

$$
\begin{aligned}
R_1^\Delta &= R_2^\Delta = R_{11} + R_{12} \\
R_{12}^\Delta &= \frac{R_{11}^2 - R_{12}^2}{R_{12}}
\end{aligned}
\tag{1.14}
$$

In his work, the energy equilibrium equations were written for fluid up- and down-flow under two under two conditions (Eq. 1.16)

$$
\begin{cases}
-\dot{m}c_f \dfrac{dT_{f1}}{dz} = \dfrac{(T_{f1} - T_b)}{R_1^\Delta} + \dfrac{(T_{f1} - T_{f2})}{R_{12}^\Delta} \\
\dot{m}c_f \dfrac{dT_{f2}}{dz} = \dfrac{(T_{f2} - T_b)}{R_2^\Delta} + \dfrac{(T_{f2} - T_{f1})}{R_{12}^\Delta}
\end{cases}
\qquad (0 \le z \le H) \tag{1.15}
$$

$$
\begin{aligned}
z = 0, \quad T_{f1} &= T_f^{in} \\
z = H, \quad T_{f1} &= T_{f2}
\end{aligned}
\tag{1.16}
$$

From these equations, solutions by Laplace transformation is derived, and the resultant solution for the fluid temperature profiles (Eq. 1.17) can be expressed with the dimensionless parameters (Eq. 1.18).

$$\begin{aligned}
\Theta_1(Z) =& \cosh(\beta Z) - \frac{1}{\sqrt{1-P^2}} \left(1 - P \frac{\cosh(\beta) - \sqrt{\frac{1-P}{1+P}} \sinh(\beta Z)}{\cosh(\beta) + \sqrt{\frac{1-P}{1+P}} \sinh(\beta Z)} \right) \sinh(\beta Z) \\
\Theta_2(Z) =& \frac{\cosh(\beta) - \sqrt{\frac{1-P}{1+P}} \sinh(\beta)}{\cosh(\beta) + \sqrt{\frac{1-P}{1+P}} \sinh(\beta)} \cosh(\beta Z) + \\
& \frac{1}{\sqrt{1-P^2}} \left(\frac{\cosh(\beta) - \sqrt{\frac{1-P}{1+P}} \sinh(\beta)}{\cosh(\beta) + \sqrt{\frac{1-P}{1+P}} \sinh(\beta Z)} - P \right) \sinh(\beta Z)
\end{aligned} \tag{1.17}$$

where,

$$\begin{aligned}
\Theta = \frac{T_f(Z) - T_b}{T_f^{in} - T_b}, \quad Z = \frac{z}{H}, \quad P = \frac{R_{12}}{R_{11}} \\
\beta = \frac{H}{M c_f \sqrt{(R_{11} + R_{12})(R_{11} - R_{12})}}
\end{aligned} \tag{1.18}$$

Although this equation accounts for the fluid temperature variation along the borehole depth, it is necessary on the other hand to calculate an average fluid temperature that can be used for various purposes. A new average fluid temperature, so-called "p-linear" average, has been proposed by [Marcotte & Pasquier 2008] as shown in Eq. 1.19.

$$\left| \Delta \overline{Tf} \right| = \frac{p(|\Delta Tf_{in}|^{p+1} - |Tf_{out}|^{p+1})}{(1+p)(|\Delta Tf_{in}|^{p} - |Tf_{out}|^{p})} \tag{1.19}$$

Here, Δ means a difference with respected to the undisturbed ground temperature, T_0 (i.e. ΔTf_{in}=$Tf_{in} - T_0$). In their work, $p = -1$ was proposed using a 3D finite element model of borehole. It is shown that this proposed average value more closely fits the average fluid temperature computed with the 3D model than the typical value $T_m = (Tf_{in} + Tf_{out})/2$.

1.1.1.2 Models that account for thermal capacity effects

Most models that use the steady-state resistance approach (section 1.1.1.1) for the borehole region are strictly valid only after a few hours after a step-change since these resistance models do not consider the thermal capacity effects of boreholes. Short time response of vertical boreholes which include the thermal capacity of the borehole has become a subject of interest for precise predictions of GCHP. Lamarche et al. [Lamarche & Beauchamp 2007b] mentioned in their work the necessity of considering the grout capacity effect as follows: "First, as soon as a heat flow is imposed between the fluid and the ground, a ΔT given by $T_f - T_b(t) = q_b(t) R_b$ will be felt whereas from physical reasoning, we would expect a certain time for this to build-up. Secondly, the thermal resistance found from the steady state analysis of the grout will be overestimated from the one felt in reality". Analytical or numerical approaches have been proposed to take into account

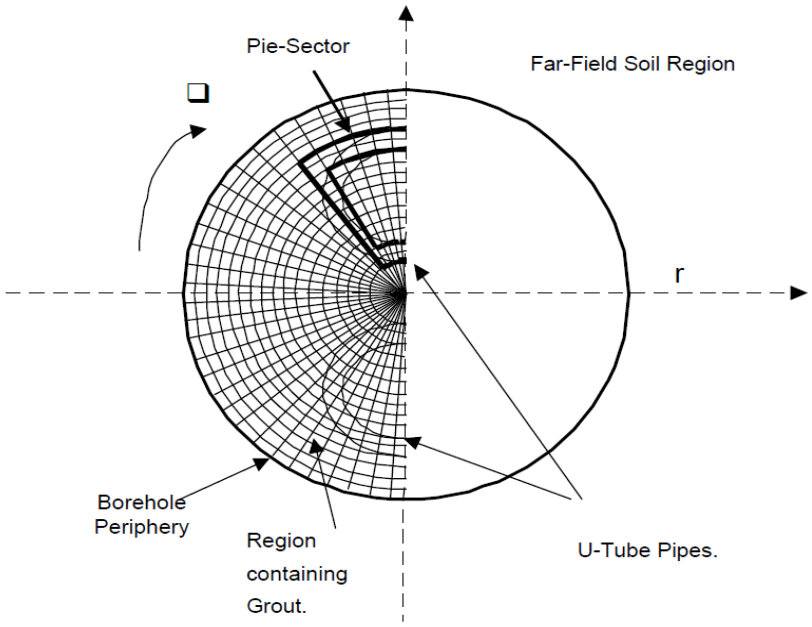

Figure 1.2: Yavusturk's numerical model using pie-sector approximation for the U-tube pipes

this effect. One of the first numerical models was accomplished in the cylindrical grid by Rottmayer et al. [Rottmayer *et al.* 1997]. The model, however, approximated the geometry of U-pipes by a pie sector shape to fit a circular form in the cylindrical grid, so that errors in heat transfer rate of this approximation was in the order of 5% compared to circular tube solution obtained by an analytical solution in the steady state regime. Then, a more detailed mesh on the same grid was proposed [Yavuzturk *et al.* 1999] to describe accurately the pipe geometry that had been over-simplified in the Rottmayer work.

Other numerical models have been developed using commercial software packages by unstructured meshes that are efficient for describing the circular form of tubes and borehole with a low order of mesh number. It is necessary to note that the pie-sector approach necessitate numerous meshes to describe the precise geometries.

Young [Young 2001] is one of the first to propose an analytical solution to include the thermal capacity within the borehole. He interpreted the buried cable solution given by Carslaw and Jaeger for the borehole-fluid capacity model, called "the borehole fluid thermal mass (BFTM) model" in his thesis.

In the buried electrical cable (BEC) model shown in Fig. 1.3, the sheath and core are assumed to be thermal masses without resistance, and the resistance between the core and soil is only considered by the insulation. For analogy between the two models BEC and BFTM, Tab. 1.2 gives the correspondent parameters. Therefore, an approximation of placing all of the grout thermal capacity at the outside of the borehole resistance (insulation in the BEC model) is automatically done by this analogy.

From the BEC model, he obtained the same solution for the BFTM model. The followings show the boundary conditions for each capacity zone (the core and the sheath).

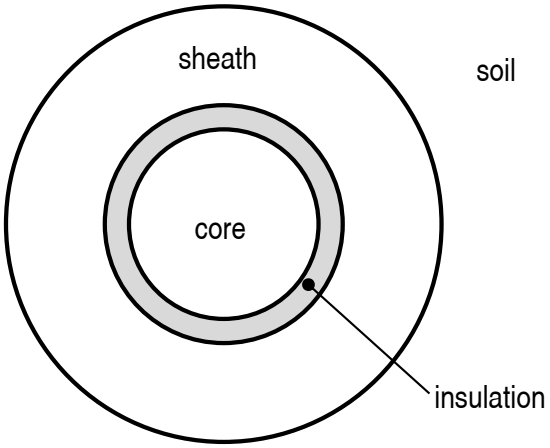

Figure 1.3: Buried cable model

Table 1.2: Model analogy between BEC and BFTM

BEC	BFTM
Insulation Thermal Resistance	Borehole Resistance
Outer Radius of the Sheath	Borehole Radius
Core Thermal Capacity	Fluid Thermal Capacity
Sheath Thermal Capacity	Grout Thermal Capacity

$$\begin{aligned} &T(r,0) = T_0, \\ &2\pi r_b k_s \left.\frac{\partial T}{\partial r}\right|_{r=r_b} = \frac{T_2 - T_1}{R} + \underbrace{A_{c2}\rho_2 c_2}_{S_2}\frac{\partial T_2}{\partial t} \end{aligned} \tag{1.20}$$

Here, the subscript 2 indicates the sheath (grout) region. For the core region (subscript 1), equivalent to the fluid, we have:

$$q_b = \frac{T_1 - T_2}{R} + \underbrace{A_{c1}\rho_1 C_1}_{S_1}\frac{\partial T_1}{\partial t} \tag{1.21}$$

From these heat balances and conditions, one dimensional (polar grid) heat diffuse equation can be solved by Laplace transform, and the solution is given by:

$$T_p(\widetilde{t}) - T_0 = \frac{q_b'}{k_s}\frac{2\alpha_1^2\alpha_2^2}{\pi^3}\int_0^\infty \frac{(1-\exp^{-\beta^2\widetilde{t}})}{\beta^3\Delta(\beta)}d\beta \tag{1.22}$$

Where,

$$\begin{aligned} \alpha_1 = \frac{2\pi r_b^2\rho_s c_s}{S_1}, \quad \alpha_2 = \frac{2\pi r_b^2\rho_s c_s}{S_2}, \quad \widetilde{U} = 2\pi R k_s \\ \Delta(\beta) = (\beta\,(\alpha_1+\alpha_2-\widetilde{U}\beta^2)J_0(\beta) - \alpha_2(\alpha_1-\widetilde{U}\beta^2)J_1(\beta))^2 \\ +(\beta(\alpha_1+\alpha_2+\widetilde{U}\beta^2)Y_0(\beta) - \alpha_2(\alpha_1-\widetilde{U}\beta^2)Y_1(\beta))^2 \end{aligned} \tag{1.23}$$

In his work, he used the multipole expression [Bennet *et al.* 1987] for the value of the borehole resistance and Eq. 1.2 for the core radius. He modified this BEC model for the BFTM by moving part of the thermal capacity of the grout inside of the thermal resistance, using a grout allocation factor (GAF), which was defined as Eq. 1.24. This optimal GAF(f) value was given in his thesis for a range of cases.

$$S_{1f} = S_1 + S_2 f, \quad S_{2f} = S_2(1-f), \quad \text{with } 0 < f < 1 \tag{1.24}$$

Lamarche [Lamarche & Beauchamp 2007b] developed an analytical solution that takes into account different materials: grout and soil, in a closed form, allowing the short time response of boreholes. The following problems (Eq. 1.25-1.26) were solved by Laplace Transformation under different boundary conditions, where T_1 represents the grout temperature and T_2 soil temperature.

$$\frac{1}{\alpha_b}\frac{\partial T_1}{\partial t} = \frac{\partial^2 T_1}{\partial r^2} + \frac{1}{r}\frac{\partial T_1}{\partial r}, \;\; r_{eq} < r < r_b, \;\; t > 0 \tag{1.25}$$

$$\frac{1}{\alpha_s}\frac{\partial T_2}{\partial t} = \frac{\partial^2 T_2}{\partial r^2} + \frac{1}{r}\frac{\partial T_2}{\partial r}, \;\; r_b < r_b, \;\; t > 0 \tag{1.26}$$

In these equations, the two boundary conditions are used: the total heat per unit length q_b (Eq. 1.27), and convective heat transfer condition (Eq. 1.28).

$$\begin{aligned} T_1(r,0) = T_2(r,0) = T_0, \quad & -k_b \left.\frac{\partial T_1}{\partial r}\right|_{r=r_{eq}} = q_b(t) \\ T_1(r_b,t) = T_2(r_b,t), \quad & -k_b \left.\frac{\partial T_1}{\partial r}\right|_{r=r_b} = -k_s \left.\frac{\partial T_2}{\partial r}\right|_{r=r_b} \end{aligned} \tag{1.27}$$

$$\begin{aligned} T_1(r,0) = T_2(r,0) = T_0, \quad & -k_b \left.\frac{\partial T_1}{\partial r}\right|_{r=r_eq} = h(T_f - T_1(r_{eq},t)) \\ T_1(r_b,t) = T_2(r_b,t), \quad & -k_b \left.\frac{\partial T_1}{\partial r}\right|_{r=r_b} = -k_s \left.\frac{\partial T_2}{\partial r}\right|_{r=r_b} \end{aligned} \tag{1.28}$$

The resultant solutions for each boundary condition are presented in Eq. 1.29 and Eq. 1.30 respectively.

$$\begin{aligned} T_p(\widetilde{t}) =& T_1(1,\widetilde{t}) = T_0 + \frac{q_b}{k_s} \underbrace{\frac{8\widetilde{k}}{\pi^5\delta^2}\int_0^\infty \frac{(1-\exp^{-\beta^2\widetilde{t}})}{\beta^5(\phi^2+\psi^2)}d\beta}_{G_{st_q}(1,\widetilde{t})} \\ \text{where, } \widetilde{k} =& \frac{k_s}{k_b}, \; \gamma = \sqrt{\frac{\alpha_b}{\alpha_s}}, \; \widetilde{t} = \frac{\alpha_b t}{r_{eq}^2}, \; \delta = \frac{r_b}{r_{eq}} \\ \phi =& Y_1(\beta)[Y_0(\beta\delta\gamma)J_1(\beta\delta) - Y_1(\beta\delta\gamma)J_0(\beta\delta)\widetilde{k}\gamma] \\ & - J_1(\beta)[Y_0(\beta\delta\gamma)Y_1(\beta\delta) - Y_1(\beta\delta\gamma)Y_0(\beta\delta)\widetilde{k}\gamma] \\ \psi =& J_1[(\beta)J_0(\beta\delta\gamma)Y_1(\beta\delta) - J_1(\beta\delta\gamma)Y_0(\beta\delta)\widetilde{k}\gamma] \\ & - Y_1(\beta)[J_0(\beta\delta\gamma)J_1(\beta\delta) - J_1(\beta\delta\gamma)J_0(\beta\delta)\widetilde{k}\gamma] \end{aligned} \tag{1.29}$$

$$
\begin{aligned}
T_p(\widetilde{t}) =& T_1(1,\widetilde{t}) = T_f + (T_0 - T_f)\underbrace{\frac{16\widetilde{k}\widetilde{H}}{\pi^4\delta^2}\int_0^\infty \frac{exp^{-\beta^2\widetilde{t}}}{\beta^3(\phi_c^2+\psi_c^2)}d\beta}_{G_{st_c}(1,\widetilde{t})} \\
\text{where, } \widetilde{k} =& \frac{k_s}{k_b},\ \gamma = \sqrt{\frac{\alpha_b}{\alpha_s}},\ \widetilde{t} = \frac{\alpha_b t}{r_{eq}^2},\ \delta = \frac{r_b}{r_{eq}},\ \widetilde{H} = \frac{hr_{eq}}{k_b} \\
\phi_c =& [\widetilde{H}J_0(\beta) + \beta J_1(\beta)][J_0(\beta\delta\gamma)Y_1(\beta\gamma) - J_1(\beta\delta\gamma)Y_0(\beta\delta)\widetilde{k}\gamma] \\
& - [\widetilde{H}Y_0(\beta) + \beta Y_1(\beta)][J_0(\beta\delta\gamma)J_1(\beta\delta) - J_1(\beta\delta\gamma)J_0(\beta\delta)\widetilde{k}\gamma] \\
\psi_c =& [\widetilde{H}Y_0(\beta) + \beta Y_1(\beta)][J_0(\beta\delta\gamma)Y_1(\beta\gamma) - J_1(\beta\delta\gamma)Y_0(\beta\delta)\widetilde{k}\gamma] \\
& - [\widetilde{H}Y_0(\beta) + \beta Y_1(\beta)][Y_0(\beta\delta\gamma)J_1(\beta\delta) - Y_1(\beta\delta\gamma)J_0(\beta\delta)\widetilde{k}\gamma]
\end{aligned}
\tag{1.30}
$$

Although Lamarche's model gives a good agreement with COMSOL in a concentric geometry case (equivalent radius model), a comparison with an actual U-tube configuration model of COMSOL gives small differences for short time scales. Moreover, the short circuit between the U-tube legs cannot be accounted for by this model. It is due to the limitation of the analytical solutions to treat the real U-tube configuration; in fact, no exact solution is known for that case.

1.1.2 Mid- to long-time scale region

The mid- to long-time scale region is generally defined as the ground region outside the borehole. In this domain, different time scales can be found over the system operation. According to these time scales, the number of dimensions that need to be included may vary. For short-duration, a one-dimensional model that account for a radial heat diffusion may be sufficient. If boreholes are closely-spaced, thermal interference among boreholes has to be considered by a 2D model $T(x, y, t)$, and finally a 3D approach, giving $T(x, y, z, t)$ will be necessary to account for the axial effects occuring after a certain number of years of operation. In this section, different models, valid for each time scale, will be presented. Analytical approaches are mainly presented as they are generally regarded as more practical to use. The related methods (section 1.1.2.2 and 1.1.2.4) that were developed to exploit the analytical solutions will be introduced in this part as well.

1.1.2.1 A borehole case (1D)

As briefly mentioned above, the heat diffusion or absorption from or to a borehole can be modeled by a one-dimensional method in a cylindrical grid. In this case, the temperature distribution can be expressed by a form of $T(r, t)$. Some analytical solutions [Ingersoll & Plass 1948], [Carslaw & Jaeger 1947], [Ingersoll *et al.* 1954] have been used for this problem. The infinite line source (ILS) model was introduced by Lord Kevin, and then Ingersoll et al. [Ingersoll & Plass 1948] utilized this method for the BHE modeling. Many other authors adopted the ILS in their models particularly for ground modeling. The ILS can predict the radial temperature profile around a line source that is embedded in a homogeneous medium with an infinite length. The heat transfer rate over the borehole depth is regarded as constant, which lead to the one-dimensional problem (Eq. 1.31).

$$T_0 - T(r,t) = \frac{q}{2\pi k_s}\int_{\frac{r}{2\sqrt{\alpha t}}}^{\infty}\frac{\exp^{\beta^2}}{\beta}d\beta = \frac{q}{2\pi k_s}I(X) \text{ where}, X = \frac{r}{2\sqrt{\alpha t}} \tag{1.31}$$

However, it is not valid to predict the temperature distribution before a certain time of operation; generally, it is acceptable for use after $t > 20r^2/\alpha$. This limitation is due to the fact that the heat source is assumed to be a line source. The value of $I(X)$ was pre-calculated [Bose *et al.* 1985] and given by a tabulated or graphical form. For practice, an approximation for this value can be used as follows [Jun *et al.* 2009]:

When $0 < X \leq 1$,

$$\begin{aligned} I(X) =& 0.5(-\ln X^2 - 0.57721566 + 0.99999193X^2 - 0.24991055X^4 \\ &+ 0.05519968X^6 - 0.00976004X^8 + 0.00107857X^{10}) \end{aligned} \tag{1.32}$$

When $X \geq 1$,

$$I(X) = \frac{1}{2X^2\exp(X^2)}\frac{A}{B} \tag{1.33}$$

where,
$A = X^8 + 8.5733287X^6 + 18.059017X^4 + 8.637609X^2 + 0.2677737$
$B = X^8 + 9.5733223X^6 + 25.6329561X^4 + 21.0996531X^2 + 3.9684969$

To remove this limitation coming from the line source assumption, a cylindrical source can be used, where the heat is emitted or absorbed at the wall ($r = r_b$) of the cylindrical source that is placed in the same infinite homogeneous medium as the ILS case. This cylindrical heat source (CHS) theory proposed by Carslaw [Carslaw & Jaeger 1947] was revisited by Ingersoll [Ingersoll *et al.* 1954] to show that there is an analytical solution to the transient heat transfer. Two different equations were presented under two different cases: constant heat transfer rate and constant wall temperature at the cylinder wall. The former case is presented here (Eq. 1.34) because heat flux boundary case at the borehole wall are frequently used for typical models. Here, $p = r/r_b$ is the ratio between a measured radius and a borehole radius, and J_0, J_1, Y_0, and Y_1 are the bessel functions of order 0 and 1.

$$\begin{aligned} T_0 - T_s &= q\frac{G(F_O,p)}{k_s} \\ G(F_O,p) &= \frac{1}{\pi^2}\int_0^{\infty} f(\beta)d\beta \\ f(\beta) &= \frac{\exp^{-(\beta^2 F_O)} - 1}{\beta^2(J_1^2(\beta) + Y_1^2(\beta))}[J_0(p\beta)Y_1(\beta) - J_1(\beta)Y_0(p\beta)] \end{aligned} \tag{1.34}$$

For this function G, Bernier [Bernier 2001] proposed approximated equations for the values of p=1,2,5, and 10 (Eq. 1.35).

$$\begin{aligned} &p{=}1 \quad G = 10^{[-0.89129+0.36081\times\log_{10}(F_O)-0.05508\times\log_{10}^2(F_O)+3.59617\times10^{-3}\times\log_{10}^3(F_O)]} \\ &p{=}2 \quad G = 10^{[-1.4541+0.89933\times\log_{10}(F_O)-0.31193\times\log_{10}^2(F_O)+0.061119\times\log_{10}^3(F_O)]} \\ &p{=}5 \quad G = 10^{[-3.0077+2.25606\times\log_{10}(F_O)-0.79281\times\log_{10}^2(F_O)+0.134293\times\log_{10}^3(F_O)]} \\ &p{=}10 \quad G = 10^{[-9.1418+11.7025\times\log_{10}(F_O)-7.09574\times\log_{10}^2(F_O)+2.269837\times\log_{10}^3(F_O)]} \end{aligned} \tag{1.35}$$

All the analytical models presented here are based on one-dimensional approach, so they were oriented for a borehole. When the soil domain is composed of several boreholes, it is possible to extend the solutions to a 2D case by a superposition technique.

1.1.2.2 Boreholes thermal interference (2D)

When several boreholes are used, the thermal interaction between them has to be considered. This interaction can be approximated by superposition as mathematically shown in Eq. 1.36 with its correspondent schematic (Fig. 1.4).

$$T_0 - T_j(t) = T_0 - T(r_{b,j}, t) + \sum_{i=1, i\neq j}^{N_{BHE}} (T_0 - T(r_{i-j}, t)) \tag{1.36}$$

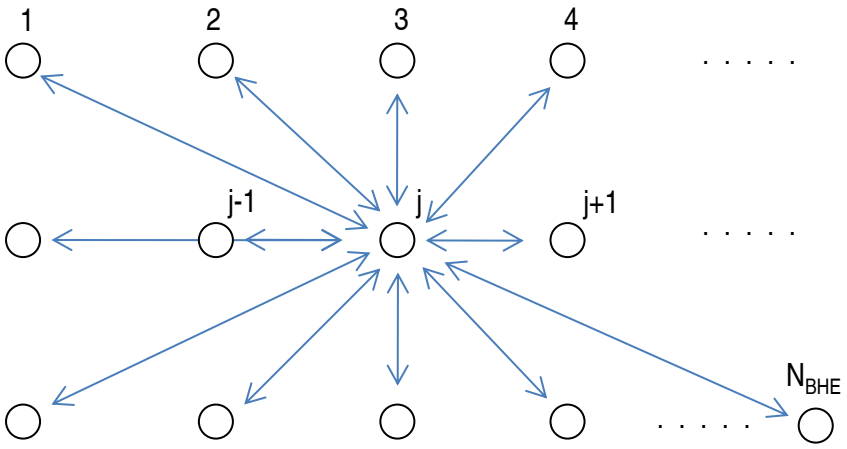

Figure 1.4: Schematic of the principle of spatial superposition

Once each borehole wall temperature is known using this equation for all boreholes, the average borehole temperature of the whole bore field is simply calculated by:

$$T_{ave}(t) = \sum_{j=1}^{nb_{BHEs}} T_j(t)/nb_{BHE_s} \tag{1.37}$$

This average value is useful for defining the g-function of a given bore field, which will be presented in the section 1.1.3.

Pinel [Pinel 2003] proposed a two-dimensional (x, y) numerical model in a nonuniform Cartesian grid with a greater mesh concentration near boreholes. Pinel's model was developed to calculate a penalty temperature, T_p shown in Eq. 1.38 in order to complete a 2D bore-field model from the 1D cylindrical model. The temperature T_p was, at first, proposed and evaluated by Kavanaugh et al. [Kavanaugh & Rafferty 1997]. Pinel's work was a proposition to improve this value of T_p. To obtain the value, Pinel simulated two different cases by his numerical model. The first is the real borefield of several boreholes case, and the second is the same borefield but composed of a single borehole that emits/absorbs the same heat flux used for each borehole of the first borefield. In the first case, the average borehole wall temperatures, $\overline{T_{b,nb}}$, can be obtained by Eq. 1.39, where nb is the number of boreholes.

$$T_b = T_0 - q\frac{G(F_O, p)}{k_s} + T_p \tag{1.38}$$

$$\overline{T_{b,nb}} = \frac{\Sigma_{n=1}^{nb} T_{b,n}}{nb} \tag{1.39}$$

The value of T_p is obtained by subtracting the wall temperature of a single borehole $T_{b,1b}$ from the average wall temperature of the entire borefield case as shown in Eq. 1.40.

$$T_p = \overline{T_{b,nb}} - T_{b,1b} \tag{1.40}$$

In his work, it was concluded that the value of T_p could be calculated every two weeks (336 hours) in annual hourly simulation, thus reducing computation time.

1.1.2.3 Axial effect (3D)

It is necessary to take into account the axial effects that are caused by the surface and bottom boundaries of the borefield. According to Eskilson [Eskilson 1987], axial effects start to be significant after a time period of Eq. 1.41; consequently, the models abovementioned (ILS, CHS) are strictly not valid after this time period.

$$t > \frac{H^2}{90\alpha} \tag{1.41}$$

Finite line source model

Zeng et al. [Zeng *et al.* 2002] proposed an analytical solution that allows to calculate the temperature difference between the far-field and the borehole wall temperature in a semi-infinite medium. In this approach, a finite-line source is placed vertically starting at the ground surface, that is $z = 0$. The ground surface temperature of ground is regarded as constant. In order to realize this boundary conditions, he adopted an mirror image of the source.

As shown in Fig. 1.5, each increment dh of the line source can be regarded as a punctual source. Therefore, the temperature increase at a time t for a point $m(r, z)$ can be calculated as Eq. 1.42.

$$d(T_0 - T(r,z)) = \frac{q}{4\pi k_s} \frac{\operatorname{erfc}\left(\frac{\sqrt{r^2+(z-h)^2}}{2\sqrt{\alpha t}}\right)}{\sqrt{r^2+(z-h)^2}} dh \tag{1.42}$$

Then, we can get the final formula of FLS (Eq. 1.43) by integrating Eq. 1.42 not only for the finite line source but also for the mirror image source from 0 to H. This equation represents a difference between the far-field undisturbed temperature and one at a point (r, z) for a borehole subjected to a constant heat transfer per unit length q.

$$T_0 - T(r,z,t) = \frac{q}{4\pi k_s} \int_0^H \left(\frac{\operatorname{erfc}\left(\frac{\sqrt{r^2+(z-h)^2}}{2\sqrt{\alpha t}}\right)}{\sqrt{r^2+(z-h)^2}} - \frac{\operatorname{erfc}\left(\frac{\sqrt{r^2+(z+h)^2}}{2\sqrt{\alpha t}}\right)}{\sqrt{r^2+(z+h)^2}} \right) dh \tag{1.43}$$

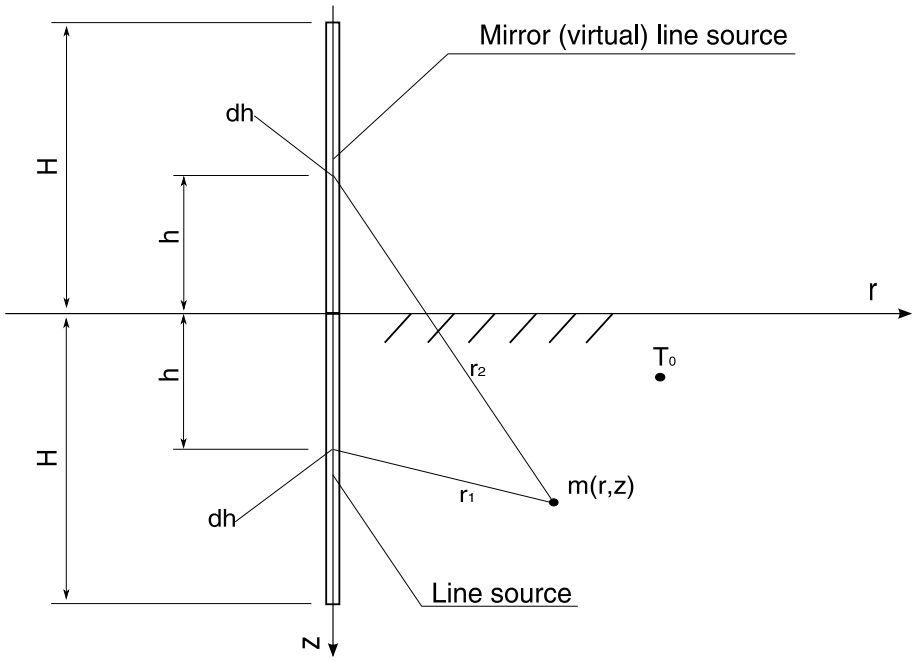

Figure 1.5: mirror image principals

Moreover, Eq. 1.43 can be integrated over the borehole height to obtain the average temperature at a given r. Imposing $r = r_b$ on Eq. 1.44, the average borehole wall temperature can be obtained:

$$T(r,t) = \frac{1}{H}\int_0^H T(r,z,t)dz \tag{1.44}$$

Lamarche et al. [Lamarche & Beauchamp 2007a] simplified Eq. 1.44 by a single integral. This new contribution is due to a common interest of obtaining only the average temperature over the borehole height instead of a calculation of all the temperatures. They compared this simplified model (Eq. 1.45) with Zeng's method (Eq. 1.43 and 1.44). It is proved that the suggested simple model is about 3500 times faster than the other.

$$T_0 - T(r,t) = \frac{q}{2\pi k_s}\left(\int_\beta^{\sqrt{\beta^2+1}} \frac{\operatorname{erfc}(\gamma z)}{\sqrt{z^2-\beta^2}}dz - D_A - \int_{\sqrt{\beta^2+1}}^{\sqrt{\beta^2+4}} \frac{\operatorname{erfc}(\gamma z)}{\sqrt{z^2-\beta^2}}dz - D_B\right) \tag{1.45}$$

where,

$$\begin{aligned} D_A =& \sqrt{\beta^2+1}\operatorname{erfc}(\gamma\sqrt{\beta^2+1}) - \beta\operatorname{erfc}(\gamma\beta) - \frac{e^{-\gamma^2(\beta^2+1)} - e^{-\gamma^2\beta^2}}{\gamma\sqrt{\pi}} \\ D_B =& \sqrt{\beta^2+1}\operatorname{erfc}(\gamma\sqrt{\beta^2+1}) - 0.5\beta\operatorname{erfc}(\gamma\beta) + \sqrt{\beta^2+4}\operatorname{erfc}(\gamma\sqrt{\beta^2+4}) \\ & - \frac{e^{-\gamma^2(\beta^2+1)} - 0.5(e^{-\gamma^2\beta^2} + e^{-\gamma^2(\beta^2+4)})}{\gamma\sqrt{\pi}} \\ \gamma =& \frac{1}{2\sqrt{F_O}}, \quad F_O = \frac{\alpha t}{H^2}, \quad \beta = \frac{r}{H} \end{aligned} \tag{1.46}$$

Costes et al. [Costes & Peysson 2008] followed the same mathematical process used in Lamarche's work to obtain a formula for $D > 0$, where D is the distance of the borehole top from the ground surface. The resultant equation is presented in Eq. 1.47. Imposing $t \to \infty$ on this equation, it becomes the same formula of the FLS steady-state model proposed by Sheriff [Sheriff 2007] for the same case of $D > 0$.

$$
\begin{aligned}
&T_0 - T(r,t) = \frac{q}{2\pi k_s}(A - B) \\
&A = \int_{\beta}^{\sqrt{\beta^2+1}} \frac{\operatorname{erfc}(yz)}{\sqrt{z^2-\beta^2}} dz - \left(\sqrt{\beta^2+1}\,\operatorname{erfc}(y\sqrt{\beta^2+1}) - \beta\,\operatorname{erfc}(y\beta) - \frac{\mathrm{e}^{-y^2(\beta^2+1)} - \mathrm{e}^{-y^2\beta^2}}{y\sqrt{\pi}} \right) \\
&B = -\frac{D}{H} \int_{\sqrt{\beta^2+(\frac{2D}{H})^2}}^{\sqrt{\beta^2+(1+\frac{2D}{H})^2}} \frac{\operatorname{erfc}(yz)}{\sqrt{z^2-\beta^2}} dz + \left(1 + \frac{D}{H}\right) \int_{\sqrt{\beta^2+(1+\frac{2D}{H})^2}}^{\sqrt{\beta^2+(2+\frac{2D}{H})^2}} \frac{\operatorname{erfc}(yz)}{\sqrt{z^2-\beta^2}} dz \\
&\quad + F\left(y, \sqrt{\beta^2 + (1+\frac{2D}{H})^2}\right) - \frac{1}{2}\left[F\left(y, \sqrt{\beta^2 + (2+\frac{2D}{H})^2}\right) + F\left(y, \sqrt{\beta^2 + (\frac{2D}{H})^2}\right) \right] \\
&\quad \text{where,} \\
&\quad y = \frac{H}{2\sqrt{\alpha t}}, \quad F(y,z) = \int \operatorname{erfc}(yz) dz = z\,\operatorname{erfc}(yz) - \frac{\mathrm{e}^{-y^2z^2}}{y\sqrt{\pi}}
\end{aligned}
\tag{1.47}
$$

1.1.2.4 Variable heat transfer rate

The solutions presented in the previous are expressed for a constant value of q. In practice, this heat transfer rate to the ground is variable as building loads vary with time. In order to adapt a variable heat transfer rate to the analytical formulas, the temporal superposition method has to be applied. A simple case that was also used in Bernier's work [Bernier 2001] is presented here, as shown in Fig. 1.6. In this figure, three heat pulses are considered. To calculate $\Delta T(T_0 - T_s(r,t))$ at the end of three time intervals, i.e., at t_3, each time interval with a different heat transfer rate, q_1, q_2, and q_3, has to be modified by prevailing previous heat transfer rates with taking into account the superimposed effect as shown in the lowest graph in Fig. 1.6. If the CHS model is used for this example, the temperature difference at T_3 can be expressed as Eq. 1.48.

$$
\begin{aligned}
T_0 - T_s =& q_1 \frac{(G(F_{Ot_3-0}) - G(F_{Ot_3-t_1}))}{k_s} \\
&+ q_2 \frac{(G(F_{Ot_3-t_1}) - G(F_{Ot_3-t_2}))}{k_s} + q_3 \frac{G(F_{Ot_3-t_2})}{k_s}
\end{aligned}
\tag{1.48}
$$

As seen in this example, the number of terms in the summation is equal to the number of time intervals, and this number will increase as time progresses. As a result, annual hourly simulations require a large number of terms. Moreover, all these terms should be recalculated in each time step because there is no recurrence. Yavuzturk et al. [Yavuzturk & Spitler 1999] proposed to average the loads that occur more than a certain time ago by a single average load while leaving the short-term loads intact. It comes from the fact that the importance of a load at a given time step diminishes for subsequent time steps as time goes. Yavuzturk et al. referred to this as "load aggregation". Bernier et al. [Bernier *et al.* 2004] proposed to aggregate loads by time period: a day (X_d), a week (X_w), a month

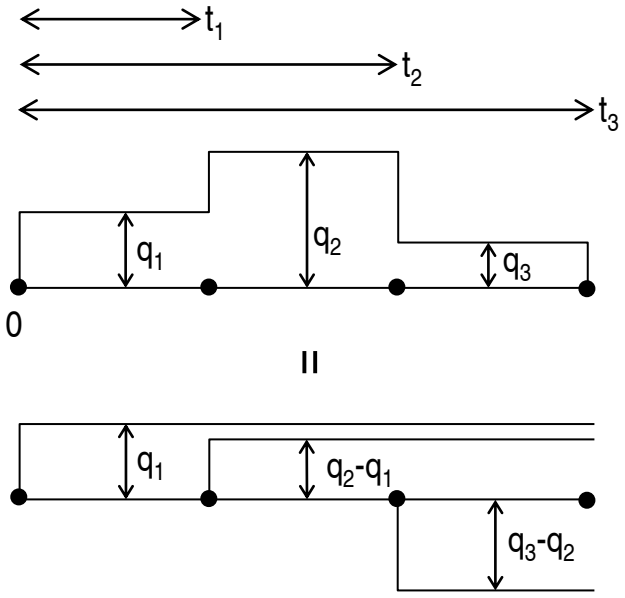

Figure 1.6: Schematic of the principle of temporal superposition

(X_m), and years (X_y) while keeping the immediate loads (X_h) inherent. In this so-called "Multiple Load Aggregation Algorithm (MLAA)", 12, 48, 168, and 360 hours were set as a proposed scheme for X_h, X_d, X_w, and X_m respectively.

1.1.3 Existing GHEs models

In this section, some complete models are presented that were developed by combining different solutions partly presented in the earlier part of this section. Therefore, genuine characteristics inherent in a selected solution affect the model capacity for use. The early remarkable studies (section 1.1.3.1 and 1.1.3.2) were done by Swedish authors, and their contributions to the geothermal modeling is still valuable as used as a reference for validation of a new model or providing with source codes to the several computer programs (EED, GLHEPRO, and etc).

1.1.3.1 Eskilson's g-function

Eskilson [Eskilson 1987] employed a two-dimensional numerical model to model a single GHE. The finite difference method was used in the very coarse ground meshes as seen in Fig. 1.7. In this modeling, he used a resistance value, R_b for modeling the part of inside borehole. The multipole expression [Bennet *et al.* 1987] similar to Eq. 1.9 was used for the resistance value.

He proposed thermal response factors which relate the temperature difference between the far-field and the borehole wall temperature. This response factor was referred to as "g-function", and it is commonly called "Eskilson's g-function". For general use, the g-function was defined as a function of three dimensionless numbers: $\frac{r_b}{H}$, $\frac{B}{H}$, $\frac{t}{t_s}$. Here, the steady-state time-scale, t_s, was defined in [Claesson & Eskilson 1988] by:

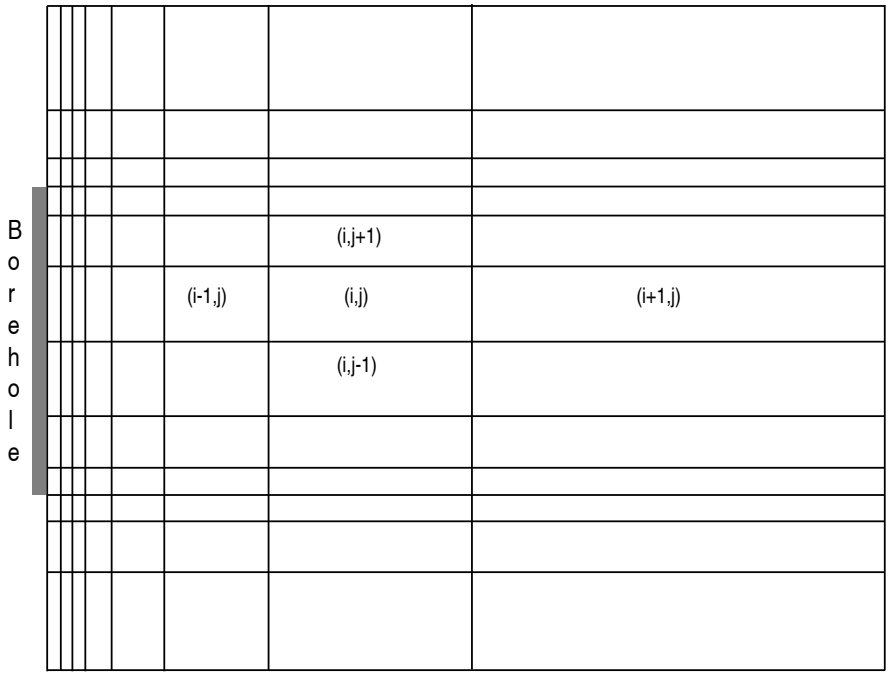

Figure 1.7: Two-dimensional radial-axial mesh used in Eskilson's work

$$t_s = \frac{H^2}{9\alpha} \tag{1.49}$$

In his work, the g-function was obtained by imposing an arbitrary borehole wall temperature T_b and measuring the resultant heat transfer rates per meter at the same wall. As shown in Eq. 1.50, the resulting g-function is a function of t/t_s, r_b/H, and B/H where B is the distance between adjacent GHEs. It should be noted that each g-function are valid for particular bore field geometries (square, L-shaped etc...).

$$T_0 - T_b = \frac{q}{2\pi k_s} g(t/t_s, r_b/H, B/H) \tag{1.50}$$

Eskilson provided a number of g-functions but for limited bore-field geometries that are mostly based on a rectangular or linear grid pattern. It is one of the main shortcomings of the g-function model together with the compulsory approximation that all temperatures T_b were regarded as the same even if many cases were not belonged to such a case. All the g-functions were set by fixing r_b/H=0.0005, and Eq. 1.51 was proposed for other cases other than this value. Here, r_b^* is the real radius of borehole, and r_b is a calculated value for a given H to match the value of 0.0005. According to the author, it is an approximation, but the associated error was less than 0.3% for a small variation in the two radius.

$$g(t/t_s, r_b^*/H) = g(t/t_s, r_b/H) - \ln(r_b^*/r_b) \tag{1.51}$$

Fig. 1.8 shows an example of Eskilson's g-function for 6 boreholes, plotted by varying B/H. As seen in this figure, curves increase linearly until t equals to the steady-state time, t_s, i. e. , at ln(t/t_s)=0. After this point, each curve reaches a plateau towards a steady-state condition. As shown in Fig. 1.8, the influence of neighboring boreholes is

important when the borehole distance is small (i.e. B/H is small), resulting in a large difference between the borehole wall and the undisturbed soil temperature.

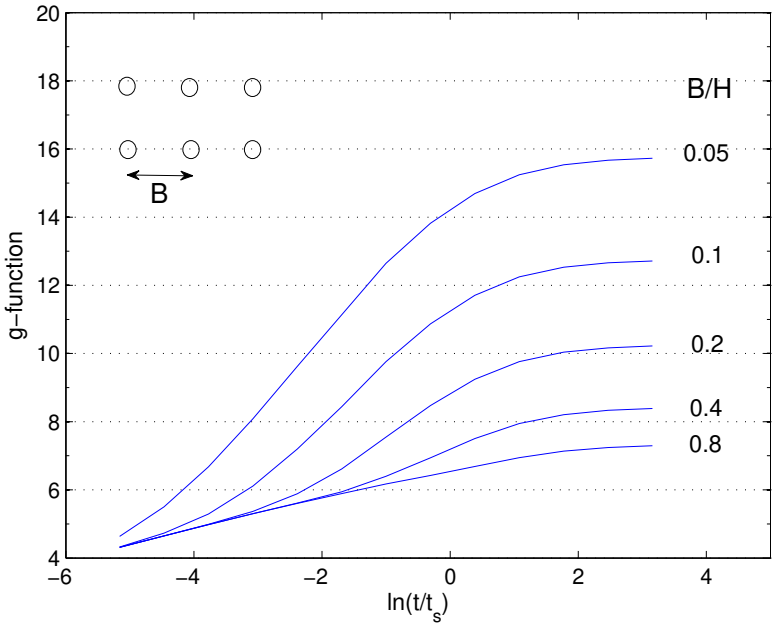

Figure 1.8: An example of Eskilson's g-fuction for 6 boreholes (2×3)

Eskilson proposed the following limit for the g-function model:

$$t > \frac{5r_b^2}{\alpha} \tag{1.52}$$

This limit is due to the fact that the grout region will be normally handled under the quasi steady-state with this g-function and the mesh in the vicinity of borehole wall is not sufficiently detailed. In fact, he obtained the value of $5r_b^2/\alpha$ by estimating the steady-state time for the grout region in a typical case and multiplying it by a coefficient. For a typical case, this value can be in the order of 3 to 6 hours [Lamarche & Beauchamp 2007b].

Yavuzturk et al. [Yavuzturk & Spitler 1999] used a detailed two dimensional numerical model in order to extend the g-function to the short-time scales. The numerical model is spatially discretized as presented in Fig. 1.9. In a given heat transfer rate, the temperature differences between the U-pipe wall and the far-field were evaluated by the numerical model. The extended curve of g-function for the short-time scales was obtained by Eq. 1.53, where a total resistance value was used for estimating the borehole wall temperature from the obtained tube-wall temperatures to match Eskilson's formula. This total resistance is the sum of the grout resistance proposed by Paul (Eq. 1.5), a pipe resistance, and a convective resistance between fluid and the U-pipes. The final g-function curve was added to Eskilson's one for dimensionless times ($\ln(t/t_s)$) between -15.5 and -7.3. This range can be interpreted as times of 2.5 minutes to 200 hours for a typical case. Fig. 1.10 shows the short time-step plotted side by side with the Eskilson's.

$$g(t/t_s, r_b/H) = \frac{2\pi k_s}{q}(\overline{T_p} - (R_t q) - T_0) \tag{1.53}$$

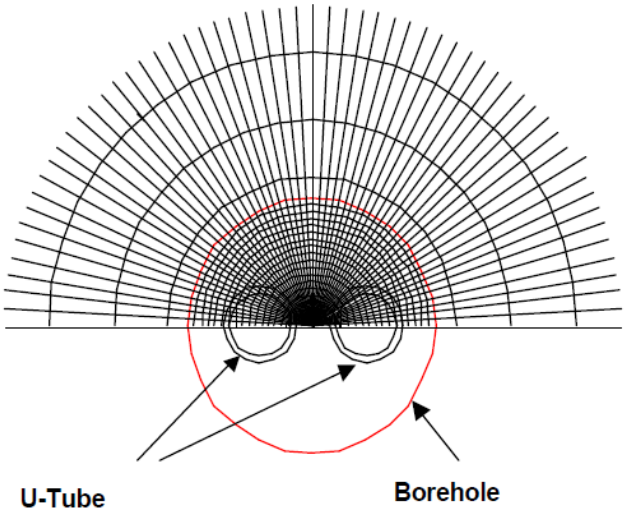

Figure 1.9: Example numerical grid near the borehole center used for Yavuzturk's work (Fig. 4. 3 in [Yavuzturk 1999])

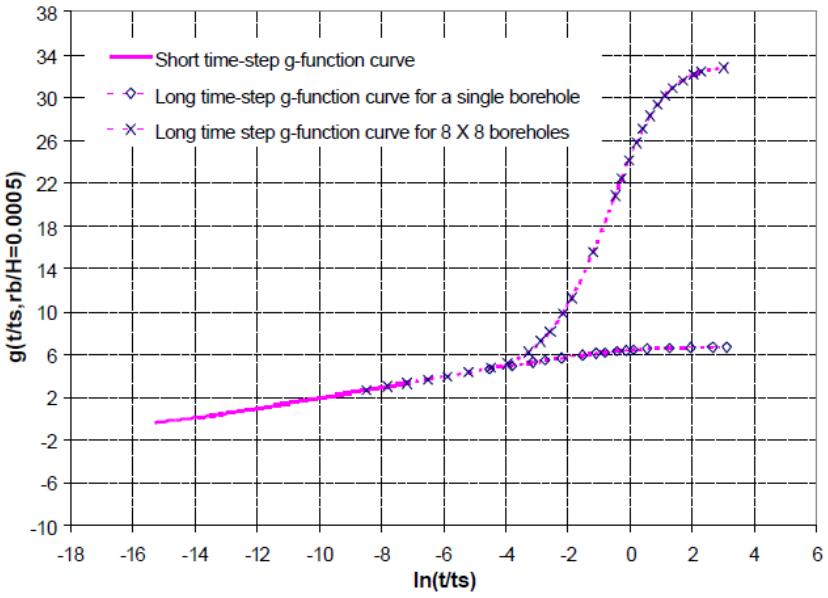

Figure 1.10: Short time-step g-function curve as an extension of the long time-step g-functions [Yavuzturk 1999]

Sheriff [Sheriff 2007] redrew the g-function by using the FLS model presented in the section 1.1.2.3. The same process for the development of Eskilson's g-functions was used but the boundary condition, which she defined as imposing a heat transfer rate in the borehole walls instead of imposing a fixed wall temperature. The author compared the FLS-generated g-function curve with Eskilson's as shown in Fig. 1.11. In her work, the error between the two models was larger for small values of B/H and for large numbers of boreholes; for instance, the error of the steady-state value at ln(t/t_s)=3.2, correspondent to 620 years in her example, is of about 26.5% for 10×10 bore-field with 0.05 of B/H. However, errors were only in the order of under 3.4% for times inferior to the value ln(t/t_s)=-2.3, which corresponds to 2.6 years.

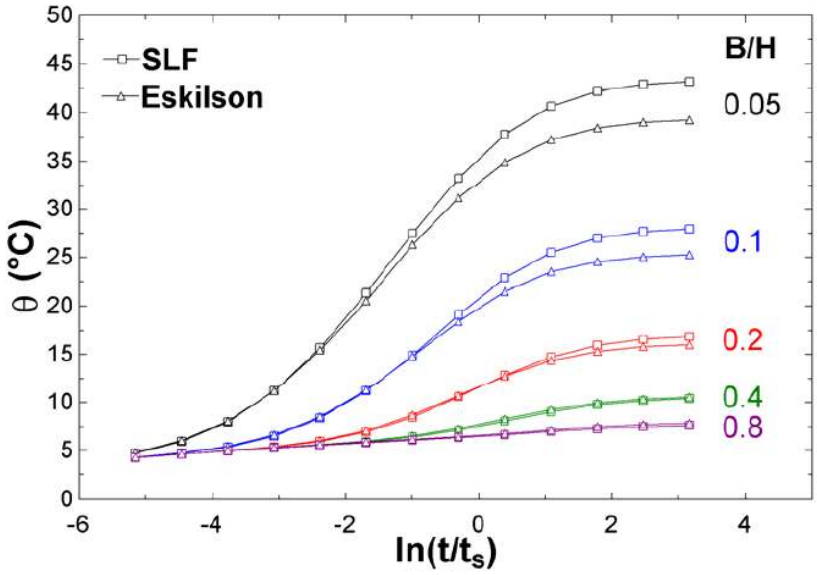

Figure 1.11: Comparison of the g-function generated by FLS model to Eskilson's for 32 boreholes (8×4) [Sheriff 2007]

The g-function approach have been popularly used for various purposes. Above all, Cauret et al. [Cauret & Bernier 2009] applied it to the modeling of an underground compact collector where each branch of the compact collector was considered as a vertical borehole to create a g-function for a given configuration of collectors. In this case, the FLS model for D>0 (see Eq. 1.47) was used for over the height of the collector, i.e. from a depth of 1 to 3m in order to take into account the effect of ground surface.

On the other hand, Bernier [Bernier 2006] used this g-function for calculation of the penalty temperature T_p that is also essential to GHEs dimensioning expressed by Eq. 1.54. By using g-functions, it can be expressed as Eq. 1.55, where g_n signifies the g-function of the borefield composed of several boreholes in a specific configuration, and g_1 for one borehole case.

$$L = \frac{q_h R_b + q_y R_{10y} + q_m R_{1m} + q_h R_{6h}}{T_m - (T_s + T_p)} \tag{1.54}$$

$$T_p = \frac{q}{2\pi k_s} \times (g_n(t/t_s, B/H) - g_1(t/t_s)) \tag{1.55}$$

Finally, the g-function is exploited by the temporal superposition technique to take into account the variable q. The g-function curves are normally generated by tabulated data, so the required value of g-function at a specific time step in simulation has to be calculated by interpolation of the adjacent tabulated data.

1.1.3.2 Duct Storage (DST) model

DST model was a stand-alone software inspired by Hellström [Hellström 1989] to model the seasonal ground storage system. Afterward, it has been integrated with TRNSYS as one of the TESS modules (Type 557). The model has been validated by many authors [Shonder *et al.* 1999] [Thornton *et al.* 1997]..., so that it has largely become a reference for testing other methods.

It has a very complicated model structure[1] while it is relatively compact in terms of calculation time in spite of using the numerical approach. Three solutions are obtained in each ground region defined by the author: A global solution, a steady-flux solution, and a local radial solution. A final solution in each time step can be obtained by superposing the solutions.

Above all, the global solution can be obtained by a ordinary heat conduction problem in the two-dimensional axial-radial coordination (r, z) with two heat source terms as seen in Eq. 1.56. This model uses the explicit finite difference method (FDM). The solution accounts for the heat transfer processes between the ground surface and the storage soil volume that contains boreholes, between different parts of this storage volume, and between the storage volume and its surrounding ground etc. The two source terms will be obtained by the other two solutions. The term q_{sf} is due to heat redistribution within the storage volume accounting for circulation of the heat carrier fluid, and it is obtained by the steady-flux solution. The heat source term q_l originates from the local problem. An example of a mesh used for the global problem is shown in Fig. 1.12.

$$C\frac{\partial T}{\partial t} = \nabla \cdot (\lambda \nabla T) + q_{sf} + q_l \tag{1.56}$$

The local solution is the thermal heat transfer process around the individual borehole, obtained by a one-dimensional radial mesh represented in Fig. 1.13. Therefore, the local temperature T_l, expressed as Eq. 1.57 with a heat sink, accounts for short-time variation, for example, at the borehole wall. This heat sink term q_l is used for communication with the global model (see Eq. 1.56). However, the local model that explains the heat transfer process around a borehole is assumed to be the same in a given subregion which contains many parts of boreholes as seen in the right of Fig. 1.13. Therefore, the term q_l is the average heat transfer rate from the fluid to the local problem as Eq. 1.58, where E_k is the amount of injected heat to a subregion k during a global time-step t_g for the subregion volume V_k.

$$C\frac{\partial T_l}{\partial t} = \lambda(\frac{\partial^2 T_l}{\partial r^2} + \frac{1}{r}\frac{\partial T_l}{\partial r}) - q_l \quad r_b < r \leq r_1 \tag{1.57}$$

$$q_l = \frac{E_k}{t_g V_k} \tag{1.58}$$

The term q_{sf} can be calculated by

[1] Detailed graphical explanations can be found in [Chapuis & Bernier 2009]

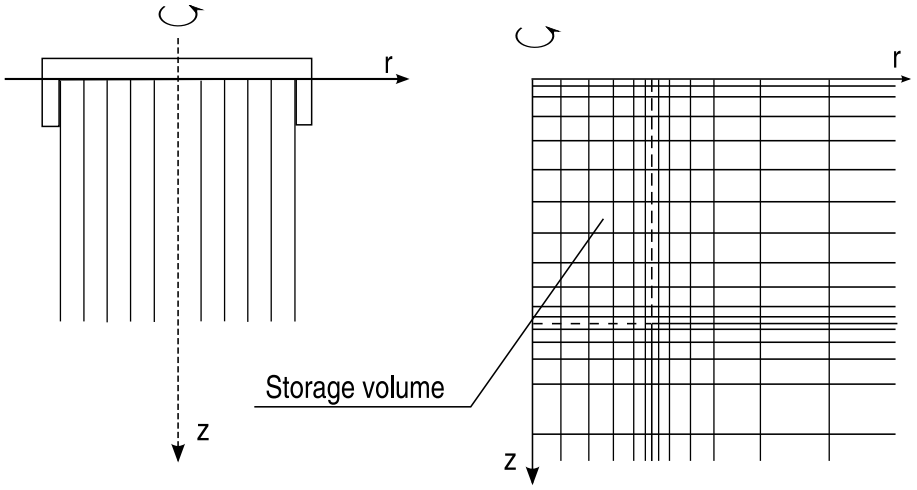

Figure 1.12: a) An example of a schematic of a storage system and b) a mesh used for the global problem, where the zone inside dashed lines means the storage volume

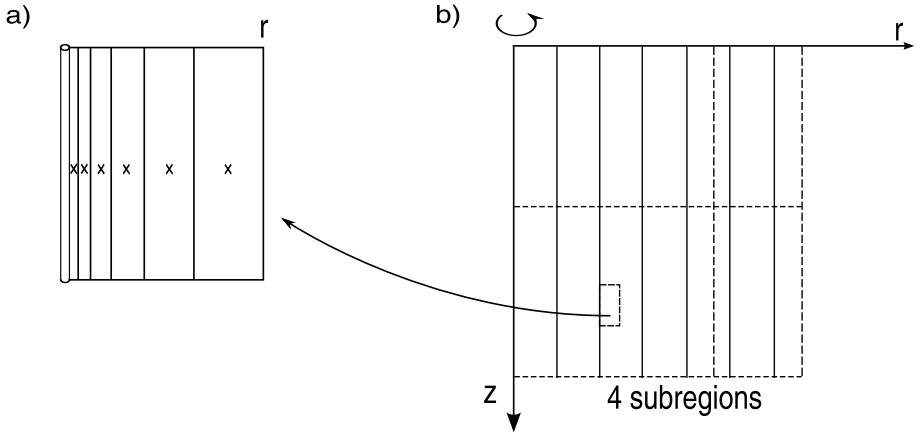

Figure 1.13: a) An example of a mesh for the local problem in a subregion b) division of the storage volume into four subregions

$$q_{sf} = \frac{C_f Q_f}{V_k}(1 - \beta_{sf}^k)(T_g^k - T_{g,i,j}^k) \tag{1.59}$$

Here, the damping factor for the steady-flux part is

$$\beta_{sf}^k = \mathrm{e}^{-\frac{\alpha_v V_k}{C_f Q_f}}, \quad \alpha_v = \lambda[r_1\sqrt{\frac{1}{2}(\ln(\frac{r_1}{r_b}) - \frac{3}{4} + 2\pi\lambda R_b)}]^{-2} \tag{1.60}$$

As seen above, this term is used to redistribute heat caused by circulation of fluid. The average global temperature T_g^k and the global cell temperature $T_{g,i,j}^k$ in the subregion k are used. The soil temperature at any point can be obtained by superposing the temperatures calculated by the three different models as Eq. 1.61, where j' means a appropriate nodal point in the local mesh.

$$T = T_{g,i,j}^k + T_{l,j'}^k + T_{sf,j'}^k \tag{1.61}$$

In this model DST, the exact locations of the boreholes are not known, but the regularly positioning boreholes are only regarded in cylindrical symmetry. This characteristic is the principal shortcoming of the model in use for simulation of the geothermal system because many GHEs are arranged in irregular geometries such as L-form or I-form around a building.

1.1.3.3 Various numerical models

In general, the steady-state or the approximation of equivalent diameter is assumed for part of inside the borehole in the methods previously presented. It causes errors for short-time analysis [Cui *et al.* 2008] [Lamarche & Beauchamp 2007b] [Kim *et al.* 2010b]. Thus, as seen in the previous sections, most of the analytical-based models are valid after each time-criterion defined by the author or presumed from the principle of model.

In recent years, many numerical models have been developed. A mesh has been generated for the whole domain of ground or even for the grout region. Some numerical models are presented in this section.

Rottmayer et al. [Rottmayer *et al.* 1997] proposed a quasi-3D model that in the cylindrical grids (θ,r,z); thus, it concerned naturally a one-borehole case. Assuming that the heat transfer rate in the vertical direction is negligible, no axial conduction is considered. Therefore, each slice cylinder is independently calculated over the length of borehole, but only coupling to the model of fluid that circulates through all the cylinders. The borehole geometry was considered as pie-sector shape as explained in the section 1.1.1.2.

A Swiss model [Huber & Schuler 1997] was developed in the similar principles. The two-dimensional radial-axial grid was also used in the model but until the radius of 2m, beyond which a solution belonging to a group of analytical solutions of the line source theory was applied to provide the outer boundary condition at the cylinder wall. Other than Rottmayer, the part of the grout was regarded as a single mesh with the equivalent capacity : $C = c\rho\pi(r_b^2 - 4r_{pi}^2)$. Then, the heat flux among the grout, the soil, and the fluid was obtained by using the resistance value. This model has been integrated to TRNSYS as Type 451, which has been used for the short-time simulation ([Kummert & Bernier 2008], [Kim *et al.* 2010a]) because of its ease in access. Different soil properties for each horizontal layer can be simulated with Type 451. However, this model can only treat a double-U-tube case that is the common case in Europe.

A commercial code (ANSYS) of finite element method (FEM) was used for a single borehole by Cui et al. [Cui *et al.* 2008]. This work is focused on the short-time analyses so that the 2-dimensional (x, y) problem was only considered. Using the commercial code ANSYS, more detailed unstructured mesh was adopted for part of the grout together with the vicinity of the borehole as presented in Fig. 1.14. Similarly, Li et al. [Li & Zheng 2009] used a detailed mesh to develop a 3D finite volume method (FVM) model but regarding the U-tube as a resistance model unlike Cui's model.

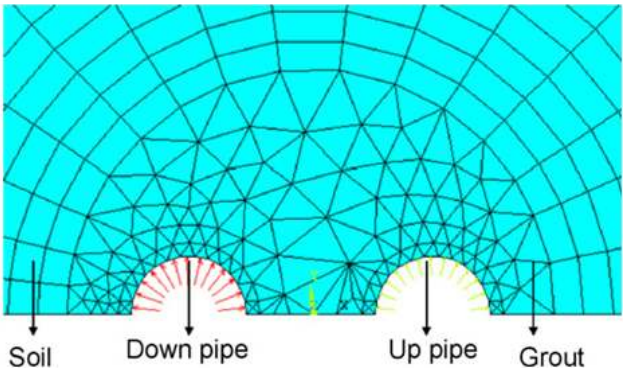

Figure 1.14: a detailed mesh used in Cui's work [Cui *et al.* 2008]

On the other hand, Lee et al. [Lee & Lam 2008] developed a 3D FDM model using the rectangular coordinate system with an irregular grid scheme as seen in Fig. 1.15. In this grid, several boreholes can be simulated but in limited flexibility. It was one of the first pure-numerical 3D models for a bore-field simulation, but the modeling of the grout region was replaced by a resistance value as other traditional models. To couple this resistance model with the rectangular-grid model, the authors recommended to multiply q_b calculated by the resistance model by a correction factor 1.047, which was obtained by a comparison with the cylindrical source model.

Finally, He et al. [He *et al.* 2009] developed dynamic GHE models in a finite volume solver of GEMS2D and GEMS3D representing two- and three-dimensional version respectively. They found that the model GEMS3D coupled to a fluid transport model can account for the effect of the thermal mass of the circulating fluid and the dynamics of fluid transport through the loop. They highlighted that this effect might be important where heat pumps and circulating pumps switch on and off during a given hour.

It should be noted that the detailed mesh necessitates a long calculation time in numerical modeling. In fact, most of the numerical models presented in this section are capable of simulating only a single-borehole case where the modeling for 3D effects can be achieved by using two-dimensional grid (r, z). Only Lee's model can handle the multi-boreholes case, but it is incapable to analyze the short-time analysis. As for modeling using commercial solvers (ANSYS, Fluent, COMSOL, GEMS,...), it is difficult to couple obtained models to a commercial software package for a full-system simulation.

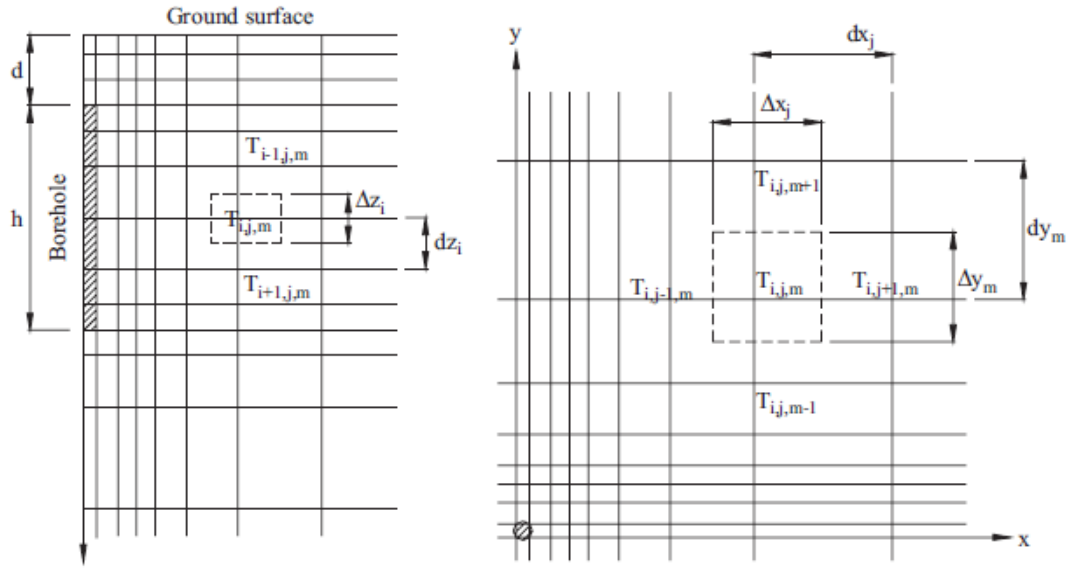

Figure 1.15: A grid scheme used in Lee's model (Fig. 2. in [Lee & Lam 2008])

1.2 State model reduction techniques

From its advent in the automatic field, model reduction has been the subject of various research domains over the last 40 years [Petit 1991] [Gao *et al.* 2004]. As recognized in the naming, the reduction techniques are used for accelerating calculation time by mathematically reducing the original problem order in numerical approaches.

Several works have been done particularly in the domain of building energy simulation [Lefebvre 2007]. In this domain, a fine analysis on the thermal behavior of building elements are increasingly required. As a result, model reduction can be naturally used for the case of increased meshes resulted from detailing geometries.

The thermal bridge analysis is, among them, one of the main subjects for use of the techniques. Two-dimensional models for the corner wall where the phenomenon is normally found were developed [Oulefki 1993] [Déqué *et al.* 2001]. Similarly, the heat transfer (2D) in contact of the soil with the building slab was also modeled [Morlot 1999] [Biyaali 1995] [Mokhtari 1988]. Gao et al. [Gao *et al.* 2008] developed a 3D model of the wall as a module for use in a simulation tool. Some works for other building elements were also carried out, i.e. for roof components [Barrio 1999], hollow blocks walls [Gao *et al.* 2004], and an entire envelop of a single-zone building [Ménézo 1999]. Together with these kinds of analyses, a reduction model has been developed [Barrio *et al.* 2000] for thermal control application in buildings as well.

Various methods have been introduced, and many new methods are under development. In this section, some state model reduction techniques based on modal analysis used in this dissertation will be treated in detail while other methods are briefly mentioned.

1.2.1 Reduction techniques

Before discussion, it is worthwhile to mention that most of the methods have been developed for the linear and time-invariant system. Under these assumptions, many mathematical modifications can be achieved with veritable efficiency for the transient simulation. In contrary to this condition, an obtained low-order model may have to be redefined as time or physical condition changes, which cannot guarantee the advantage of the reduction techniques. The following methods are based on such a condition.

Different ways of categorization are possible for the techniques. In this thesis, the methods are classified by the kind of transformed basis, as follows:

- Modal basis method (MB)
- Balanced realization method (BR)

For explanation, a heat transfer case (1D) in the ground can be considered as given:

$$\frac{\partial}{\partial t}T(x,t) = \alpha\frac{\partial^2 T}{\partial x^2} \tag{1.62}$$

This equation can be considered linear and time-invariant when soil properties λ, ρ, c are regarded constant; consequently $\alpha(=\frac{\lambda}{\rho c})$ constant. For numerical analysis, the continuous problem must be converted into an algebraic problem. Thus, the spatial discretization of Eq. 1.62 leads to the following linear equation system (Eq. 1.63). A simple example is presented in Annex (B) for further understanding of this conversion and the reduction process that will be explained later.

$$\dot{T}(t) = C^{-1}AT(t) + C^{-1}B'U(t) \tag{1.63}$$

Where $T(t)$, the approximated state vector (dimension: n, 1), is the assembly of the time-dependent node temperatures of the system, that is, $T(t)$ contains all the temperatures of nodes of which locations are defined by the spatial discretization: $T(t)$ = {$T_1(t)$, $T_2(t)$, $T_3(t)$,..., $T_n(t)$}, where 1, 2, 3, ... , n indicate the node number order in a mesh generation. The matrix C, the square capacitance matrix (dimension: n, n), is related to the thermal inertia of the finite volumes, and the matrix A, the square conductance matrix, contains thermal relations among the nodes represented by the state vector $T(t)$. $U(t)$, the solicitation vector (dimension: p, 1), represents the boundary conditions of the system, therefore; the matrix B', a rectangular matrix (dimension: n, p), represents physical relation between the boundary conditions and the system.

In dynamic simulations, only the evolution of some particular values is concerned; for example, temperatures or heat flux in specific boundaries. For these values, an "observation" equation can be defined:

$$Y(t) = JT(t) + DU(t) \tag{1.64}$$

The output vector $Y(t)$ (dimension: q, 1) is the assembly of the concerning outputs, J, the observation matrix (dimension: q, n) and D, the direct transmission matrix (dimension: q, p) are defined under the physical correlation with the state vector and the solicitation vector, respectively. The state models mentioned above is a complete expression for the dynamic simulation. However, to reduce the initial problem order (n), change into a particular basis has to be considered for these models.

For the so-called modal basis (MB) method, the state models (Eq. 1.63, 1.64) are modified as an expression of a linear combination of eigenfunctions. Here, the eigenvectors and eigenvalues vis-a-vis the matrices $C^{-1}A$ are used. A detailed explanation on this basis-change will be presented in the next section with introduction of some well-known methods.

The second category used the balanced transformation to change the basis. This method, also called the inner symmetrization, was proposed by Moore [Moore 1981], and several works ([Glover 1984], [Barrio 1999], [Ménézo 1999], [Déqué *et al.* 2001], [Gao *et al.* 2008], and so on) have been carried out with this method. In his method, the basis change is based on the controllability and observability concepts that are used in automatic control. Simply speaking, the controllability is the possibility to acquire and vary the model states using the system inputs, while the observability to establish the states from the outputs [Déqué *et al.* 2001]. The states that are controllable or observable are defined by their controllability gramian W_C and observability gramian W_O. More precisely [Petit 1991], the controllability gramian can be mathematically defined by successively imposing a unit impulse (*Dirac* function) on each component $U_{i,(i=1...p)}$ of the input vector. The correspondent state vectors[2] of a problem $x^i(t)_{,i=1...p}$ can be assembled to construct a matrix **X**(t):

$$\mathbf{X}(t) = [x^1(t) \quad x^2(t) \quad ... \quad x^p(t)] \tag{1.65}$$

If the initial states are neglected, this matrix can be written as:

$$\mathbf{X}(t) = \exp^{(C^{-1}At)} C^{-1}B' \tag{1.66}$$

Finally, The gramian matrix W_C that quantifies the controllability can be established as:

$$W_C = \int_0^\infty \mathbf{X}\mathbf{X}^T dt = \int_0^\infty \exp^{(C^{-1}At)} C^{-1}B'B'^T(C^{-1})^T \exp^{(A^T(C^{-1})^Tt)} dt \tag{1.67}$$

In the same way, the unit impulse is imposed on each component $x_{k,k=1...n}$ of the state vector, and then n vectors $y^k(t)_{,k=1...n}$ become alike components of a matrix **Y**(t) (see Eq. 1.68) so as to evaluate the observability of system.

$$\mathbf{Y}(t) = [y^1(t) \quad y^2(t) \quad ... \quad y^n(t)] \tag{1.68}$$

It can be rewritten in the same way:

$$\mathbf{Y}(t) = J \exp^{(C^{-1}At)} \tag{1.69}$$

Thus, we get:

$$W_O = \int_0^\infty \mathbf{Y}^T\mathbf{Y} dt = \int_0^\infty \exp^{(A^T(C^{-1})^Tt)} J^T J \exp^{(C^{-1}At)} dt \tag{1.70}$$

Generally, these gramians are solutions of the following Lyapunov equation as well:

$$\begin{cases} (C^{-1}A)W_C + W_C(C^{-1}A)^T = -(C^{-1}B')(C^{-1}B')^T \\ (C^{-1}A)^T W_O + W_O(C^{-1}A) = -J^T J \end{cases} \tag{1.71}$$

[2]The state vector $T(x)$ of Eq. 1.63 becomes $x(t)$ for this example.

The transition matrix P (see Eq. 1.72 [3]) that is used for a basis change can be obtained regarding the product $W_C W_O$. This means that the resulting system has the same degree of controllability and observability, called also the balanced realization technique. Then, the system become controllable as well as observable in the new basis 1.73, derived from Eq. 1.63-1.63.

$$T(t) = P_{Mo} X(t) \tag{1.72}$$

$$\begin{cases} \dot{X}(t) = \Omega_{Mo} X(t) + B_{Mo} U(t) \\ \\ Y(t) = H_{Mo} X(t) + G_{Mo} U(t) \end{cases} \tag{1.73}$$

where,

$$\Omega_{Mo} = P_{Mo}^{-1} C^{-1} A P \qquad B'_{Mo} = P_{Mo}^{-1} C^{-1} B \qquad H_{Mo} = J P_{Mo} \tag{1.74}$$

On the other hand, the obtained matrices W_C and W_O are the same and diagonal, and the diagonal matrix consists of the so-called Hankel singular values[4] [Ménézo 1999] sorted as: $\omega_1 \geq \omega_2 \geq, ..., \geq \omega_n > 0$. Therefore, we get:

$$W_C = W_O = \begin{bmatrix} \omega_1 & & & 0 \\ & \omega_2 & & \\ & & \ddots & \\ 0 & & & \omega_n \end{bmatrix} \tag{1.75}$$

To reduce a state model size, it is necessary to evaluate which state components $X_k(t)$ that correspond to Hankel singular values respectively are important on the controllability/ observability. In fact, small Hankel singular values require much energy to be reached, consequently producing little energy on the output [Gao *et al.* 2004]. Accordingly, if existing ω_s for which $\omega_s \gg \omega_{s+1}$, the state elements $X_k(t)_{,k=s+1,...n}$ relative to $\omega_{k,k=s+1,...n}$ can be truncated regarding that this part would not be contributed to the dynamic evolution of the system. Letting $X_1(t) = \{X_k(t)\}_{,k=1,...,s}$ and $X_2(t)$ for the remainders, the state models (Eq. 1.73) can be separated into the two part as:

$$\begin{Bmatrix} \dot{X}_1 \\ \dot{X}_2 \end{Bmatrix} = \begin{bmatrix} \Omega_{11} & \Omega_{12} \\ \Omega_{21} & \Omega_{22} \end{bmatrix} \begin{Bmatrix} X_1 \\ X_2 \end{Bmatrix} + \begin{bmatrix} B_1 \\ B_2 \end{bmatrix} U$$
$$Y = \begin{bmatrix} H_1 & H_2 \end{bmatrix} \begin{Bmatrix} X_1 \\ X_2 \end{Bmatrix} + DU \tag{1.76}$$

Assuming $\dot{X}_2 = 0$, the reduced state model by Moore's method can be obtained as Eq. 1.77.

$$\begin{cases} \dot{X}_1(t) = A_{Mo} X(t)_1 + B_{Mo} U(t) \\ \\ Y(t) = H_{Mo} X(t)_1 + G_{Mo} U(t) \end{cases} \tag{1.77}$$

where,

$$\begin{array}{ll} A_{Mo} = \Omega_{11} - \Omega_{12}\Omega_{22}^{-1}\Omega_{21} & B_{Mo} = B_1 - \Omega_{12}\Omega_{22}^{-1} B_2 \\ H_{Mo} = H_1 - H_2\Omega_{22}^{-1}\Omega_{21} & G_{Mo} = G - H_2\Omega_{22}^{-1} B_2 \end{array} \tag{1.78}$$

[3] Here, $X(t)$ indicates a vector of a new state, so don't be confused with $\mathbf{X}(t)$ of Eq. 1.65.

[4] These values are the square roots of eigenvalues of the product $W_C W_O$.

All the methods above-mentioned are based on the truncation method. So-called Eitelberg's method [Bierman 1972] [Eitelberg 1982], however, utilizes a minimization method. Under specific inputs such as a step or impulse, reduced-model matrices are defined by minimizing the error of response between the initial model and the reduced one. Although obtained reduced models are precise, it is difficult to implement the models because of complexity of required processes.

1.2.2 Modal-basis truncation methods

1.2.2.1 Modal basis

As briefly mentioned in the previous, some of the methods belonging to the modal-basis category will be treated in this section. Above all, it is valuable to recall that this modal basis system can be obtained by the matrix diagonalization. Therefore, other than Moore's one (Eq. 1.72), the transition matrix P used for this method is direct products of the matrix $C^{-1}A$ of Eq. 1.63. According to the principle of diagonalization detailed in Annex (A), the eigenvectors $\psi_{i,(i=1,...,n)}$ obtained from $C^{-1}A$ compose directly the matrix P: $P = [\psi_1\psi_2...\psi_i...\psi_n]$, and the associated eigenvalues λ_i become the elements of the diagonal matrix W (Eq. 1.79). Other than the balanced realization method[5], this diagonal matrix W makes it possible for modes to be independent one another, allowing each mode to have a explicit physical meaning. Here, these eigenvalues are always real/ negative values if the matrices C, A are symmetric.

$$W = \mathrm{diag}(\lambda_i) = \begin{bmatrix} \lambda_1 & & & 0 \\ & \lambda_2 & & \\ & & \ddots & \\ 0 & & & \lambda_n \end{bmatrix} \tag{1.79}$$

As a result, the modal-basis state models of the initial models (Eq. 1.63-1.64) using the correlations (Eq. 1.81) are given as:

$$\dot{X}(t) = WX(t) + BU(t) \tag{1.80a}$$

$$Y(t) = HX(t) + DU(t) \tag{1.80b}$$

where,

$$T(t) = PX(t) \qquad W = P^{-1}C^{-1}AP \qquad B = P^{-1}C^{-1}B' \qquad H = JP \tag{1.81}$$

The vector $X(t)$ becomes the modal state that indicates an assembly of modes of the system relative to the dynamic evolution of the system. As done in Moore's method, the size of state models can be reduced by truncating some modes whose contributions to the system evolution are regarded as insignificant. Supposing $X_1(t)$ as an important part of modes consequently to be selected, the modal-basis models can be subgrouped by:

$$\begin{Bmatrix} \dot{X}_1 \\ \dot{X}_2 \end{Bmatrix} = \begin{bmatrix} W_1 & 0 \\ 0 & W_2 \end{bmatrix} \begin{Bmatrix} X_1 \\ X_2 \end{Bmatrix} + \begin{bmatrix} B_1 \\ B_2 \end{bmatrix} U$$
$$Y = \begin{bmatrix} H_1 & H_2 \end{bmatrix} \begin{Bmatrix} X_1 \\ X_2 \end{Bmatrix} + DU \tag{1.82}$$

[5]For example in Moore's, the matrix Ω is not diagonal.

In the same way, assuming that X_2 do not contributes to the dynamics of system but only to the steady state, we get the size-reduced state model:

$$\dot{X}_1(t) = W_1 X(t)_1 + B_1 U(t) \tag{1.83a}$$

$$Y(t) = H_1 X(t)_1 + GU(t) \tag{1.83b}$$

where,

$$X_2 = -W_2^{-1} B_2 U, \qquad G = D - H_2 W_2^{-1} B_2 \tag{1.84}$$

The process of reduction in the modal analysis is summarized in Fig. 1.16. Therefore, it remains to select which modes to be truncated in order to define the reduction matrices W_1, H_1, B_1, and G. The well-known criteria will be presented in the following section.

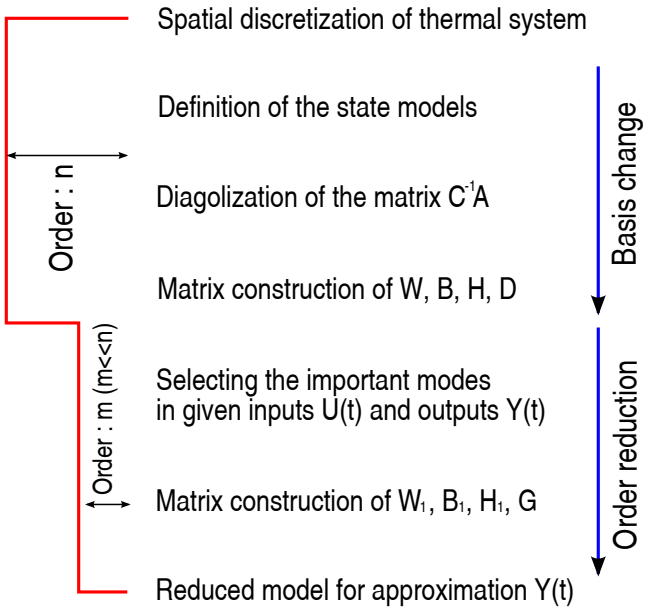

Figure 1.16: Principle of the process of the modal method

1.2.2.2 Criteria of mode selection

There are several methods in selecting the modes that are regarded as important ones in each method. The well-known methods that will be presented are as follows:

- Marshall method
- Litz method (spectral analysis)
- Linear Aggregation method

Marshall method

Proposed by Marshall [Marshall 1966], this is one of the oldest and simplest methods. This uses a criterion of the temporal predominance of system. For a typical thermal system where all the eigenvalues (λ_i) are real and negative, the time constants can be defined as:

$$\tau_i = -\frac{1}{\mathrm{Re}(\lambda_i)} \tag{1.85}$$

For the matrix partition (Eq. 1.82), the sorting of the eigenvalues (λ_i) can be done by:

$$\mathrm{Re}(\lambda_n) < ...\mathrm{Re}(\lambda_2) < \mathrm{Re}(\lambda_1) < 0 \tag{1.86}$$

Consequently, the correspondent time-constants (τ_i) are placed in a descending order for the matrix $W = \mathrm{diag}(\lambda_1, \lambda_2, ..., \lambda_n)$:

$$\tau_1 > \tau_2 ... > \tau_c > ... > \tau_n \tag{1.87}$$

As the solution of Eq. 1.80 for the upcoming time step ($t + \Delta t$) can be expressed by a summation of the series of $\mathrm{e}^{-\Delta t/\tau_i}$, some time-constants that are sufficiently small do not contribute to this dynamics, giving $\mathrm{e}^{-\Delta t/\tau_i} \approx 0$ for $i \geq c$. Accordingly, the modes can be separated by two group: so-called fast modes and slow modes. The fast modes ($\tau_c, ..., \tau_n$,) are normally determined in a given time step Δt by:

$$\tau_i < \frac{\Delta t}{4} \tag{1.88}$$

Thus, X_1 of Eq. 1.83 consists of only the slow modes, but the fast will be used for ensuring the conservation of the steady-state [Fossard 1970] (see Eq. 1.84) as it is supposed that each reaches instantly to its asymptotic value. The Marshall method gives satisfactory results in many cases, but it does not allow a significant reduction of the initial model.

Litz method

As described in the previous, the Marshall method does not take into account the influence of system solicitation and observation on the modes, but only considering a system evolution by C and A. This may cause errors to estimate a transient behavior of system in a specific case where the rapid modes, considered negligible, can be strongly excited with affecting on the output Y. Consequently, Litz [Litz 1981] proposed to investigate combinations of inputs-outputs for each mode.

Considering a j^{th} component of the output for the i^{th} component excited by a unit step (*Heaviside* function), the integration of Eq. 1.80 can give:

$$X^k = W^{-1}[\mathrm{e}^{Wt} - I]B_k \tag{1.89}$$

Where B_k represents the k^{th} column. The correspondent output $y^j(t)$ is obtained by introducing Eq. 1.89 in Eq. 1.80b:

$$y_j^k(t) = D_{jk} + \sum_{i=1}^{n} \frac{H_{ji}B_{ik}(1 - \mathrm{e}^{\lambda_i t})}{\lambda_i} \tag{1.90}$$

For the steady-state, this step response can be expressed:

$$y_j^k(\infty) = D_{jk} + \sum_{i=1}^{n} \frac{H_{ji}B_{ik}}{\lambda_i} \tag{1.91}$$

With this formula, Eq. 1.90 can be rewritten:

$$y_j^k(t) = y_k^j(\infty) - \sum_{i=1}^{n} \frac{H_{ji}B_{ik}\mathrm{e}^{\lambda_i t}}{\lambda_i} \tag{1.92}$$

or

$$\frac{y_j^k(t)}{y_j^k(\infty)} = 1 - \sum_{i=1}^{n} \alpha_{jki}\mathrm{e}^{\lambda_i t} \tag{1.93}$$

where

$$\alpha_{jki} = \frac{H_{ji}B_{ik}}{\lambda_i y_j^k(\infty)} \tag{1.94}$$

The coefficients α_{jki} represent the contribution of the mode i in Eq. 1.93 under the couple input k - output j, integrating its observability and controllability. Several works ([Sicard *et al.* 1985] [Bacot *et al.* 1984] [Chen 1989], and etc.) have been done with this method, which can give more detailed descriptions.

Linear Aggregation method

Linear aggregation (LA) method proposed by Aoki [Aoki 1968] has been applied and optimized by several authors ([Michailesco 1979] [Oulefki 1993] [Jaafar *et al.* 1990] [Petit 1991] [Morlot 1999]).

A linear relation between two states X and X_1 is introduced by using a aggregation matrix L(m,n):

$$X_1(t) = LX(t) \tag{1.95}$$

Comparing the one obtained by left-multiplying Eq. 1.80a by L with Eq. 1.83a, the existence of the aggregation relation can be assured if:

$$\begin{array}{rcl} W_1 L & = & LW \\ B_1 & = & LB \\ X_1(0) & = & LX(0) \end{array} \tag{1.96}$$

It is interesting to note that the matrix W_1 of the aggregation model conserves the m eigenvalues of the initial model. That is, for:

$$W\psi_i = \lambda_i \psi_i \tag{1.97}$$

Multiplying left by L with the relation of Eq. 1.96, we get:

$$W_1(L\psi_i) = \lambda_i(L\psi_i) \tag{1.98}$$

Thus, it shows that $L\psi_i$ is a eigenvector of W_1 associated with λ_i if $L\psi_i \neq 0$. From this property, the aggregation relation can be obtained by a simple projection, so we get L in the following form (after sorting):

$$L(\mathrm{m},\mathrm{n}) = [\quad I_{(\mathrm{m},\mathrm{m})} \quad \| \quad 0 \quad] \tag{1.99}$$

As for the characterizing matrices of the aggregation model, i.e., W_1, B_1, H_1, and G, the size-reduced matrices W_1 and B_1 can be obtained by the criterion of "energy" defined

by control engineers. The contribution of the so-called energy for each mode can be obtained by a difference of $Y(t) - Y(\infty)$ under the input types (*Durac* or *Heaviside*). In the same way for Litz's method, the state for a unit step (*Heaviside*) gives Eq. 1.89, and for the *Durac* function it gives:

$$X^k = \mathrm{e}^{Wt} B_k \tag{1.100}$$

The asymptotic states are thus respectively:

$$X^k_\infty = -W^{-1} B_k \qquad \text{for } \textit{Heaviside} \tag{1.101}$$

$$X^k_\infty = 0 \qquad \text{for } \textit{Durac} \tag{1.102}$$

Considering a difference matrix ΔX (dimension: n,p), where the K^{th} column can be written as a vector:

$$\Delta X^k = X^k - X^k_\infty \tag{1.103}$$

From the previous relations, we get:

$$\Delta X^k = \mathrm{e}^{Wt} W^{-1} B_k \quad \text{or} \quad \Delta X = \mathrm{e}^{Wt} W^{-1} B \qquad \text{for } \textit{Heaviside} \tag{1.104}$$

$$\Delta X^k = \mathrm{e}^{Wt} B_k \quad \text{or} \quad \Delta X = \mathrm{e}^{Wt} B \qquad \text{for } \textit{Durac} \tag{1.105}$$

Similarly,

$$\Delta Y^k = H X^k + DU - H X^k_\infty - DU = H \Delta X^k \tag{1.106}$$

and therefore:

$$\Delta Y = H \Delta X \tag{1.107}$$

The criterion J relative to the norm of ΔY can be defined:

$$J = \int_0^\infty \|\Delta Y\|_s^2 \, dt \tag{1.108}$$

where the norm $\|\Delta Y\|_s$ of the matrix ΔY, called norm Shur [Lascaux & Theodor 1986] is:

$$\|\Delta Y\|_s^2 = \sum_{j=1}^{p} \sum_{i=1}^{q} \Delta Y^2(i,j) \tag{1.109}$$

or

$$\|\Delta Y\|_s^2 = \mathrm{Tr}(\Delta Y \Delta Y^T) = \mathrm{Tr}(\Delta Y^T \Delta Y) \tag{1.110}$$

Replacing ΔY by its expression of ΔX (1.107), we obtain:

$$J = Tr(H^T H S) \tag{1.111}$$

with

$$S = \int_0^\infty \Delta X^T \Delta X dt \tag{1.112}$$

By introducing the matrix E as defined:

$$E = H^T H \otimes S \tag{1.113}$$

where $\otimes$ represents the matrix product in a term by term fashion, allowing a simple formula of the criterion J:

$$J = \sum_{i=1}^{n} \sum_{j=1}^{n} E_{ij} \tag{1.114}$$

To determine this so-called contribution matrix E, some processes are followed. Eq. 1.104 and Eq. 1.105 can be merged as:

$$\Delta X = \mathrm{e}^{Wt} W^{-r} B \quad \begin{cases} r = 0 & \text{for } \textit{Durac} \\ r = 1 & \text{for } \textit{Heaviside} \end{cases} \tag{1.115}$$

The matrix S is given:

$$S = \int_0^\infty \mathrm{e}^{Wt} (W^{-r} B)^T (W^{-r} B) \mathrm{e}^{Wt} dt \tag{1.116}$$

For reference, S is also the solution of Lyapunov equation:

$$WS + SW = -(W^{-r} B)^T (W^{-r} B) \tag{1.117}$$

The matrix W being diagonal, the general terms of S can be expressed:

$$S_{ij} = -\frac{\sum_{k=1}^{p} B_{ik} B_{jk}}{(\lambda_i \lambda_j)^r (\lambda_i + \lambda_j)} \tag{1.118}$$

Finally, the general term of E_{ij} is:

$$E_{ij} = -\frac{\sum_{l=1}^{q} H_{li} H_{lj} \sum_{k=1}^{p} B_{ik} B_{jk}}{(\lambda_i \lambda_j)^r (\lambda_i + \lambda_j)} \tag{1.119}$$

The contribution of "energy" d_i of each mode can be given:

$$d_i = \frac{E_{ii}}{\sum_{i=1}^{n} E_{ii}} \tag{1.120}$$

where E_{ii} is the diagonal terms of E:

$$E_{ii} = -\frac{\sum_{l=1}^{q} \sum_{k=1}^{p} H_{li}^2 B_{ik}^2}{2\lambda_i \lambda_i^{2r}} \tag{1.121}$$

With this contribution, we can preclassify the modes for instance in a descending order of the terms E_{ii}. From this sorting, only the m modes can be preserved for the reduced model by such a criterion[6]:

$$\sum_{i=1}^{m} E_{ii} / \sum_{i=1}^{n} E_{ii} \times 100 \geq 99(\%) \tag{1.122}$$

Additionally, a detailed analysis has been done for this energy contribution of modes [Michailesco 1979] [Jaafar *et al.* 1990] [Petit 1991]. In the studies, it is proved that some modes selected by Eq. 1.122 can be anew excluded if the sign of E_{ij} is negative for the case of $E_{ii} \approx E_{jj}$ and $\lambda_i \approx \lambda_j$.

Finally, the matrices H_1 and G can be directly acquired as usual by Eq. 1.84. On the other hand, Michailesco [Michailesco 1979] proposed a optimized method to obtain the reduced observation matrix H_1 by an approach of minimization that is not handled in this dissertation.

This LA method will be used here for development of new GHE models from the facts that:

- LA is relatively simple to be implemented and explicit to understand (based on the modal basis)
- it is precise as a concept of so-called controllability and observability is included together with a temporal criterion based on the time constants
- it is efficient in terms of reduction
- belonging to modal basis methods, it is possible to make use of the characteristics of eigenfunctions

1.3 Conclusion

Several methods of GHE modeling have been reviewed in this section. In the domain of short-time scale denoting the borehole region, many authors proposed resistance models assuming the quasi-steady state. The formulas were obtained by experiment or analytical modification, but it is still difficult to choose a model without knowing its limitation in a specific case. Actually, these do not take into account the thermal capacity so that analyses in small time-steps are not allowed with this kind of model. Accordingly, some tried to consider these effects analytically or numerically with various approximations.

For the ground defined as the domain of mid-long timescale in this thesis, the traditional analytical solutions have been frequently used. Each of the three solutions presented as ILS, CHS, and FLS can only be validated in a certain range of times because hypotheses are differently defined as previously explained. For small time-steps, the CHS model is considered as an exact solution while the FLS model gives the most accurate results for the long time simulation. Philippe et al. [Philippe *et al.* 2009] provided the validity ranges for these models in a typical condition. Fig. 1.17 was obtained by the authors for under following conditions: H=100m, q=500$\mathrm{W/m}$, r_b=0.05m, α=0.53$\times 10^{-6}\mathrm{m^2/s}$, and k=2$\mathrm{W/mK}$. However, other than these results, the short-times errors up to 10% between CHS and ILS would be smaller when the flux variation would be modest over

[6] 99% can be modified as 99.9% or etc, but the model precision may be dependent of this choice.

the time steps of simulation. Likewise, the long-times errors between ILS and FLS will be negligible for cases that the annual thermal loads are balanced. On the other hand, numerical models on this domain were generally developped for limited bore-field configuration: regular arrangements (DST) or single borehole case, and in many cases coarse mesh types were adopted.

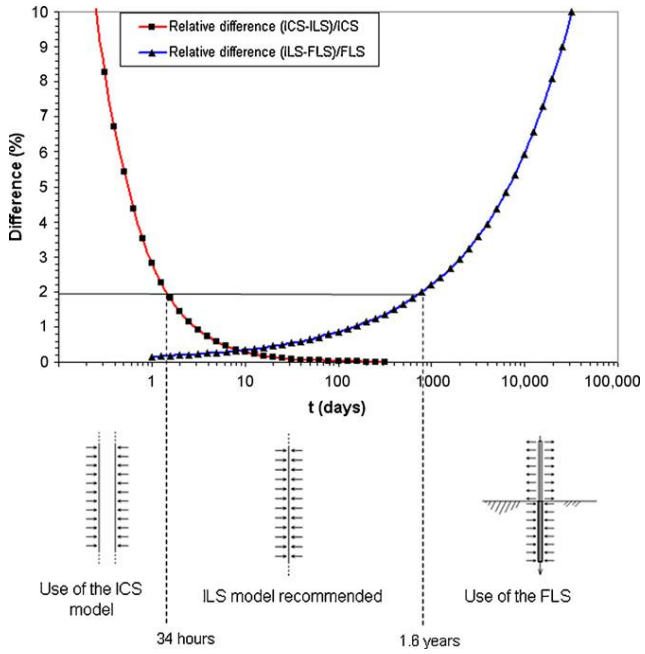

Figure 1.17: Validity ranges for all three models for typical operating conditions (Fig. 13 in [Philippe *et al.* 2009]

At present, several simulation tools are available that select and combine the methods presented here, so the tools can give different accuracy according to principals of selected methods. Spitler et al. [Spitler *et al.* 2009] compared some simulation tools with experimental data. 3 vertical boreholes, each approximately 75 meters deep, are installed. For simulation, the ground thermal conductivity was set as 2.55 $\mathrm{W/mK}$, volumetric specific heat as 2012 $\mathrm{kJ/m^3K}$. Fig. 1.18 shows the exit fluid temperatures (ExFT) obtained by the in-situ measurement and calculated by one-hour time-step simulations of various existing tools after about 6-months operation. In this figure, most of the models predict the ExFTs within approximately 1˚C except HVACSIM+. This 1˚C error[7] may be acceptable for some simulation purposes. For instance, Bernier et al. [Bernier *et al.* 2007] proposed that GHE models should predict the ExFT (or EWT, heat pump entering water temperature) within about 2˚C to obtain energy consumption results of heat pumps with an accuracy of the order of $\pm 5\%$.

However, as defined in the introduction, it is required to finely analyze the physical phenomena in the borehole and ground to investigate under-sizing of borehole and so-called solar-recharged hybrid cases. This objective obliges the models to be capable to

[7]The models were simulated in an open-loop case, i.e. the entering fluid temperatures to boreholes (EFT) measured by the experiment were used as input values for calculating the ExFTs. However, in real use of GHE models the simulation should be done in a close-loop configuration (HP-GHE-Load part) by iteration.

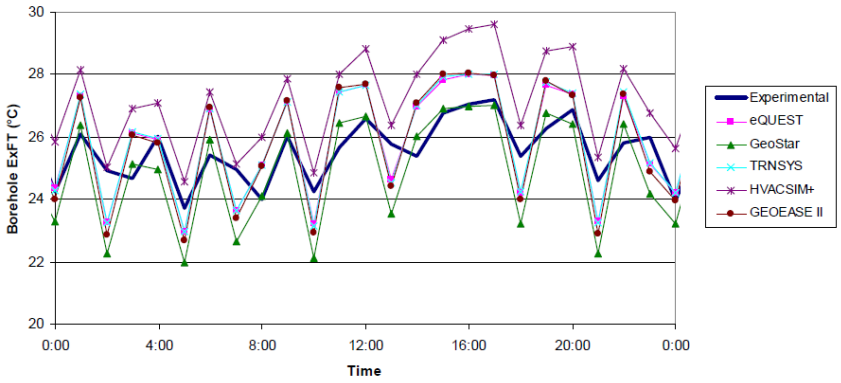

Figure 1.18: borehole ExFTs for a typical summer day (Fig. 3 in [Spitler *et al.* 2009])

predict not only accurate ExFTs but also the temperature distribution within and around boreholes in depths for almost all cases in short time-steps even less than few minutes. Here, it is worthwhile to recall that most existing models have been developed only for an estimation of ExFTs. Accordingly, a new 3D numerical model with detailed meshes can be a possible answer although it is time-consuming. As heat transfer in the ground with GHE can be considered linear-invariant in typical cases, the state model reduction techniques reviewed can be applied to this model. Detailed descriptions of the model will be presented in the following chapters.

Chapter 2

Development of a numerical 3D model

In this chapter, a new GHE model will be described. When three dimensional transient simulations are performed, computer memory and calculation time become an issue. Therefore, several numerical methodologies were applied in this model to make it more efficient: decomposition, state reduction technique, coupling methods.

In Section 2.1, a 2D case of a single slice model obtained by decomposing the soil domain in the vertical direction is first presented as it is complicated to present directly the 3D model. The finite element method (FEM) in unstructured meshes, horizontal domain-decomposition, the reduced model (RM) will be included in this 2D case. Then, the slice soil model (2D) will be self tested to verify numerical pertinence of the different methodologies.

Section 2.2 presents coupling methods proposed for the FEM to couple the sub-zone models: spatial and temporal. Even if these proposed methods have been verified in the section 2.1, details are demonstrated here. In the same way, 2D spatial coupling is first presented, and its extension to 3D coupling is followed. In terms of temporal coupling of sub-zones adopting different time-steps, only 2D case is proposed since almost the same processes are used for the 3D case.

Finally, the model assembly for a complete 3D is given in Section 2.3.

2.1 Ground slice model (2D)

A slice model of the ground soil volume is introduced as shown in Fig. 2.1 but for a 2D case. This strategy of using slices was motivated by the fact that each slice model has normally an identical mesh configuration, so that the matrices of a slice model, obtained by certain time-consuming processes such as diagonalizing, inversing, and etc... necessary for the state model reduction technique, can be directly used for other slices.

This slice model if defined as 2D can be regarded as a complete model of the relatively long-borehole (case 1) compared to the simulation duration, as proposed by [Eskilson 1987]:

$$\alpha t \leq \frac{H^2}{90} \tag{2.1}$$

In addition, it is suitable to use severally these pre-defined slice models for describing

the fluid temperature variation with borehole depth (case 2). For the 3D simulation (Section 2.3), the slice models can account for the thermal interaction in the vertical direction (case 3).

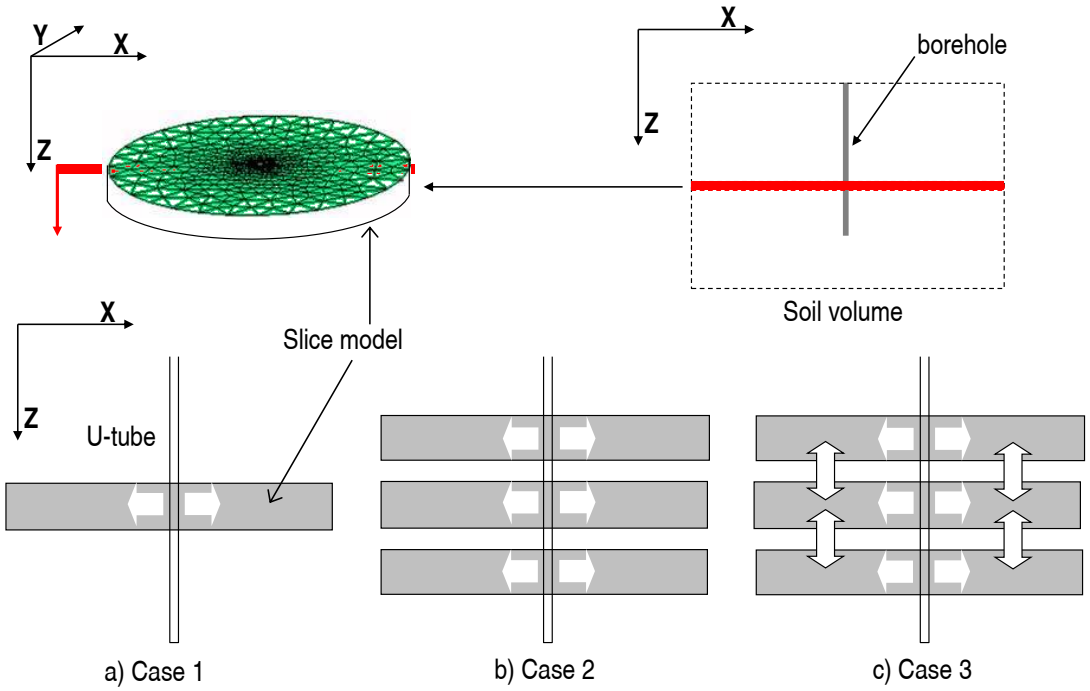

Figure 2.1: Slice model in the 3 different cases: 2D (Section 2.1), quasi 3D, and 3D (Section 2.3)

2.1.1 Mesh generation

As mentioned in the previous section, a fine mesh should be used in this model. Polar and Cartesian meshes can not be easily used because of the U-tube configuration found in boreholes. As a result, an unstructured mesh based on the *Delaunay* triangulation for the horizontal plan was adopted in this work. The mesh is generated by Gmsh (*www.geuz.org/gmsh*), which is shown in Fig. 2.2. The mesh generator outputs mesh information (i.e. a mesh file *.msh*) so that the grid information can be integrated to the code with an additional identification procedure.

The ground size to be considered increases when operation time progresses. Eskilson [Eskilson 1987] proposed a criterion on the maximum radial range[1] according to the time:

$$r_{\max} = 3\sqrt{\alpha t_{\max}} \tag{2.2}$$

From this criterion, a 100m-radius soil domain is, for instance, suitable for a long time simulation of about 20 years.

[1]This range is really a maximum value, i.e. it was obtained by imposing a constant heat. In the common HP operation, it will be largely smaller with variable heat transfer rates and the non-continuity of operation.

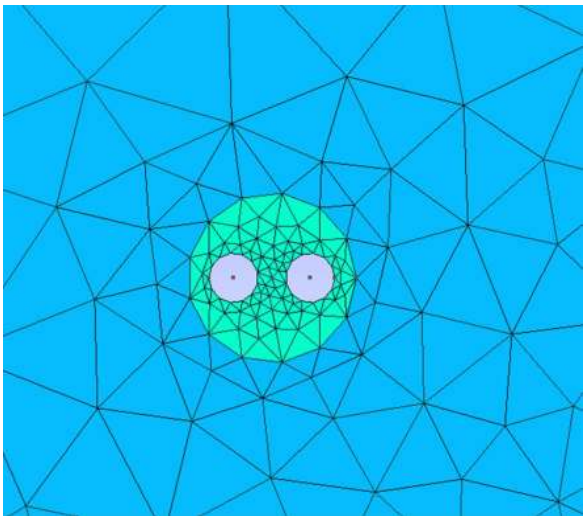

Figure 2.2: Example of the Delaunay triangular mesh by Gmsh

2.1.2 FEM model

2.1.2.1 Selection of the FEM

The unstructured mesh is a good solution because of the flexible mesh generation and consequently the possibility to obtain a lower mesh number in a complex configuration system. However, it can be cumbersome to handle this unstructured mesh in the FVM that is on the other hand relatively easy to sub-structure.

For example, the fluxes from or to a control volume should be accurately evaluated to guarantee the FVM model precision because the physical evolution in the control volume is determined from the energy balance across the mesh frontier. Having been generally assumed in the FVM that the geometrical center point of the mesh represents an whole control volume, we can not assure the orthogonality between a mesh line and the center-to-center axis across the line. This non-orthogonal relationship must be corrected in the FVM.

For detail, the general heat diffusion term of a control volume V_p can be expressed by the spatial discretization of domain as Eq. 2.3 for a linear system. Here, f indicates the frontier, and $\underline{\mathbf{S}}$ a surface vector that is perpendicular to the concerned surface of the volume in direction and has the same surface area in value. Thus, the last term gives a summation of the heat fluxes around mesh frontiers. In a structured mesh case, this heat flux can be simply obtained by Eq. 2.4 because $\underline{\mathbf{S}}$ and $\underline{\mathbf{d}}$ are in the same direction.

$$\int_{\mathrm{V_p}} \nabla \cdot (\lambda \nabla T) \mathrm{dV} = \sum_f \underline{\mathbf{S}} \cdot (\lambda \nabla T)_f = \lambda \sum_f \underline{\mathbf{S}} \cdot (\nabla T)_f \tag{2.3}$$

$$\underline{\mathbf{S}} \cdot (\nabla T)_f = |\underline{\mathbf{S}}| \frac{T_n - T_p}{|\underline{\mathbf{d}}|} \tag{2.4}$$

Otherwise for a non-orthogonal case, we can define the heat flux terms as Eq. 2.5 by using the same relation but adding a correction term.

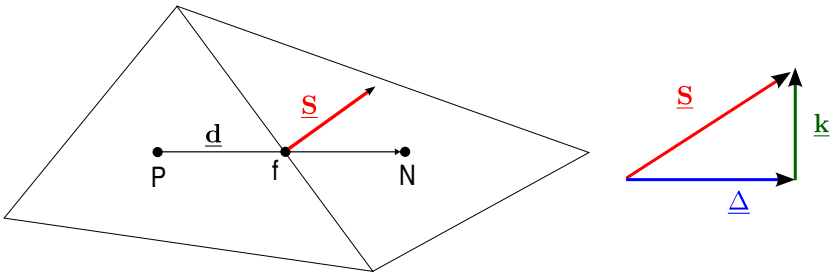

Figure 2.3: Vectors to be considered in a triangular unstructured mesh

$$\underline{\mathbf{S}} \cdot (\nabla T)_f = \underbrace{\underline{\Delta} \cdot (\nabla T)_f}_{\text{orthogonal contribution}} + \underbrace{\underline{\mathbf{k}} \cdot (\nabla T)_f}_{\text{non-orthogonal contribution}} \tag{2.5}$$

Where the vectors $\underline{\Delta}$ and $\underline{\mathbf{k}}$ have got to satisfy the following condition (see also Fig. 2.3):

$$\underline{\mathbf{S}} = \underline{\Delta} + \underline{\mathbf{k}} \tag{2.6}$$

The vector $\underline{\Delta}$ is chosen to be parallel with $\underline{\mathbf{d}}$. It allows to use Eq. 2.4 on the orthogonal contribution while limiting the less accurate method only to the non-orthogonal part. Different methods can be used for calculating this non-orthogonal part, but it is necessary for accuracy to additionally consider all the adjacent meshes of the concerned two meshes P, N particularly for the temperature gradient (∇T).

These proposed correction methods, for example, the least-square approach [Demirdzic & Muzaferija 1995] that breaks the reciprocal relation between the meshes, could make the conductance matrix A (Eq. 1.63) asymmetric. This asymmetry gives conjugate complex-type eigenvalues that are not explicit whether their relative modes are dominant or not in the modal-basis reduction technique. In addition, different thermal properties between adjacent FVM control volumes must also be averaged with approximation. As a result, the FEM, a method free from these approximations by its reciprocal and vertex-basis nature, is applied in the model.

2.1.2.2 FEM model

For FEM, the weak formulation of the governing equation 2.7 could be achieved by using some mathematical modification using a weighting function T^*. The obtained low-order equation 2.8 is not handling the non-orthogonal nature in the process of the matrices definition. It is because the *Laplacian* operator ∇^2 is weaken to ∇ in order for T. The procedure to this low-order equation is well-known (refer to [Huebnet 2001]).

$$\int_{\mathrm{V}} \rho c \frac{\partial}{\partial t} T \mathrm{dV} + \int_{\mathrm{V}} \lambda \nabla^2 T \mathrm{dV} = 0 \tag{2.7}$$

$$\int_{\mathrm{V}} \rho c \frac{\partial}{\partial t} T \mathrm{dV} + \int_{\mathrm{V}} \nabla T^* \lambda \nabla T \mathrm{dV} = 0 \quad \forall T^* \tag{2.8}$$

For simple explanation, the heat transfer problem 2.8 will be assumed in a two-dimensional case as mentioned above. Therefore, the height of the slice model are handled as infinite (case 1 in Fig. 2.1). As for the boundary conditions, fluxes are imposed at the outer walls of pipes. These fluxes on each tube, each leg of U-tube, could be iteratively calculated by a coupling with a fluid model.

Ahead of transforming Eq. 2.8 to the algebraic equation (1.63), an approximation of temperatures inside a mesh element is supposed by an interpolation function (Eq. 2.9 and 2.10). In this work, all the expressions are described for the 2D triangulation mesh.

$$T^e(x,y,t) = \begin{bmatrix} N_1^e(x,y) & N_2^e(x,y) & N_1^e(x,y) \end{bmatrix} \begin{Bmatrix} T_1^e(t) \\ T_2^e(t) \\ T_3^e(t) \end{Bmatrix} = \begin{bmatrix} N^e(x,y) \end{bmatrix} \left\{ T^e(t) \right\} \tag{2.9}$$

$$N_i(x,y) = \frac{a_i + b_i x + c_i y}{2\Delta} \tag{2.10}$$

where, a_i, b_i, c_i will be defined by the geometric information in each element, and Δ the area of the element considered.

For the temperature gradient, another function could be employed from N_i formulation.

$$\begin{bmatrix} M \end{bmatrix} = \begin{bmatrix} \frac{\partial N_1}{\partial x} & \frac{\partial N_2}{\partial x} & \frac{\partial N_3}{\partial x} \\ \\ \frac{\partial N_1}{\partial y} & \frac{\partial N_2}{\partial y} & \frac{\partial N_3}{\partial y} \end{bmatrix} = \frac{1}{2\Delta} \begin{bmatrix} b_1 & b_2 & b_3 \\ c_1 & c_2 & c_3 \end{bmatrix} \tag{2.11}$$

From these approximations, the weak formulation (Eq. 2.8) for an element could be expressed as Eq. 2.12, adding a flux (W/m) boundary condition on pipe walls if the element belongs to a pipe wall mesh.

$$\{T^*\}^T \left([C^e]\{T^e\} - [A^e]\{T^e\} - [B'^e]\{U^e\} \right) = 0 \tag{2.12}$$

Because the weight function T^* is an arbitrary function, only the right part of Eq. 2.12 is required to be zero. The capacity matrix C^e, the conductance matrix A^e, and the matrix B^e for the element considered could be expressed by a combination of the approximation functions N and M as:

$$[C^e] = \int_\Delta \rho c_p [N]^T [N] \mathrm{d}\Delta \tag{2.13}$$

$$[A^e] = -\int_\Delta [M]^T \lambda [M] \mathrm{d}\Delta \tag{2.14}$$

$$[B'^e] = -\int_\mathrm{l} [N]^T \mathrm{dl} \tag{2.15}$$

For the triangulation mesh, the matrices (Eqs. 2.13-2.15) can also be expressed [Huebnet 2001] as:

$$[C^e] = \frac{\rho c_p \Delta}{12} \begin{bmatrix} 2 & 1 & 1 \\ 1 & 2 & 1 \\ 1 & 1 & 2 \end{bmatrix} \tag{2.16}$$

$$[A^e] = [K_c^{e\vdash}] = -\frac{\lambda}{4\Delta}\begin{bmatrix} b_1^2+c_1^2 & b_1b_2+c_1c_2 & b_1b_3+c_1c_3 \\ b_2b_1+c_2c_1 & b_2^2+c_2^2 & b_2b_3+c_2c_3 \\ b_3b_1+c_3c_1 & b_3b_2+c_3c_2 & b_3^2+c_3^2 \end{bmatrix} \tag{2.17}$$

$$[B'^e] = [F^{e\vdash}] = \frac{l}{2}\begin{Bmatrix} 1 \\ 1 \end{Bmatrix} \tag{2.18}$$

All these matrices (Eqs. 2.16-2.18) defined for each element of a soil volume have to be assembled element-by-element (Eq. 2.19), by overlapping of mesh nodes for completing the algebraic Eq. 1.63.

$$\sum_e [C^e] = C, \quad \sum_e [A^e] = A, \quad \sum_e [B'^e] = B' \tag{2.19}$$

2.1.2.3 Reduced model in FEM

The sub-zone models of a slice model (2D), that will be explained in the next section "domain decomposition" (section 2.1.3), can be defined by the FEM matrices. Each sub-zone model is expressed by Eqs. 1.63 and 1.64. In this case, the capacity matrix C is not diagonal other than the FVM model case but symmetric, and the matrix A is apparently symmetric. The vector of observation Y is composed of the n node temperatures and boundary temperatures that will be used for coupling with adjacent sub-zones of the slice model. Selecting these boundary mesh nodes will be demonstrated in the section 2.2. The solicitation vectors $U(t)$ for each sub-zones are differently defined, which will be also detailed in the section 2.2.

Under these input-output vectors U and Y, the matrices B' and J are constructed according to the physical relationship. After diagonalization of the product matrix $C^{-1}A$, we can get the modal basis matrices W, B, H, and D. As we use the method of linear aggregation (LA) in this model, these matrices will be directly and indirectly included in the criterion equation (1.121) that select dominant modes for the low-order state models (Eqs. 1.83a and 1.83b).

The results on this reduction models for a slice model will be presented and discussed in the section 2.1.4.

2.1.3 Domain decomposition

Generally, the matrix calculation time that is normally in the function of N^3 can be reduced by sub-structuring, as shown in Eq. 2.20, where the coefficient b is normally larger than a because of the necessity of the iteration among subregions (n : number of sub-zones, N : mesh number of a subzone).

$$a(nN)^3 \gg bn(N)^3 \tag{2.20}$$

Thus, the model efficiency in terms of calculation time is enhanced with the sub-zone decomposition of the model presented in Fig. 2.4. In this paper, 4 subzones were proposed, each of which covers a distinct soil region (see Fig. 2.4b). This method makes it possible to use different time steps for each sub-zone, which could generally be helpful for a fast calculation. Additionally, this decomposition is indispensable to take advantage

of the state model size reduction technique (see also the section 2.1.4.3). The decomposition has another benefit that, in the presence of multiple boreholes, the matrices definition and their modification for a borehole sub-zone could be reused for other boreholes sub-zones (see Fig. 2.4c).

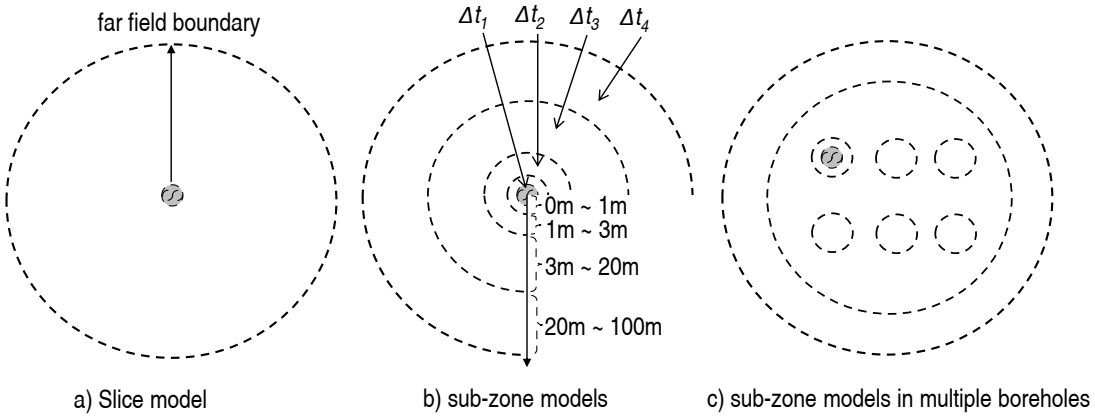

Figure 2.4: Decomposition of a slice model by sub-zone models

2.1.4 Results of a slice model

Simulations are carried out to self-test various methodologies used in this 2D slice model. The parameters and boundary conditions used for the simulations are presented in Tables 2.1 and 2.2, respectively. Two cases of heat injection are tested: constant flux case for the steady state regime or relatively long time analysis; sinusoidal flux case for the alternative operating analysis (Tab. 2.2).

Table 2.1: Simulation parameters

Parameters	Unit	Value
Borehole radius	m	0.055
External U pipe radius	m	0.016
U pipe distance (center to center)	m	0.06
U Pipe number in a borehole		1
Soil conductivity	W/m ˚C	3.5
Grout conductivity	W/m ˚C	1.3
Soil diffusivity	m^2/s	1.62×10^{-6}
Grout diffusivity	m^2/s	3.33×10^{-7}
Basic time step	hr	1
Error criterion for iteration	%	10^{-4}

2.1.4.1 Mesh independency

The mesh independency concerning simulation results is important for numerical solution because it will decide model relevance and lightness in terms of error and calculation time, respectively. For this purpose, an error evaluation has been defined, based on

Table 2.2: Boundary conditions

Boundaries	Unit	Value
Initial soil temperature	˚C	10
Far field temperature	˚C	10
Constant flux density in each pipe	$\mathrm{W/m^2}$	300
Sinusoidal flux density in each pipe	$\mathrm{W/m^2}$	$200 + 100\sin(2\pi t/24\mathrm{h})$

the maximum temperature difference between the two compared models, and this error evaluation (Eq. 2.21) will be used for other simulation results in this work.

$$\text{Maximum error} = \max|T_{ref} - T_{test}| \tag{2.21}$$

Fig. 2.5 shows the result on the comparison of different mesh models for the mean borehole wall temperature when injecting constant heat. The first three mesh models (n = 1918, 1406, 1018) have the maximum error less than 0.1 ˚C, correspondent relative error 0.43%, among them, which was comparatively smaller than other models (n = 625 and 313). Therefore, the mesh model whose order is n = 1018 was selected as the reference simulation mesh model, and the equivalent mesh resolution is used in the simulations of this thesis. This mesh configuration is presented in Fig. 2.6 and the correspondent mesh information in Tab. 2.3.

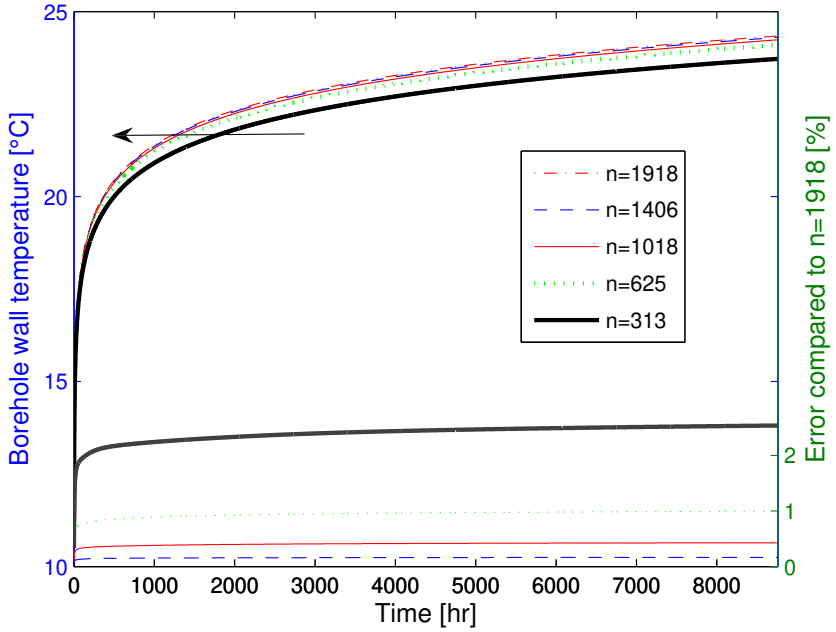

Figure 2.5: Comparison of temperature evolution and error estimation according to mesh resolution

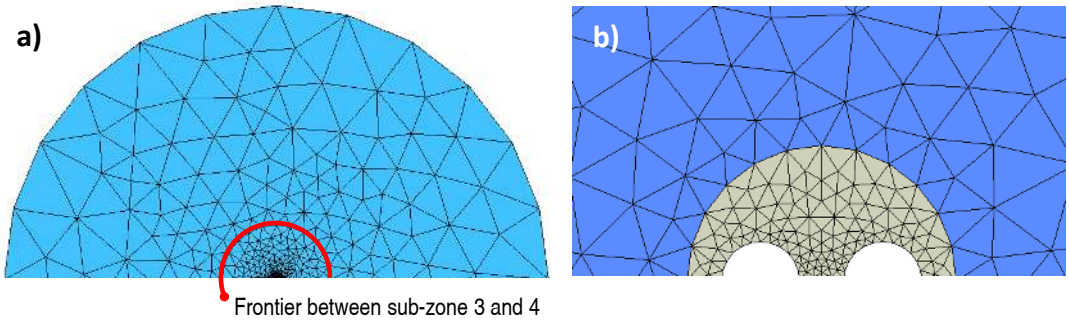

Figure 2.6: (a) Mesh for soil domain ($n = 1028$) and (b) magnification of the mesh near the U-tube

Table 2.3: Mesh information used for the slice model

Mesh information	Unit	Value
Total nodes number		1018
Total number in 4 sub-zone models (from the borehole zone to the exterior zone)		474/140/203/201
Average mesh size	m^2	1.5798×10
Maximum mesh size	m^2	3.1906×10^2
Minimum mesh size	m^2	4.1557×10^{-6}

2.1.4.2 Model validation

In order to validate our approach and show the efficiency of the method proposed in this work, the numerical model is compared to an analytical model, the infinite line source (ILS) [Ingersoll *et al.* 1954]. This test case has been chosen because small errors for each time step in a numerical model could normally be accumulated for long time analysis in the geothermal system. Fig. 2.7 shows the results of this comparison of the borehole wall temperature given by the reduced model (RM) and the ILS. As shown, the relative error (Eq. 2.22) between both approaches is relatively important at startup (small F_O, where F_O is the Fourier number = $\alpha t/r_b^2 < 20$). This is to be expected as it is a well-known fact [Ingersoll *et al.* 1954] that the ILS is inaccurate for $F_O < 20$. Therefore, the RM is more accurate than the ILS for the short time scale. On the other hand, the comparison for $F_O > 20$ shows an acceptable error, which is becoming smaller as F_O increases. This error is probably caused by the genuine characteristics of nume rical methods: rounding off/ truncation errors, relatively coarse meshes compared to the extremely detailed mesh, FEM order (1^{st} order in this thesis), and etc.

$$\text{Relative error} = \left| \frac{\text{Numerical value} - \text{Analytical value}}{\text{Numerical value} - \text{Initial value}} \right| \times 100\% \tag{2.22}$$

For a detail test of each method, the sub-zone models using the coupling method (spatial and temporal) are first compared to the entire slice model (no decomposition). To show the pertinence of our decomposing-coupling approach, no reduction technique is used in this comparison. Fig. 2.9 shows the temperature evolution on the borehole wall for the models examined: 1. entire complete model (CM), 2. decomposed CM, and 3. decomposed CM using different time-steps. The results of the models are in good

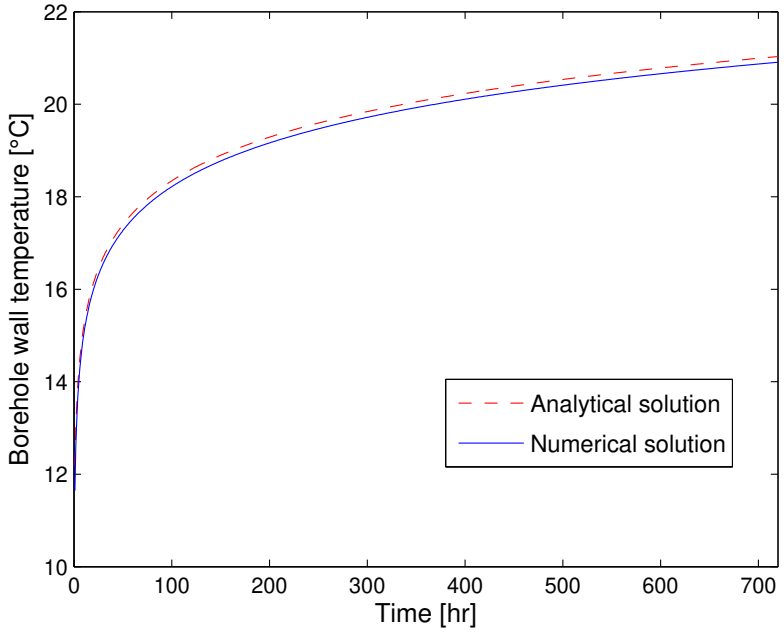

Figure 2.7: Borehole wall temperature comparison between the numerical and analytical solutions

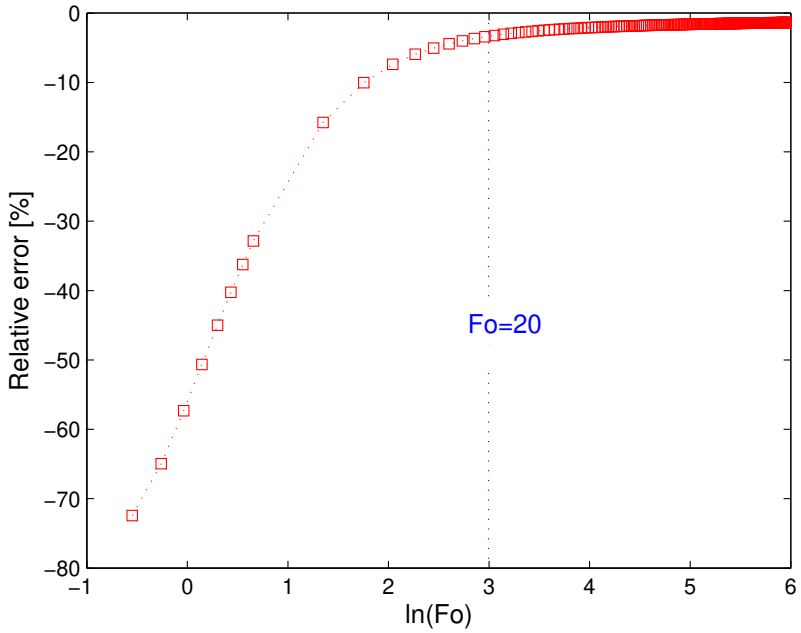

Figure 2.8: Relative error estimation between the numerical and analytical results

agreement. The maximum error of the spatial coupling was 0.00038 ˚C, and 0.078 ˚C for the spatial and temporal coupling that will be detailed in the section 2.2.2.

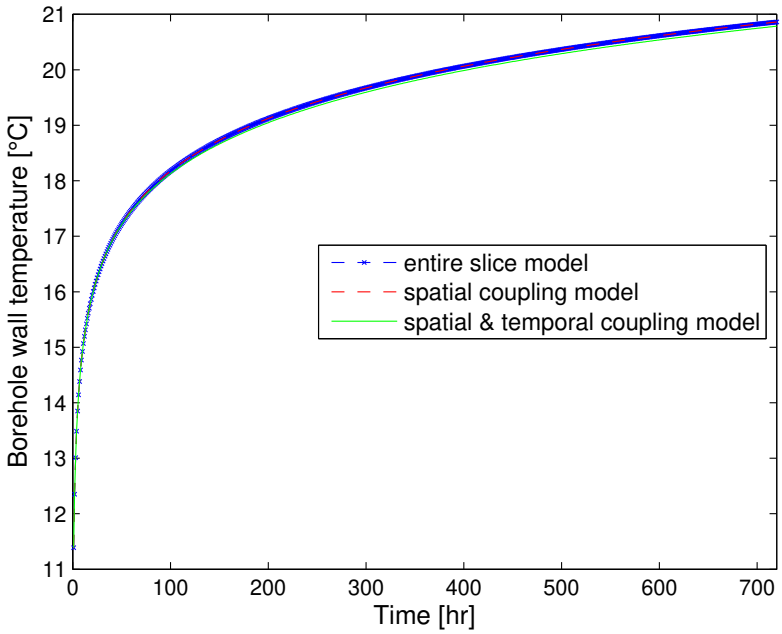

Figure 2.9: Verification of the spatial/ temporal coupling methods

2.1.4.3 Comparison between complete and reduced models

For the reduced model (RM) simulation, four sub-zones are used and each sub-zone has a different simulation time step: 1h, 6h, 1day, and 1week from the borehole to exterior, respectively while the complete model (CM) has only one time step (1h) for all the sub-zones. The complete model (CM) uses all of the system modes and is compared to the reduced model (RM) using the linear aggregation (LA) technique with 99% energy criterion: $(= \Sigma_{i=1}^{m} E_{ii} / \Sigma_{i=1}^{n} E_{ii} \times 100(\%))$.

As shown in Fig. 2.10, RM model and CM are in good agreement with the maximum error of 0.31 ˚C. The selected modes ratio of RM model to CM is about 6% ($66 \ll 1018$), consequently reducing computational time (see Tab. 2.4). This efficiency could be explained by the result presented in Fig. 2.11. Each subzone model has an unambiguous energy distribution; that is, some primary modes might decide the dynamic evolution in the given time step, which did not appear in the original entire slice model [Kim *et al.* 2009].

Subsequently, a dynamic heat injection is studied for evaluating the validity of the modeling in the case of short time operation. The heat flux is supposed to be sinusoidal as explained with Tab. 2.2. Fig. 2.12 shows the pipe wall mean temperature evolution for CM and RM models with different energy criteria in order to observe the energy criterion impact. Above all, the two models (CM and RM 99%) are in good agreement with a maximum error 0.274 ˚C. However, other models with 95 and 85% energy criteria have 1.29 and 2.40 ˚C in maximum error, respectively. Although the amount of the selected modes decreases according to the energy criterion, the amount of the selected modes is not greatly different among the reduced models (see the graph legend: 66,31, and 13

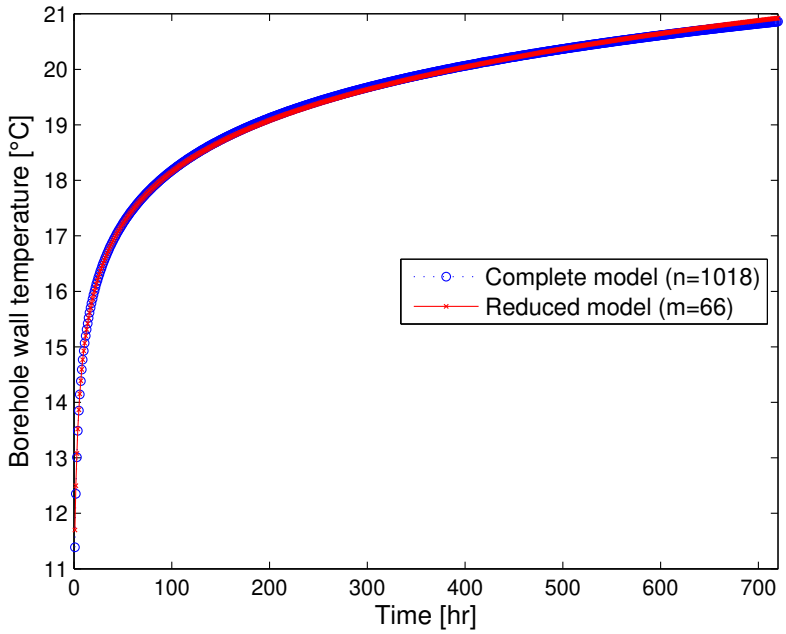

Figure 2.10: Reduced model (LA) results compared to the sub-zone complete model

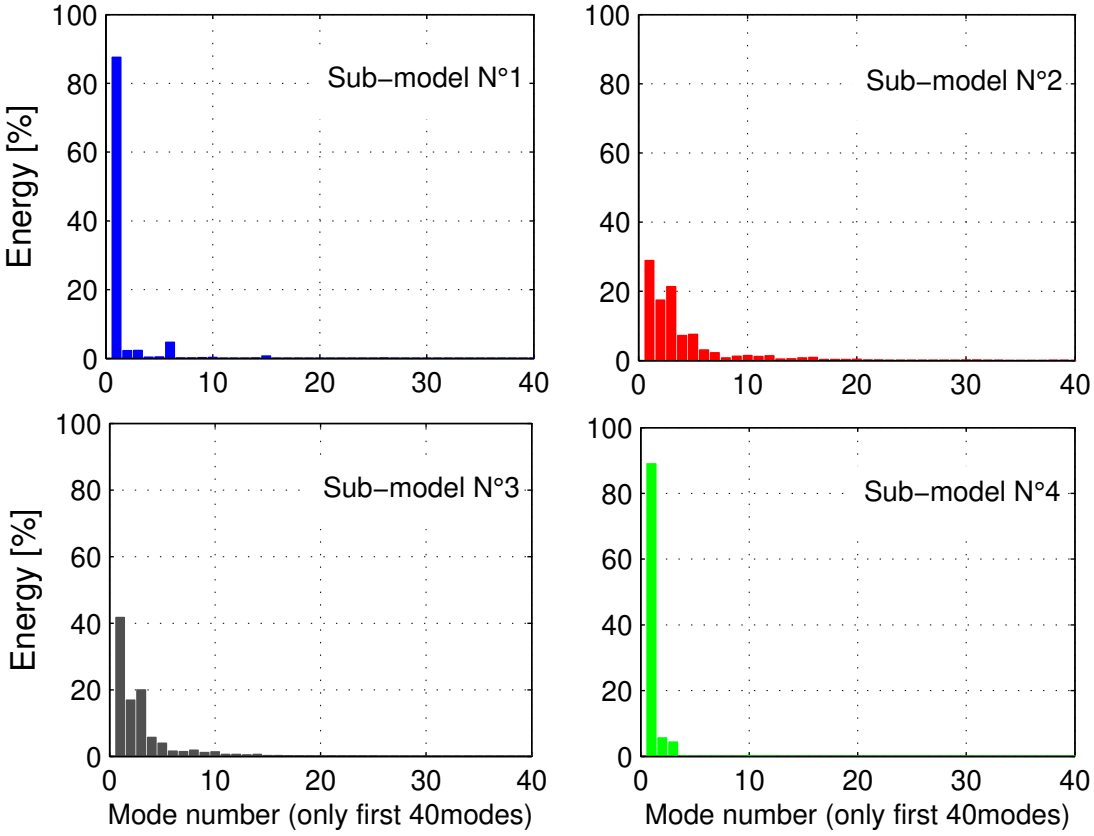

Figure 2.11: Energy distribution (LA method) for each sub-zone model

modes selected for diffrent RM). Furthermore, the CPU time for the transient calculation among the different reduced models was almost similar. Therefore, using RM-LA 99% could be a good solution in this decomposed slice model.

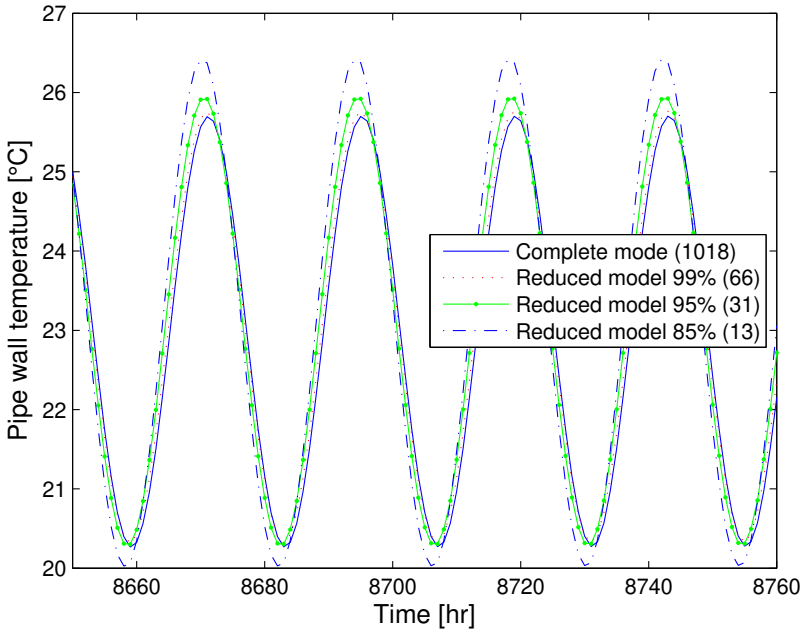

Figure 2.12: Results on using various energy criteria in LA reduced model

In order to further examine the RM precision compared to the CM and generalize the proven results, we use the bode diagrams. For this simulation, the output mean temperature on the pipe wall is observed when the input flux on the same wall is introduced in the borehole region. First of all, the result (see Fig. 2.13) shows that the magnitude difference between CM and RM is almost zero for frequencies lower than 2×10^{-2} which corresponds about 5 min excitation period. In terms of the phase difference, the two models have nearly the same response in the area lower than the frequency 2×10^{-3}. Although this frequency matches about 50 min excitation period, this period level would be sufficient for application within geothermal system simulation field even for the short time analysis. Actually, a simulation with a time step 1 min with 10 min periodic input fluxes (between the frequencies 2×10^{-2} and 2×10^{-3}) showed a good concordance between the CM and RM with a slight error less than the result of Fig. 2.12.

In the bode diagram, the diverging point between the two model (RM and CM) will be shifted toward left if the concerned domain becomes lager, for example from the borehole domain to 100m radius domain i.e. s1→s4. It means that the reduced model covering a large volume and containing different mesh scales cannot give the precise results within $\Delta t = 1h$ that is too small for the far area [Kim *et al.* 2009]. Therefore, the corresponding larger Δt should be chosen for parts of far-area from the boreholes. It can partly explain why it is indispensable to decompose the domain of a large system in order to use the reduction technique. Additionally, some requirements in choosing the time steps Δt_i of each sub-zone are described in Annex C.

In terms of the calculation time, the RM is compared with different versions of CMs.

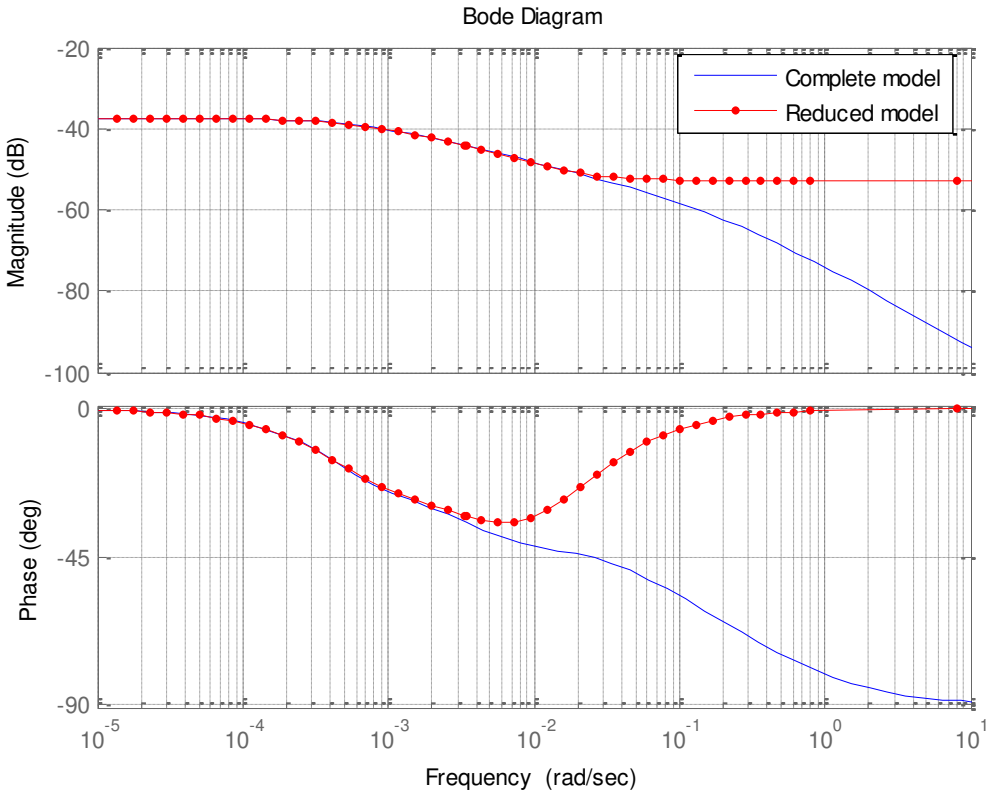

Figure 2.13: Bode diagrams of full-order model and low-order model (RM 99%) in the borehole region

Tab. 2.4 indicates CPU time results allowing to check the performance of the used methods. For the results, a constant heat transfer rate was used during a month with one-hour time step. It is proved from these results that the techniques used in this work are pertinent to reduce the calculation time. Firstly, compared to the initial slice model, the decomposed model is more rapid but not so much as it was expected (Eq. 2.20). It would be due to the iteration part of among the sub-zones. However, this decomposition method allows to implement the other methods: time steps differentiating and then reducing for each sub-zone, which are sufficiently efficient as seen in the table.

Table 2.4: CPU time of RM compared with other CMs (2D case)

Model	Description	CPU time
CM	entire slice model (no sub-zone)	2454s
CM	only time step for all sub-zones	1968s
CM	different time steps Δt_1, Δt_2, Δt_3, Δt_4	675s
RM	Δt_1, Δt_2, Δt_3,Δt_4 + reduction (LA)	91s

2.2 Proposition of coupling methods of sub-domains (2D&3D)

Modeling large-systems particularly for the transient simulation is an interesting area for application of the reduction techniques. As briefly explained in the section 2.1.4.3, the decomposition is one of the satisfactory approaches. On the other hand, once a domain has been decomposed, the obtained sub-zone models should be adequately coupled to guarantee the model accuracy. Some coupling methods have been proposed by [Biyaali 1995] [Morlot 1999] [Oulefki 1993]. In this thesis, we proposed another coupling method that is appropriate for our modeling principals.

2.2.1 Spatial coupling (2D&3D)

First, a general coupling method in FVM is presented, and then the difference nature between the methods (FEM vs. FVM) is given. In the FVM, determining the node (control volume) temperature is achieved by a flux balance across all the frontiers of the control volume in each time step. Therefore, decomposed sub-zone models in FVM is easily regrouped by a communication of fluxes if they are known at the decomposition border. The simulation in each sub-zone model runs separately under different fluxes, and then typical iteration continues until a convergence: becoming the fluxes as the same (see Fig. 2.14).

A new coupling method in the FEM starts with the general concept of FVM coupling. Similarly, the sub-zone models can be iteratively coupled with certain variables at the border. However, the vertexes of triangle meshes in the FEM become directly the temperature nodes that are assembled in the vector $T(t)$. Thus, other than the FVM, a temperature-flux interaction can be supposed. In Fig. 2.15-a, the left sub-zone can be modeled with boundary temperatures T_P that will be provided by the right sub-zone model. In the right model, fluxes calculated from the left model are imposed on the border to calculate the whole temperature field.

According to the principal of the FEM, the temperature evolution of a node is influenced by all the surrounding elements. This character requires a cumbersome tactic for

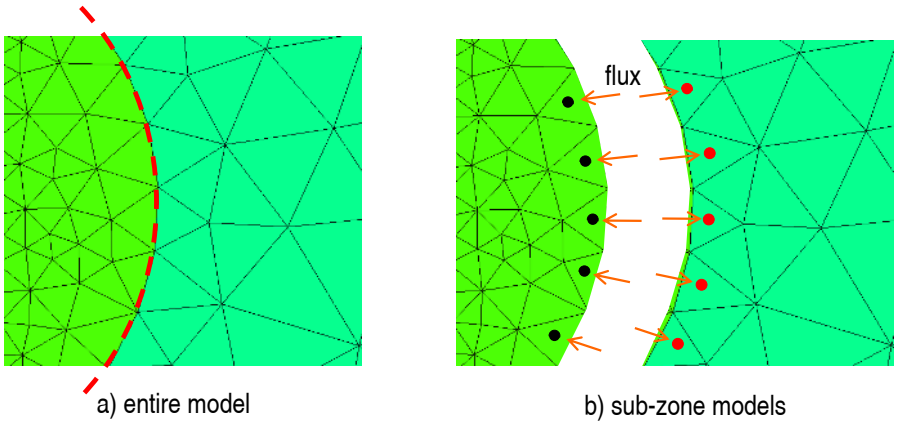

Figure 2.14: Coupling principal in FVM

coupling. The nodes (T_L) for the left side sub-zone model contain all the information of the surrounding elements because all the nodes temperatures to be calculated are interior to the border. Whereas, the nodes (T_P) on the border for the right side sub-zone model include only the information of the right side model elements. This fact could give some erroneous results when using FEM. Therefore, it is proposed that supplementary meshes shown in Fig. 2.15-b are taken into account for an exact solution. All the processes for mathematical restitution of these additional meshes will be described in the following parts.

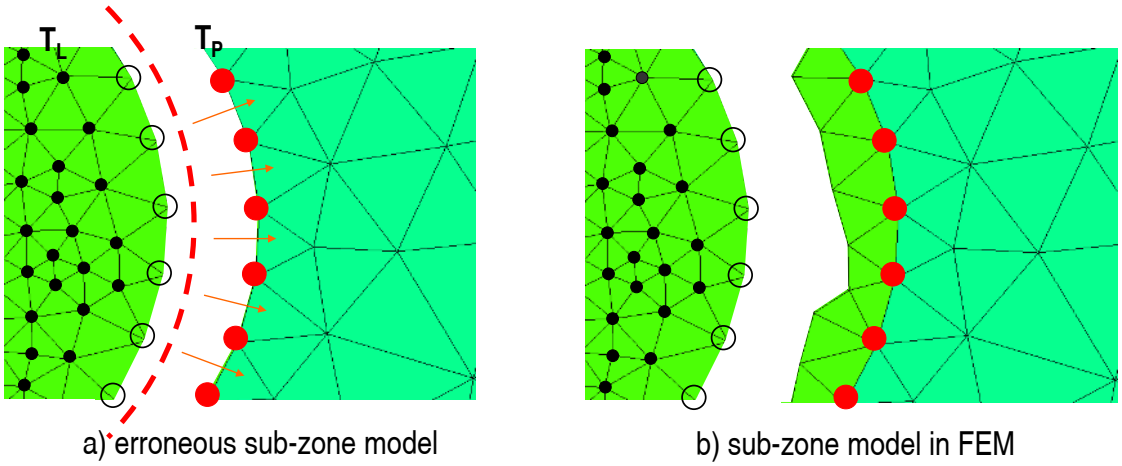

Figure 2.15: Problematic of the coupling method in FEM

2.2.1.1 2D FEM case

The algebraic equation we obtained by FEM can be rewritten for the left sub-zone model (index $s1$) as:

$$C^{s1}\dot{T}^{s1}(t) = A^{s1}T^{s1}(t) + B'^{s1}U^{s1}(t) \tag{2.23}$$

In this equation, the number of terms of the temperature vector $T^{s1}(t)$ is the same as

one of mesh vertexes. To remove the nodes on the frontier in this equation, which leads to a temperature-imposed boundary (see the left model in Fig. 2.15-b), some matrices modification has to be carried out. First of all, the state vector $T^{s1}(t)$ and its correspondent rows in each matrix, A^{s1}, B'^{s1} (Eq. 2.23) need to be rearranged for dividing them into two parts: the inside temperatures T_L and the border temperatures T_P. Thus, it can be given as:

$$\begin{bmatrix} C_{LL}^{s1} & C_{LP}^{s1} \\ C_{PL}^{s1} & C_{PP}^{s1} \end{bmatrix} \begin{Bmatrix} \dot{T}_L^{s1} \\ \dot{T}_P^{s1} \end{Bmatrix} = \begin{bmatrix} A_{LL}^{s1} & A_{LP}^{s1} \\ A_{PL}^{s1} & A_{PP}^{s1} \end{bmatrix} \begin{Bmatrix} T_L^{s1} \\ T_P^{s1} \end{Bmatrix} + \begin{bmatrix} B_L'^{s1} \\ B_P'^{s1} \end{bmatrix} U^{s1}(t) \tag{2.24}$$

From this equation, a new model with a temperature-imposed boundary (T_P) could be obtained as:

$$C_{LL}^{s1}\dot{T}_L^{s1}(t) = A_{LL}^{s1}T_L^{s1}(t) - C_{LP}^{s1}\dot{T}_P^{s1}(t) + A_{LP}^{s1}T_P^{s1} + B_L'^{s1}U^{s1}(t) \tag{2.25}$$

Where, all the matrices relative to T_P^{s1} can be integrated into the matrix $B_L''^{s1}$ to assemble all the solicitations in an input vector $U'^{s1}(t)$, so that the final equation could be expressed as:

$$C_{LL}^{s1}\dot{T}_L^{s1}(t) = A_{LL}^{s1}T_L^{s1}t + B_L''^{s1}U'^{s1}(t)$$

$$\begin{cases} B_L''^{s1} = \begin{bmatrix} B_L'^{s1} & A_{LP}^{s1} - C_{LP}^{s1}/\Delta t & C_{LP}^{s1}/\Delta t \end{bmatrix} \\ U'^{s1}(t) = \begin{Bmatrix} U^{s1}(t) & T_P^{s1,n+1} & T_P^{s1,n} \end{Bmatrix}^T \end{cases} \tag{2.26}$$

As mentioned above, the concern is to take into account the additional information of the supplementary meshes (see the added mesh of the right model in Fig. 2.15-b). The partial matrices C_{PL}^{s1}, C_{PP}^{s1}, A_{PL}^{s1}, A_{PP}^{s1}, and $B_P'^{s1}$ which were removed by the above process have to be restored into the matrices of sub-model $s2$ (the right model) because all these matrix terms related to the vector T_P^{s1} are the exact same as ones of the supplementary meshes.

The sub-zone model $s2$ can be expressed as follows if no boundary condition is supposed:

$$C^{s2}\dot{T}^{s2}(t) = A^{s2}T^{s2}(t) \tag{2.27}$$

In the same way for $s1$, the row order of the state vector $T^{s2}(t)$ and the matrices need to be rearranged for a matrix modification. It gives:

$$\begin{bmatrix} C_{PP}^{s2} & C_{PL}^{s2} \\ C_{LP}^{s2} & C_{LL}^{s2} \end{bmatrix} \begin{Bmatrix} \dot{T}_P^{s1} \\ \dot{T}_L^{s2} \end{Bmatrix} = \begin{bmatrix} A_{LL}^{s2} & A_{LP}^{s2} \\ A_{PL}^{s2} & A_{PP}^{s2} \end{bmatrix} \begin{Bmatrix} T_P^{s1} \\ T_L^{s2} \end{Bmatrix} \tag{2.28}$$

Here, we should keep in mind that the nodes T_P^{s1} also belong to the sub-zone model $s2$, and at the same time they will be given to the sub-zone $s1$ during coupling. However, the same truncation process separating T_L^{s2} and T_P^{s2} will take place for this sub-model $s2$ if coupled with a sub-model $s3$.

The partial matrices removed in $s1$ have to be inserted in this equation of $s2$ so as to restore the element informations that had been lost in the decomposition process for FEM. Thus, we get:

$$\begin{bmatrix} C_{PP}^{s2}+C_{PP}^{s1} & C_{PL}^{s2} \\ C_{LP}^{s2} & C_{LL}^{s2} \end{bmatrix} \begin{Bmatrix} \dot{T}_P^{s1} \\ \dot{T}_L^{s2} \end{Bmatrix} = \begin{bmatrix} A_{LL}^{s2}+A_{PP}^{s1} & A_{LP}^{s2} \\ A_{PL}^{s2} & A_{PP}^{s2} \end{bmatrix} \begin{Bmatrix} T_P^{s1} \\ T_L^{s2} \end{Bmatrix} + \begin{bmatrix} -C_{PL}^{s1}/\Delta t & C_{PL}^{s1}/\Delta t + A_{PL}^{s1} \\ 0 & 0 \end{bmatrix} \begin{Bmatrix} T_{P-C}^{s1,n+1} \\ T_{P-C}^{s1,n} \end{Bmatrix} \tag{2.29}$$

In this equation, $B_P'^{s1}$ is not considered because in 2D case U^{s1} contains only the fluxes imposed on the pipe walls. As a result, all the terms in B_P^{s1} are zeros. The new input vector found in the last term of Eq. 2.29 is the assembly of certain nodes connected to T_P^{1s}. These nodes are notated as T_{P-C}^{s1} shown in Fig. 2.16. In the equation, n and $n+1$ indicate the present and the following time step, respectively. The last matrix that is multiplied by the input vector is obtained by the temporally implicit scheme as it was the same for Eq. 2.26. For reference, the partial matrices C_{PL}^{s1}, A_{PL}^{s1} of the sub-model $s1$ have to be reduced in dimension of column to match the number of nodes T_{P-C}^{s1}: from (dim(T_P^{s1}), dim(T_L^{s1})) to (dim(T_P^{s1}), dim(T_{P-C}^{s1})), knowing that the terms unrelated to T_{P-C}^{s1} are always zeros in the matrices C_{PL}^{s1} and A_{PL}^{s1}.

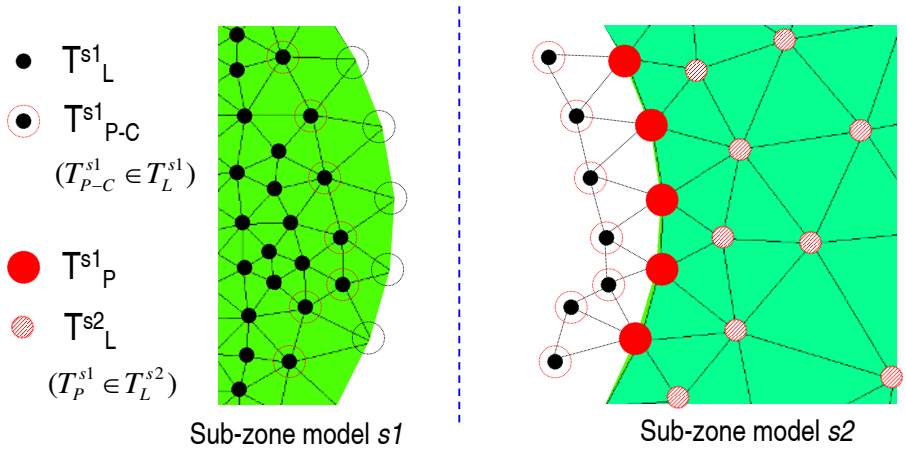

Figure 2.16: Notation of nodes used for the matrix restitution

As a result, the sub-zone models can be simultaneously calculated with an iterative method, using the temperatures on/ near the frontier as boundary variables (Fig. 2.17). The proposed method is precise (see the section 2.1.4.2) because the lost informations has been restored. For example, the error will vary according to the decomposition position for the erroneous coupling method while our method is free from the mesh resolution in the frontier. For multi coupling of sub-zone models, the similar modification of matrices can be achieved (e.g. between $s2$ and $s3$ or $s3$ and $s4$).

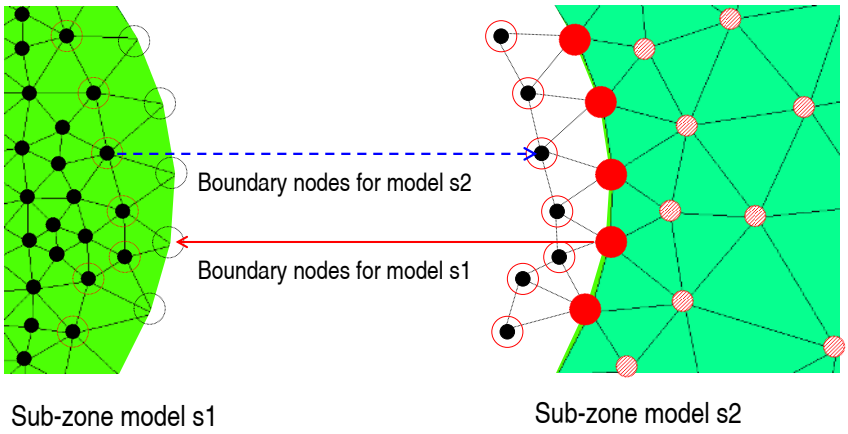

Figure 2.17: Proposition of new boundaries for coupling sub-zone models in FEM

2.2.1.2 3D coupling

The coupling must be extended to the 3D case 2.3 where the slices are piled up to the height of soil volume. In this model 3D, the FVM approach is used in the vertical direction. It is because the meshes in this direction is structured and consequently ensures the symmetry of matrices. It also allows for a relatively simple modeling compared to FEM particularly for the coupling. The final model is therefore developed under the mixed approach of FEM and FVM.

The matrix C for each 3D sub-zones are obtained by the same way as the 2D case, but the terms of each matrix are multiplied by the sub-zone height Δz to extend to a 3D case. For the conductance matrix A, refer to Eq. 1.43 in the section 2.3.1. Thus, only the modification of the matrix B' and the input vector $U(t)$ are presented here.

Above all, a vector of $U^{\mathbf{S}1}(t)$ defined for the 3D case[2] can be given:

$$U^{\mathbf{S}1}(t) = \left\{ \begin{array}{ll} T_{bot}^{\mathbf{S}1,n+1} & \text{dimension : } n(T_L^{\mathbf{S}1}) \\ T_{top}^{\mathbf{S}1,n+1} & n(T_L^{\mathbf{S}1}) \\ \varphi_{dw} & 1 \\ \varphi_{up} & 1 \\ T_P^{\mathbf{S}1,n+1} & n(T_P^{\mathbf{S}1}) \\ T_{P,bot}^{\mathbf{S}1,n+1} & n(T_P^{\mathbf{S}1}) \\ T_{P,top}^{\mathbf{S}1,n+1} & n(T_P^{\mathbf{S}1}) \\ T_P^{\mathbf{S}1,n} & n(T_P^{\mathbf{S}1}) \end{array} \right\} \tag{2.30}$$

[2]For the 3D case, the index of sub-zone models is expressed by a bold and capital letter: **S**1, other than the 2D case: s1

Here, the dimension $n(T_L^{\mathbf{S}1})$ indicates the node number relative to $T_L^{\mathbf{S}1}$ shown in Eq. 2.24 and Fig. 2.16. It is worthwhile to note $T_{P-C}^{\mathbf{S}1} \in T_L^{\mathbf{S}1}$ and $T_P^{\mathbf{S}1} \in T_L^{\mathbf{S}2}$ in counting the node number. φ_{dw} and φ_{up} represent average fluxes calculated at the wall of each leg of U-tube, denoting dw for downward flow and up for upward flow. $T_P^{\mathbf{S}1}$ are the nodes on the border, given by the sub-model $\mathbf{S}2$. Using the FEM in the horizontal direction, the temperatures $T_{P,top}^{\mathbf{S}1}$ and $T_{P,top}^{\mathbf{S}1}$ obtained by the upper (top) and lower (bot) sub-zones must be considered in this 3D coupling. The temporal expression n or $n+1$ for the input vector $U^{\mathbf{S}1}(t)$ is given under the same implicit scheme as the 2D case.

The correspondent matrix $B_L''^{\mathbf{S}1}$ is given by:

$$B_L''^{\mathbf{S}1} =$$

$$\underbrace{\left[B'^{\mathbf{S}1}_{LL,bot}\right.}_{T^{\mathbf{S}1,n+1}_{bot}} \underbrace{B'^{\mathbf{S}1}_{LL,top}}_{T^{\mathbf{S}1,n+1}_{top}} \underbrace{B'^{\mathbf{S}1}_{L,\varphi(dw)}}_{\varphi_{dw}} \underbrace{B'^{\mathbf{S}1}_{L,\varphi(up)}}_{\varphi_{up}} \underbrace{A^{\mathbf{S}1}_{LP} - C^{\mathbf{S}1}_{LP}/\Delta t}_{T^{\mathbf{S}1,n+1}_{P}} \underbrace{B'^{\mathbf{S}1}_{LP,bot}}_{T^{\mathbf{S}1,n+1}_{P,bot}} \underbrace{B'^{\mathbf{S}1}_{LP,top}}_{T^{\mathbf{S}1,n+1}_{P,top}} \underbrace{\left.C^{\mathbf{S}1}_{LP}/\Delta t\right]}_{T^{\mathbf{S}1,n}_{P}}$$

(2.31)

As seen in Eq. 2.31, $B_L''^{\mathbf{S}1}$ is composed of terms that are defined by physical relations with the input vector $U^{\mathbf{S}1}$. The terms $A^{\mathbf{S}1}_{LP} - C^{\mathbf{S}1}_{LP}/\Delta t$ and $C^{\mathbf{S}1}_{LP}/\Delta t$ can be defined in the same way as the 2D case (Eq. 2.26). For the definition of other terms, it is more convenient in terms of understanding and programming to employ another simple case.

Briefly, the same process as it was done (Eq. 2.24) for 2D case can be performed.

As Fig. 2.18, we think of a simple 3D sub-zone case where it is supposed that boundary conditions of the outer wall of the soil volume are adiabatic and vertical sub-zones are coupled by the fluxes defined by the FVM. This model $\mathbf{S}1$ can be given as Eq. 2.32.

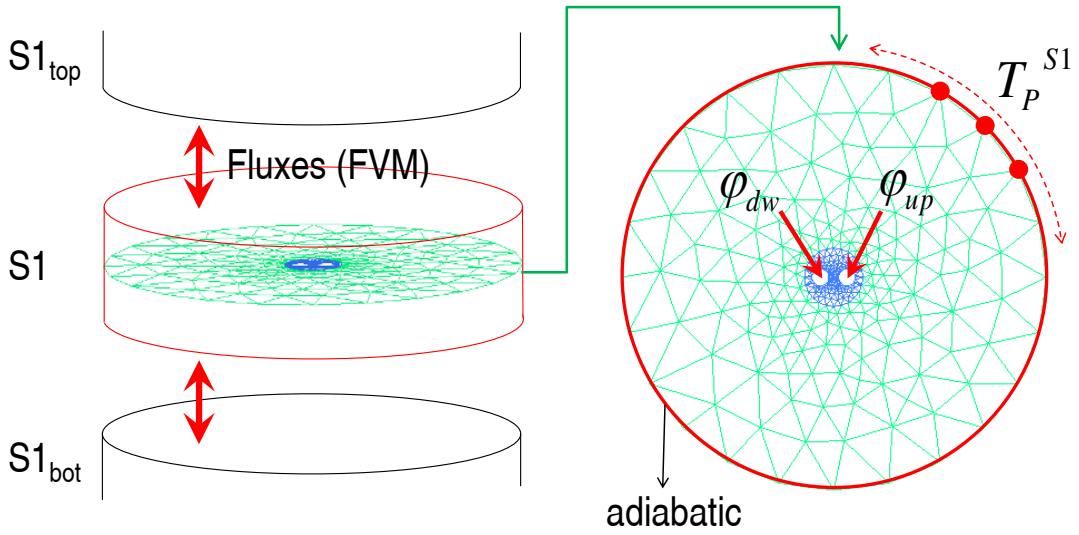

Figure 2.18: A sub-zone case used for defining the terms of matrix $B_L''^{\mathbf{S}1}$ of Eq. 2.31

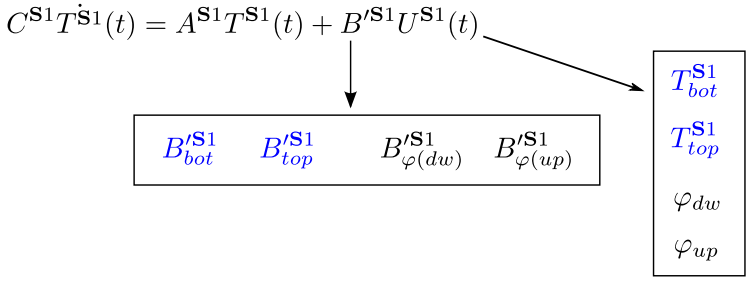

(2.32)

Here, we should know that the nodes $T^{\mathbf{S1}}$ include $T^{\mathbf{S1}}_L$ and $T^{\mathbf{S1}}_P$, likewise for $T^{\mathbf{S1}}_{bot}$ and $T^{\mathbf{S1}}_{top}$. The construction of sub-matrices of $B'^{\mathbf{S1}}$ can be carried out by the FEM principals; that is, $B'^{\mathbf{S1}}_{bot}$ and $B'^{\mathbf{S1}}_{top}$ can be defined by the negative of Eq. 2.36, and $B'^{\mathbf{S1}}_{\varphi(dw)}$ and $B'^{\mathbf{S1}}_{\varphi(up)}$ by Eq. 2.18 with identifying concerning nodes among $T^{\mathbf{S1}}(t)$.

After the separating process similar to Eq. 2.24, we get:

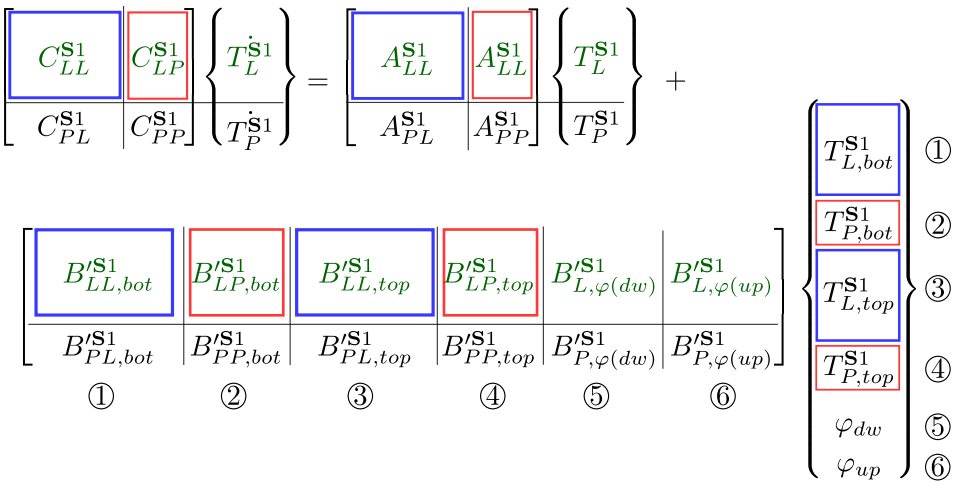

(2.33)

These partial matrices shown in Eq. 2.33 become directly the same terms of Eq. 2.31 (the exactly same notations are used, and matrix dimensions are identical as well). Here, if Δz is identical for all the sub-zone models, we have $B'^{\mathbf{S1}}_{LL,bot} = B'^{\mathbf{S1}}_{LL,top}$ and $B'^{\mathbf{S1}}_{LP,bot} = B'^{\mathbf{S1}}_{LP,top}$, but always $B'^{\mathbf{S1}}_{L,\varphi(dw)} \neq B'^{\mathbf{S1}}_{L,\varphi(up)}$.

On the other hand, the output vector $Y^{\mathbf{S1}}(t)$ is logically defined as:

$$Y^{\mathbf{S1}}(t) = \left\{ \begin{array}{ll} T^{\mathbf{S1}}_L & \text{dimension :} \quad n(T^{\mathbf{S1}}_L) \\ \overline{T^{\mathbf{S1}}_{p(dw)}} & 1 \\ \overline{T^{\mathbf{S1}}_{p(up)}} & 1 \\ T^{\mathbf{S1}}_{P-C} & n(T^{\mathbf{S1}}_{P-C}) \end{array} \right. \tag{2.34}$$

Firstly, the terms $T^{\mathbf{S1}}_L$ are provided as boundary conditions to the neighboring top and bottom sub-zone models. The average temperatures $\overline{T^{\mathbf{S1}}_{p(dw)}}$ and $\overline{T^{\mathbf{S1}}_{p(up)}}$ are the variables to

couple with a fluid model. Last terms of $T_{P-C}^{\mathbf{S}1}$ are the boundary values to the sub-zone model $\mathbf{S}2$ as shown in Fig. 2.17.

Therefore, a 3D sub-zone model $\mathbf{S}1$ has been completed with the new input vector $U^{\mathbf{S}1}(t)$. The matrices J and D of Eq. 1.64 are physically defined under the relations with the vectors $T_L^{\mathbf{S}1}$ and $U^{\mathbf{S}1}(t)$ (Eq. 2.30).

For the rest of the sub-zone models $\mathbf{S}i$: $\mathbf{S}2$, $\mathbf{S}3$, $\mathbf{S}4$. . ., all the same processes as $\mathbf{S}1$ are repeated, and then the obtained matrices are still modified by Eqs. 2.27-2.29 to couple with the sub-zone model $\mathbf{S}(i-1)$, so-called the left side model of Fig. 2.16.

Finally, we get the $U^{\mathbf{S}i}$ and $Y^{\mathbf{S}i}$ for $i \geq 2$ as follows:

$$U^{\mathbf{S}i}(t) = \left\{ \begin{array}{c} T_{L,bot}^{\mathbf{S}i,n+1} \\ T_{L,top}^{\mathbf{S}i,n+1} \\ \\ T_{P}^{\mathbf{S}i,n+1} \\ T_{P,bot}^{\mathbf{S}i,n+1} \\ T_{P,top}^{\mathbf{S}i,n+1} \\ T_{P}^{\mathbf{S}i,n} \\ \\ {}^{*}T_{P-C}^{\mathbf{S}(i-1),n+1} \\ {}^{*}T_{P-C,bot}^{\mathbf{S}(i-1),n+1} \\ {}^{*}T_{P-C,top}^{\mathbf{S}(i-1),n+1} \\ {}^{*}T_{P-C}^{\mathbf{S}(i-1),n} \end{array} \right\}, \qquad Y^{\mathbf{S}i}(t) = \left\{ \begin{array}{c} T_{L}^{\mathbf{S}i} \\ {}^{*}T_{P}^{\mathbf{S}(i-1)} \\ T_{P-C}^{\mathbf{S}i} \end{array} \right\} \tag{2.35}$$

The matrix $B''^{\mathbf{S}i}$ can be defined as previously explained, corresponding to this input vector $U^{\mathbf{S}i}(t)$. Here, defining the matrix terms relative to $T_{P-C}^{\mathbf{S}(i-1)}$ also requires the identification process to be positioned in appropriate rows in the matrix $B''^{\mathbf{S}i}$, connecting with the terms $T_P^{\mathbf{S}(i-1)}$ of the sub-zone model $\mathbf{S}i$ ($T_P^{\mathbf{S}(i-1)} \in T_L^{\mathbf{S}(i)}$). In the case of the presence of multi-boreholes, the repetition as many as the number of boreholes will be required for the terms marked by *. This mark * will be usually found in the sub-zone model $\mathbf{S}2$.

Although this spatial coupling method is proved to be relevant as given in the section 2.1.4.2, this method remains challenged to be optimized in terms of faster computing. It is briefly given as follows.

If it is assumed that the vertical fluxes are approximately the same for all the elements of a given sub-zone model, the temperatures $\{T_{L,bot}^{\mathbf{S}i}\}$ and $\{T_{L,top}^{\mathbf{S}i}\}$ (e.g. dimension: 474 in Tab. 2.3) can be averaged as $\overline{T_{L,bot}^{\mathbf{S}i}}$ and $\overline{T_{L,top}^{\mathbf{S}i}}$ (dimension: 1). This is intuitively rational because firstly the heat transfer rate in the vertical direction is relatively small, and secondly the horizontal heat diffusion behavior around a borehole has almost between

adjacent slices.

This can lead to assuring calculation time reduction in decomposition/coupling process. It is because the dimension $(2N + \alpha)$ of input vector $U^{\mathbf{S}i}(t)$ can be largely reduced into $(2 + \alpha)$ as well as the dimension $(N + \beta)$ of $Y^{\mathbf{S}i}(t)$ into $(1 + \beta)$, replacing $T_L^{\mathbf{S}i}$ by $\overline{T_L^{\mathbf{S}i}}$; N is the node number of a sub-zone model, and α and β the dimension of extra parts in each vector.

In addition, if the flux boundaries are allowed among slices, it is possible to use Eq. 2.37 instead of Eq. 2.36 for a vertical heat flux calculation on the FEM triangle element, where dz is the center-to-center distance of slices $((\Delta z + \Delta z_{bot(top)})/2)$. Accordingly, while the terms $K_c^{E\perp}$ are inserted to the matrix A as well as $B''(t)$ (negative) in the actual case, $F^{E\perp}$ will only be used for $B''(t)$ in the flux boundary case. This change makes it possible to easily differentiate Δz for the slices, allowing to reduce the total slice number.

$$K_c^{E\perp} = \frac{dz\Delta}{12}\begin{bmatrix} 2 & 1 & 1 \\ 1 & 2 & 1 \\ 1 & 1 & 2 \end{bmatrix} \tag{2.36}$$

$$F^{E\perp} = \frac{\varphi^{\perp}\Delta}{3}\begin{Bmatrix} 1 \\ 1 \\ 1 \end{Bmatrix} \tag{2.37}$$

It is because the eigenfunctions used for slices of different heights will be the same if Eq. 2.37 is used by the following relations[3]:

$$\begin{aligned} \text{if} \quad & C_1 = \beta C_2,\ A_1 = \beta A_2,\ \ \text{where}, \beta = \Delta z_1/\Delta z_2 \\ & \lambda_1 = \lambda_2,\ \psi_1 = \psi_2 \end{aligned} \tag{2.38}$$

This is easily proven by the eigenfunction principals given as well in Annex A. As a result, this characteristic allows to use the same state models but G for all the slices, using less computer memory.

2.2.2 Temporal coupling (2D)

In each sub-zone model, different time steps are chosen not only for a faster calculation but also for subserving the state model reduction technique. Thus, the Lagrange interpolating polynomial [Chapra & Canale 2002] is applied for interpolation or extrapolation required for the temporal coupling between the sub-zone models as below.

$$\begin{aligned} f_n(x) &= \sum_{i=0}^{n} L_i(x) f(x_i) \\ \text{where},\ L_i(x) &= \prod_{j=0,\ j\neq i}^{n} \frac{x - x_j}{x_i - x_j} \end{aligned} \tag{2.39}$$

Here, $\prod$ designates "the product of". For instance, the linear (the first order: $n = 1$) interpolation was expressed as follows:

[3]Where $A_1 \neq \beta A_2$ when using Eq. 2.36

$$f_1(x) = \frac{x - x_1}{x_0 - x_1} f(x_0) + \frac{x - x_0}{x_1 - x_0} f(x_1) \tag{2.40}$$

In the same way, the parabolic (the second order: $n = 2$) version is:

$$f_2(x) = \frac{(x - x_1)(x - x_2)}{(x_0 - x_1)(x_0 - x_2)} f(x_0) + \frac{(x - x_0)(x - x_2)}{(x_1 - x_0)(x_1 - x_2)} f(x_1) + \frac{(x - x_0)(x - x_1)}{(x_2 - x_0)(x_2 - x_1)} f(x_2) \tag{2.41}$$

Above all, the time steps should be given by the following: $\Delta t^{s(i+1)} = \alpha_i \times \Delta t^{si}$ where α must be a natural number. Subsequently, the occurrence of the current time $t_n^{s(i+1)}$ for the sub-zone model $s(i+1)$ is always accompanied by the one of t_n^{si}, that is, positioning t_n^{si} and $t_n^{s(i+1)}$ at the same time-line (Fig. 2.19). This condition allows easy programming.

As shown in Fig. 2.19, the boundary temperatures defined in the section 2.2.1 are communicated at the proper time-level because each sub-zone model will be calculated in its own time-step. For detail, the partial output vectors T_{P-C}^{si} obtained from the left-side model of the figure at t_{n+1}^{si} will be extrapolated with the past values at t_n^{si} or even at t_{n-1}^{si} for the parabolic case. This extrapolated output will be used as the input value of the sub-zone model $s(i+1)$. From this input, the sub-zone model $s(i+1)$ can be calculated to provide the output at the time level $t_{n+1}^{s(i+1)}$, and then this output will be interpolated in the same way to provide the boundary temperature of the sub-zone model si at t_{n+1}^{si}. This procedure will be iterated until a convergence.

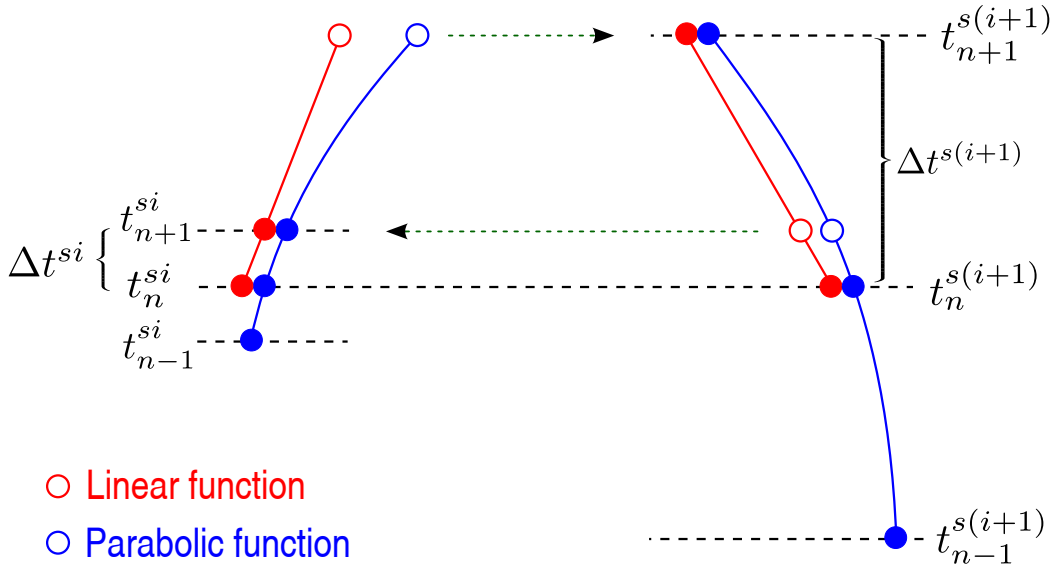

Figure 2.19: Schematic of the functions used in the temporal coupling

The various cases are tested for this coupling method. The boundary conditions and the sizes of the sub-zone models are the same as used in the section 2.1.4. First, Fig. 2.20 indicates the constant flux case in Δt_{s1} =1hr. The tested time ratio of $\Delta t_i, i = s1, ..., s4$ is $1 : 6 : 24 : 168$ representing 1hr, 6hr, 1day, and 1week, respectively. In the same way, the sinusoidal case of heat flow rates is shown in Fig. 2.21. In the two cases, the average pipe wall temperatures are measured.

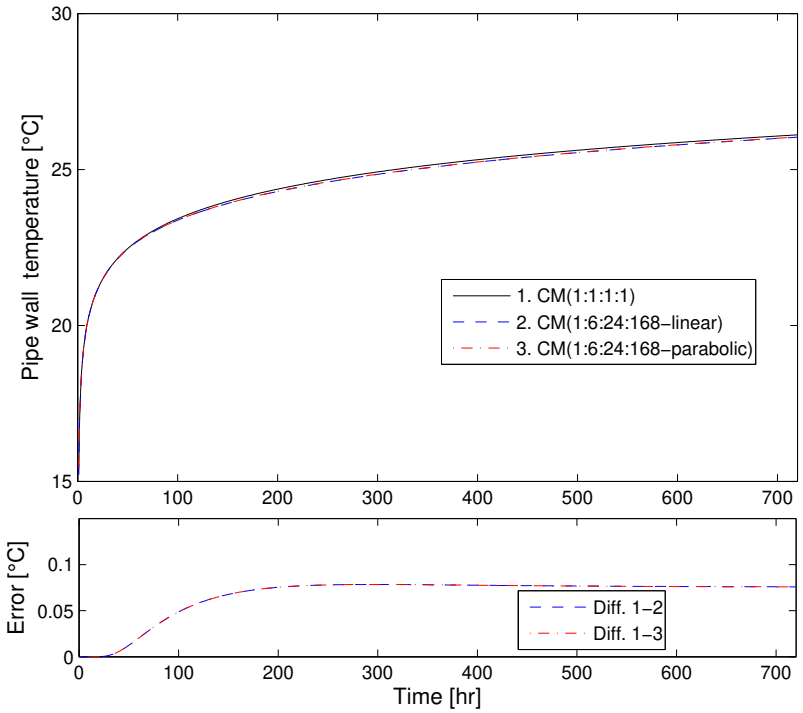

Figure 2.20: Comparison of linear/ parabolic function for a constant flux case

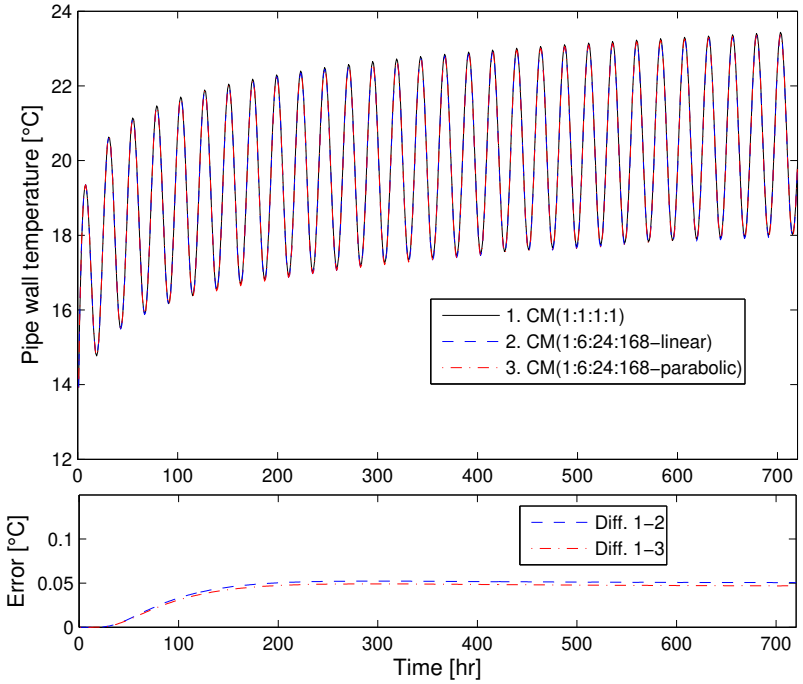

Figure 2.21: Comparison of linear/ parabolic function for a sinusoidal flux case

The errors between the linear and parabolic function are not distinguished, and the maximum error of Fig. 2.20 is less than 0.08 ˚C even if the boundary flux is exaggeratively set up as about 60 W/m for a borehole. This is generally considered as an acceptable error and even diminished for the sinusoidal flux case (Fig. 2.21) that is closer to a real case.

Fig. 2.22 gives errors at the frontier of the sub-zone models of $s1$ and $s2$ where the coupling method is adopted. In this figure, the average temperature $\overline{T_P^{s1}}$ is plotted in the sub-zone $s2$ in each 6hr. From the fact that the sub-zone models are iteratively calculated, the errors between Fig. 2.21 and Fig. 2.22 has almost the same order.

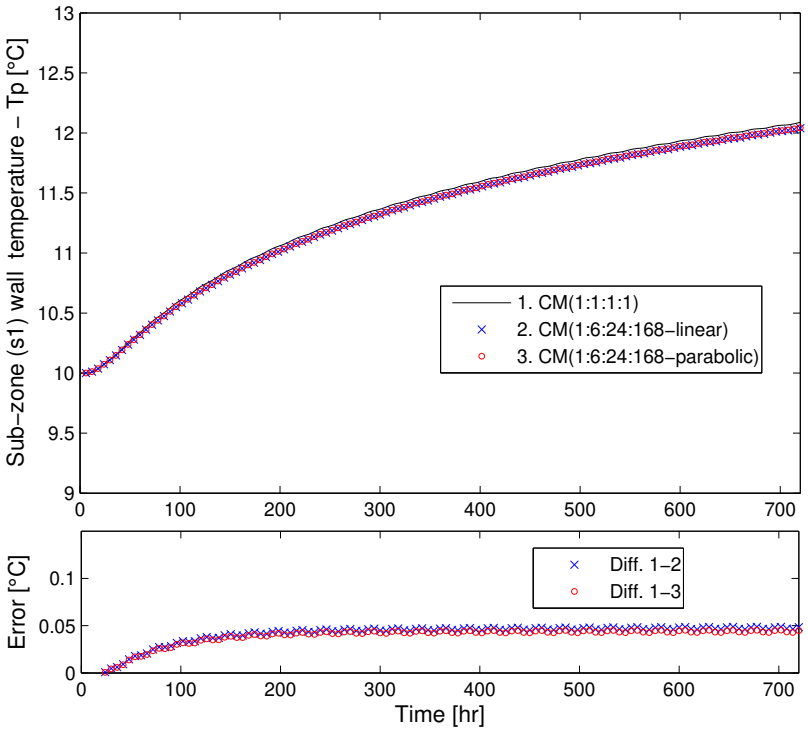

Figure 2.22: Comparison of $\overline{T_P^{s1}}$ linear/ parabolic function (a sinusoidal flux case)

Additionally as seen in Fig. 2.23 extending the errors to 7200hr, the error resulted from the temporal coupling is not accumulated but diminished as simulation progresses, which is very important in the numerical approach particularly to ensure the model pertinence for the long time simulation of GCHP.

As a result, differences between the linear and parabolic function are not significant for all the tests, so the choice is not important to model precision in the implicit scheme. It can be partly explained that the uncertain evolution of variables for the future $n+1$ is estimated using only the present and past ones. This also means that the higher order: 3, 4, ... can not enhance the precision in this kind of temporal coupling. Instead, the time ratio is more sensible to the precision as tested in Fig. 2.24. Here, the errors increase with a high ratio, representing 1hr, 1day, 1week, and 6weeks.

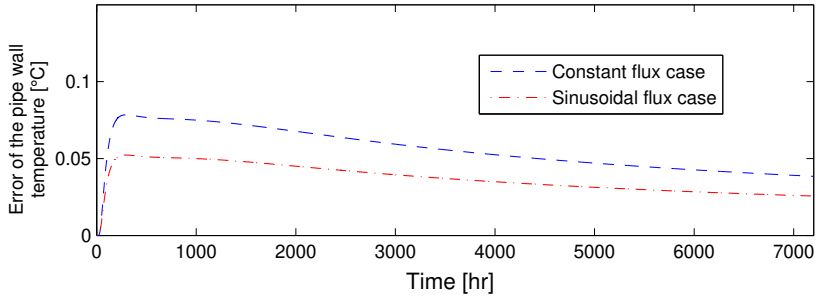

Figure 2.23: Extension of the errors of linear function plotted in Figs. 2.20-2.21

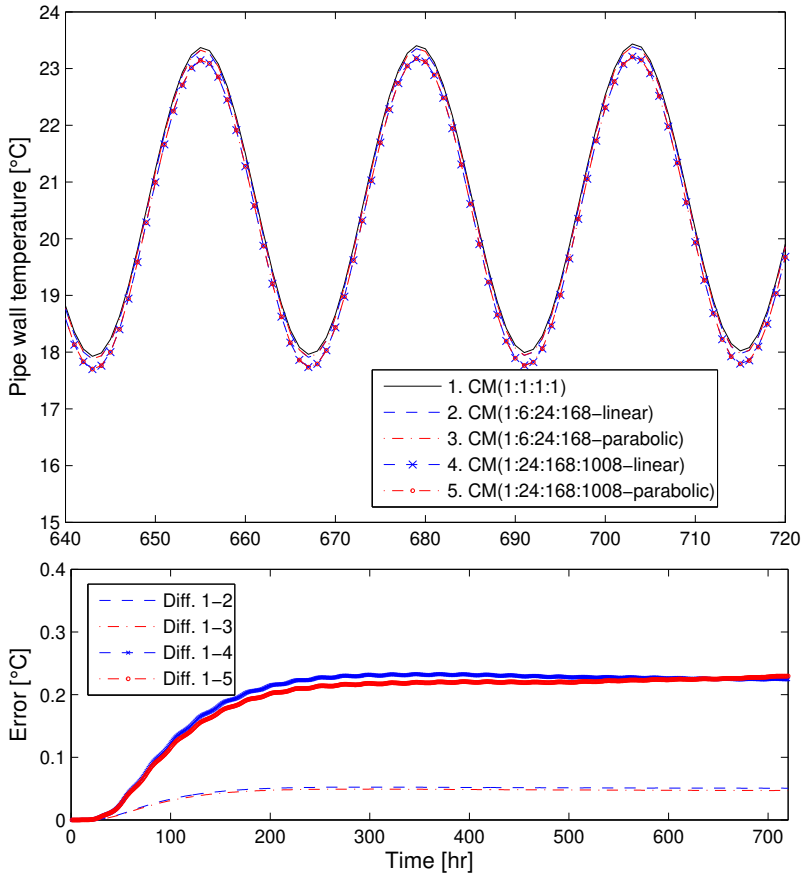

Figure 2.24: Pipe average temperatures (zoomed at 640-720hr) and errors (0-700hr) between the different ratios

2.3 Complete model (3D)

2.3.1 Assembly of sub domains

In order to complete the 3D reduced model (3D-RM), some assumptions are supposed which are partly relative to the common mathematical/ physical treatment of the governing equation or to geometries of the soil domain.

- The soil property (λ, ρ, c) is considered constant (linear and invariant)
- The three-dimensional conductive heat-transfer is only considered in the Cartesian by the mixed approaches (FEM-FVM)
- The perfect thermal contact between the materials is supposed
- The flux φ is uniformly imposed around the U-pipe wall
- The same geometries is assumed for all slices of soil volume (even for h<D and h>H+D)
- The height of slice Δz is the same for all slices
- The soil has homogeneous properties (but this assumption can be modified)

In these assumptions, the governing equation (Eq. 2.42) can be discretized by the FEM as seen in the section 2.1 for the horizontal direction (x,y) and then by the FVM for the vertical direction.

$$\frac{\partial}{\partial t}T(x,y,z,t) = \alpha\left(\frac{\partial^2 T}{\partial x^2} + \frac{\partial^2 T}{\partial y^2} + \frac{\partial^2 T}{\partial z^2}\right) \tag{2.42}$$

All the matrices Eqs. 2.13-2.15 of 2D FEM case can be redefined for a 3D case by multiplying Δz for each matrix. To account for the vertical conductive heat-transfer by the FVM, the vertical term $K_c^{E\perp}$ (Eq. 2.36) must be combined in the conductance matrix[4] A^E as:

$$A^E = K_c^{E\perp} + \Delta z \cdot K_c^{e\vdash} \tag{2.43}$$

Thus, we get the complete equation of a sub-zone model as:

$$\begin{aligned} &C^{\mathbf{S}i}\dot{T}^{\mathbf{S}i}(t) = A^{\mathbf{S}i}T^{\mathbf{S}i}(t) + B''^{\mathbf{S}i}U^{\mathbf{S}i}(t) \\ &\text{where, } \sum_E [C^E] = C,\ \sum_E [A^E] = A,\ \sum_E [B''^E] = B'' \end{aligned} \tag{2.44}$$

This equation will be changed in the modal basis ($X(t)$) and reduced in order by the LA method so that we get:

$$\begin{aligned} \dot{X}_1^{\mathbf{S}i}(t) &= W_1^{\mathbf{S}i}X^{\mathbf{S}i}(t) + B_1^{\mathbf{S}i}U^{\mathbf{S}i}(t) \\ \widetilde{Y}^{\mathbf{S}i}(t) &= H_1 X_1^{\mathbf{S}i}(t) + GU^{\mathbf{S}i}(t) \end{aligned} \tag{2.45}$$

[4]The capital letter E means an element of the 3D case

To temporally discretize $\dot{X}_1^{\mathbf{S}i}(t)$, the implicit scheme is used for these sub models, leading to the final equation:

$$X^{n+1} = (I - \Delta t W_1)^{-1} X^n + (I - \Delta t W_1)^{-1} \cdot \Delta t B_1 U^{n+1} \quad \text{for } \forall \mathbf{S}i \tag{2.46}$$

All the sub-zone models obtained will be assembled to build up the whole soil volume. As seen in Fig. 2.25, each sub-zone is "donut"-shaped that is identical in the vertical direction. The iteration is severally carried out across the borders of sub-zones including an iteration with the fluid model. In this figure, the very top slice sub-zone models are differently defined by the fact that they contact the ground surface while the dimensions and the properties are the same as the other slices. Other models given in this figure will be presented in the following section.

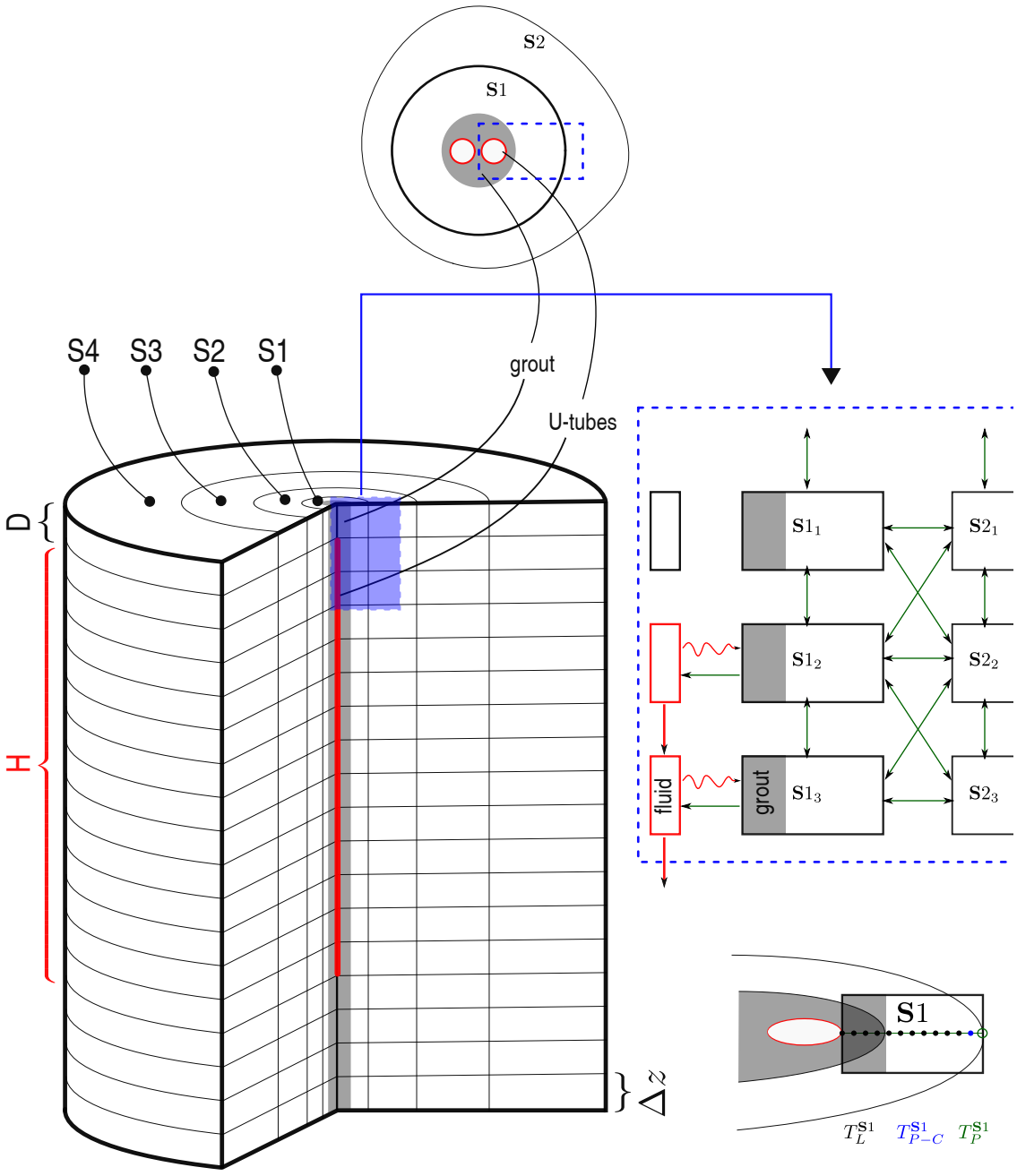

Figure 2.25: Assembly of the sub domains for a 3D approach

2.3.2 Complete model

The fluid model can be written as Eq. 2.47 when GCHP system is switch-on, where l=1 for downward flow and 2 for upward flow. As shown in Eq. 2.48, the relatively small capacity for pipes is neglected using only their resistance. For the switch-off ($\dot{m}$=0), only the resistance R_p for the pipes will be included in the R.

$$\pi r_{pi}^2 \Delta z \rho_f c_f \frac{dT_{f,n}}{dt} = \dot{m} c_f (T_{f,n+(-1)^l} - T_{f,n}) + \frac{\overline{T}_{po} - T_{f,n}}{R} \tag{2.47}$$

$$R = R_p + R_f = \frac{\ln(r_{po}/r_{pi})}{2\pi \Delta z k_p} + \frac{1}{2\pi \Delta z r_{pi} h_f} \tag{2.48}$$

where,

$$\begin{aligned} h_f &= 0.023 Re_f^{0.8} Pr_f^{0.3} \frac{k_f}{2r_{pi}} \text{ for cooling} \\ h_f &= 0.023 Re_f^{0.8} Pr_f^{0.4} \frac{k_f}{2r_{pi}} \text{ for heating} \\ \text{with } Re_f &= \frac{2\dot{m}}{\pi \mu_f r_{pi}},\ Pr_f = \frac{c_f \mu_f}{k_f} \end{aligned} \tag{2.49}$$

To simplify this formulation (Eq. 2.49) proposed by [Dittus & Boelter 1930], a mean value of 0.35 is used for the exponent of Prandtl number as it was done in other exising models [Yavuzturk 1999] [Lee & Lam 2008].

The model 3D-RM can account for the surface effects by differently defining the conductance matrix A and solicitation vector $U(t)$ (therefore, modifying the matrix B'') of the first slice model. First, in the term $K_c^{E\perp}$ defined by Eq. 2.36, dz is given by $\Delta z/2$ for the upper-part heat transfer other than the other slices where $K_c^{E\perp}$ is the sames for upper and lower-part heat transfer and dz is always equal to Δz if each slice has the same height Δz. Finally, all the upper slice temperatures in the vector $U(t)$ will be replaced by the ambient temperature T_{ext} or the equivalent temperature T_e that includes the solar-radiation effect. Moreover, if coordinate information will be given for a building position, the related meshes can be identified and then exposed to a building temperature e.g. 20 ˚C. This characteristic might be useful for an application to a horizontal or a short-length heat exchanger cases.

$$T_e = T_{ext} + \frac{\alpha E}{h_{ext}} \tag{2.50}$$

where, α is the absorption coefficient, and E the total solar radiation received by the surface, and h_{ext} the convective heat transfer coefficient.

Finally, the iteration among the sub-zone models will be continued until a maximum error is less than an error criterion. Here, the error is defined by intermediate values of boundaries Γ (e.g. $T_P^{\mathbf{S}i}$) for each iteration (j).

$$\text{Maximum error} = \max\left(\frac{|\Gamma^{j+1} - \Gamma^j|}{\Gamma^j} \times 100(\%)\right) \tag{2.51}$$

2.3.3 Results and discussion

The 3D-RM model will be largely validated in the section 4. Here we only investigate the reduction part and its efficiency.

The matrices given in the previous parts are differently defined according to Δz, by which the dominant modes can vary. The number of these modes is shown in Tab. 2.5 for each case of Δz under the same conditions as the 2D simulation (section 2.1.4). The smaller the height of a sub-zone model (Δz) was, the more modes are selected particularly for sub-zones of larger dimension (**S**3, **S**4). This inefficiency, however, cannot much affect the total model efficiency because the sub-zone models **S**3 and **S**4 are only to be calculated every 24 and 168 time steps respectively in the example. Although it is not handled in this thesis, an optimization can also be achieved by regrouping several slices of such sub-zones **S**3 or **S**4. It allows not only the similar reduction efficiency as 2D case (see the decreasing number of the modes shown by the bold numbers of the table) but also to reduce the total number of sub-zones.

Table 2.5: Number of Selected modes in different Δz

Sub-zone	Total modes	Selected modes according to Δz					
		1m	5m	10m	30m	100m	∞(2D)
S1 (0-1m)	474	14	10	10	10	10	10
S2 (1-3m)	140	53	32	31	31	31	31
S3 (3-20m)	203	**118**	**44**	**30**	**23**	**22**	**21**
S4 (20-100m)	201	**197**	**174**	**163**	**130**	**13**	**4**
S1-**S**4	1018	382	260	234	194	76	66

While the selected modes in the 3D-RM are less than 10% compared to the CM particularly for **S**1, **S**2, the calculation time cannot be reached at the same efficiecy. It is because the vector $U^{\mathbf{S}i}(t)$ and the correspondent matrix $B''^{\mathbf{S}i}$ are still including the terms $T_{L,bot}^{\mathbf{S}i,n+1}$,$T_{L,top}^{\mathbf{S}i,n+1}$ (Eq. 2.35) of initial order to couple with the upper and lower slices. Nevertheless, the total time-efficiency[5] compared to the initial model (no sub-structuring and a time-step for all sub-zones) will be surely assured.

Even if the present model 3D-RM is a complete model and accounts for details of the bore-field, some remain optimized relative to accelerate calculation time as partly mentioned and proposed in this section:

- optimizing time-step ratios according to the correspondent sub-zone model sizes and number
- replacing the temperatures of the adjacent upper/ lower slices by average fluxes
- regrouping the slices of sub-zones of larger size (**S**3, **S**4)
- double reduction (reducing→regrouping→re-reducing) to reduce iterations of the vertical direction and to finally select less modes

[5]The exact CPU time comparison cannot be provided because the initial 3D model (i.e. 30540 meshes for 30 slices) cannot be modeled with a normal computer memory

Chapter 3

Hybrid model

The model 3D-RM explained in the section 2 is developed to investigate the thermal impact on the soil domain as briefly demonstrated in the introduction. Various simulations would be expected to study different cases of GCHP system such as solar recharging. In this case, other elements of system should be assembled to be iteratively calculated with a GHE model. Even if the 3D-RM can be directly used in this purpose, it is more practical to employ a compact model that is only to estimate the fluid temperatures. A common simulation tool TRNSYS is chosen to implement this model (TRNSYS types).

In this section, a new model, so-called hybrid (HM), is presented that has partly the same numerical approaches as the 3D-RM while using analytical solutions in part as seen in Fig. 3.1. These methodologies are all presented in the previous section and in the section of literature review. This kind of model structure is similar to Yavusturk's recent work [Yavuzturk *et al.* 2009] that combined a numerical model for boreholes with the g-function for the neighboring ground. It is naturally inspired by the fact that the problem is characterized by various time-scales with rapid (less than an hour) changes inside the borehole and slow variation of ground temperature far away from the borehole. However, his numerical model is based on a very simple model where a single mesh is adopted, assuming the equivalent diameter.

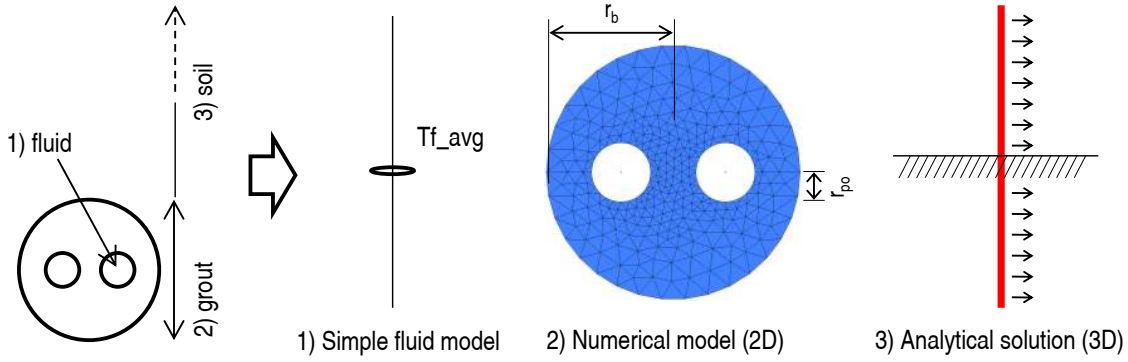

Figure 3.1: Schematic of the hybrid model

Thus, one of the main differences of HM to Yavuzturk's one is that it can describe borehole configurations by unstructured meshes (*Gmsh*). The detailed demonstration will be given in the following sections.

3.1 Borehole/ Fluid model

In order to accelerate calculation and couple a borehole model (BHE-RM) with an analytical solution, some hypotheses are assumed as follows:

- All the properties of the soil/grout are regarded as constant values (linear and time-invariant).
- Two-dimensional (x, y) heat transfer is assumed for the borehole domain (grout).
- U-tube and fluid capacities are neglected.
- The fluxes are equally distributed all around the pipe wall.
- The temperatures of a borehole wall boundary are assumed to be the same.
- An arithmetic mean value is used for an average fluid temperature.

The two-dimensional numerical equation with heat fluxes given on each pipe wall can be defined for a case for one U-tube inserted as:

$$\begin{aligned} C\dot{T}(t) &= AT(t) + B'U(t) \\ \text{where, } U(t) &= \begin{Bmatrix} \varphi_{dw} \\ \varphi_{up} \end{Bmatrix} \end{aligned} \tag{3.1}$$

The boundary nodes (T_P) at the borehole wall are reserved to be replaced by an analytical solution. Accordingly, the same processes of Eq. 2.24-2.26 in the section 2.2.1.1 are used. The resultant new input vector $U(t)$ is given:

$$U(t) = \begin{Bmatrix} \varphi_{dw} \\ \varphi_{up} \\ T_P^{n+1} \\ T_P^{n} \end{Bmatrix} \tag{3.2}$$

We get the correspondent vector of observation $Y(t)$:

$$Y(t) = \begin{Bmatrix} \overline{T}_{dw} \\ \overline{T}_{up} \\ \varphi_b \end{Bmatrix} \tag{3.3}$$

Where, the average temperatures $\overline{T}_{dw}$ and $\overline{T}_{up}$ will be used to associate with a fluid model in each time step, and the total flux φ_b across a borehole wall will be an input value for the analytical model that will be explained later. Here, the flux (W/m) across a borehole wall in an element can be calculated as Eq. 3.4, where dl is a side-length of a triangular element to which the borehole wall belongs.

$$\varphi_b = -\int \lambda \overrightarrow{\text{grad}T} \cdot \vec{\text{n}} dl \tag{3.4}$$

The gradient temperature $\overrightarrow{\text{grad}T}$ can be calculated by using M (Eq. 2.11). The unit normal vector $\vec{\text{n}}$ on a side ($\overline{p_1 p_2}$) of triangle can be obtained by the following equation that uses coordinates of points consisting of the triangle:

$$\text{for a triangle } (p_1(x_1,y_1),\ p_2(x_2,y_2),\ p_3(x_3,y_3))$$
$$\vec{\mathrm{n}}_{\overline{p_1p_2}} = \left(\frac{(X_{13}Y_{23} - X_{23}Y_{13})(Y_{23} - Y_{13})}{\sqrt{x_3^2 + y_3^2}}, \frac{(X_{13}Y_{23} - X_{23}Y_{13})(X_{13} - X_{23})}{\sqrt{x_3^2 + y_3^2}} \right) \tag{3.5}$$
$$\text{where, } X_{13} = x_1 - x_3, Y_{13} = y_1 - y_3 \quad X_{23} = x_2 - x_3, Y_{23} = y_2 - y_3$$

These state models will be transformed into the modal basis to use the reduction technique. The same reduction processes as used for the 3D-RM are carried out.

For the outlet fluid temperature, a simple fluid model that uses average temperatures of fluid is used and iteratively calculated with the borehole model as seen in Fig. 3.2. The iteration process is as follows:

In each time step,

1. assuming fluxes φ_{dw} and φ_{up} on the U-tube walls
2. calculating the U-tube wall temperature $\overline{Tp}_{dw}$ and $\overline{Tp}_{up}$ under the assumed fluxes in the borehole model
3. predicting Tf_{dw} and Tf_{up}, using the obtained temperatures $\overline{Tp}_{dw}$ and $\overline{Tp}_{up}$ and the initial guessed fluxes φ_{dw} and φ_{up} (Eq. 3.6a)
4. recalculating the fluxes φ_{dw} and φ_{up}, and then iterating the same process until the convergence (Eqs. 3.6b-3.6c)

In this iteration (the first iterative loop in Fig. 3.2), the following three equations are used:

$$Tp_{dw} - Tf_{dw} = R\varphi_{dw} \tag{3.6a}$$
$$\varphi_{dw} = \frac{\dot{m}c_{pf}(Tf_{bot} - Tf_{in})}{H} \tag{3.6b}$$
$$Tf_{dw} = \frac{Tf_{in} + Tf_{bot}}{2} \tag{3.6c}$$

Here, Tf_{in} and $\dot{m}$ with a given R are input values of simulation, so the four unknown values: Tp_{dw}, Tf_{dw}, φ_{dw}, and Tf_{bot} will be obtained from these three equation and the BHE-RM model.

3.2 Soil model

The soil domain can be replaced by analytical solutions presented in the review section. Above all, the FLS model (Eq. 1.43 in the section 1.1.2.3) is used to take into account the 3D effect that dominates after a long-time operation of system. Then, this FLS will be used for generating a thermal response curve (Fig. 3.2). Since this soil model will be used to provide boundary temperatures to the two-dimensional BHE-RM, the average temperature along the borehole height (H) can only be concerned (Eq. 1.44). For this average value, the fast formula (Eqs. 1.45-1.46) proposed by Lamarche et al. is used. Thus, the present version of HM cannot take into account the surface layer D, i.e. D=0 for all cases.

Since a single borehole case is supposed for the solution, the spatial superposition method presented in the section 1.1.2.2 also has to be employed for the multi-bore field case. From these solutions, the thermal response data for a given bore-field geometry can be obtained, the process of which has already been reviewed in the section 1.1.3.1. For an accurate solution (Fig. 1.17), the approximated CHS model (Eq. 1.35) is also used in short-time ranges.

3.3 TRNSYS types of the model

For simulation purpose, the models presented here are assembled as types to be implemented in the TRNSYS: hybrid model (HM) and thermal response generator (TR-G). Above all, the HM is composed of three sub-parts as shown in Fig. 3.2. The thermal response data are to be linear-interpolated to coincide these tabulated values that are given in some specific time points with the simulation time. Then an iteration is running up to convergence.

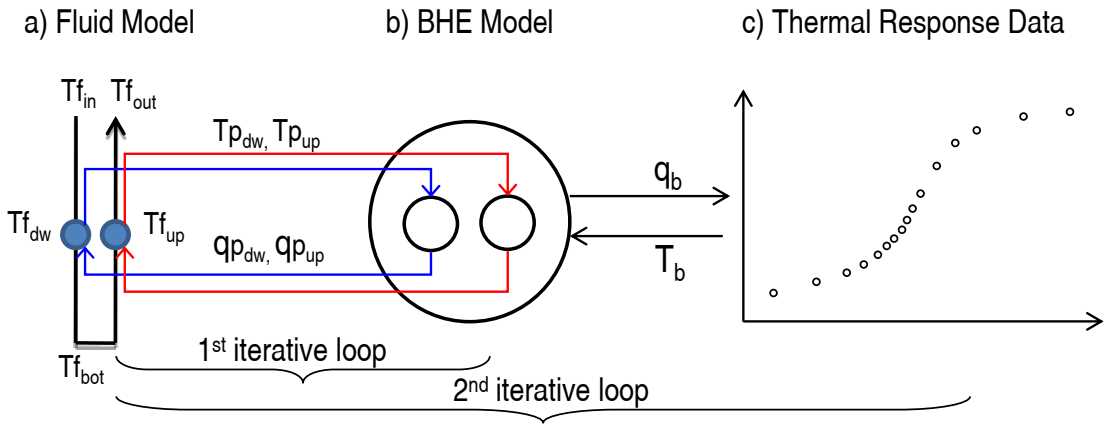

Figure 3.2: Structure of HM and iterative computation

A thermal response generator is integrated in a TRNSYS type as well. The type (TR-G) can be used before a real simulation to generate the thermal response data for an user-defined BHEs geometry. The resultant response data file (*.txt) will be inserted into the type (HM) via "external files" button of the type. Fig. 3.3 shows how to simulate a GCHP project with the developed types (the type HM will be connected with other components of system). The mesh file (*.msh) can be selected out of a mesh file library previously prepared by *Gmsh* to simulate most of the general BHE geometries.

3.4 Capacity effect of HM

The main contribution of this model HM is that it takes into account the capacity of grout with a detailed mesh but without increasing calculation time. To test the model, it is compared with two existing models in the TRNSYS library:

- Type 557 also known as the DST model, commonly used for GHEs simulation, was

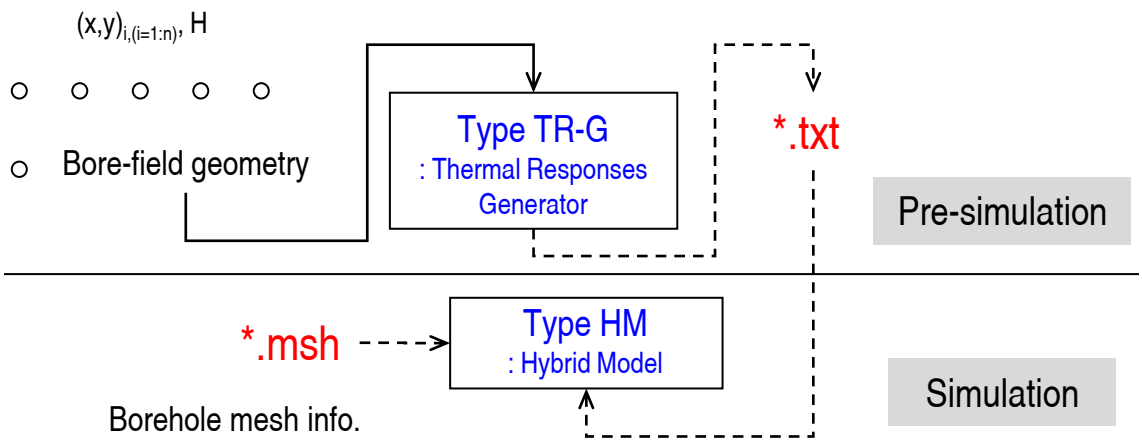

Figure 3.3: TRNSYS simulations with the developed types

selected as it does not take into account the grout capacity effects and uses a numerical/analytical approach with relatively coarse meshes.

- Type 451 [Huber & Schuler 1997] was chosen for comparing the HM in terms of the capacity effects. It also has a relatively coarse grid.

The parameters used are given in Tab. 3.1. Although the HM model can take into account the interaction between boreholes, this comparison is limited to a single borehole case. As explained above, the pre-simulation must be performed to establish the thermal response data (*g-function*). Fig. 3.4 shows these responses based on the parameters in Tab. 3.1.

Table 3.1: Simulation parameters

Parameter	Unit	Value	Parameter	Unit	Value
H	m	100	ρ_f	$\mathrm{kg/m^3}$	1021
r_b	m	0.08	c_c	J/kg°C	3900
r_{pi}	m	0.013	c_s	J/kg°C	1077
r_{po}	m	0.016	c_f	J/kg°C	5551
Number of U-tube		2	k_c	W/m°C	2.0
T_0	°C	11.75	k_s	W/m°C	2.78
ρ_c	$\mathrm{kg/m^3}$	1000	k_f	W/m°C	0.3068
ρ_s	$\mathrm{kg/m^3}$	2006			

In order to compare different models, two input scenarios were examined. The first imposes four consecutive cycles during which the borehole operates for 12 hours with a flow rate of 0.08 L/s and a temperature of 10°C followed by a period of 12 hours of zero flow. The second scenario uses the same flow rate and same temperature but with a higher operating frequency of 30 minutes. In all cases the simulations are performed with a time step of 10 minutes in TRNSYS.

The simulation results of the first scenario are shown in Fig. 3.5. In the results, ExFTs are not too different. These results show that the models are suitable for an estimation

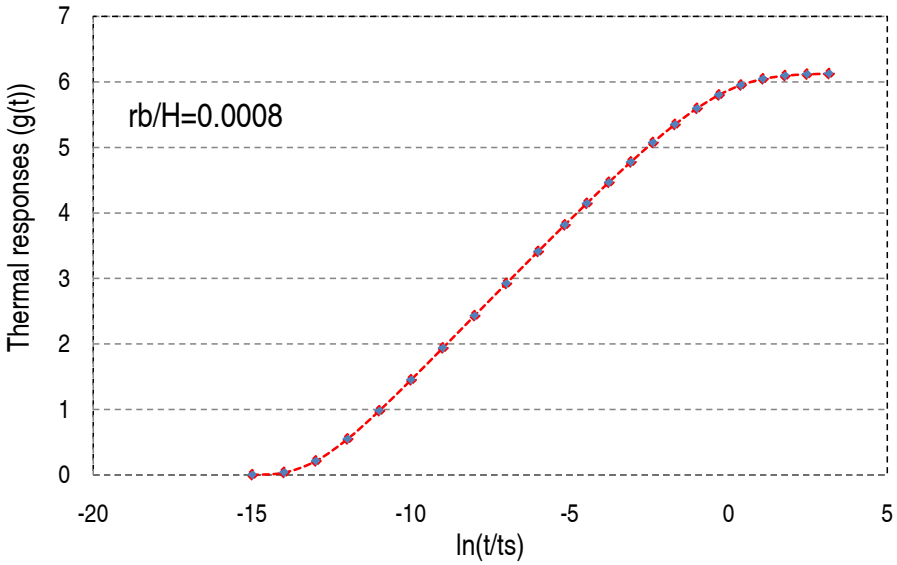

Figure 3.4: *g-function* used in this study

of response in the case of slow solicitation, giving the same precision. Fig. 3.6 shows different behaviors depending on whether the capacity of the grout is taken into account or not. The DST model responds very quickly to the solicitations with large fluctuations. These results clearly indicate that a model of GHEs must be carefully selected, especially where the GCHP system is subjected to faster variation of loads. The HM model gives comparable results with those of Type 451. HM is efficient in terms of computing time, even if it uses a very fine mesh for the borehole domain. In these simulations, the model uses only 4 modes among the 341 initial modes induced by the finite element method. The calculation time is considerably reduced (about 99% faster) without compromising accuracy.

The simulation results also show that the capacity effect should be considered in case of fast solicitations. In addition, the developed model is very flexible compared to existing models in TRNSYS for describing any desired configuration of bore-field.

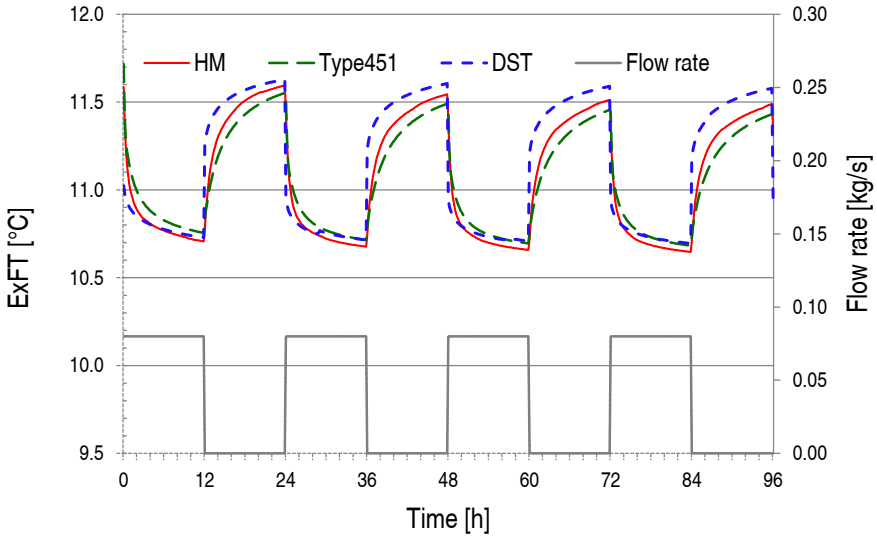

Figure 3.5: Curves of models when operating with a simple profile

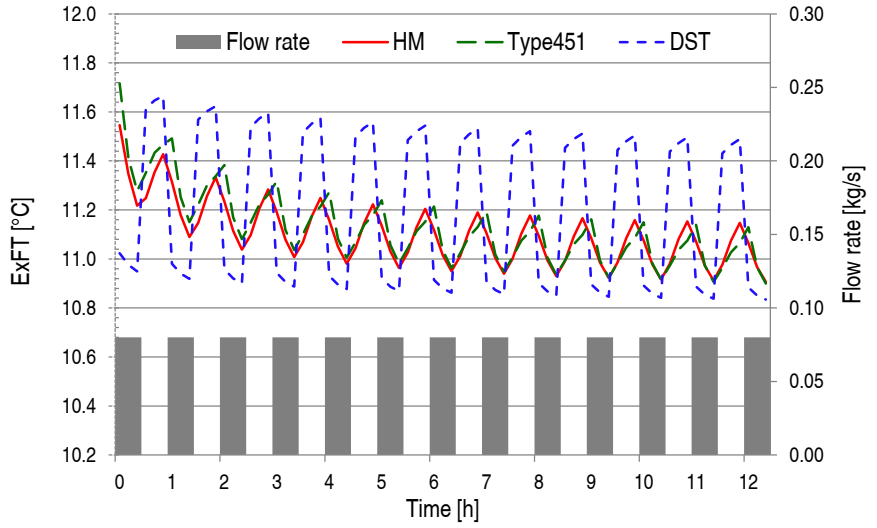

Figure 3.6: Curves of models when operating with a dynamical profile

Chapter 4

Experimental verification

4.1 Experimental set-up

To validate the 3D-RM, an experimental set-up has been installed at EDF's R&D research center. Since the 3D-RM was originally developed to precisely predict the thermal behavior of the GHEs and their vicinity soil, measuring is carried out at several points even inside the borehole in this experimentation. This installation was connected to an existing natural climate platform to simulate the realistic GCHP case. The details will be presented in the following sections.

4.1.1 "Natural climate" plateform

The natural climate platform (Fig. 4.1) is designed to test GCHP in a natural climate over one or more years. It consists of a 3000 m^2 area dedicated to the installation of ground collectors and a control room equipped with several heat pumps. This facility is used to: experimentally check ground collector sizing; evaluate the impact of ground heat exchangers on the surrounding ground; measure ground heat exchanger performance and heat pump COP.

Figure 4.1: The natural climate platform of EDF

The set-up used in the present study is shown in Fig. 4.2. It consists of a water-to-water heat pump connected to the ground collector field. The operation of the heat

pump is driven by a control loop which mimics the operation of a real house, which insulated level and heated volume can be adjusted, and is driven by real-time weather. Thus, whenever house heating is required the heat pump is activated to heat a 500 liter tank which acts as a house. The house load is rejected outside using an air cooler loop (cf. Fig. 4.3).

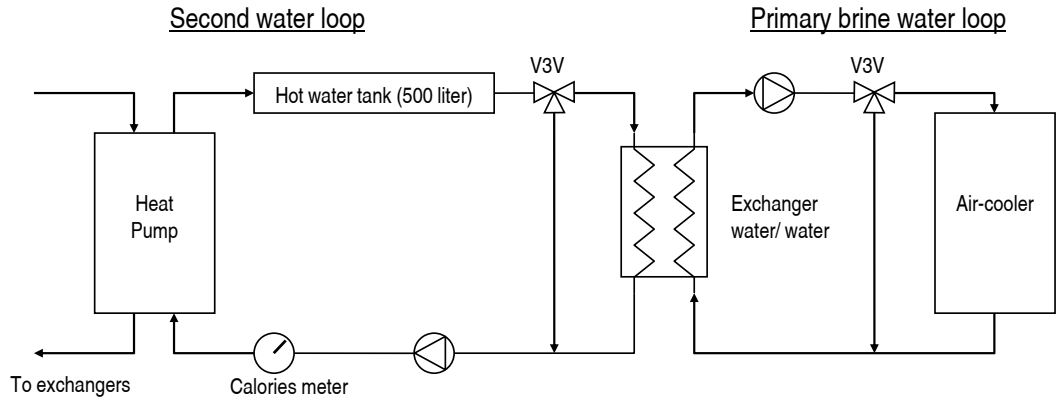

Figure 4.2: Experimental set-up used in the present study

Figure 4.3: Heat pump and second water loop with 500l water tanks (left) and Air cooler (right)

More precisely, the functioning of the platform is based on an hourly operation and on the heat pump internal control of the water return temperature as a function of the outside air temperature. For each hour, the energy needs of the simulated house are calculated based on the average outside air temperature of the previous hour. Once the energy needs are calculated, the air cooler loop is started. Then, the water return temperature to the heat pump falls until the starting of the heat pump. A calories meter measures the energy supplied to the water tank loop and the control system stops the air cooler loop as soon as the calculated value of energy needs is reached. Thus, the water return temperature increases, inducing the heat pump stop. This control strategy permits to reproduce a functioning close to a real one.

The platform is therefore equipped to systematically measure the following parameters:

- thermal energy supplied to the air cooler loop
- water flow rate and temperatures (inlet/ outlet) at the evacuation exchanger
- absorbed electrical energy (compressor and circulating pumps)
- brine and water temperatures (inlet/ outlet) at the evaporator and condenser of the heat pump
- brine flow rate at the evaporator
- outside air temperature and humidity
- far-field ground temperatures at 2, 5 and 20 meters deep

4.1.2 Description of the experimentation

4.1.2.1 Drilling and system set-up

3-GHEs, spaced 10m apart, have been installed on the field test platform. A depth of 39m was reached for an exchanger and a 40m one for the two others. This different borehole length of 39m, borehole (N°2) in Fig. 4.6, was due to landsliding during withdrawing of drill pipes. The soil is composed of dense sand until about 20m, penetrated by limestone thin layers. To prevent the soil to collapse during drilling operation (Fig. 4.4), a casing (Fig. 4.5) was introduced in this region. For depths deeper than the sand region, the soil consists of limestone, compact or crushed ("white clay"). The total GHEs length is 119m that is slightly undersized for the 9kW HP previously installed[1]. However, the load part that is controlled by the air-cooler loop of the test platform was adjusted to this GHEs sizing[2]. In operation, this oversized heat pump, compared to load and source sides runs with shorter cycles than it normally does.

Figure 4.4: Drilling operation and borehole

[1]The designed length was evaluated around 150m, i.e. 3 GHEs of 50m deep but a break was met at 42.5m deep during the first borehole drilling

[2]The resultant load is equivalent to a moderately insulated house of $115\mathrm{m}^2$ in a french cold region

Figure 4.5: Case inserting

4.1.2.2 Measuring points

To validate the 3D-RM, temperatures are measured in the circulating fluid as well as on U-tubes wall. As seen in Fig. 4.6, the fluid temperatures are measured near the manifolds. More precisely, the intrusive sensors (PT100) are inserted into the inlet and outlet manifolds of the borehole N°2. Therefore, it allows to measure the entering fluid temperature (EFT) and the exiting one (ExFT) of the borehole N°2 but at a distance from the borehole head. This was chosen because intrusive sensors through polyethylene pipe at the borehole head could have induced fluid leaks. This location of fluid measuring points implies to model the horizontal connexion part between the boreholes and manifold well, in order to compare experimental results with simulation ones.

Here, some notations on the fluid temperatures are required to avoid confusion. EFT and ExFT are experimentally measured in the manifolds whereas the fluid temperatures at a head of borehole are evaluated by the GHE model itself and used as an inlet parameter for the model as well. The latter will be called by EFTbore and ExFTbore while the formers will be mentioned by EFTcol and ExFTcol thereafter.

In addition, temperature sensors (PT100) equip two U-tubes walls in two boreholes (N°1 and N°2 in Fig. 4.6) and are positioned at 5 different depths. Sensors were introduced at the same depths in a reference borehole, drilled between boreholes N°1 and N°2 (Fig. 4.6) to investigate thermal interferences.

The sensor depths are 2, 5, 10, 35 and 38.5 m for each leg (downward and upward) of one U-tube. This positioning shifted by 1m for the 39m-long borehole (N°2) and sensors are positioned at 1, 4, 9, 34 and 37.5m deep.

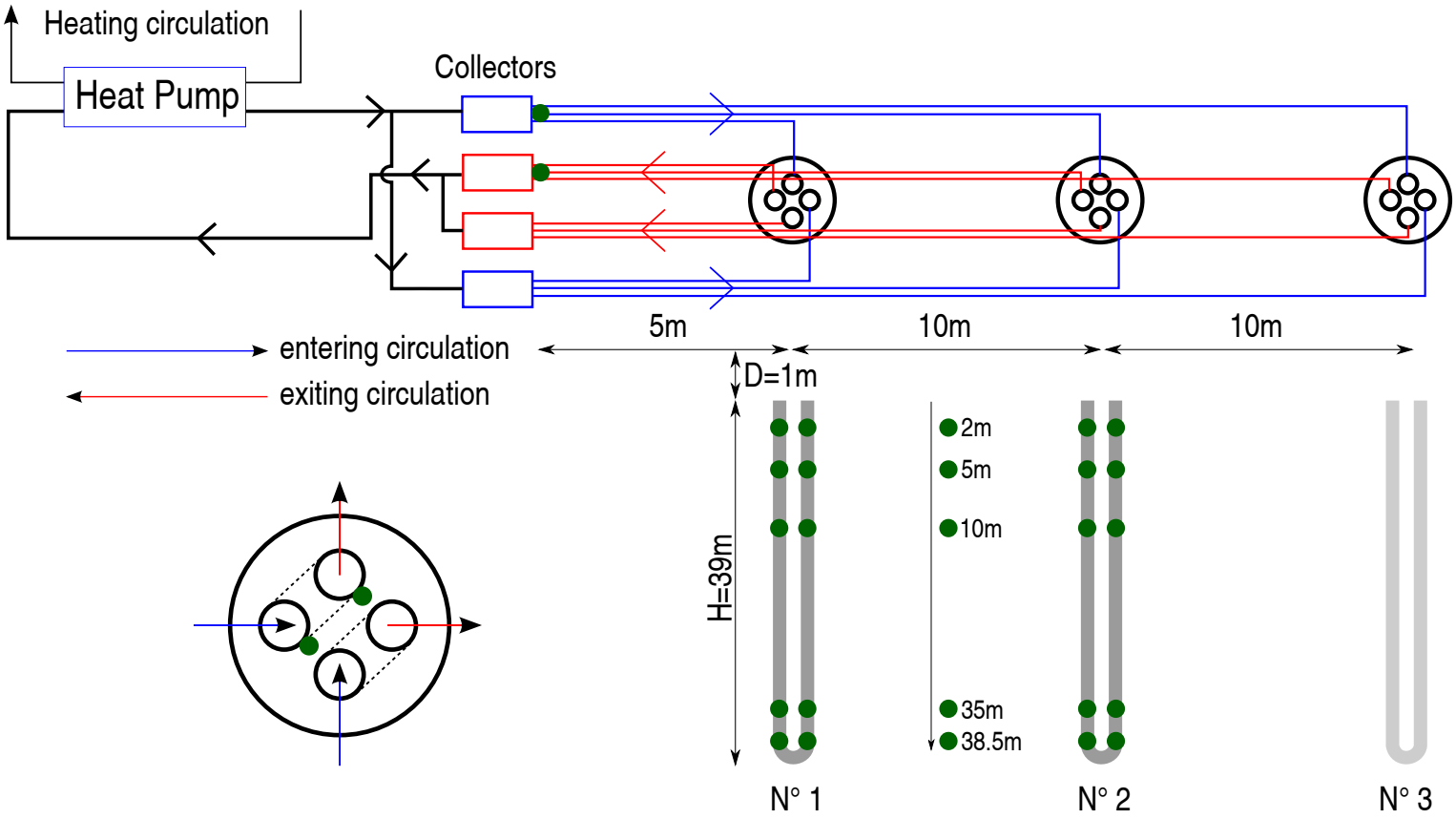

Figure 4.6: Configuration of 3-boreholes and measuring points

4.1.2.3 Experimental uncertainty

The measuring uncertainty of PT100 temperature sensors is 0.1˚C. This uncertainty value is acceptable for validation of fluid temperatures. However, a supplementary uncertainty has to be added for U-tubes wall temperature values. After introducing the U-tubes equipped with sensors, the casing (section 4.1.2.1) had to be removed. For this operation, sensors cables had to be cut (Fig. 4.7). The additional connexion of sensor cables induced by casing removal implies an added uncertainty of 0.2˚C. Consequently, the measuring uncertainty of U-tube wall temperatures is 0.3˚C.

Figure 4.7: Sensor cable cutting and connecting to the manifold well (here, red pipes contain the sensor cables)

Moreover, two configuration aspects can have consequences on the values of some parameters. The first aspect concerns the manifold well configuration. As seen in Fig. 4.8 and 4.9, the manifolds are assembled in a buried well. Even if they are insulated, they are exposed to the ambient temperature via a metallic cover. Therefore, if the fluid stay a relatively long time in the manifolds (when the heat pump is stopped), its temperatures, measured as EFTcol and ExFTcol, can be influenced by the ambient one. The second aspect is induced by the required casing of the upper part of boreholes. To introduce this temporary tubing, the drilling diameter has to be larger than usual one. This point has to be taken in account for modeling parameters.

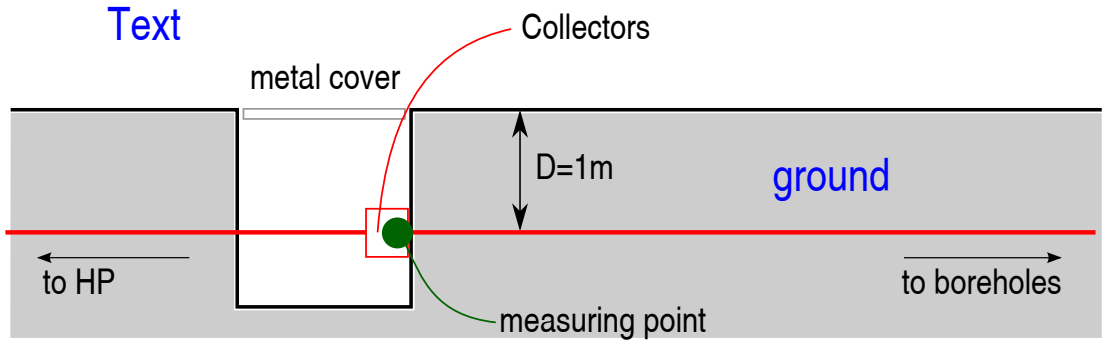

Figure 4.8: Details of the ground configuration of pipe collectors

Figure 4.9: Manifolds and Temperature sensors (left) and Metallic cover of the manifold well (right)

4.2 Model description

As seen previously, in order to compare experimental and calculated results, the pipe connexion part has to be modeled, coupled with boreholes model. The developed model 3D-RM is validated by comparison with experimental results during a full month. This validation will be completed by model comparison presented in the section 5.

4.2.1 Modeling of boreholes

In general, the thermal interferences between GHEs do not need to be considered after only a month of operation particularly for the boreholes spaced 10m apart with a ratio of 0.25 (spacing/ depth). Accordingly, a single GHE (N°2) is only modeled in this section. 3 sub-zones are used and their sizes are given in Fig. 4.10.

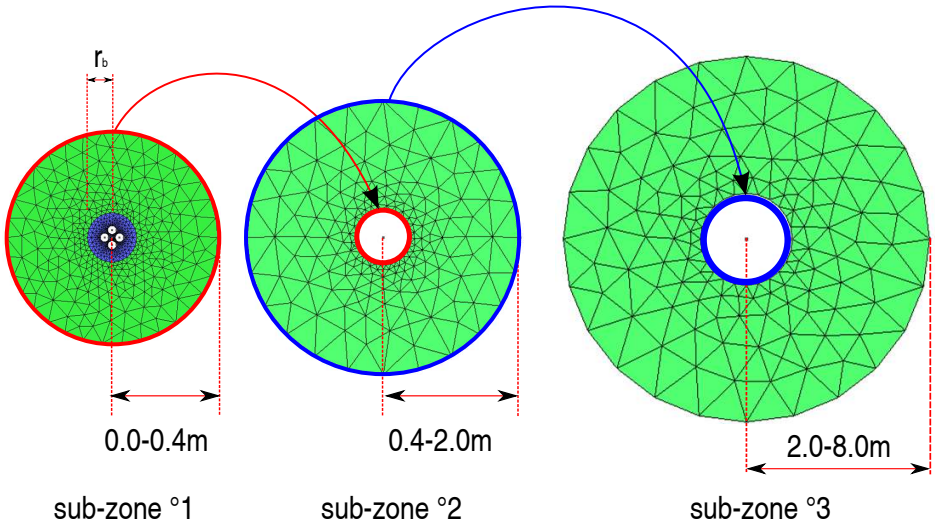

Figure 4.10: 3 sub-zones used for experimental validation

Here, the borehole diameter is equivalently assumed as 18.6cm, obtained by averaging two different diameters: 22cm resulting from pre-tubing (until about 17m) and design

diameter 16cm. According to the dimension of each sub-zone model, the adequate time steps are chosen. For example, for a 10-minutes time-step simulation, we used a ratio of 1:10:60 indicating 10min:1h40min:10h (see Annex C).

The 3 sub-zones will be piled up to a total height of the soil volume (>H+D). In this case, 1, 38, and 5m are set up for D, H, and the deep soil volume, respectively. Since Δz is fixed by 1m, total 44 slices: 1+38+5 are used.

4.2.2 Modeling of the pipe connexion part

Since the configuration of the connection part of soil is 3D as previously shown, it is also not trivial to model this part. In addition, the initial temperatures of soil are not obvious even after the tube embedding, and the conductivity of soil varies greatly according to humidity in this surface soil. Actually, the season when the experimentation has been carried out is humid. Despite of these complicated situations, we simplified the part of soil around connection tubes

Fig. 4.11 shows meshes used in the simple model. 2-dimensional approach is used that treat the soil as a dimensionless length in the axial direction of connection pipes. Thus, an average amount of fluxes along the pipe length (15m until the borehole N°2) is given as a boundary value for this 2D soil model. To take into account the fluid capacity, the control volumes of fluid are modeled as done in the 3D-RM.

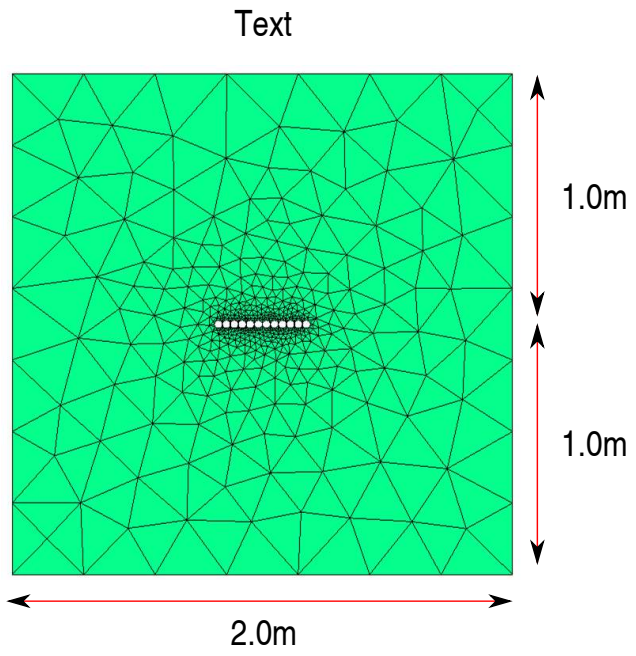

Figure 4.11: 2-dimensional modeling of part of connection

4.2.3 Simulation parameters

The thermal properties of materials are given in Tab. 4.1. The working fluid circulating inside U-tubes is a water-antifreeze mixture (monoethylene glycol 30%) with a freezing point of -16 ˚C. The soil conductivity is obtained by a thermal response test carried out

for this project. However, since the fluid temperatures for this test were measured at the points "col", the 3D-RM has been used in advance to calibrate the thermal response date. This data calibration is explained in Annex D. Briefly, a value of 2.3 W/m˚C was obtained for k_s from the initial bulk value 2.78 W/m˚C. The other properties are defined as typical ones.

Table 4.1: Properties used in the simulation

	Property	Unit	Value
Pipe	Conductivity	W/m˚C	0.4
Grout	Conductivity	W/m˚C	2.0
	Volumetric heat capacity	J/m^3˚C	3.9×10^6
Soil	Conductivity	W/m˚C	2.3
	Density	kg/m^3	2300
	Specific heat capacity	J/kg ˚C	1135.06
Fluid	Conductivity	W/m˚C	0.45
	Density	kg/m^3	1051.9
	Specific heat capacity	J/kg ˚C	3590
	Dynamic viscosity	kg/ms	0.0052

The sub-model sizes and related data are given in Tab. 4.2.

Table 4.2: Model sizes and mesh information

	unit	value
Borehole radius (r_b)	m	0.093
Pipe outer radius (r_{po})	m	0.016
Pipe outer radius (r_{pi})	m	0.013
Center-to-center distance of pipes	m	0.057
Radius of sub-zone 1	m	0.4
Radius of sub-zone 2	m	0.4-2.0
Radius of sub-zone 3	m	2.0-8.0
Δz (slice height)	m	1
H	m	38
D	m	1
z> H+D	m	5
Length of the connection tube to borehole $\mathrm{N}^\circ2$	m	15
Soil model size for connection part	m	2×2
Mesh number for sub-zone 1		664
Mesh number for sub-zone 2		179
Mesh number for sub-zone 3		147
Total Mesh number		43560
Mesh number for connection part		560

For simulation condition, the undisturbed ground temperature measured on the platform is 11.75˚C. For the initial surface temperature, a value of 8˚C is obtained during the calibration of the thermal response test (see Annex D). The simulation parameters are given in Tab. 4.3.

Table 4.3: Simulation parameters

	Unit	Value
Initial temperature for ground	˚C	11.75
Initial temperature for surface	˚C	8
Time step ratio for sub-zones 1:2:3 in 10min simulation	min	10:100:600
Time step ratio for sub-zones 1:2:3 in 1min simulation	min	1:20:600

4.3 Results comparison

Usually, a GHE model is validated by comparison of the fluid temperature at the outlet of the borehole field. Beside this classical result, the 3D-RM permits to calculate temperature distribution along the U-tubes pipes and then precisely evaluate the borehole field behavior. As mentioned previously, simulation results and experimental ones are compared with one-month data.

4.3.1 Fluid temperature

4.3.1.1 Results

The 3D-RM results for ExFTcol are compared with the experimentation in Fig. 4.12. The curve "Exp" represents 10min-interval points obtained from experimental data measured each minute. Accordingly, the 3D-RM simulation is carried out in a 10-minutes time step. In Fig. 4.12, the x axis label indicates time steps of 10 min, therefore 4500 mean 45000 min (one-month data).

Under the given simulation conditions, experimental and 3D-RM results are globally in very good agreement, with errors (Eq. 4.1) less than 1˚C during all simulation periods. Moreover, the dynamic behavior of the borehole is very well reproduced.

$$\mathrm{Error}[^{\circ}\mathrm{C}] = \mathrm{T_{sim}} - \mathrm{T_{exp}} \tag{4.1}$$

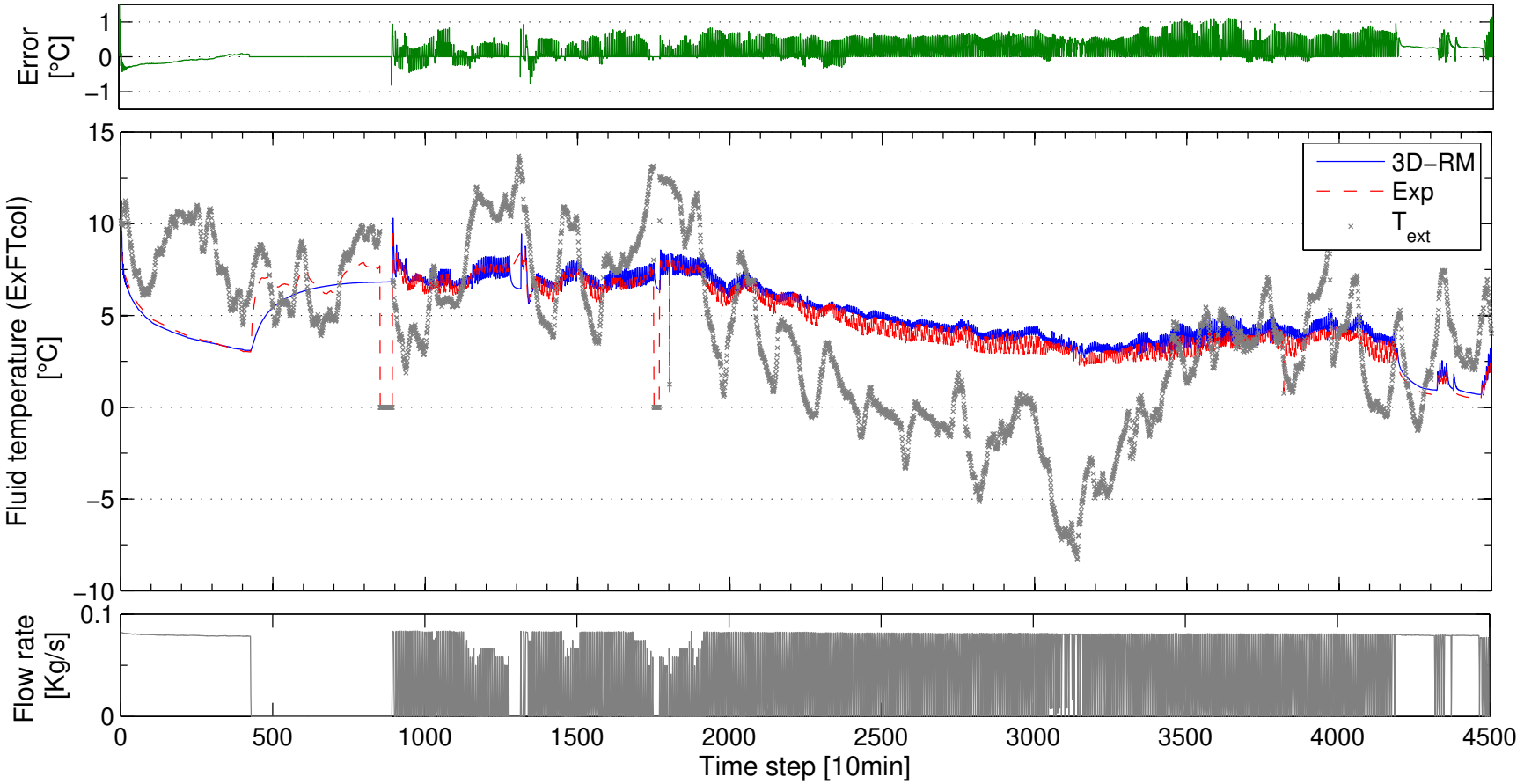

Figure 4.12: Comparison of ExFTcol during one-month simulation in a 10-minutes time step

Additionally, the fluid temperature variation inside a U-tube is plotted in Fig. 4.13. This result gives a good agreement with the typical exponential evolution. The distribution of temperature evolution between the two legs of the U-tube is similar as found in the well-known models [Lamarche *et al.* 2010] [Lee & Lam 2008], showing a lager temperature change in the downward flow than in the upward one.

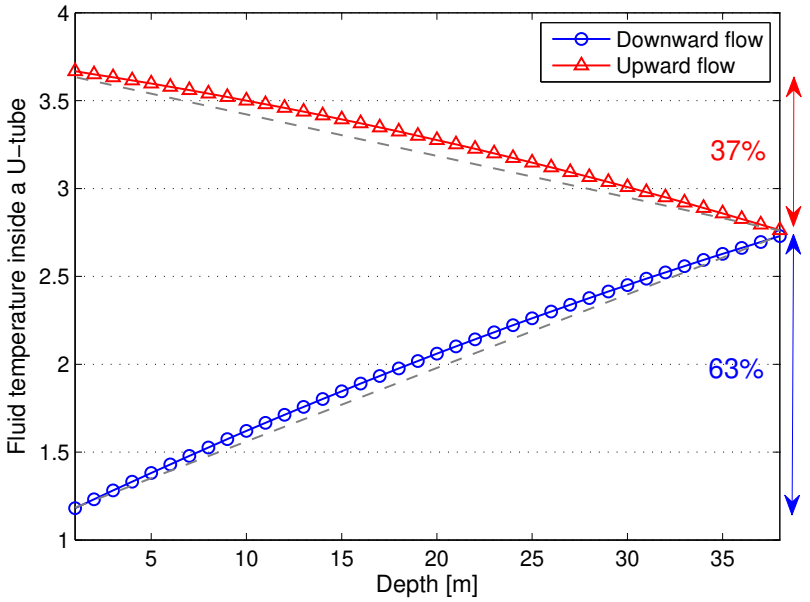

Figure 4.13: Fluid temperature variation inside a U-tube when the simulation time step is 300)

4.3.1.2 Error analysis

The main source of errors can be found when zooming Fig. 4.12. Fig. 4.14 shows a magnification of time steps 3500-3540 where maximum errors are found. This figure highlights the averaging effect of averaging values for 10 min particularly for flow rates where the square signal is clearly out of shape. In addition, fluid models of both 3D-RM (borehole part) and connexion part are not totally linked but separately solved then coupled. Therefore, simulation responses are shifted during some periods.

To verify the real influence of time-step on the results, the original experimental data, recorded each minute, are compared to simulation results obtained with a time-step of 1 min for the "critical" period (3500-3540) as shown in Fig. 4.15. The maximum errors are in a whole less than 0.5 ˚C and the dynamic behavior is reproduced more accurately than with a 10min time step. Obviously, this one-min time step gives more accurate results for other periods.

Fig. 4.16 highlights the second source of difference between 3D-RM and experimentation results. As explained above, the calculated value of ExFTcol corresponds to the fluid temperature at the end of the horizontal connexion pipe, 1m deep while the measured value is the fluid temperature in the manifold, positioned in a well exposed to the ambient temperature. When the heat pump is ON, the fluid velocity is high enough to prevent its temperature to be influenced by the ambient one. On the contrary, when the

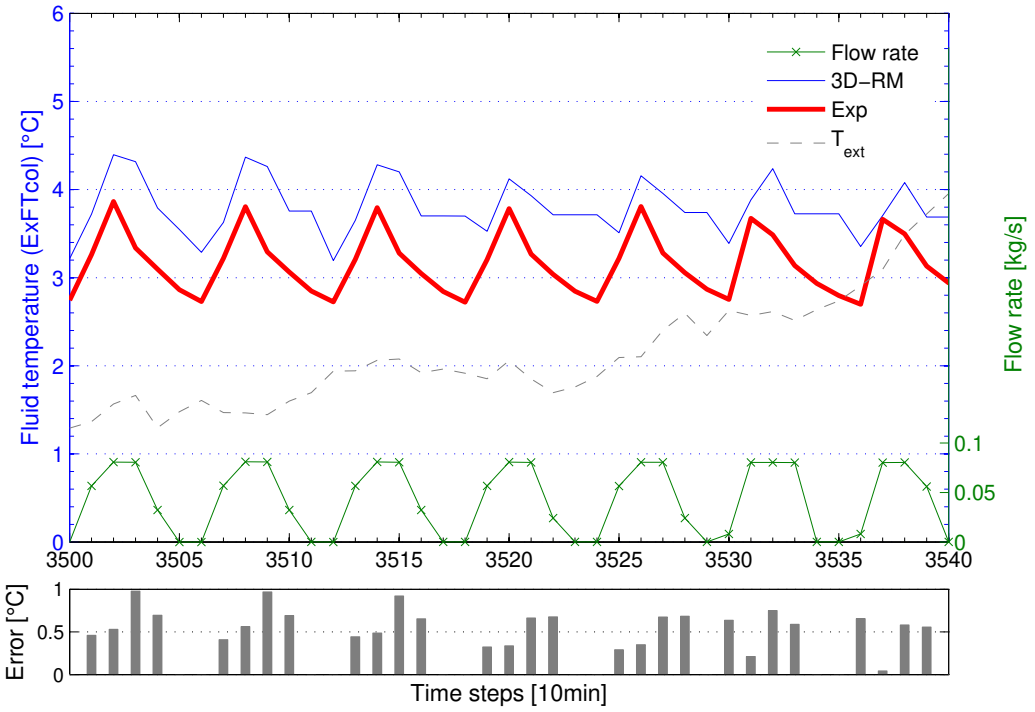

Figure 4.14: Zoom of time steps 3500-3540 of Fig. 4.12

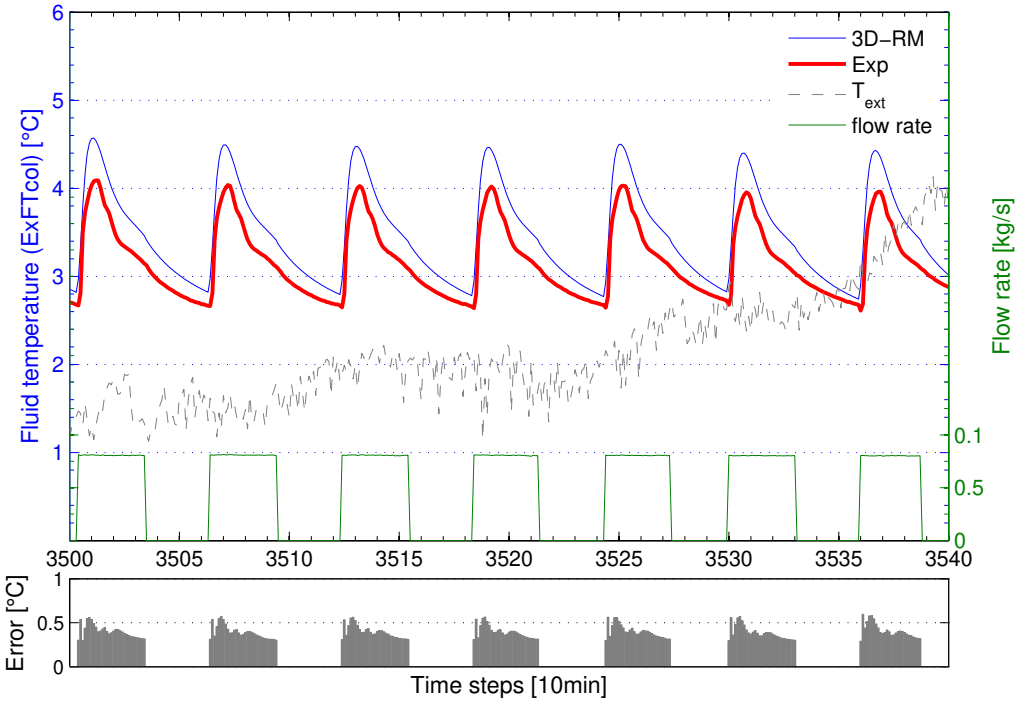

Figure 4.15: One-minute simulation for the period 3500-3540

heat pump is OFF, the fluid stagnates in the manifold and its temperature can be influenced by the ambient one. This behavior is particularly visible in Fig. 4.16 and 4.17 where ExFTcol values are similar when the fluid circulates and quite different, with a derivation of the experimental value, when the fluid is stopped. It can be noticed in Fig. 4.17 that as soon as the HP starts, experimental and simulation values of ExFTcol meet very well.

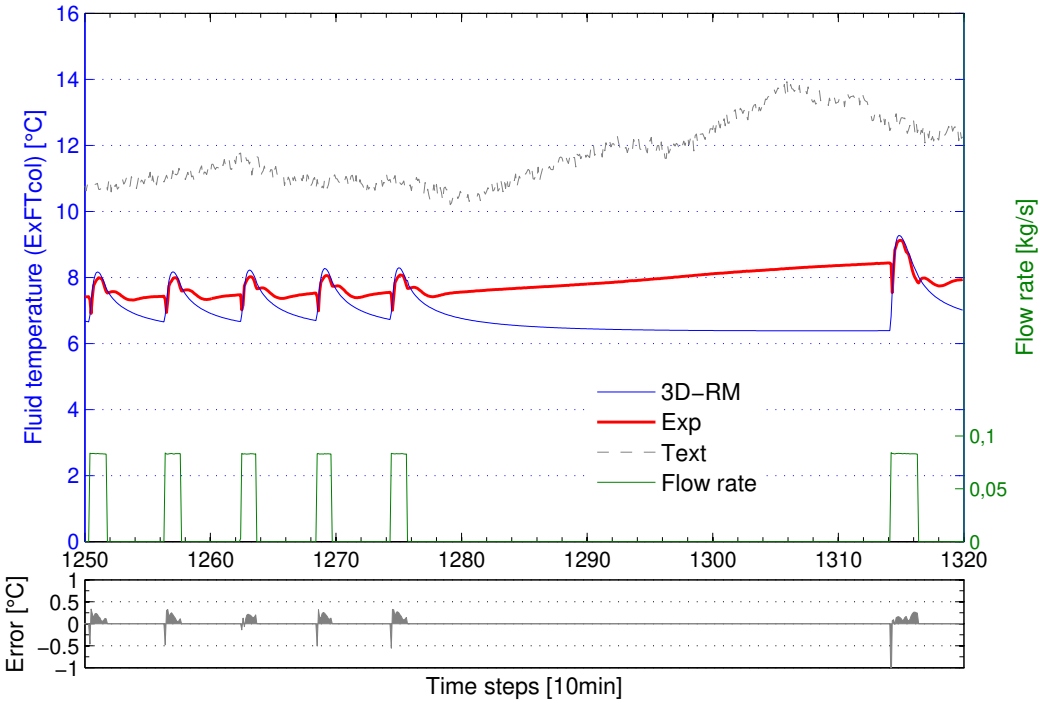

Figure 4.16: One-minute simulation for the period 1250-1320

These last three figures (4.15, 4.16, 4.17) show that 3D-RM coupled with a connexion pipe model reproduces very accurately the fluid evolution in the borehole field, in particular when the simulation time-step is small enough as the measuring interval, avoiding unrealistic flow rate values.

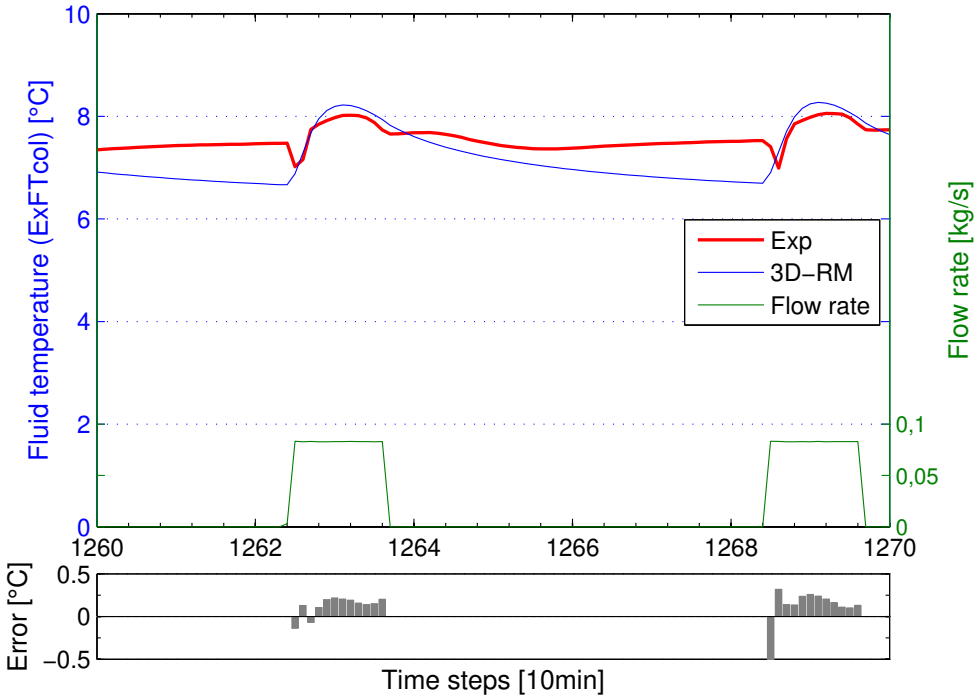

Figure 4.17: Zoom of time steps 1260-1270 of Fig. 4.16

4.3.2 Temperatures in the borehole

As the 3D-RM was developed to accurately estimate the temperature distribution in the borehole, a comparison of experimental and calculated wall pipes temperatures is presented in this part.

4.3.2.1 Simulation principle

For each slice, the 3D-RM calculates 8 wall temperatures for each pipe of a U-tube, as seen in Fig. 4.18.

Two cases are considered for calculation of fluxes on the pipe wall: case 1 and case 2. For both cases, an average temperature of pipe wall $\overline{T_p}$ is used to calculate the fluid temperature T_f. The fluid model for T_f is assumed as a lumped capacity model. Therefore, the fluid temperature is regarded to be equal inside the fluid control volume.

Then, for the case 1, the fluxes are equally imposed on each segment of wall by calculating an average flux from $\overline{T_p}$, as seen in Fig. 4.19, left part. This case of flux calculation is the most common one in geothermal modeling, and it is currently used in the 3D-RM. Recently, in a detailed model [Li & Zheng 2009] using fine meshes, this assumption was used and validated with fluid temperatures.

In the case 2 (right part of Fig. 4.19), different fluxes are calculated for each segment of wall. To simulate this case, the 3D-RM has been modified so that the fluxes can be calculated from each T_p instead of $\overline{T_p}$. Even if this case seems to be more realistic, it remains an approximation as the mean fluid temperature is used, as for case 1, for estimating the fluxes on the wall circumference.

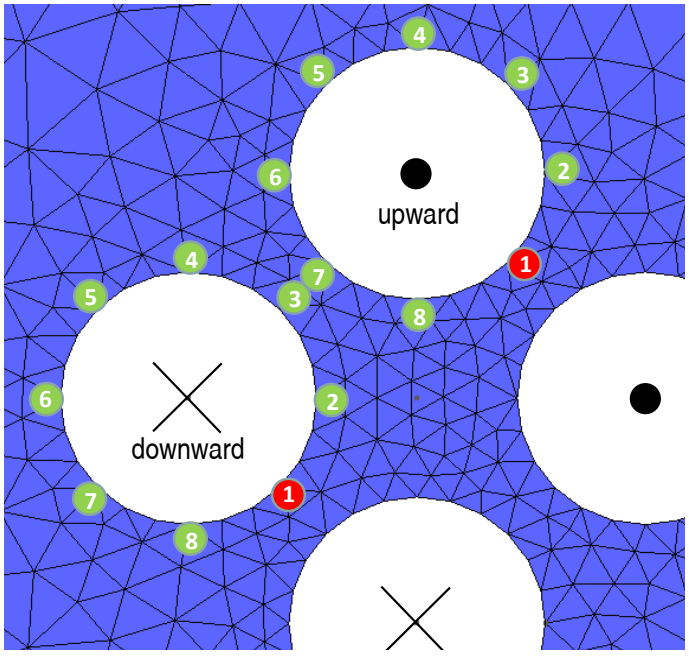

Figure 4.18: Numbering of measuring points around the pipe wall

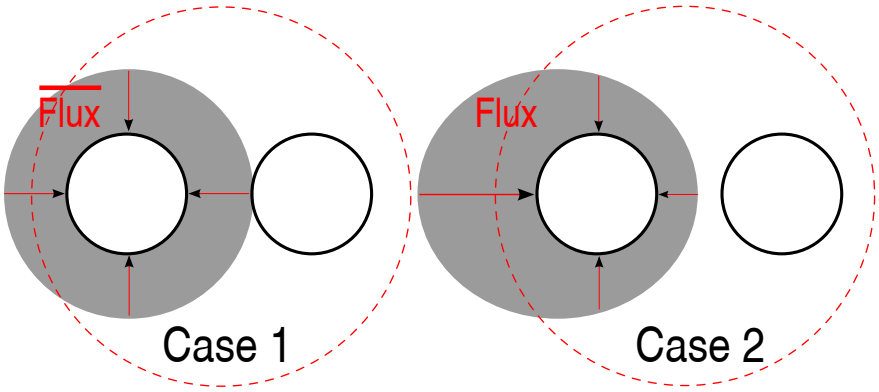

Figure 4.19: Schematic of different cases in calculating fluxes

Fig. 4.20 shows, in both cases, the distribution of temperature around the wall pipes circumference for a depth of 10m as an example. The upper part of the figure refers to the case 1 and the lower part to the case 2. The left part concerns the downward pipe while the right curves concern the upward one. This figure clearly illustrates the thermal interferences between pipes with the minimum values of temperature found in the inner part of the borehole : points 1 and 2 for the downward pipe and points 7 and 8 for the upward pipe.

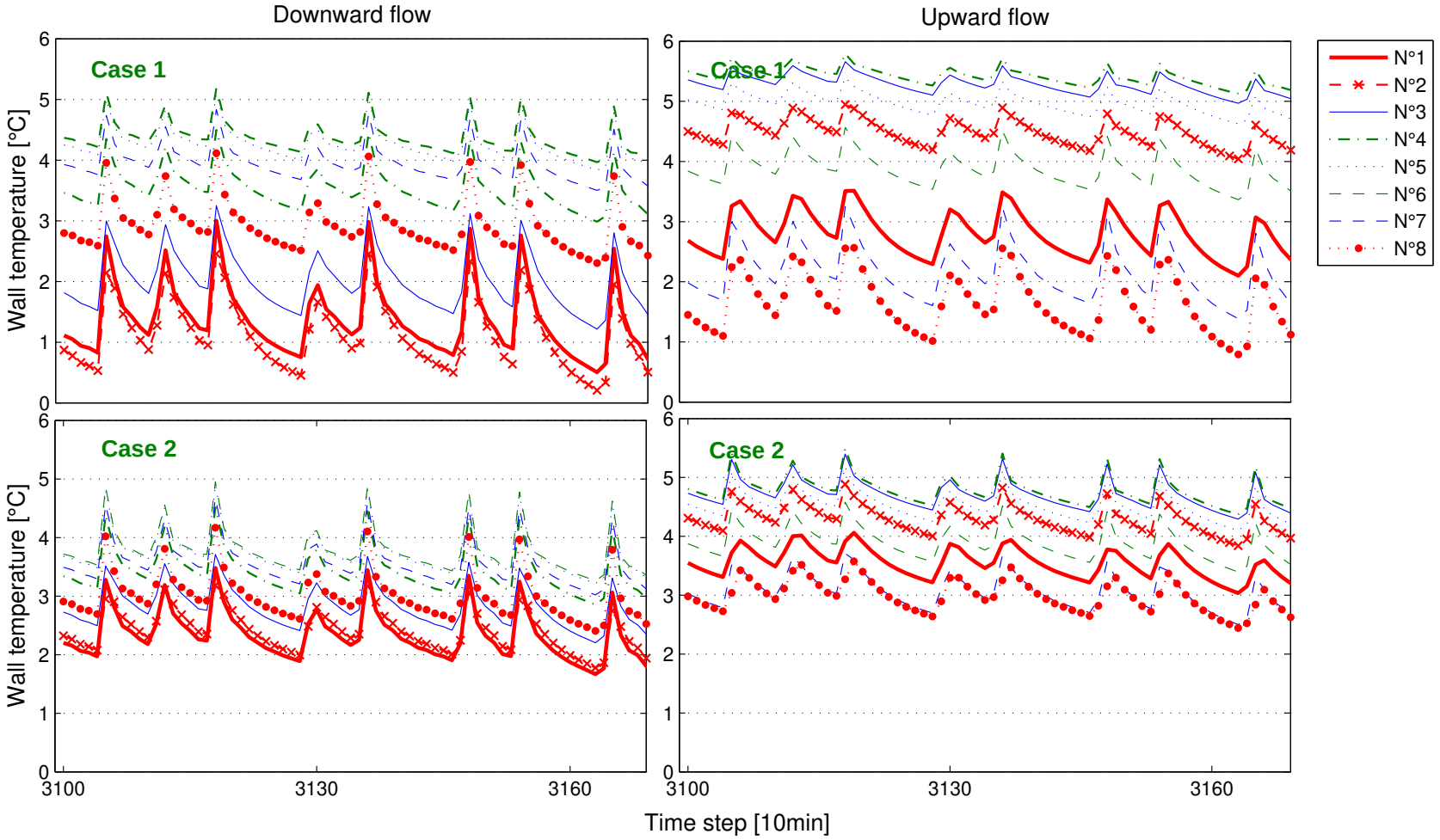

Figure 4.20: Temperature distribution in two cases at a depth of 10m

4.3.2.2 Results comparison

The simulated results coming from the two cases explained above are compared each others and with experimental results, that are given for different depths (z): 2, 5, 10, 35, and 38.5 m, corresponding respectively to Fig. 4.21 to 4.25. For all the figures, a typical period of 700 min is chosen (3100 to 3170 with a time-step of 10 min).

Although the temperature sensors are expected to be placed close to the point $n°1$ of Fig. 4.18, such a position can not be ensured to be kept during inserting U-tubes and grouting operations. This position can have moved between at least points $n°2$ and $n°8$. Then, the experimental data are compared with simulation ones for $n°1$, $n°2$, and $n°8$.

In the following figures, as for Fig. 4.20, the upper part refers to the case 1, the lower part to the case 2, the left part to the downward pipe and the right part to the upward one. Some interesting results can be highlighted:

1. The experimental values of wall pipes temperatures are effectively included between calculated values of $n°2$ and $n°8$ even if the upward pipe values in case 2 are slightly higher than experimental ones. In particular, in case 1, the experimental values are positioned between points $n°1$ and $n°8$ for the downward pipe and between points $n°1$ and $n°2$ for the upward pipe. These simulation results, consisting in finding the temperature sensors position, can be considered as a first validation of the 3D-RM.

2. As expected, the wall temperatures of downward pipe are lower than upward pipes ones, meaning that more fluxes are absorbed in the downward pipe. This difference decreases in deeper zone where the fluid temperatures in the two pipes are very close (cf. Fig. 4.13).

3. The case 1 induces more scattered curves compared to the case 2. This is an expected result that the build-up effect of temperature is stronger in the inner grout part of case 1 as the temperature distribution around the tube can not affect flux distribution.

These experimental data do not permit to choose and validate a calculation method for heat flux (cases 1 or 2). These two cases are designed to give different distributions of fluxes and consequently temperatures. To accurately compare these methods, an experimental set-up which permits the temperature measurement on the pipe circumference is necessary.

However, for average pipe wall temperatures and fluid ones, both cases give almost the same results. Fig. 4.26 shows the average pipe wall temperatures at the measuring depths for the two cases. The results are quite similar even if the case 2 provides slightly higher temperatures. Fig 4.27 compares the results of case 1 and case 2 in terms of outlet fluid temperature (ExFTcol). The two approaches are also very similar, with error less than 0.2˚C, and 0.1˚C in average.

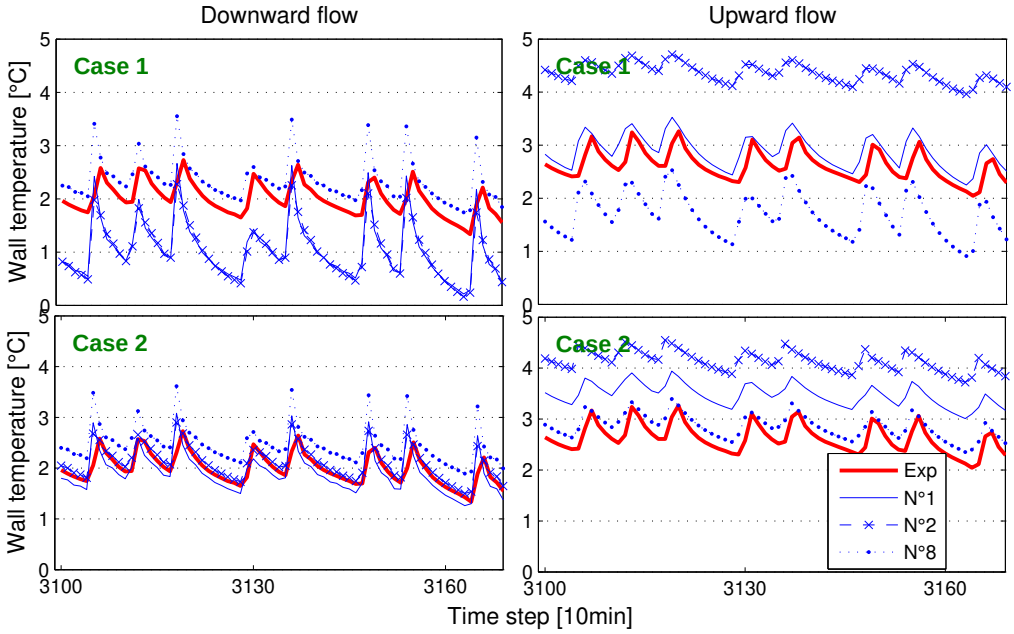

Figure 4.21: Tube wall temperatures for different cases at z=2m

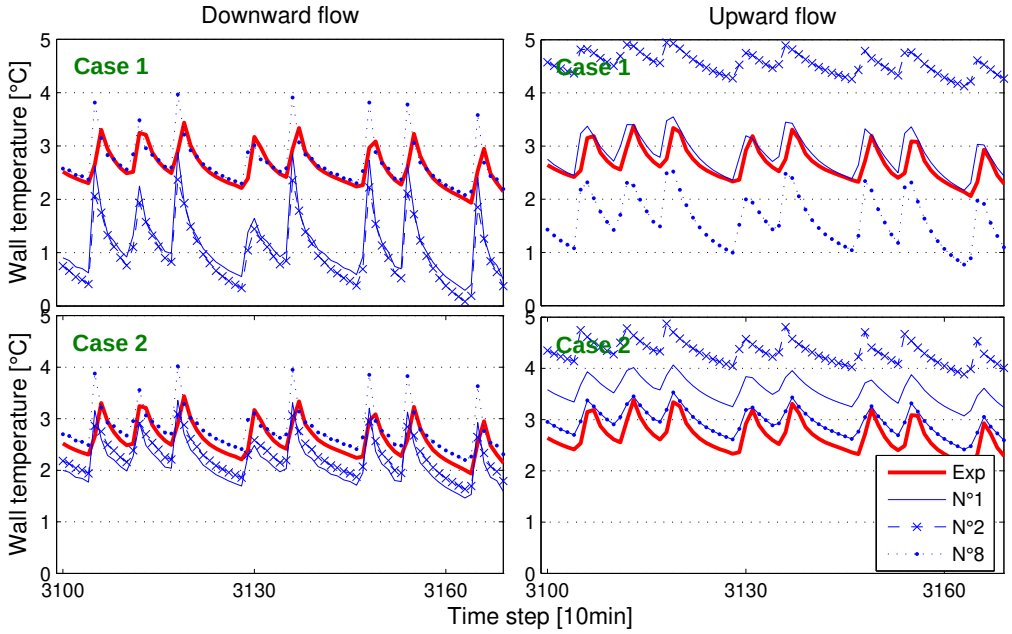

Figure 4.22: Tube wall temperatures for different cases at z=5m

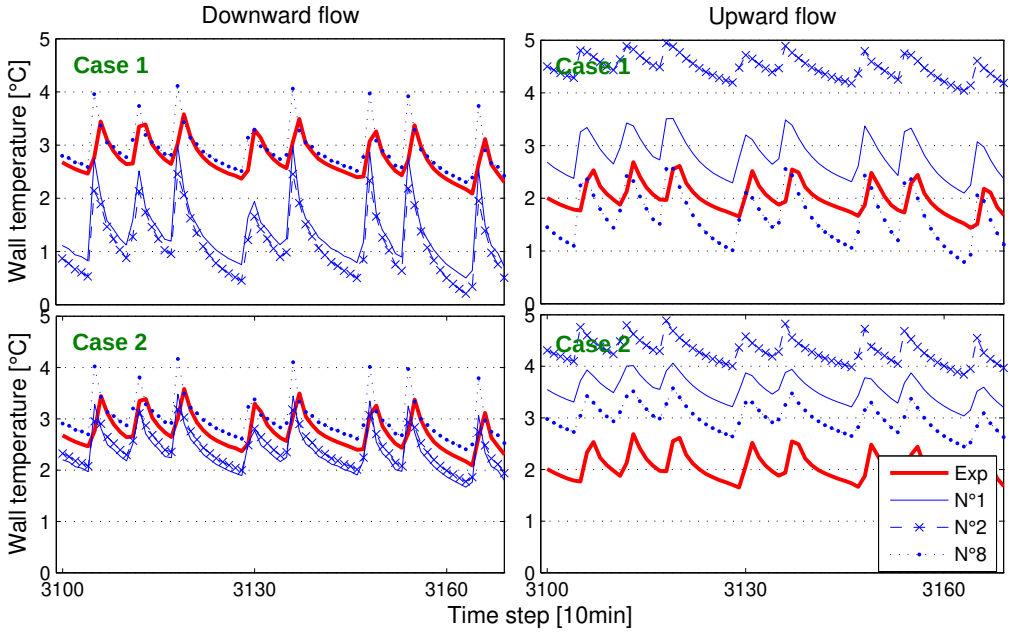

Figure 4.23: Tube wall temperatures for different cases at z=10m

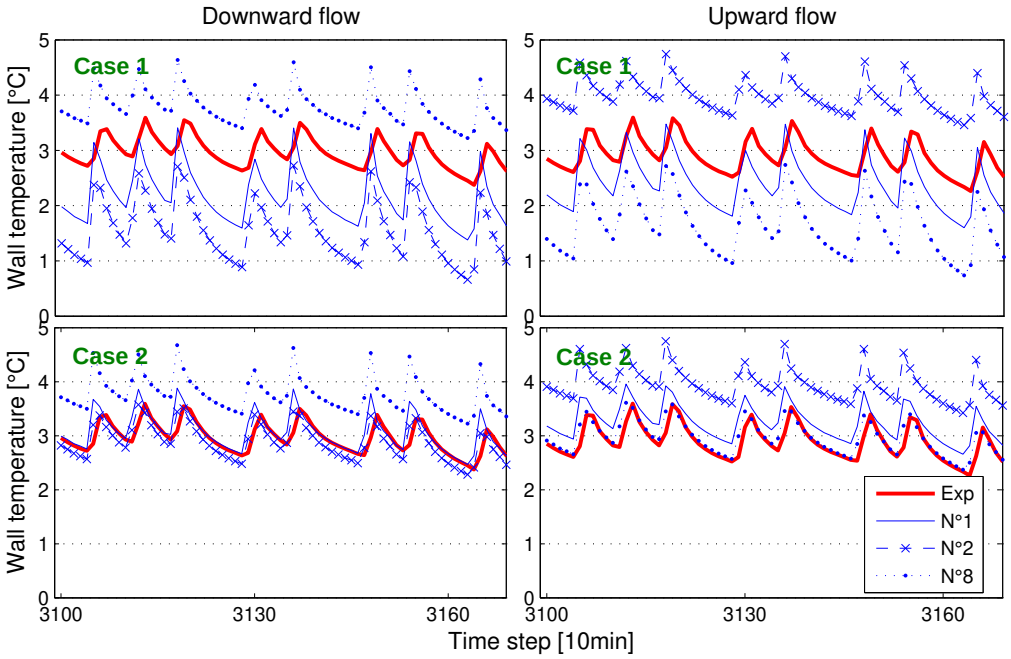

Figure 4.24: Tube wall temperatures for different cases at z=35m

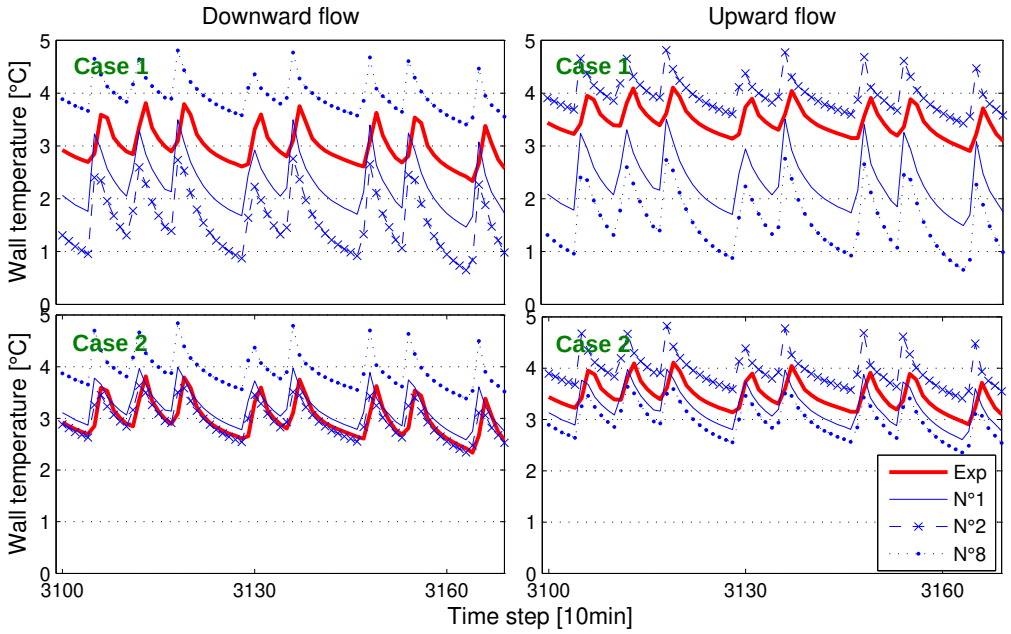

Figure 4.25: Tube wall temperatures for different cases at z=38.5m

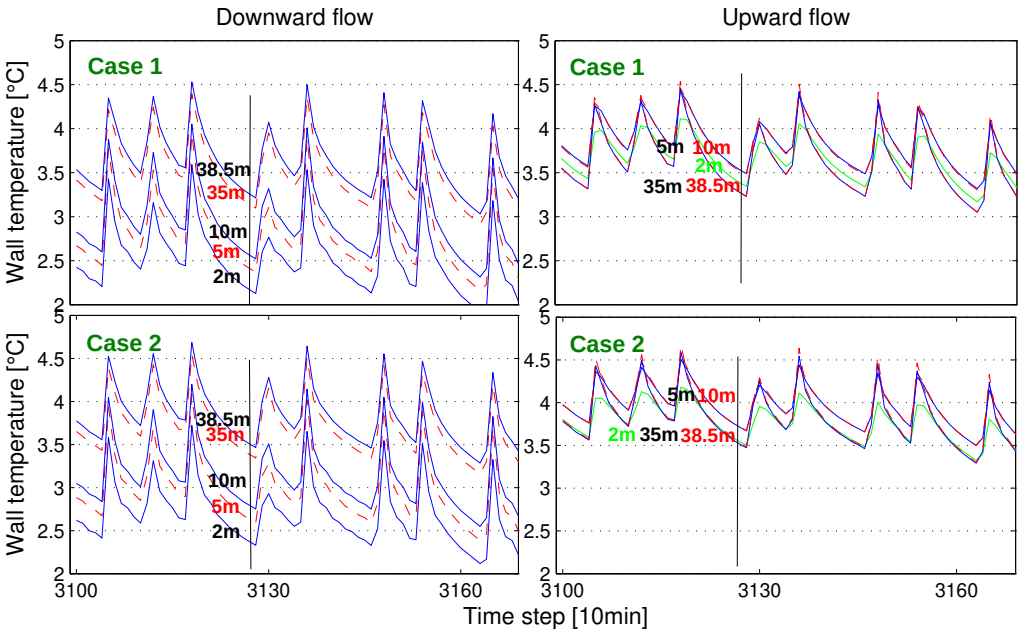

Figure 4.26: Tube wall average temperatures for different cases

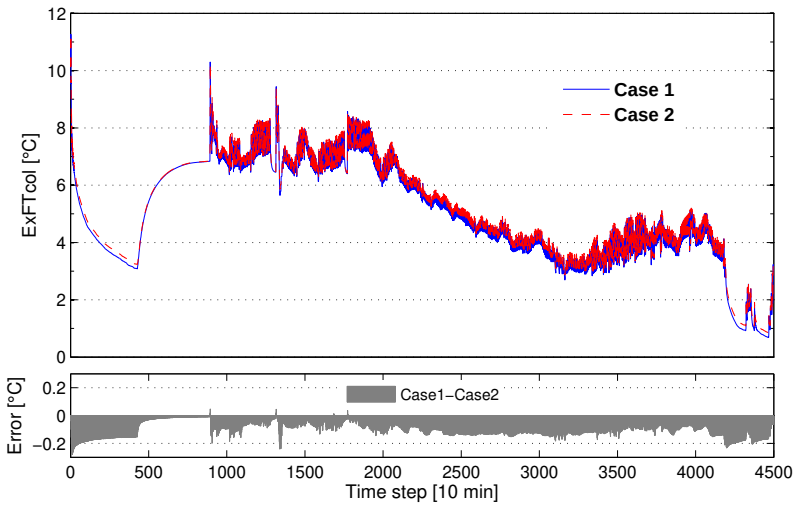

Figure 4.27: Comparison of ExFTcol for the different cases

4.3.3 Comparison between CM and RM

Although the 3D-RM showed its pertinence in the previous sections, it is meaningful to still test the model in terms of the applied approaches such as the model reduction and the domain decomposing-coupling. To test errors due to the methods mentioned, different versions of the 3D-RM are compared at ExFTcol. Complete models (CM) that do not truncate any modes, i.e. without reducing, are used in two cases: 3 different time steps case and a single time step case in order to test temporal-coupling errors. Fig. 4.28 gives simulation results for three cases: 3D-RM, 3D-CM_{3dts}, and 3D-CM_{1dt}.

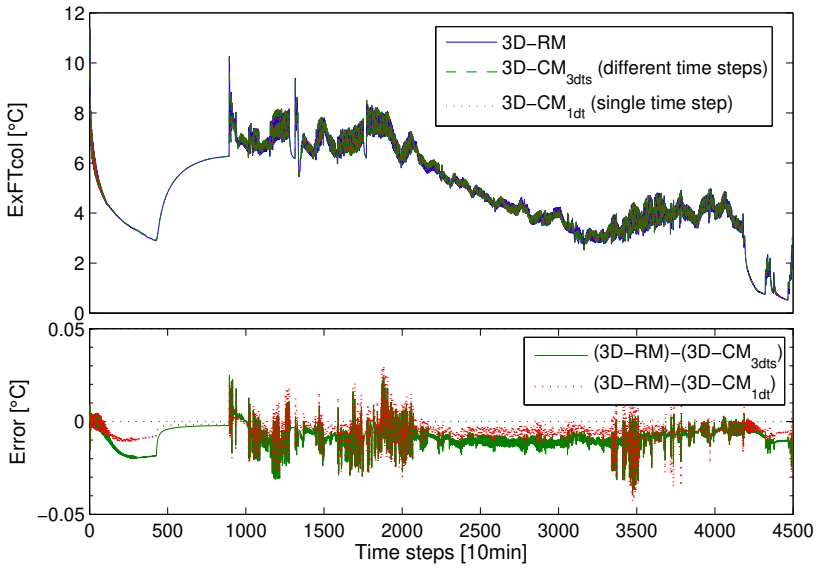

Figure 4.28: Comparison of ExFTcol for the different cases

As shown in the figure, the maximum error is less than 0.05 ˚C that is regarded as totally negligible in the GHE modeling even if errors are apparently found in mode-

reducing and domain-coupling.

For the 3D-RM, about 20% modes are selected to simulate this case, giving 219/990; it gives 40/664, 46/179, and 133/147 for each sub-zone slice model. Although the CPU time cannot be compared in each simualtion as the connenction soil model is not treated by the reduction technique, the 3D-RM is apparently more rapid than 3D-CM_{3dts}, and it is even more efficient when compared with 3D-CM_{1dt}.

Chapter 5

Model simulation

5.1 Validation and comparison with OSU experimental data

As shown in the section of literature review, the existing models give different results on ExFT. Permitted from the authors, the figure (1.18) has been reproduced by the developped models in this thesis. The simulation parameters and defined models are presented in AnnexF.

Fig. 5.1 a) shows simulation results on a typical day after about 6-months operation of system. The original figure (see figure-b) is also presented for comparison.

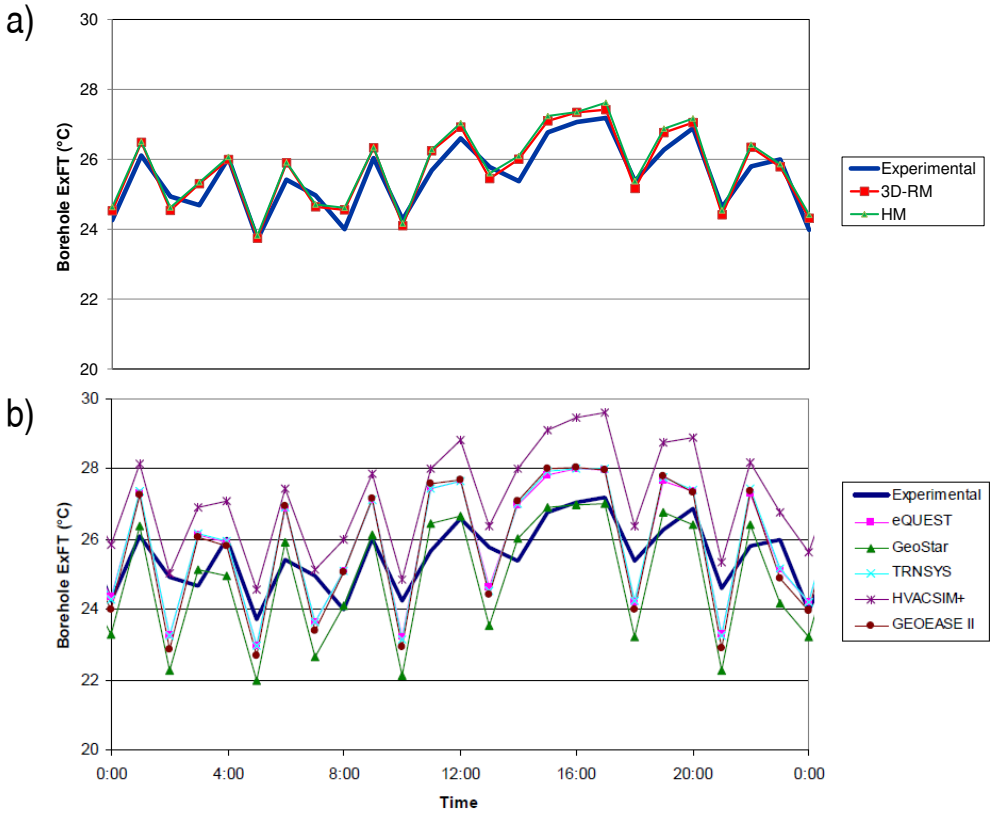

Figure 5.1: a) Simulation results of our models b) Different results of existing models

As shown in this figure, the developed models give very similar results with the experimental curve for ExFT in contrary to the other models. It is mainly due to the fact that most existing models did not consider the thermal capacity effect inside boreholes.

5.2 TRNSYS simulations

In order to test the actual impact of different models on the GCHP performance, a realistic but typical case in the TRNSYS [Klein *et al.* 2006] is simulated. The 3D-RM is used for this simulation together with the TRNSYS models that have also been used for testing HM (Section 3.4). However, the type 451 considers 2 U-Tubes. Thus, tube diameters were modified to make it an equivalent one-U-tube case.

For the simulation, a well-insulated family house located in Montréal, Canada was selected. A commercially available geothermal heat pump (water/air) was selected to cover at least 70% of the building thermal loads. This resulted in a maximum heating load of 5.27 kW with a corresponding heat pump capacity of 4.04 kW. For assuring thermal comfort, an auxiliary heater was added for use when the heat pump capacity is insufficient. The indoor air temperature was set at 20˚C for heating and 25˚C for cooling. The main characteristics of the GHE are given in Tab. 5.1. A commercially available heat pump was selected. The variation of the COP of the heat pump is presented in Figure 1 as a function of the entering fluid temperature to the heat pump in both heating and cooling.

Table 5.1: Simulation parameter

Parameter	Unit	Value
GHE length	m	100
GHE radius	m	0.055
U-tube outer radius	m	0.016
U-tube inner radius	m	0.013
Distance for tube centre from GHE centre	m	0.03
Number of U-tubes inside BHE		1
Total dimension of ground radius	m	100
Ground model depth	m	150
Sub-zone height, Δz	m	5
Time step ratios for the sub-zones		$1:6:24:168$
Ground thermal conductivity	W/m˚C	1.9
Ground thermal diffusivity	m^2/s	1.62×10^{-6}
Grout thermal conductivity	W/m˚C	1.3
Fluid mass flowrate	kg/s	0.3
Fluid heat capacity	J/kg ˚C	4190
Fluid density	kg/m^3	1000

Fig. 5.3 shows a comparison of the thermal responses between the DST, type 451, and 3D-RM models for a 140 hour period in January (Fig. 5.3). A zoomed portion is provided in Fig. 5.4. A 10 minutes time step was used in all cases. All three cases used the same inlet fluid temperature (shown as one of the curves in Fig. 5.3) obtained from a preliminary simulation. As indicated in both figures, the mass flow rate is either 0.3

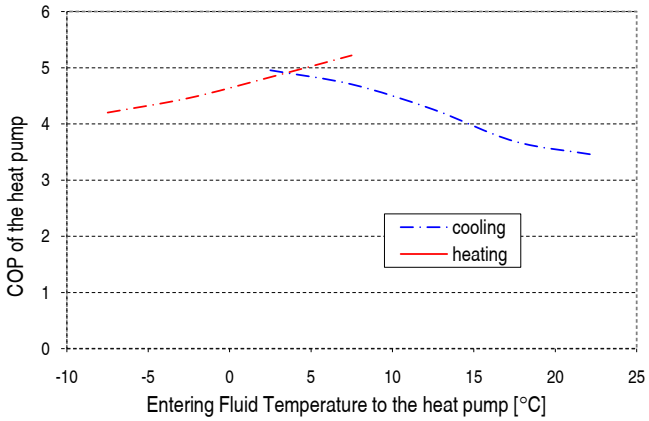

Figure 5.2: COP of the heat pump as a function of the entering fluid temperature

kg/s when the heat pump is operating or 0 when it is off. During the first 18 hours, the heat pump is cycling and the outlet fluid temperatures predicted by the three models are in very good agreement. Fig. 5.3 also shows other periods of cycling with similar agreement. When the heat pump is off for a significant amount of time (such as around the 420th hour), the 3D-RM and type 451 model (which both account for grout capacity) are in close agreement but they differ from the DST model (which do not account for grout capacity). When the heat pump is starting up (see near the 510th hour in Fig. 5.4), the 3D-RM and the type 451 predictions are in close agreement but they exhibit a difference of some 1˚C with the DST model. Again, thermal capacity is responsible for this discrepancy.

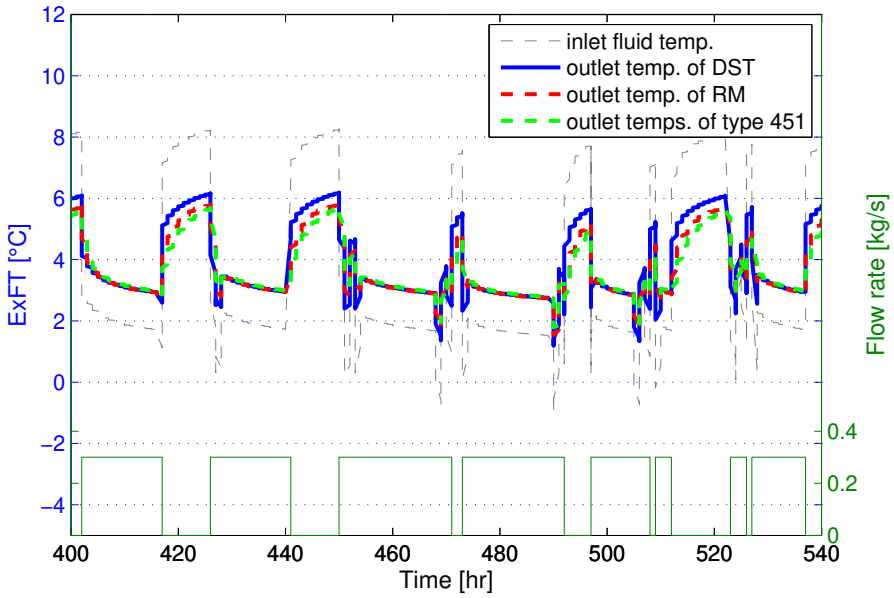

Figure 5.3: Simulation comparison between DST / RM / type 451

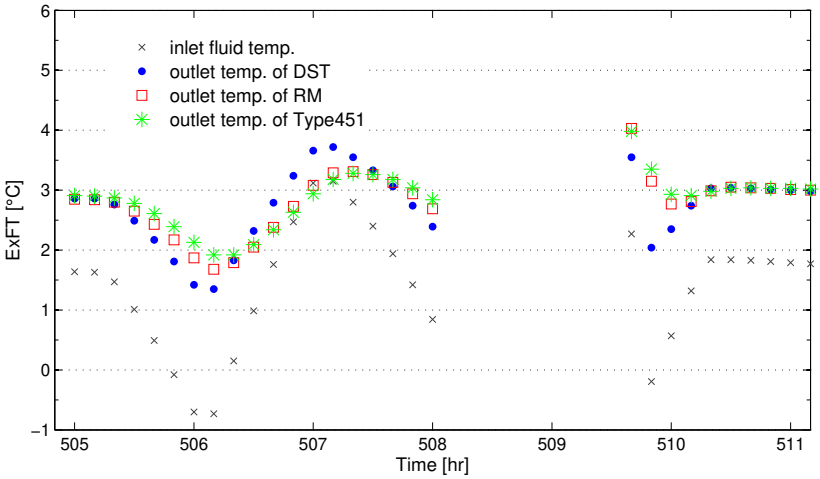

Figure 5.4: zoomed portion around the 508th hour

Annual simulations for the different models were also carried out by letting each system determine its inlet and outlet fluid temperatures (recall that in Fig. 5.3, the same inlet fluid temperatures were used). Fig. 5.5 shows the resulting inlet fluid temperature to the heat pump for a particular day in December. The DST model exhibits large fluctuations while the other two models show much smaller amplitude due to the capacity effects. Tab. 5.2 shows the annual energy consumption of the same system but for three different borehole models. As shown in this table the differences are not significant. Nonetheless, the DST model predicts a slightly higher annual energy consumption than the other two models. This is due to the fact that the DST model predicts, on average, lower inlet fluid temperatures to the heat pump when it is operating which leads to lower COP and corresponding higher energy consumption. However, despite these differences, the annual energy consumption is approximately the same for the DST and 3D-RM model, indicating that grout capacity might not be significant in terms of annual heat pump energy consumption.

Table 5.2: Total energy consumption

Model	Total heat transfered to/from house [kWh]	Heat pump energy consumption [kWh]	Auxiliary heater [kWh]	Average COP
DST	12517	2777	60	4.41
RM	12528	2698	73	4.52
Type 451	12524	2698	65	4.53

From these results, it can be concluded that the common hypothesis given for DST model are largely acceptable to use for simulation particularly in calculation of energy consumption of a typical case. This result also confirms the error range 2˚C of fluid temperatures as a acceptable one in evaluating HP energy consumption [Bernier *et al.* 2007] as briefly mentioned in the literature review.

Although the fluctuated behavior of a model around an average value (see DST model curve in Fig. 5.5) is acceptable for the annual estimation of energy consumption, it is not

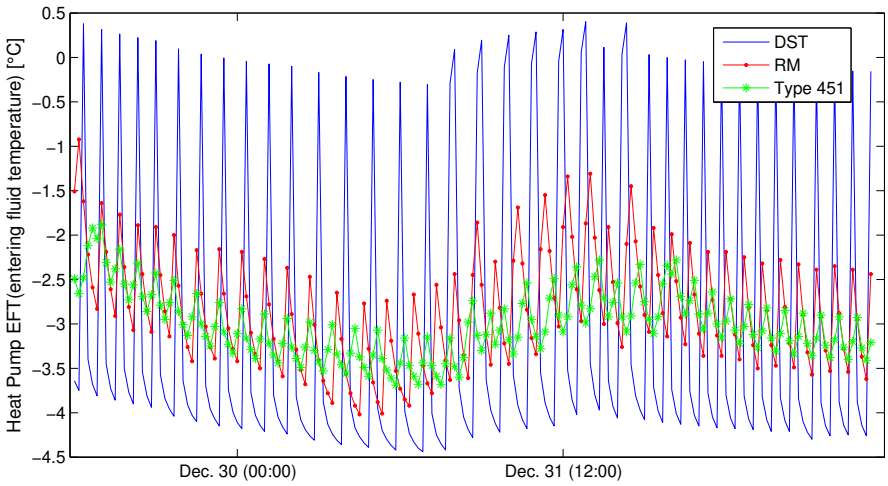

Figure 5.5: Heat pump EFTs comparison between the models

evident that the similar results can be found in dynamic cases such as recharging GCHP system and etc. In addition, the accurate impact on the ground particularly around boreholes can not be investigated by common models.

Conclusion and Perpectives

In France, the high capital cost of Ground Heat Exchangers (GHE) installation is one of the main market barriers for the development of Ground Coupled Heat Pumps (GCHP), particularly for existing buildings. Consequently, various studies on reducing GHE sizing and thus the total system cost are widely carried out. However, appropriate GHE sizing is critical for long-term performances of GCHP and soil protection. Then, efforts to reduce the required GHE length must be carefully evaluated with reliable simulations that accurately predict transient phenomena inside and around GHEs. Thus, a model should be able to reproduce the fast dynamics of GHEs occurring within a short time over a long period (at least several months). The development of such a model was the purpose of this work.

A new numerical 3D model (3D-RM) has been developed using different methodologies that permit to efficiently reduce calculation time and computer memory. Unstructured meshes described the borehole/ soil domain in detail to enhance model precision with no hypotheses commonly used for the GHE modeling. The state model reduction technique has been applied in the finite element method (FEM). Since the state model reduction techniques are generally sensitive to the given simulation time step, the soil domain has been decomposed in order to adopt different time-steps for each sub-domain. This is allowed as the domain includes different time scales with distinct dimensions (from pipes to a large soil volume of far-field). New coupling methods have been proposed and validated in this work as well.

This model 3D-RM has been validated comparing experimental results obtained from a test set-up in a natural climate. The results show that the model is relevant to precisely predict temperatures inside GHEs and in the vicinity of the GHEs as well as fluid temperature variation even in a very short time step. This implies that further improvement of the developed model is needed in terms of computing time to accurately calculate the fluid temperatures for simulations of long-period system operation.

This validation highlights scattered variation of temperatures inside the borehole. A temperature difference of some degree is found in the inner-grout part. This result shows that an accurate model, capable to predict temperature distribution inside the borehole is needed for finely evaluating thermal behavior of GHE. In particular, so-called critical zones suspected to have frost damage due to unexpected thermal conditions can be detected with this model 3D-RM.

On the other hand, a hybrid model (HM) has been developed using analytical and numerical approaches as part of this work. This HM is composed of a simplified fluid model, a numerical borehole model, and the thermal response of bore field obtained from well-known analytical solutions. It was originated to predict global parameters such as fluid temperatures more rapidly than the 3D-RM.

Although both developed models give better results in short time steps than the other

classical models, each can be distinctly used as different capacity and features are found for each model. The HM, thanks to its rapidity, is able to simulate global parameters over long periods of simulation. This makes this model suitable to evaluate the annual heat pump performances even over several years. The HM is also rapid enough to be used for control strategy of GCHP. The 3D-RM is more adequate to precisely investigate boreholes parameters, heat transfer inside boreholes, and thermal impact on the surrounding ground. Actually, sizing evaluation of GHEs for so-called "hybrid" system configuration (e.g. direct solar-recharging) or detailed simulations of innovative GHEs are expected to be carried out with the 3D-RM.

Finally, the development of the 3D-RM can be an initiation to accurately model the typical GHEs whether it is horizontal, vertical or else within an acceptable computing time. In fact, the 3D-RM can easily be modified for horizontal ground heat exchangers or air-to-ground exchangers. With respect to the reduction techniques, it is hoped that the proposed methodologies in this work can contribute to modeling of various large systems.

Bibliography

[Aoki 1968] M. Aoki. *Control of Large-Scale Dynamic Systems by Aggregation*. IEEE Transactions Automatic Control, vol. AC 13, no. 3, 1968.

[Bacot *et al.* 1984] P. Bacot, A. Neveu and J. Sicard. *Analyse modale des phénomènes thermiques en régime variable dans le bâtiment*. Revue Générale de Thermique, no. 267, pages 189 – 201, 1984.

[Barrio *et al.* 2000] Elena Palomo Del Barrio, Gilles Lefebvre, Philippe Behar and Noël Bailly. *Using model size reduction techniques for thermal control applications in buildings*. Energy and Buildings, vol. 33, no. 1, pages 1 – 14, 2000.

[Barrio 1999] E. Palomo Del Barrio. *Roof components models simplification via statistical linearisation and model reduction techniques*. Energy and Buildings, vol. 29, no. 3, pages 259 – 281, 1999.

[Bennet *et al.* 1987] J. Bennet, J. Claesson and G. Hellström. *Multipole Method to Compute the Conductive Heat Transfer to and between Pipes in a Composite Cylinder*. Technical report Notes on Heat Transfer 3-1987, Department of Building Physics, Lund Institute of Technology, Lund, Sweden, 1987.

[Bernier & Shirazi 2007] M. Bernier and A. S. Shirazi. *Solar heat injection into boreholes: A preliminary analysis*. In 2nd Canadian Solar Buildings Conference, Calgary, Canada, June 10-14 2007.

[Bernier *et al.* 2004] M. A. Bernier, R. Labib, P. Pinel and R. Paillot. *A Multiple Load Aggregation Algorithm for Annual Hourly Simulations of GCHP systems*. HVAC & R Research, vol. 10, no. 4, pages 471 – 487, 2004.

[Bernier *et al.* 2007] M. Bernier, M. Kummert and S. Bertagnolio. *Development and application of test cases for comparing vertical ground heat exchanger models*. In Building Simulation 2007, pages 1462 – 1469, Beijing, China, 2007.

[Bernier 2001] M. A. Bernier. *Ground-coupled heat pump system simulation*. ASHRAE Transactions, vol. 106, no. 1, pages 605–616, 2001.

[Bernier 2006] M. A. Bernier. *Closed-Loop Ground-Coupled Heat Pump System*. ASHRAE Journal, vol. 48, no. 9, pages 12–19, 2006.

[Bierman 1972] G. J. Bierman. *Weighted least squares stationary approximations to linear systems*. IEEE Transactions Automatic Control, vol. AC 17, pages 752–761, 1972.

[Biyaali 1995] A. E. Biyaali. *Réduction des systèmes complexes multi-entrées multi-sorties application aux singularités thermiques dans les bâtiments*. Doctoral thesis, Faculté des sciences, Université Abdelmalek Essaadi, Tétouan, Morocco, 1995.

[Bose *et al.* 1985] J. E. Bose, J. D. Parker and F. C. McQuiston. *Design/ data manual for closed-loop ground-coupled heat pump systems*. Technical report, Atlanta, 1985.

[Bose 1984] J. Bose. *Closed Loop Ground-coupled Heat Pump Design Manual*. Technical report Engineering Technology Extension, Oklahoma State University, 1984.

[Carslaw & Jaeger 1947] H. S. Carslaw and J. C. Jaeger. Conduction of heat in solids. Oxford, 1947.

[Cauret & Bernier 2009] O. Cauret and M. Bernier. *Experimental validation of an underground compact collector model*. In Effstock 2009, numéro 44, Stockholm, 2009.

[Chapra & Canale 2002] S. C. Chapra and R. P. Canale. Numerical methods for engineers. McGraw-Hill, 4th édition, 2002.

[Chapuis & Bernier 2009] S. Chapuis and M. Bernier. *Seasonal storage of solar energy in borehole heat exchangers*. In Building Simulation 2009, pages 599–606, Glasgow, Scotland, July 2009.

[Chen 1989] M. Chen. *Nouvelle solution modale pour des parois de bâtiments*. Doctoral thesis, Ecole des Mines de Paris, France, 1989.

[Chiasson & Yavuzturk 2003] A. Chiasson and C. Yavuzturk. *Assessment of the viability of hybrid geothermal heat pump systems with solar thermal collectors*. ASHRAE Transactions, vol. 109, no. 2, pages 487–500, 2003.

[Claesson & Eskilson 1988] J. Claesson and P. Eskilson. *Conductive heat extraction to a deep borehole: Thermal analyses and dimensioning rules*. Energy, vol. 13, no. 6, pages 509 – 527, 1988.

[Costes & Peysson 2008] V. Costes and P. Peysson. Capteurs géothermiques verticaux enterrés: Validation expérimentale de nouveaux modèles développés dans l'environnement trnsys. Projet d'initiation à la recherche et au développement, INSA de Lyon, Lyon, France, 2008.

[Cui *et al.* 2008] P. Cui, H. Yang and Z. Fang. *Numerical analysis and experimental validation of heat transfer in ground heat exchangers in alternative operation modes*. Energy and Buildings, vol. 40, no. 6, pages 1060 – 1066, 2008.

[Demirdzic & Muzaferija 1995] I. Demirdzic and S. Muzaferija. *Numerical method for coupled fluid flow, heat transfer and stress analysis using unstructured moving meshes with cells of arbitrary topology*. Computer Methods in Applied Mechanics and Engineering, vol. 125, no. 1-4, pages 235 – 255, 1995.

[Dittus & Boelter 1930] FW Dittus and LMK Boelter. Technical report 2, Univ Calif (Berkeley) Pub Eng, 1930.

[Déqué *et al.* 2001] F. Déqué, F. Ollivier and J. J. Roux. *Effect of 2D modelling of thermal bridges on the energy performance of buildings: Numerical application on the Matisse apartment*. Energy and Buildings, vol. 33, no. 6, pages 583 – 587, 2001.

[Eitelberg 1982] E. Eitelberg. *Comments on a model reduction by minimizing the equation error*. IEEE Transactions Automatic Control, vol. AC 27, pages 1000–1002, 1982.

[Eskilson 1987] P. Eskilson. *Thermal Analysis of Heat Extraction Boreholes*. Doctoral thesis, Department of Mathematical Physics, University of Lund, Lund, Sweden, 1987.

[Fossard 1970] A. Fossard. *On a method for simplifying linear dynamic systems*. IEEE Transactions Automatic Control, vol. AC-15, pages 267 – 272, 1970.

[Gao *et al.* 2004] Y. Gao, J. J. Roux, C. Teodosiu and L. H. Zhao. *Reduced linear state model of hollow blocks walls, validation using hot box measurements*. Energy and Buildings, vol. 36, no. 11, pages 1107 – 1115, 2004.

[Gao *et al.* 2008] Y. Gao, J.J. Roux, L.H. Zhao and Y. Jiang. *Dynamical building simulation: A low order model for thermal bridges losses*. Energy and Buildings, vol. 40, no. 12, pages 2236 – 2243, 2008.

[Gehlin 2002] S. Gehlin. *Thermal Response Test - Method Development and Evaluation*. Doctoral thesis, Lulea University of Technology, Sweden, 2002.

[Glover 1984] K. Glover. *All optimal Hankel norm approximations of linear multivariable systems and their L_8-error bounds*. International Journal of Control, vol. 3, no. 6, pages 1115–1193, 1984.

[Gu & O'Neal 1998] Y. Gu and D. L. O'Neal. *Development of an equivalent diameter expression for vertical U-tubes used in ground-coupled heat pumps*. ASHRAE Transactions, vol. 104, pages 347–355, 1998.

[He *et al.* 2009] M. He, S. Rees and L. Shao. *Simulation of a domestic ground source heat pump system using a transient numerical borehole heat exchanger model*. In Building Simulation 2009, pages 607–614, Glasgow, Scotland, July 2009.

[Hellström 1989] G. Hellström. *Dunt Groud Heat Storage Model, Manual for Computer Code*. Technical report, Department of Mathematical Physics, University of Lund, Box 118, S-221 00 Lund, Sweden, 1989.

[Hellström 1991] Goran Hellström. *Ground Heat Storage; Thermal Analysis of Duct Storage Systems*. Doctoral thesis, Department of Mathematical Physics, University of Lund, Lund, Sweden, 1991.

[Huber & Schuler 1997] A. Huber and O. Schuler. *Berechnungsmodul für Erdwärmesonden*. Technical report ENET-Nr. 9658807, Forschungsprogramm UAW des BEW, Bern, 1997.

[Huebnet 2001] K. H. Huebnet. The finite element method for engineers. Wiley-interscience, 4th édition, 2001.

[Ingersoll & Plass 1948] L. R. Ingersoll and H. J. Plass. *Theory of the ground pipe heat source for the heat pump*. Heating, Piping and Air conditioning, vol. 20, pages 119–122, 1948.

[Ingersoll *et al.* 1954] L. R. Ingersoll, O. J. Zobel and A. C. Ingersoll. Heat conduction with engineering geological and other applications. Mc Graw-Hill, New York, NY, USA, second édition, 1954.

[Jaafar *et al.* 1990] M. T. Ben Jaafar, R. Pasquetti and D. Petit. *Model reduction for thermal diffusion: application to a heat transmission tube model*. International journal for numerical methods of engineering, 1990.

[Jun *et al.* 2009] L. Jun, Z. Xu, G. Jun and Y. Jie. *Evaluation of heat exchange rate of GHE in geothermal heat pump systems*. Renewable Energy, vol. 34, no. 12, pages 2898 – 2904, 2009.

[Kavanaugh & Rafferty 1997] S. P. Kavanaugh and K. Rafferty. Ground-source heat pumps: Design of geothermal systems for commercial and institutional buildings. Atlanta: American Society of Heating, Refrigerating and Air-Conditioning Engineers, Inc., 1997.

[Kavanaugh 1985] S. Kavanaugh. *Simulation and Experimental Verification of Vertical Ground-coupled Heat Pump System*. Doctoral thesis, Oklahoma State University, USA, 1985.

[Kim *et al.* 2009] E. J. Kim, J. J. Roux, M. Bernier and O. Cauret. *Problématique de la modélisation numérique d'échangeurs géothermiques verticaux*. In 9ème CIFQ sur la Thermique des Systèmes, pages 95 – 100, Lille, France, 2009.

[Kim *et al.* 2010a] E. J. Kim, J. J. Roux, M. Bernier and O. Cauret. *A new borehole heat exchanger (BHE) model based on state model reduction techniques analysis*. In Clima 2010 - 10th REHVA World Congress, Atalya, Turkey, 2010.

[Kim *et al.* 2010b] E. J. Kim, J. J. Roux, G. Rusaouen and F. Kuznik. *Numerical modelling of geothermal vertical heat exchangers for the short time analysis using the state model size reduction technique*. Applied Thermal Engineering, vol. 30, no. 6-7, pages 706 – 714, 2010.

[Klein *et al.* 2006] S. A. Klein, W. A. Beckman and J. W. Mitchell. Trnsys 16 - a transient system simulation program. Solar Energy Laboratory, University of Wisconsin, Madison, USA, 2006.

[Kummert & Bernier 2008] M. Kummert and M. Bernier. *Sub-hourly simulation of residential ground coupled heat pump systems*. Building Services Engineering Research and Technology, vol. 29, no. 1, pages 27–44, 2008.

[Lamarche & Beauchamp 2007a] L. Lamarche and B. Beauchamp. *A new contribution to the finite line-source model for geothermal boreholes*. Energy and Buildings, vol. 39, no. 2, pages 188 – 198, 2007.

[Lamarche & Beauchamp 2007b] L. Lamarche and B. Beauchamp. *New solutions for the short-time analysis of geothermal vertical boreholes*. International Journal of Heat and Mass Transfer, vol. 50, no. 7-8, pages 1408 – 1419, 2007.

[Lamarche *et al.* 2010] L. Lamarche, S. Kajl and B. Beauchamp. *A review of methods to evaluate borehole thermal resistances in geothermal heat-pump systems*. Geothermics, vol. 39, no. 2, pages 187 – 200, 2010.

[Lascaux & Theodor 1986] P. Lascaux and R. Theodor. Analyse numérique matricielle appliquée à l'art de l'ingénieur, volume 1 - 2. Masson, 1986.

[Lee & Lam 2008] C. K. Lee and H. N. Lam. *Computer simulation of borehole ground heat exchangers for geothermal heat pump systems*. Renewable Energy, vol. 33, no. 6, pages 1286 – 1296, 2008.

[Lefebvre 2007] G. Lefebvre. La méthode modale en thermique. Ellipses, 2007.

[Li & Zheng 2009] Z. Li and M. Zheng. *Development of a numerical model for the simulation of vertical U-tube ground heat exchangers*. Applied Thermal Engineering, vol. 29, no. 5-6, pages 920 – 924, 2009.

[Litz 1981] L. Litz. *Order reduction of linear state space model via optimal approximation of the non-dominant modes*. Large Scale System, no. 2, pages 171 – 184, 1981.

[Man *et al.* 2010] Y. Man, H. Yang and J. Wang. *Study on hybrid ground-coupled heat pump system for air-conditioning in hot-weather areas like Hong Kong*. Applied Energy, vol. 87, no. 9, pages 2826 – 2833, 2010.

[Marcotte & Pasquier 2008] D. Marcotte and P. Pasquier. *On the estimation of thermal resistance in borehole thermal conductivity test*. Renewable Energy, vol. 33, no. 11, pages 2407 – 2415, 2008.

[Marshall 1966] S. A. Marshall. *An approximate method for reducing the order of a linear system*. Control, vol. 10, pages 642 – 643, 1966.

[Michailesco 1979] G. P. Michailesco. *Approximation des systèmes complexes par des modèles de dimensions réduites*. Doctoral thesis, Université de Paris XI, France, 1979.

[Ménézo 1999] C. Ménézo. *Contribution à la modélisation du comportement thermique des bâtiments par couplage de modèles réduits*. Doctoral thesis, INSA de Lyon, Lyon, France, 1999.

[Mokhtari 1988] A. M. Mokhtari. *Etude du comportement thermique des bâtiments en contact avec le sol par l'analyse modale*. Doctoral thesis, INSA de Lyon, Lyon, France, 1988.

[Moore 1981] B. C. Moore. *Principal component analysis in linear systems: controllability, observability, and model reduction*. IEEE Transactions on Automatic Control, vol. 26, no. 1, pages 17–32, 1981.

[Morlot 1999] R. Morlot. *Contribution au dévéloppement de méthodes de réduction de systèmes thermiques complexes*. Doctoral thesis, INSA de Lyon, Lyon, France, 1999.

[Oulefki 1993] A. Oulefki. *Réduction de modèles thermiques par amalgame modal*. Doctoral thesis, Ecole Nationale des Ponts et Chaussées, France, 1993.

[Paul 1996] N. D. Paul. The effect of grout thermal conductivity on vertical geothermal heat exchanger design and performance. Master's thesis, South Dakota State University, USA, 1996.

[Petit 1991] D. Petit. *Réduction de modèles de connaissance et identification de modèles d'ordre réduit*. Doctoral thesis, Université de Provence (Aix-Marseille I), France, 1991.

[Philippe *et al.* 2009] M. Philippe, M. Bernier and D. Marchio. *Validity ranges of three analytical solutions to heat transfer in the vicinity of single boreholes*. Geothermics, vol. 38, no. 4, pages 407 – 413, 2009.

[Pinel 2003] P. Pinel. Amélioration, validation et implantation d'un algorithme de calcul pour évaluer le transfert thermique dans les puits verticaux de systèmes de pompes a chaleur géothermiques. Master's thesis, Département de Génie Mécanique, Ecole Polytechnique de Montréal, Montréal, Canada, 2003.

[Remund 1999] C. P. Remund. *Borehole thermal resistance: laboratory and field studies*. ASHRAE Transactions, vol. 105, pages 439 – 445, 1999.

[Rottmayer *et al.* 1997] S. P. Rottmayer, W. A. Beckman and J. W. Mitchell. *Simulation of a Single Vertical U-Tube Ground Heat Exchanger in an Infinite Medium*. ASHRAE Transactions, vol. 103, no. 2, pages 651–659, 1997.

[Sharqawy *et al.* 2009] M. H. Sharqawy, E. M. Mokheimer and H. M. Badr. *Effective pipe-to-borehole thermal resistance for vertical ground heat exchangers*. Geothermics, vol. 38, no. 2, pages 271 – 277, 2009.

[Sheriff 2007] F. Sheriff. Génération de facteurs de réponse pour champs de puits géothermiques verticaux. Master's thesis, Département de Génie Mécanique, Ecole Polytechnique de Montréal, Montréal, Canada, 2007.

[Shonder & Beck 1999] J. A. Shonder and J. V. Beck. *Field test of a newmethod for determining soil formation thermal conductivity and borehole resistance*. ASHRAE Transactions, vol. 106, pages 843–850, 1999.

[Shonder *et al.* 1999] J. A. Shonder, V. Baxter, J. Thornton and P. Hughes. *A new Comparison of vertical ground heat exchanger design methods for residential applications*. ASHRAE Transactions, vol. 105, no. 2, 1999.

[Sicard *et al.* 1985] J. Sicard, P. Bacot and A. Neveu. *Analyse modale des échanges thermiques dans le bâtiment*. International Journal Heat transfer, vol. 28, pages 111 – 123, 1985.

[Spitler *et al.* 2009] J. Spitler, J. Cullin, E. Lee, D. Fisher, M. Bernier, M. Kummert, P. Cui and X. Liu. *Preliminary Intermodel Comparison of Ground Heat Exchanger Simulation Models*. In Effstock 2009, numéro 115, Stockholm, 2009.

[Thornton *et al.* 1997] J. W. Thornton, P. J. Hughes, T. P. McDowell, D. Pahud, J. A. Shonder and G. Hellström. *Residential Vertical Geothermal Heat Pump System Models: Calibration to data*. ASHRAE Transactions, vol. 103, no. 2, pages 660–674, 1997.

[Trillat-Berdal *et al.* 2006] V. Trillat-Berdal, B. Souyri and G. Fraisse. *Experimental study of a ground-coupled heat pump combined with thermal solar collectors*. Energy and Buildings, vol. 38, no. 12, pages 1477 – 1484, 2006.

[Yang *et al.* 2010] H. Yang, P. Cui and Z. Fang. *Vertical-borehole ground-coupled heat pumps: A review of models and systems*. Applied Energy, vol. 87, no. 1, pages 16 – 27, 2010.

[Yavuzturk & Spitler 1999] C. Yavuzturk and J. D. Spitler. *A short time step response factor model for vertical ground loop heat exchangers*. ASHRAE Transactions, vol. 105, no. 2, pages 475–485, 1999.

[Yavuzturk & Spitler 2000] C. Yavuzturk and J. D. Spitler. *Comparative study of operating and control strategies for hybrid ground-source heat pump systems using a short time step simulation model*. ASHRAE Transactions, vol. 106, no. 2, pages 192–209, 2000.

[Yavuzturk *et al.* 1999] C. Yavuzturk, J. D. Spitler and S. J. Rees. *A Transient Two-Dimensional Finite Volume Model for the Simulation of Vertical U-Tube Ground Heat Exchangers*. ASHRAE Transactions, vol. 105, no. 2, pages 465–474, 1999.

[Yavuzturk *et al.* 2009] C. Yavuzturk, A. D. Chiasson and J. E. Nydahl. *Simulation Model for Ground Loop Heat Exchangers*. ASHRAE Transactions, vol. 115, no. 2, pages 45–59, 2009.

[Yavuzturk 1999] C. Yavuzturk. *Modeling of vertical ground loop heat exchangers for ground source heat pump systems*. Doctoral thesis, Oklahoma State University, USA, 1999.

[Young 2001] T. Young. Development, verification, and design analysis of the borehole fluid thermal mass model for approximating short term borehole thermal response. Master's thesis, Oklahoma State University, USA, 2001.

[Zeng *et al.* 2002] H. Y. Zeng, N. R. Diao and Z. H. Fang. *A Finite Line-Source Model for Boreholes in Geothermal Heat Exchangers*. Heat Transfer - Asian Research, vol. 31, no. 7, pages 558–567, 2002.

[Zeng *et al.* 2003] H. Zeng, N. Diao and Z. Fang. *Efficiency of Vertical Geothermal Heat Exchangers in the Ground Source Heat Pump System*. Journal of Thermal Science, vol. 12, no. 1, pages 77–81, 2003.

Annexes

Appendix A

Theoretical bases of modal analysis

A.1 Diagonalization

The homogeneous problem associated with Eq. 1.63 is:

$$C\dot{T}(t) = AT(t) \tag{A.1}$$

Thus, the solution of Eq. A.1 is generally in the form of:

$$T(t) = \psi \mathrm{e}^{\lambda t} \tag{A.2}$$

Here, ψ is called "relaxation mode". This form of solution leads to:

$$\lambda C\psi \mathrm{e}^{\lambda t} = A\psi \mathrm{e}^{\lambda t} \tag{A.3}$$

We get:

$$(A - \lambda C)\psi = 0 \tag{A.4}$$

Considering the case of other than $\psi = 0$, we have necessarily:

$$\det(A - \lambda C) = 0 \quad \text{or} \quad \det(C^{-1}A - \lambda I) = 0 \tag{A.5}$$

From this condition, the solution is obtained by finding the eigenvectors λ_i of the matrix $C^{-1}A$ to which the eigenvectors ψ_i are relative. Accordingly, these eigenvectors construct the transition matrix P:

$$P = \begin{bmatrix} (\psi_1)_1 & (\psi_2)_1 & . & . & (\psi_n)_1 \\ (\psi_1)_2 & (\psi_2)_2 & . & . & (\psi_n)_1 \\ . & . & . & & . \\ . & . & & . & . \\ (\psi_1)_n & (\psi_2)_n & . & . & (\psi_n)_n \end{bmatrix}_{(n\times n)} \tag{A.6}$$

The orthogonality (see Annex A.2) of ψ_i vis-a-vis the capacitance matrix C gives the following equation[1]:

$$P^T C P = I \quad \text{or} \quad P^T = P^{-1}C^{-1} \tag{A.7}$$

[1]Here, P is newly composed of normalized vectors of ψ_i regarding C

From the Eq. A.3 ($\lambda_i C\psi_i = A\psi$), we can directly obtain:

$$P^T AP = \begin{bmatrix} \lambda_1 & & & & & \\ & \lambda_2 & & & 0 & \\ & & \lambda_3 & & & \\ & & & . & & \\ & & & & . & \\ & 0 & & & . & \\ & & & & & \lambda_n \end{bmatrix} = W = P^{-1}C^{-1}AP \tag{A.8}$$

This matrix W is diagonal and the eigenvalues (λ_i) become the diagonal elements. The last term of Eq. A.8 shows the digonalization of Eq. 1.63, replacing $T(t)$ by a new state vector $X(t)$:

$$\begin{aligned} &\text{Let} \quad T(t) = PX(x), \\ &\dot{X}(t) = \underbrace{P^{-1}C^{-1}AP}_{W} X(t) + P^{-1}C^{-1}BU(t) \end{aligned} \tag{A.9}$$

A.2 Characteristics of modal analysis

A.2.1 Real-negative eigenvalues

Considering two conjugate eigenvectors:

$$\begin{aligned} \lambda &= a + bj \quad \text{for } \psi \\ \overline{\lambda} &= a - bj \quad \text{for } \overline{\psi} \end{aligned} \tag{A.10}$$

From Eq. A.4, we get:

$$(A - \lambda C)\psi = 0 \tag{A.11a}$$

$$(A - \overline{\lambda} C)\overline{\psi} = 0 \tag{A.11b}$$

With multiplying Eq. A.11a by $\overline{\psi}^T$, Eq. A.11b by ψ^T:

$$\overline{\psi}^T A\psi = (a + bj)\overline{\psi}^T C\psi \tag{A.12a}$$

$$\psi^T A\overline{\psi} = (a - bj)\psi^T C\overline{\psi} \tag{A.12b}$$

By subtracting Eq. A.12b from Eq. A.12a, it gives:

$$0 = 2bj\psi^T C\overline{\psi} \tag{A.13}$$

If the matrices C and A are defined symmetrical[2], the equation is obliged to have $b = 0$. As a result, all the eigenvalues are always real for the case.

Additionally, multiplying Eq. A.11 by ψ^T, we get:

$$\lambda\psi^T C\psi = \psi^T A\psi \tag{A.14}$$

It gives:

[2] C is normally defined positive and symmetrical in a thermal system, but A can be non-symmetrical depending on mesh types and used methods.

$$\lambda = \frac{\psi^T A \psi}{\psi^T C \psi} = -\frac{\psi^T K \psi}{\psi^T C \psi} \tag{A.15}$$

Therefore, the eigenvalues are negative values because $K = -A$ and C are defined positive.

A.2.2 Orthogonality

Considering two distinct eigenvalues λ_i and λ_j, correspondent with ψ_i and ψ_j respectively. From the definition, it gives:

$$\lambda_i C \psi_i = A \psi_i \tag{A.16a}$$

$$\lambda_j C \psi_j = A \psi_j \tag{A.16b}$$

Multiplying Eq. A.16a by ψ_j^T and Eq. A.16b by ψ_i^T, and then subtracting, we obtain:

$$0 = (\lambda_i - \lambda_j) \psi_i^T C \psi_j \tag{A.17}$$

As it is known that $\lambda_i \neq \lambda_j$ by hypothesis, it gives compulsorily:

$$\psi_i^T C \psi_j = 0 \tag{A.18}$$

This equation can be interpreted as the orthogonality of the eigenvectors ψ_i and ψ_j vis-a-vis the matrix C.

A.2.3 Normalization of eigenvectors

For two eignevectors U, V of a thermal system, we can define their scalar product as follows:

$$\langle U, V \rangle = U^T C V = V^T C U = \langle V, U \rangle \tag{A.19}$$

In the our case, the norm of the vector ψ_i is given by:

$$\|\psi_i\|^2 = \psi_i^T C \psi_i \tag{A.20}$$

Thus, the modal basis can be normalized by using for all the eigenvectors:

$$\hat{\psi}_i = \frac{\psi_i}{\|\psi_i\|} \quad \text{with} \quad \|\hat{\psi}_i\| = 1 \tag{A.21}$$

This normalization regarding C gives following numerical advantages.

Above all, if ψ_i is the eigenvector of $C^{-1}A$, $C^{\frac{1}{2}}\psi_i$ is the eigenvector of $C^{-\frac{1}{2}} A C^{-\frac{1}{2}}$ from the followings:

$$\begin{aligned} C^{-1} A \psi_i &= \lambda_i \psi_i \qquad \Leftrightarrow \\ C^{-\frac{1}{2}} A \psi_i &= \lambda_i C^{\frac{1}{2}} \psi_i \qquad \Leftrightarrow \\ (C^{-\frac{1}{2}} A C^{-\frac{1}{2}}) C^{\frac{1}{2}} \psi_i &= \lambda_i C^{\frac{1}{2}} \lambda_i \end{aligned} \tag{A.22}$$

$C^{-\frac{1}{2}}AC^{-\frac{1}{2}}$ is always symmetrical (Eq. A.23) under the condition that both C and A are symmetrical. This characteristic has an interest of rapid calculation for its diagonalization.

$$[C^{-\frac{1}{2}}AC^{-\frac{1}{2}}]^T = [C^{-\frac{1}{2}}]^T A^T [C^{-\frac{1}{2}}]^T = C^{-\frac{1}{2}}AC^{-\frac{1}{2}} \tag{A.23}$$

In addition, the followed equation can be proved with the eigenvector orthogonality:

$$I = P^T C P \quad \text{or} \quad P^{-1} = P^T C \tag{A.24}$$

With this correlation, P^{-1} can be directly obtained instead of effectuating a matrix inversion. This method allows a fast calculation for a problem of large-size systems, at the same time, preventing round-off errors.

Appendix B

Simple example of reduction process

A simple wall example of the Marshall reduction technique is presented herein, which is supposed to be easier and more explicit to follow up. Marshall method uses the temporal criterion that is simple, but it has the same procedure of reduction with Litz and LA. Hence, it can be an analogy for understanding the borehole case (LA) that is presented in the text.

B.1 Building wall example

As shown in Fig. B.1, we may consider a simple wall case. For simplicity, 1D modeling of the finite volume method (FVM) was employed. The correspondent wall properties and simulation properties are listed in Tab. B.1.

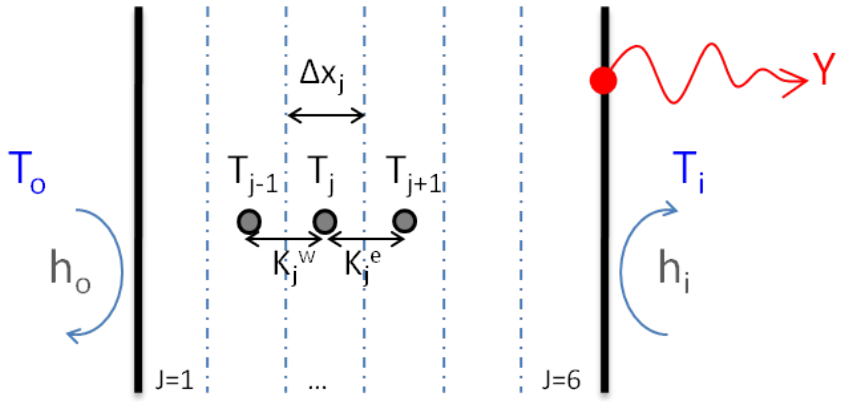

Figure B.1: Schematic of the simple wall example

Eq. B.1 and Eq. B.2 shows how the state model matrices (Eq. 1.63-1.64) can be comprised for the given meshes of the simple wall shown in Fig2-1-1 when using the equivalent mesh space Δ x.

$$\rho_j c_j \Delta x_j \frac{\partial T_j}{\partial t} = K_j^w (T_{j-1} - T_j) + K_j^e (T_{j+1} - T_j)$$
$$\text{where,} \quad K^w_{j(2,\ldots,5)} = K_j^e = \frac{k}{\Delta x} \quad K_1^w = \frac{1}{\frac{\Delta x}{2k} + \frac{1}{h_o}} \quad K_6^e = \frac{1}{\frac{\Delta x}{2k} + \frac{1}{h_i}} \tag{B.1}$$

Table B.1: Materials and simulation properties

Parameter	Symbol	Unit	Value
conductivity	k	W/mK	2300
specific heat	c	J/kgK	1000
thickness	x	m	0.12
Outside convective coefficient	h_o	W/m^2K	3
Inside convective coefficient	h_i	W/m^2K	18
Initial temperature		K	10

$$\varphi_{int} = -K_6^e(T_{int} - T_6) \tag{B.2}$$

These equations can be expressed by a matrix form:

$$\underbrace{\begin{bmatrix} \times & & & & & \\ & \times & & & 0 & \\ & & \times & & & \\ & & & \times & & \\ & 0 & & & \times & \\ & & & & & \times \end{bmatrix}}_{C} \dot{T} = \underbrace{\begin{bmatrix} \times & \times & & & & \\ \times & \times & \times & & 0 & \\ & \times & \times & \times & & \\ & & \times & \times & \times & \\ & 0 & & \times & \times & \times \\ & & & & \times & \times \end{bmatrix}}_{A} T + \underbrace{\begin{bmatrix} & \\ 0 & \\ & \\ & \\ & \times \end{bmatrix}}_{B'} \underbrace{\begin{Bmatrix} T_{ext} \\ T_{int} \end{Bmatrix}}_{U} \tag{B.3}$$

$$C_{ii} = \rho_i c_i \Delta x_i \qquad A_{ii} = -(K_i^w + K_i^e) \qquad B'_{62} = K_6^e$$
$$A_{ij} = K_i^w \text{ or } K_i^e$$

$$\underbrace{\begin{bmatrix} \varphi_{int} \end{bmatrix}}_{Y} = \underbrace{\begin{bmatrix} 0 & & K_6^e \end{bmatrix}}_{J} T + \underbrace{\begin{bmatrix} 0 & -K_6^e \end{bmatrix}}_{D} \underbrace{\begin{Bmatrix} T_{ext} \\ T_{int} \end{Bmatrix}}_{U} \tag{B.4}$$

From these state equations, the basis has to be changed by the diagonalization. From the correlation (Eq. 1.81), we get the new state models of modal basis with the values obtained with the properties:

$$\begin{bmatrix} \dot{X}_1 \\ \dot{X}_2 \\ \dot{X}_3 \\ \dot{X}_4 \\ \dot{X}_5 \\ \dot{X}_6 \end{bmatrix} = \underbrace{\text{diag} \begin{bmatrix} -5.85e-5 \\ -6.38e-4 \\ -2.01e-3 \\ -3.88e-3 \\ -5.74e-3 \\ -7.11e-3 \end{bmatrix}}_{W} \begin{bmatrix} X_1 \\ X_2 \\ X_3 \\ X_4 \\ X_5 \\ X_6 \end{bmatrix} + \underbrace{\begin{bmatrix} 1.14e-4 & 2.87e-5 \\ -1.94e-4 & 3.42e-5 \\ -1.88e-4 & -3.17e-5 \\ -1.56e-4 & 2.61e-5 \\ 1.11e-4 & 1.85e-5 \\ 5.76e-5 & -9.60e-6 \end{bmatrix}}_{B} \underbrace{\begin{Bmatrix} T_{ext} \\ T_{int} \end{Bmatrix}}_{U} \tag{B.5}$$

$$\underbrace{\begin{bmatrix} \varphi_{int} \end{bmatrix}}_{Y} = \underbrace{\begin{bmatrix} 1.32 & 1.57 & -1.46 & 1.20 & 0.85 & -0.44 \end{bmatrix}}_{H} \begin{bmatrix} X_1 \\ X_2 \\ X_3 \\ X_4 \\ X_5 \\ X_6 \end{bmatrix} + \underbrace{\begin{bmatrix} 0 & -2.95 \end{bmatrix}}_{D} \underbrace{\begin{Bmatrix} T_{ext} \\ T_{int} \end{Bmatrix}}_{U} \tag{B.6}$$

As seen in Eq. B.5, the diagonal matrix W can be set in a ascending order of eigenvalues with arranging the correspondent rows or column of the matrices B, H.

B.2 Model reduction

The simple wall example (n=6) can be reduced by the order of 2 (m=2) with Marshall's method for a one-hour time step (Δt) because the first two modes are the slow modes that are regarded important for the transient behavior according to the Marshall criterion: $\tau_i > 900s(\Delta t/4)$: τ= 17060, 1567, 497, 258, 174, 141. Thus, the reduced-order equations are as follows:

$$\begin{bmatrix}\dot{X}_1\\ \dot{X}_2\end{bmatrix} = \underbrace{\mathrm{diag}\begin{bmatrix}-5.85e-5\\ -6.38e-4\end{bmatrix}}_{W_1}\begin{bmatrix}X_1\\ X_2\end{bmatrix} + \underbrace{\begin{bmatrix}1.14e-4 & 2.87e-5\\ -1.94e-4 & 3.42e-5\end{bmatrix}}_{B_1}\underbrace{\begin{Bmatrix}T_{ext}\\ T_{int}\end{Bmatrix}}_{U} \tag{B.7}$$

$$\underbrace{[\varphi_{int}]}_{Y} = \underbrace{[1.32 \quad 1.57]}_{H_1}\begin{bmatrix}X_1\\ X_2\end{bmatrix} + \underbrace{[0.10 \quad -2.92]}_{G}\underbrace{\begin{Bmatrix}T_{ext}\\ T_{int}\end{Bmatrix}}_{U} \tag{B.8}$$

$$= D - H_2W_2^{-1}B_2$$

Fig. B.2 is a comparison between the complete (n=6) and the reduced model (m=2) when adopting variation for the solicitation vector: T_{int}=20°C and T_{ext}=5×sin($hour/24 \times 2\pi$)°C. The results between the two models are very similar in spite of the different orders in the given one-hour time step.

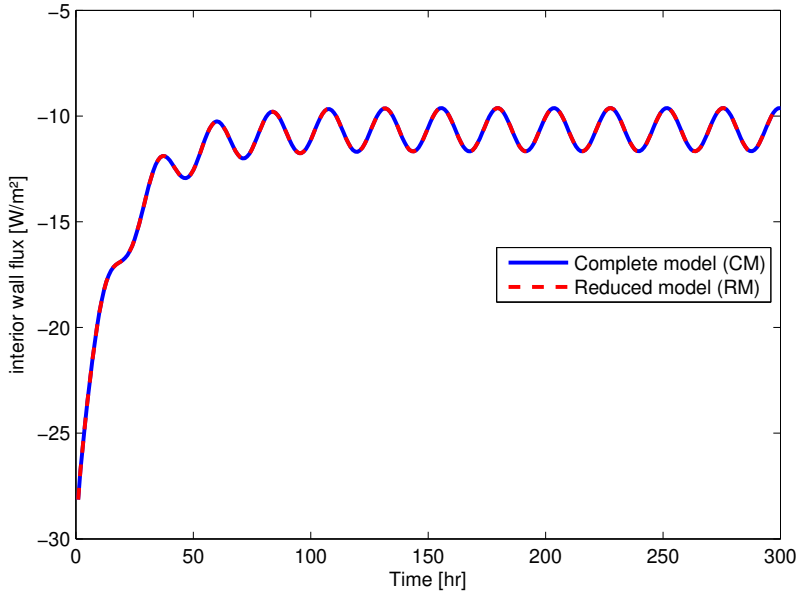

Figure B.2: Model comparison between CM and RM for the simple wall example

Appendix C

Choice of Δt_i for sub-zones

First of all, it is worthwhile to note that the generalization of a choice of time-steps is difficult in this kind of reduced model (decomposed and then coupled). This difficulty can be explained by the bode diagram (Fig. 2.13 presented in the section 2.1.4.3) as follows:

First, the divergent point (Fig. 2.13) between complete model (CM) and reduced model (RM) is affected by several parameters, to which the mesh number and size, soil or grout properties, and observation types (flux or temperatures) belong. Second, excitation of input values cannot be predicted; in fact, the bode diagram is plotted only for a certain excitation (i.e. periodic). Third, even if a critical point related to a time-step is given, it is also hard to interpret for a real simulation. In fact, the RM method is typically applied not to obtain the exactly same results with CM but to predict similar results within a acceptable range of error (cf. 0.01 ˚C difference of RM-CM in Fig. 4.28 in the section 4.3.3). This error cannot be predicted before simulation.

However, some useful points for selecting the time-steps in the 3D-RM will be discussed in this Annex.

C.1 Sub-zones sizes

Before discussions on the time-steps, sub-zone sizes have to be determined. Here, an efficient mesh generation is proposed as it is required for typical numerical models. For example, 4 sub-zones: 0-1m, 1-3m, 3-20m, 20-100m and the correspondent mesh numbers: 474, 140, 203, and 201, respectively are used in the section 2.1.3. Even if the last sub-zone covers a large soil domain of 20-100m, only 201 meshes are used. Any different decomposition can be allowed except "No decomposition"; applying RM to entire domain (1-100m) without decomposition has caused inefficiency and inaccuracy [Kim *et al.* 2009].

C.2 Time-steps ratio

A time-steps ratio has briefly been discussed in the section 2.2.2. Time steps of big ratio cause higher errors while less calculation time is required as the total number of computation for larger sub-zones are fewer during simulation in the case of the big ratio. The errors are due to the fact that the temporal coupling is used for the implicit scheme where the future temperature evolution cannot be accurately predicted.

The first sub-zone including the GHE is recommended to have sufficiently a large radius in order to lead to a small temperature gradient at the border, consequently allowing fewer errors coming from this coupling method. For example, only less than 0.1 ˚C is observed when a first zone of 1m radius is used in the examples of the section (2.2.2) in spite of an unrealistic heat injection case.

C.3 Selection example of time-steps Δt_i

It is obviously proven [Kim *et al.* 2009] that a properly large time-step according to its physical time-scale of a given domain must be chosen for use of reduction techniques. For example, a RM model with a time step of 1sec cannot acceptably predict thermal evolution of large thermal system (e.g. a soil volume of 100m by 100m) as accuracy of the RM selecting very few modes for transient analyses is generally dependent to the time-step. It can be intuitively regarded. Thus, larger time steps should be chosen as the domain sizes become bigger (e.g. from the GHE to the far-field).

Since it is difficult to find a theoretically critical time-step for a given domain as mentioned in the beginning, arbitrary but increasing time-steps have been used in the chapter 2: 1hr, 6hr, 1day, and 1week for the sub-zones (0-1m, 1-3m, 3-20m, and 100m as shown above). A RM with these arbitrary time-steps has predicted transient thermal results in a good agreement with the original CM.

This means in other words that the selection of time-steps is not too sensitive to the RM accuracy. In fact, several simulations with various ranges of time-steps have given very similar results[1] (for example, 1hr, 1day, 1week, and 6weeks). Only attention has to be paid not to choose a time-step too small for larger domains[2]; not efficient and sometimes causing a convergence problem. Therefore, the developed RM can be directly used with a relatively liberal choice of time-steps.

[1] Slightly different errors between different cases of Δt_i seem to be due to not the reduction technique but the temporal coupling scheme

[2] For simulations with a time-step of 1 minute, it is not recommended to use this 1min time-step for the second sub-zone (e.g. a sub-zone of 0.4-2.0m radius in Chapter 4)

Appendix D

Thermal response test

Generally, the thermal response test is carried out to estimate the soil conductivity together with the borehole resistance R_b. The main idea is to experimentally reproduce a thermal condition that can be directly compared with a formula of analytical solution such as the ILS theory. Since a constant heat flow rate q has to be kept during the test, a heat-injection machine is normally required. Accordingly, a slope of the curve obtained from the experimental data means a combination of thermal properties as given in Eq. D.1. The details are given in Gehlin's work [Gehlin 2002].

$$m = \frac{Q}{4\pi k_s H} \tag{D.1}$$

Fig. D.1 shows the thermal response data that were obtained by our own TRT. In this figure, the data before 10 hours are not used, regarding that the start-up times are normally disturbed by the initial conditions. The obtained slope value -1.1759 is used to calculate the thermal conductivity k_s in given conditions (Eq. D.2).

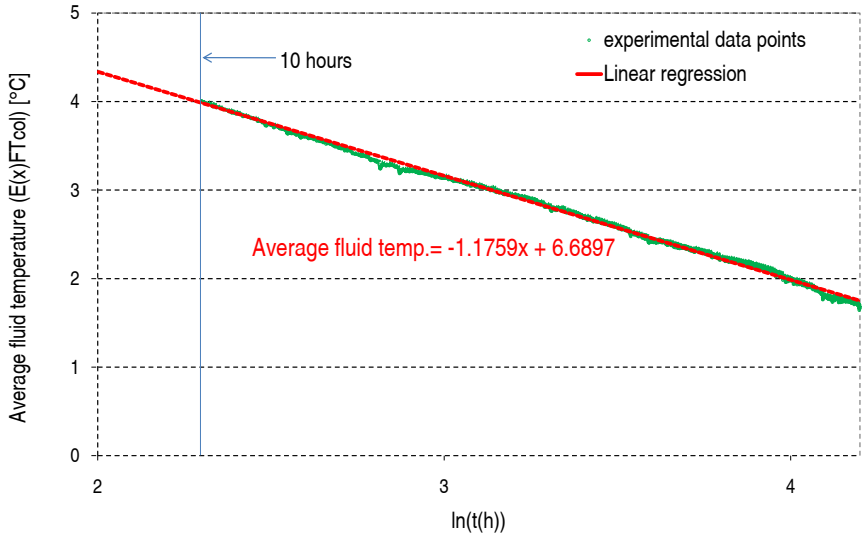

Figure D.1: Average temperatures of E(x)FT used for determination of k_s

$$k_s = \frac{Q}{4\pi m H} = \frac{4894}{4\pi(-1.1759)(40+39+40)} = 2.78\mathrm{W/m^{\circ}C} \tag{D.2}$$

From this test, we get a conductivity value 2.78$\mathrm{W/m^{\circ}C}$. However, as explained in the section 4.1.2.2, the injection power was measured near the collectors (col) by $E = \dot{m}c\Delta T$. The power must be measured at the borehole head (bore) according to the theory since an non-negligible portion of total heat exchanges is found in the connection soil part. In order to calculate the fluid E(x)FTbore, the model 3D-RM is in advance utilized. For use of the 3D-RM model, the conductivity, one of the main input values has to be beforehand determined. Therefore, an iterative calculation was effectuated for this calibration.

The calibrated conductivity 2.3 $\mathrm{W/m^{\circ}C}$ is obtained from the iterative process above mentioned. Fig. D.2 shows the simulation results of the given value. The ExFTcol (3D-RM) is close to the experimental curve. In fact, more than 0.4˚C difference is found between Δ T (col) and ΔT (bore). Actually, with the difference, we can get a value of 2.32 very close to the used conductivity 2.3 W/m˚C (Eq. D.3). On the other hand, the initial temperature of the connection soil model influences the behavior of temperature evolution but only resulting in vertical shifting of the curves. Thus, this calibration simulation allows also to determine the initial soil temperature for the connection model. 8˚C is found as an adequate initial temperature.

$$k_s^{new} = \frac{\dot{m}c\Delta T_{bore}(Q)}{4\pi mH} = k_s^{old} \times \frac{\Delta T_{bore}}{\Delta T_{col}} = 2.78 \times \frac{(2.87 - 0.47)}{2.87} = 2.32\mathrm{W/m^{\circ}C} \qquad \text{(D.3)}$$

Finally, the first case of k_s=2.78 is also presented in Fig. D.3. Other than the calibrated conductivity, the curve ExFTcol (3D-RM) is not well matched with the experimetal one.

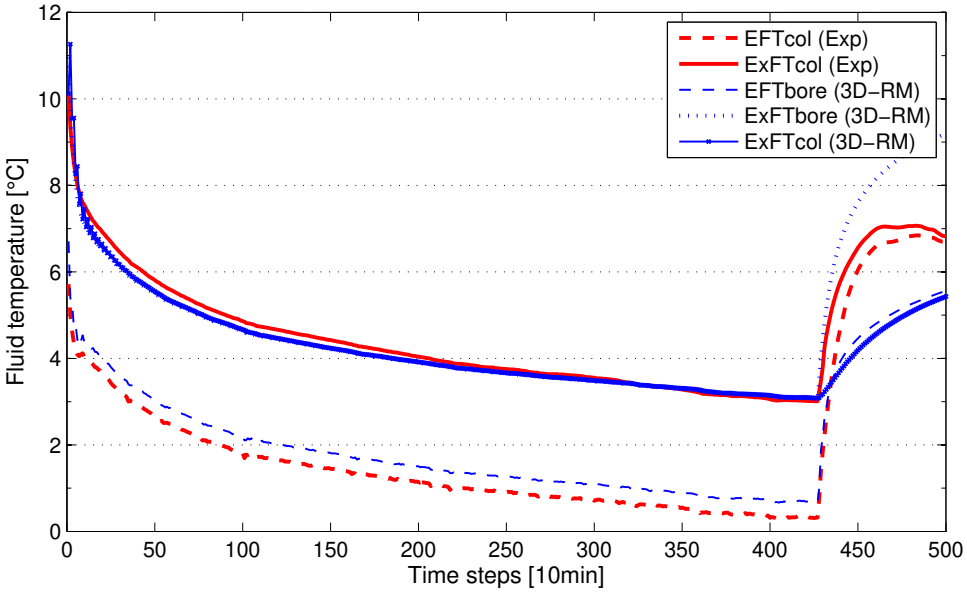

Figure D.2: results k_s=2.3 and T_0=8˚C

- EFTcol: Entering fluid temperature to boreholes, measured near the collectors
- EFTbore: Entering fluid temperature to boreholes, measured at the borehole head
- ExFTcol: Exiting fluid temperature from boreholes, measured near the collectors

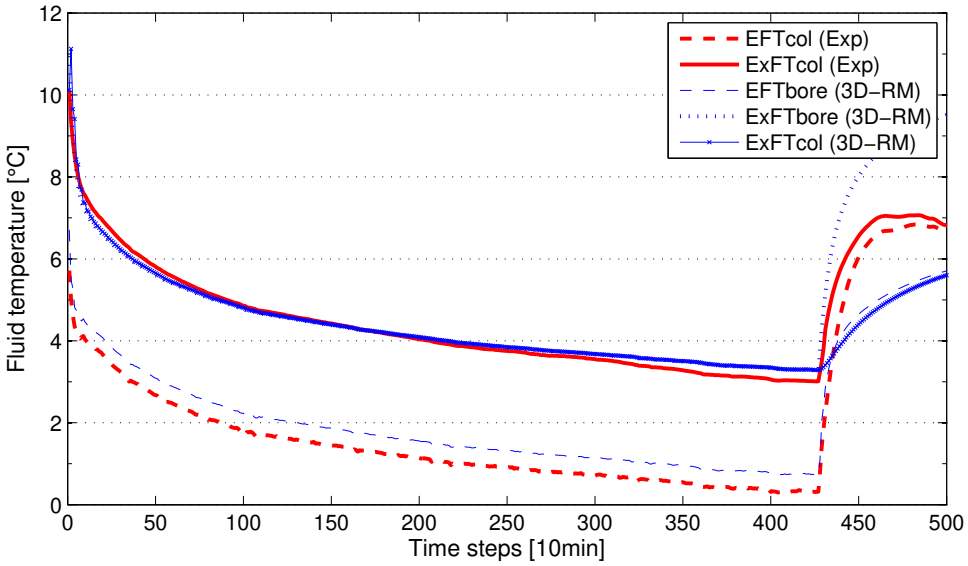

Figure D.3: results k_s=2.78 and T_0=8˚C

- ExFTbore: Exiting fluid temperature to boreholes, measured at the borehole head

Appendix E

Comparison of various k_s cases

The error range between different k_s that are commonly regarded as the most important soil property is tested even if a pertinent calibration is presented in the Appendix D. Three values of conductivity are chosen around the calibrated value: 2.0, 2.5, and 3.0 $\mathrm{W/m°C}$. Fig. E.1 gives simulation curves with the three conductivities. The errors [˚C] from the experimental data are also plotted. The variation of conductivity of 1.0 $\mathrm{W/m°C}$ (between 2.0 and 3.0) causes less than 0.5 ˚C in all the periods tested, where the GCHP functions as a real case.

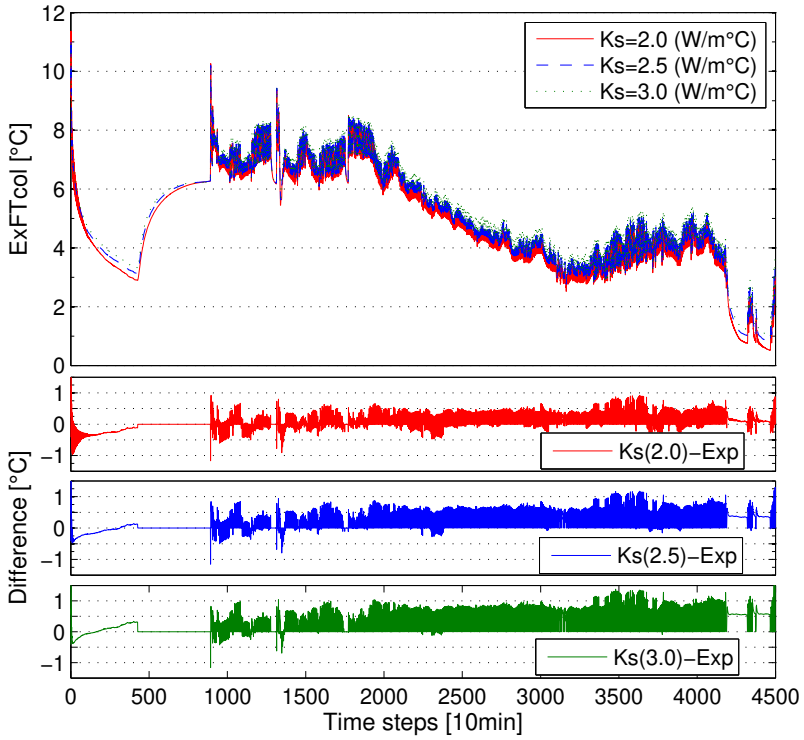

Figure E.1: Comparison of different k_s for the experimental case

Appendix F

Modeling of the OSU experimental set-up

Fig. 5.1 in the chapter 5 was plotted with the experimental data obtained from a test facility situated in Oklahoma State University. Three vertical boreholes arranged in a line, spaced 6.1m apart. The working fluid is water. Although data was collected on 1 minute intervals, the data are hourly averages for simulation of one-hour time step. The simulation conditions used are presented in Tab. F.1.

Table F.1: Parameters used for simulation of the OSU case

Parameter	Unit	Value
Average borehole depth	74.68	m
Borehole diameter	114.3	mm
Borehole shank spacing	20.32	mm
Borehole spacing	6.1	m
Ground thermal conductivity	2.55	W/m˚C
Ground heat capacity		
Pipe thermal conductivity	0.3895	W/m˚C
Undisturbed ground temperature	17.3	˚C
Nominal fluid flow rate	0.631	L/s

For the 3D-RM simulation, the 4 sub-zones are used with different time steps 1hour, 6hour, 1day, 1week. The correspondent sub-zoen sizes are 0-1, 1-10, 10-20, and 20-100m in radius. The slice height for all these sub-zones is fixed by 3.7340m, and consequently total 20 slices are used for simulating H=74.68m. The meshes generated by *Gmsh* are given in Fig. F.1.

On the other hand, Fig. F.2 gives the mesh for the borehole domain and g-function for the soil domain used for the HM simulation.

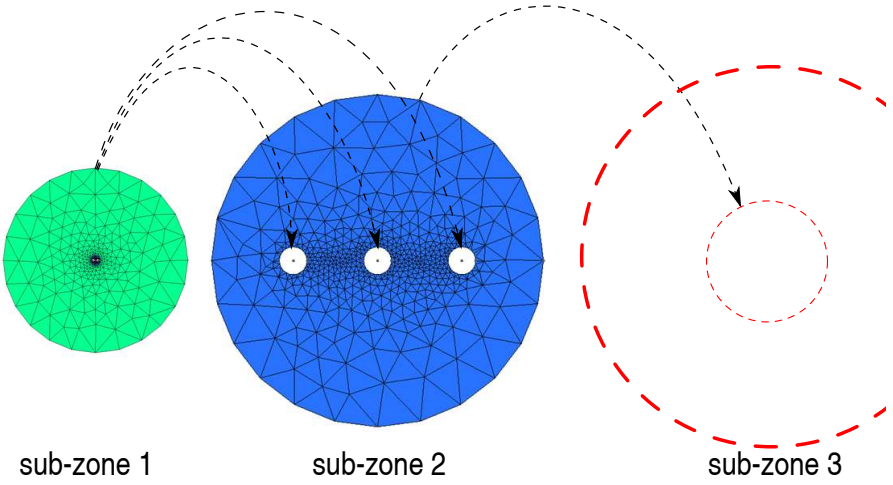

Figure F.1: Used meshes of each sub zone for 3D-RM simulation

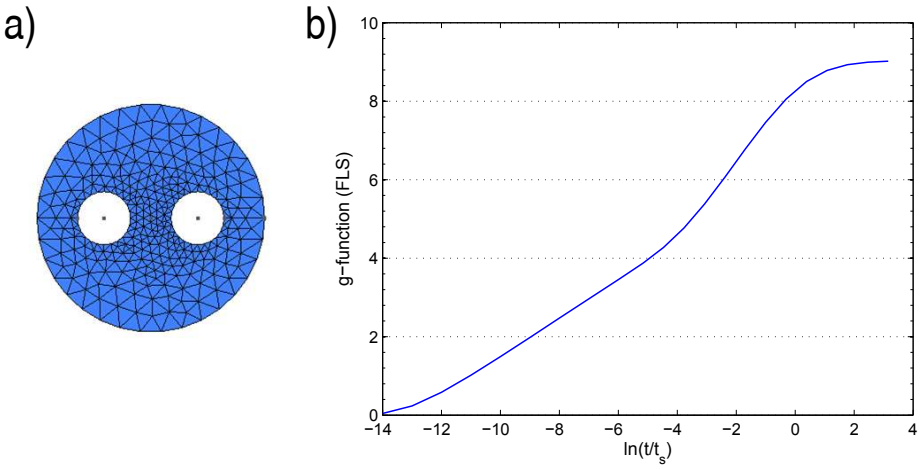

Figure F.2: a) Meshes for the borehole and b) g-function (soil domain) generated by FLS in HM

FOLIO ADMINISTRATIF

THÈSE SOUTENUE DEVANT L'INSTITUT NATIONAL DES SCIENCES APPLIQUÉES DE LYON

NOM : KIM DATE de SOUTENANCE : 21 Mars 2011 (avec précision du nom de jeune fille, le cas échéant) Prénoms : Eui-Jong
TITRE : Development of Numerical Models of Vertical Ground Heat Exchangers and Experimental Verification: Domain Decomposition and State Model Reduction Approach NATURE : Doctorat Numéro d'ordre : 2011-ISAL-0026 École doctorale : Mécanique, Énergétique, Génie Civil, Acoustique (MEGA) Spécialité : Génie Civil
Cote B.I.U. - Lyon : T 50/210/19 / et bis CLASSE :
RÉSUMÉ : Dans le contexte énergétique actuel, les pompes à chaleur (PAC) géothermiques sont parmi les technologies les plus performantes pour augmenter l'efficacité énergétique des bâtiments. Par contre le coût initial et l'encombrement des capteurs enterrés traditionnels peuvent être un obstacle à sa diffusion sur le marché des énergies renouvelables. Pour réduire ces coût et encombrement, une réflexion sur l'adjonction d'un système d'appoint et/ou de recharge thermique du sol aux capteurs enterrés est actuellement en cours de tests. Les outils actuels de modélisation des capteurs enterrés obtiennent en effet de bons résultats mais seulement pour un dimensionnement classique en régime permanent. Les modèles existants ne permettent donc pas de représenter correctement les dynamiques rapides des échanges entre le sol et les tubes et cela est d'autant plus vrai si l'on adjoint le système de recharge solaire. Par conséquence, cette thèse a pour objectif de développer les modèles fins et dynamiques nécessaires à l'analyse des phénomènes transitoires dans les capteurs enterrés eux-mêmes. Un maillage fin, sur les bases de la triangulation de *Delaunay*, est choisi pour le forage ainsi que pour le sol avoisinant. Une approche numérique en 3D (FVM + FEM) peut être obtenue sur les bases de la discrétisation spatiale du domaine. Cette approche appliquée brutalement induirait des temps de calcul très élevés et de toute façon incompatible avec les moyens informatiques ordinaires. Afin de répondre à l'ensemble de ces problèmes, différentes techniques ont été utilisées afin d'accélérer le temps de calcul: décomposition de domaine, emboîtement des pas de temps de calcul pour chaque sous-domaine, réduction des modèles d'états de chaque sous-domaine et finalement couplages temporels et spatiaux des équations de transferts de l'ensemble du problème. Ce dernier est développé particulièrement sur les bases de la méthode des éléments finis. Par ailleurs, un modèle hybride est développé en combinaison de différentes approches. Une approche numérique est adoptée pour la modélisation du puits et la modélisation des transferts de chaleur dans le sol environnant est faite par l'utilisation de solutions analytiques. Ainsi, ce modèle est implanté dans TRNSYS. Une plate-forme expérimentale comprenant trois puits verticaux couplés à une pompe à chaleur géothermique est également présentée. Les résultats expérimentaux sont comparés avec les résultats de la simulation aussi bien au niveau de la température du fluide qu'à la température à différentes profondeurs dans les puits. Le modèle développé donne des résultats très similaires avec ceux qui sont obtenus grâce à l'expérimentation même lors que les pas de temps sont très petits. Il y a des choses à améliorer dans ce modèle développé, mais cela concerne essentiellement l'accélération du temps de calcul. Nous avons constaté que les modèles que nous avons dévéloppés donnent des résultats meilleurs à pas de temps courts que les modèles classiques. Il faut donc bien préciser le domaine d'utilisation de chacun des modèles: consommation sur le long terme, stratégie de contrôle de la PAC, les transferts de chaleur à l'intérieur du puits et etc. De plus, une application du modèle dans le dimensionnement d'échangeurs ainsi que l'investigation de son impact sur le sol avoisinant est également envisagée. Finalement, la méthodologie de modélisation présentée dans ce travail pourrait être aussi utilisé pour différents types d'échangeurs, ouvrant aussi la porte à une analyse fine dans le domaine géothermique.
MOTS-CLÉ : PAC géothermique, exchangeurs géothermique verticaux, réduction des modèles d'état, décomposition de domaine, modèle hybride
Laboratoire(s) de recherches : Centre de Thermique de Lyon (CETHIL)
Directeurs de thèse : Jean-Jacques ROUX
Président de jury : Composition du jury : BERNIER Michel, CAURET Odile, LEFEBVRE Gilles, MARCHIO Dominique, ROUX Jean-Jacques, SPITLER Jeffrey